University of Reading

# Property Enhancement of Supramolecular Polymers for 3D printing

A Thesis submitted in part fulfilment of the degree of Doctor of Philosophy

**Department of Chemistry**

Sara Salimi

**September 2021**

**Declaration of Original Authorship**

I confirm that the research described in this thesis is my own work and that the use of all materials from other sources has been properly and fully acknowledged.

**Sara Salimi**

**Acknowledgments**

First and foremost, I would like to thank my supervisor, professor Wayne Hayes whom without his guidance the completion of this chapter of my life would not have been possible. His useful advice and encouragement kept me going and hopeful. I must also wholeheartedly appreciate his understanding and empathy. I should also thank Dr Lewis Hart, my fumehood neighbour, my friend, and my supervisor, for his priceless advice and friendly guidance and help. He was always available for my crazy questions and gave me confidence to carry on my project. It is also worth to mention that he never left me alone in our numerous road trips to the university of Nottingham. I would also like to extend my appreciation to Dr Barny Greenland, who never stopped believing in me and always got excited with my sudden ideas and supported them until they are actually practical. He has always been available for a chat/video call to help whenever I asked.

I should also thank university of Reading department of chemistry and pharmacy for funding my studies and made it all possible. Additionally, I would like to thank the Chemical analysis Facility (CAF) lab specifically Dr Radoslaw M. Kowalczyk and Dr Pedro Rivas Ruiz for their help with NMR and thermal analysis. Also, my gratitude goes to professor Vitaliy Khutoriyanskiy for allowing me access to the instruments in his lab. I should also appreciate Royal Society of Chemistry for awarding me with researchers mobility grant that enabled me to perform a project at the Centre for Additive Manufacturing at the university of Nottingham. My gratitude also goes to professor Ricky Wildman and professor Derek Irvine, my supervisors at the university of Nottingham for trusting and supporting me during my visit at Nottingham. My progress and learning would not have been possible without the help and guidance of Mark East, Adja Touré and Yuyang Wu. Additionally, I would like to thank Professor Clive Siviour at the university of Oxford who granted me access to his Digital Imaging Correlation facilities with the kind help of his PhD students; Peihao Song and Aaron Graham.

I would also like to express my appreciation to all my friends, lab and office mates during these years who made my PhD enjoyable for all those socialising and little scientific chats over the lunch break. My special thank is for Dr Tahkur Singh Babra who always motivated me and was an inspiration. Dr Jessica Godleman and Dr Charlotte Edwards-Gayle for all their emotional support, little girl-talks and laughter. My fellow lab mates: Dr Ashfaq Afsar, Dr Flavien Leroux, Adam O'Donnell, Alex Gavriel, Annita Mella; my office mates as well as Zoe Selfe, Jasraj Singh Babra and Nada Atallah M Aljuaid who made working in office and lab breaks delightful. My sincere gratitude also goes to the past member of the office and lab

including Dr Jessica Hutchinson, Dr Sam Burholt, Dr Oliver Balmford, Dr Hannah Bowman, Dr Iain Hopkins who shared their experiences in a truly friendly manner.

Last but most importantly, I would like to express my most sincere thanks to my parents who encouraged me and supported me all the way from the day I was born. They always believed in me and my abilities and gave me confidence to achieve whatever I have in my life. They teach me the true meaning of strength, perseverance, love and care for your loved ones. My little brother who constantly injected positive energy into my life and is a complete definition of support and unconditional love, whom I carry his love in my heart forever. My gratitude and appreciation also go to my lovely Auntie's family who kindly accommodated me during my study and never let me feel apart from family. My auntie and my uncle and my two little cousins who are now my second parents and sisters are the kindest and the most precious miracle that I was gifted. I also owe a thank to my very special and beloved husband who I am so grateful for always offering ears to my complains, taking care of me and giving unconditional love to me when I needed the most, who also made me understand what I lacked the most during the course of the first years of my PhD.

**Synopsis**

Supramolecular polymers are a class of polymers made up of low molecular weight polymers/oligomers which self-assemble through different intermolecular interactions and form a *pseudo*-high molecular weight polymer. Supramolecular polymers are recently finding ways into different applications in 3D printing. These materials can be used as inks for different type of 3D printers. The main advantage of supramolecular polymers over conventional polymers is their relatively low processing temperature. Indeed, the dissociation of low energy supramolecular interactions results in decrease in their viscosity hence they can be deposited exploiting a more efficient process. In Chapter 1 is gathered a small review of supramolecular polymers and their application in 3D printing as well as a discussion about their mechanical properties.

Next, an example application of a supramolecular polyurethane with dynamic nature in 3D printing is investigated. In Chapter 2, a supramolecular polyurethane is formulated with poly(ethylene glycol) and paracetamol and was hot-melt extruded to give rise to a drug-release implant. It was predicted that the implant is capable of fully releasing the drug in 8.5 months. Unfortunately, deformation of the printed implants was observed after the release experiment. In order to overcome this undesirable properties, Chapter 3 is investigating the reinforcement of such supramolecular polyurethanes. Utilisation of a bis-urea compound which is synthesised *in situ* during the formation of the supramolecular polyurethane as a by-product was studied as the reinforcing filler material. This method of reinforcement was studied on a variety of supramolecular materials and their properties as well as their processability and printability under extrusion condition were investigated. The same concept was also utilised in order to design a mechanical gradient part using dual-feed extrusion printer in Chapter 4. To realise the design, supramolecular polymer as well as it reinforced analogous were synthesised. These materials were then mixed at different ratios using a 3D printer to produce materials with varied mechanical properties along one dimension of the printed bar. It was shown that upon utilisation of such design, it is possible to direct the applied stress/strain to a part into a desired section.

Additionally, in Chapter 5 reinforcement of supramolecular polymers using silica nanoparticles as inorganic filler was investigated. The effect of surface functionality of the silica nanoparticles on the mechanical properties of the final composite was inspected. Then, incorporation of a type of silica nanoparticles with a reactive functionality into a supramolecular polymer using a reactive extrusion printer was also studied and generation of a nanocomposite with superior mechanical properties through formation of secondary network was observed. In addition, in order to introduce further functionality to a supramolecular polymer with adhesion ability, iron (III) oxide nanoparticles exploited.

Chapter 6 outlined the details of this study. It is demonstrated that the supramolecular polyurethane composite adhesive can bound or debound the substrates when subjected to oscillatory magnetic field. Upon exposure to the field, the magnetic particles generate heat internally which is adequate for dissociation of the supramolecular polymer and hence the loss of its viscosity.

**Table of Contents**

**Table of Figures**

**List of abbreviations**

| | |
|---|---|
| 4,4′-MDI | 4,4’-methylene diphenyl diisocyanate |
| A | Ampere |
| AFM | Atomic Force Microscopy |
| AM | Additive Manufacturing |
| AmMorph | 4-(2-Aminoethyl)morpholine |
| API | Active Pharmaceutical Ingredient |
| APTES | (3-aminopropyl)triethoxysilane |
| *Ar* | Aromatic |
| ATR | Attenuated Total Reflection |
| BHT | Butylated Hydroxytoluene |
| *br* | Broad |
| CAD | Computer-Aided Design |
| CD | Cyclodextrin |
| D | Diameter |
| *Đ* | Polydispersity Index |
| DAC | Dual Asymmetric Centrifuge |
| DBS-iPr | 1,3:2,4-di(4-*iso*propylbenzylidene)-D-sorbitol |
| DIC | Digital Image Correlation |
| DMA | Dynamic Mechanical Analysis |
| DMF | Dimethyl Formamide |
| DMSO | Dimethylsulfoxide |
| DSC | Differential Scanning Calorimetry |
| *E* | Young’s modulus |
| EtOAc | Ethyl Acetate |
| FTIR | Fourier Transform Infrared |
| G | Gauge No. |
| GPC | Gel Permeation Chromatography |
| h | Hour |
| HFIP | Hexafluoro-2-propanol |
| HPLC | High Performance Liquid Chromatography |
| Hz | Hertz |
| IH | Induction Heating |
| IMS | Industrialised Methylated Spirit |
| IR | Infrared |
| kV | Kilo Volt |
| LEVR | Linear Viscoelastic Region |
| LMWA | Low Molecular weight Additives |
| LMWG | Low Molecular Weight Gelator |
| *m* | Multiplet |

| | |
|---|---|
| mA | milliampere |
| MAS | Magic-angle Spinning |
| MGP | Mechanical gradient Polymers |
| min | Minutes |
| MS | Mass Spectrometry |
| N | Newton |
| NMR | Nuclear Magnetic Resonance |
| NP | Nanoparticle |
| OMF | Oscillating Magnetic Field |
| PBS | phosphate buffered saline |
| PDMS | Polydimethylsiloxane |
| PEG | poly(ethylene glycol) |
| PPG | poly(propylene glycol) |
| PPM | Parts per Million |
| PS | Polystyrene |
| PTES | *n*-propyltriethoxysilane |
| PTFE | Polytetrafluoroethylene |
| PU | Polyurethane |
| PVC | Polyvinyl chloride |
| px | Pixel |
| PXRD | Powder X-ray Diffraction |
| REX | Reactive Extrusion Printing |
| RI | Refractive Index |
| RSPU | Reinforced Supramolecular Polyurethanes |
| RT | Retention Time |
| SAXS | Small Angle X-ray Scattering |
| SEM | Scanning Electron Microscope |
| SiNP | Silica Nanoparticles |
| SPU | Supramolecular Polyurethane |
| TEM | transmission electron microscope |
| TEOS | tetraethyl orthosilicate |
| $T_g$ | Glass Transition Temperature |
| TGA | Thermogravimetric Analysis |
| THF | Tetrahydrofuran |
| $T_m$ | Melting Point |
| TMS | Tetramethylsilane |
| UTS | Ultimate Tensile Strength |
| UV | Ultraviolet |
| WAXS | Wide Angle X-ray Scattering |

# 1 Chapter 1

## Introduction

*Chapter 1 is based, in part, on a review article entitled 'Application of Supramolecular Polymers' that has been submitted to Reactive and Functional Polymer by A. D. O'Donnell, S. Salimi, L.R. Hart, T. S. Babra, B. W. Greenland and W. Hayes.*

### 1.1 Abstract

Typically, high molecular weight polymers exhibit desired properties to be used in different industries. However, the poor processability including high viscosity in melt is a problem to be addressed. The high energy demand of their process makes them costly and non-environmentally friendly. One approach to tackle or even overcome the issue of elevated melt viscosities of high molecular weight polymers is to employ *pseudo* high molecular weight polymers *i.e.* lower molecular weight oligomers or polymers that can self-assemble through weaker interactions in solid state to form stable high molecular weight materials under the operating conditions of the desired application. This class of polymers are called supramolecular polymers since the dynamic networks or arrays are assembled through numerous supramolecular, non-covalent interactions. These supramolecular interactions are weaker than covalent bonds (ranging from 7 kcal.mol$^{-1}$ for hydrogen bonds to 0.9 kcal mol$^{-1}$ for van der Waals interactions) still their existence considerably improves the mechanical properties of materials. As a result of assembling via these weaker interactions, the supramolecular networks dissemble into the constituent lower molecular weight oligomers or polymers when the appropriate temperature is applied to enable processing at more readily accessible conditions. This approach can be taken in order to generate materials with desirable properties with improved processability properties. In the following Chapter, the properties of supramolecular materials and their application, specifically, in additive manufacturing is discussed in more detail.

### 1.2 Supramolecular polymers

Polymers are a class of material comprising of repeating units that form a high molecular weight species. The physical properties of polymers are highly dependent on their molecular weight characteristics. For example, impact resistance, tensile strength or melt viscosity all increase by enhancement of the molecular weight of the polymer. As a result of their versatile properties, polymers have been employed in a wide variety of industrial applications ranging

from healthcare to building and construction. Based on their broad range of applications, it has been predicted that the global market size of the polymers will reaches $750 billion by 2025.[1] Undoubtedly, the performance of a specific polymer must meet the desired application and it is possible to tune physical properties by adjustment of the molecular weight or the morphology/structure of the material. For example, it has been found that increasing the molecular weight of a polymer (in the case of non-cross linked polymers), the corresponding mechanical properties improve. However, such desirable improvements in the mechanical properties can also lead to issues in terms of processing the material into the required form as a consequence of the increase in melt viscosity, ultimately to the point where the polymer does not flow. The melt viscosity of a polymer is an important factor in determining their processability, since many production methods require the material to flow continuously, e.g. extrusion or injection moulding under the desired process condition. Supramolecular polymers can be defined as a class of polymers consisting of relatively low molecular weight monomers which can self-assemble spontaneously to form higher ordered structures.[2] The polymerisation occurs through self-complementary[3,4] or complementary[5] recognition motifs. The non-covalent interaction employed include hydrogen bonding,[6,7] π- π stacking[8-10] and metal-ligands[11,12] interactions. The intermolecular interactions that form supramolecular polymers are generally an order of magnitude weaker than covalent linkages employed in 'conventional' polymers.[13,14] Based on the nature of the recognition motifs within their structure, formation of ordered or crystalline structures is even possible. In fact, synthesis of the conventional polymer is through formation of covalent bonds between the monomers which requires more energy to dissociate than supramolecular interactions. The non-covalent bonds are naturally weaker and therefore the polymerisation is thermodynamically reversible *i.e.* changes in temperature or concentration can dissociate/associate the bonds.[15] The effect of concentration and temperature on the structure of the supramolecular polymers is illustrated in Figure 1.2.1.

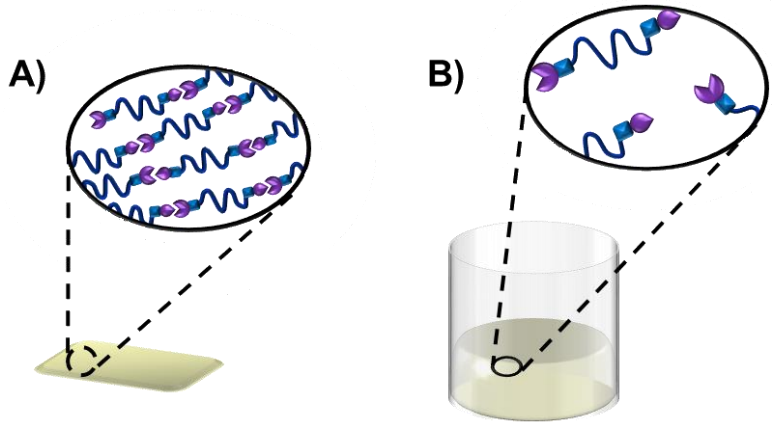


***Figure 1.2.1:*** *Schematic illustration of A) a supramolecular polymer in the solid state and B) illustrates the dissociation of the supramolecular interactions in either the melt or in solution phase resulting in the loss of visocity.*

The degree of supramolecular polymerisation in solution is determined by the association constant of the supramolecular monomers in each specific solvent.[7,16] In brief, as a result of low molecular weight of the discrete polymer molecules combined with the low concentration of assembled polymer molecules in dilute solutions or melt, supramolecular polymers generally exhibit rather low viscosity. Additionally, the tuneability of viscosity of these materials over a range of temperatures is favourable in terms of their employment in various production methods such as extrusion[17] or injection moulding.[18] Undoubtedly, the lack of solvent in these production processes is advantageous since it lowers environmental and safety concerns.[19]

Diffusion and entanglement of the chains occur more efficiently in lower molecular weight polymers. It is generally known that the dissociation of supramolecular interactions such as hydrogen bonding is reversible and requires less energy when compared to strong covalent bonds. The reversible properties of supramolecular materials have already resulted in materials with attractive features such as regaining their mechanical properties (self-healing) after damage[11] or adhesives which bond/debond in response to a specific stimuli.[20,21]

### 1.2.1 Mechanical properties of Supramolecular polymers and their applications

The versatile properties of supramolecular polymers such as their reversibility and relatively low processing temperature as well as their tuneable properties have resulted in emergence of these materials into different applications.[22] However, their mechanical properties are generally inferior to that of conventional polymers as a result of these relatively weak intermolecular interactions.[22] The inferior mechanical properties can be addressed by careful design of the recognition motif. In fact, increasing the concentration of intermolecular interactions with high binding constant or improvement of the micro phase separation of the

materials can lead to an improvement in their mechanical properties. For example, Chen and co-workers introduced a supramolecular polyurethane (SPU) featuring a quadruple hydrogen bonding recognition motif. Such quadruple hydrogen bonding motif was first reported by Meijer *et. al.* for synthesis of supramolecular polymers with comparable mechanical properties to conventional covalent polymers.[23] Chen and co-workersshowed that upon increasing the content of the hard segment (hydrogen bonding) the Young's modulus of the material increased which represents the formation of a stiffer material.[24] However, the cost of this increase is the reduction in modulus of toughness. Young's modulus represents the mechanical stiffness of a material, which is defined as the slope of first linear section of the stress-strain graph of a tensile test, while toughness is defined as the total energy which can be absorbed by a specimen before rupture. This logical trade-off mentioned between the Young's modulus and modulus of toughness is expected since by making a material more brittle it would be more prone to breakage and less elastic, therefore, the overall absorbed energy decreases. The reported tensile test graphs are shown in Figure 1.2.2. The insert shows the increase in Young's modulus by increasing the concentration of hydrogen bonding moiety. Additionally, the graph also exhibits the reduction in the area under the curves which represents the toughness of the material and its capability to absorb energy prior to failure.

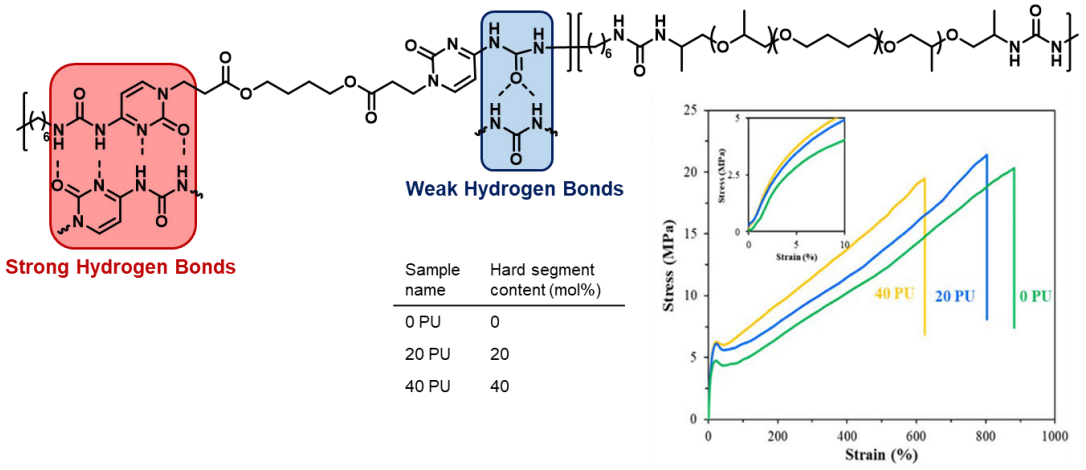


***Figure 1.2.2****: The chemical structure and tensile test graphs of the quadruple hydrogen bonding SPU reported by Chen et.al. with increasing concentration of the hard segment.[24] Reprinted with permission from 1 X. Chen, C. E. Zawaski, G. A. Spiering, B. Liu, C. M. Orsino, R. B. Moore, C. B. Williams and T. E. Long, ACS Appl. Mater. Interfaces, 2020, 12, 32006–32016. Copyright 2021 American Chemical Society."*

The effect of end groups on mechanical properties of the supramolecular polymers is also observed in other systems without quadruple hydrogen bonds at which the introduction of a benzene ring improved the molecular recognition and hence the mechanical properties.[25] The ordering of the hard groups in the reported urea and urethane systems improved upon

introduction of the aromatic ring spacer which adds to stronger recognition between the molecules. In addition, it has been shown that the morphology of soft domain also plays a crucial role in improving the mechanical properties of polymers. Hermido-Merino *et.al.* demonstrated that by selecting a suitable chain extender that is able to produce a better packing within the polymer structure, the mechanical properties (storage modulus) of the polymer were improved by around an order of magnitude compared to materials which only self-assemble through a recognition motif.[26] Additionally, it is shown that the improvement resulted from the efficient packing of the soft segment of the material is more effective than utilising recognition end groups with considerably higher association constant.[26,27] The improvement could originate from a more efficient mixing of the hard/soft domains. However, it must be noted that improving the mechanical properties of supramolecular polymeric systems through enhancement of their hard segments comes with some disadvantages. Although upon tuning the hard segments of supramolecular polymers their stiffness (Young's modulus) increased, their elasticity and modulus of toughness decreased. Accordingly, although the material becomes stiffer, they become too brittle to handle and therefore unable to form a continuous film/structure.

Supramolecular polymers have found use into different industries as a result of their remarkable properties. Different areas of application such as the biomedical sector, coatings, sensors and electronics as well as printing are exemplar industries. The Biomedical and printing industries lie within the scope of this thesis and are therefore explored in more details in the following sections.

#### 1.2.1.1 Biomedical application of supramolecular polymers

Supramolecular polymers have been studied extensively in the development of biomedical devices and therapies. The versatility and their tuneable physical and mechanical properties resulted in the development of materials for intracellular protein delivery[28], bone regeneration scaffolds[29] and to facilitate prosthesis adhesion[30] or the delivery of drugs that are unstable or prone to rapid excretion.[28,31,32] The following paragraphs describe key uses of supramolecular polymers in the biomedical field.

Nanotherapy approaches utilising supramolecular polymers for cancer treatment has recently been the recipient of attention by several groups.[33,34] Therapeutic nanoparticles have received approval for use and are now used to treat cancer patients.[35] Nanoparticles can serve as efficient drug carriers and reach the cancerous growth through blood circulation to offer a targeted drug delivery to the tumour site, thus avoiding harm to healthy tissues and overall, this approach reduces the toxicity of the drug to the patient.[35,36] Adaptable supramolecular

polymeric nanoparticles and their responsiveness to specific stimuli make them an efficient candidate as a drug carrier for localised delivery.[33,34,37] For example, Sun *et al.* have developed double responsive supramolecular nanoparticles for cancer therapy.[37] In this study, Paclitaxel, a chemotherapy medication currently used to treat several cancers, e.g. breast and lung cancers, is selected as the model drug. The particles were comprised of poly(lactic acid) that contain the drug of interest, as the core, which is decorated with cucurbit[7]uril functionalities on the surface, which in turn form inclusion complexes with adamantane functionalised PEG (Figure 1.2.3 A). Upon approaching the tumour (an environment of high oxidative stress), the GSH responsive particles undergo de-PEGylation and penetrate the cancerous cell (Figure 1.2.3 B). A high concentration of glutathione (containing disulfide bonds) inside the tumour breaks down the core of the particles and the drug is thus released in a targeted fashion (Figure 1.2.3 C). One advantage of the reported system is its high adaptivity resulting from its supramolecular assembly. Furthermore, the presence of cucurbit[7]uril on the surface of the particles enables the introduction of any adamantane functionalised shell structures to tailor the responsiveness of the particles for different disease states.

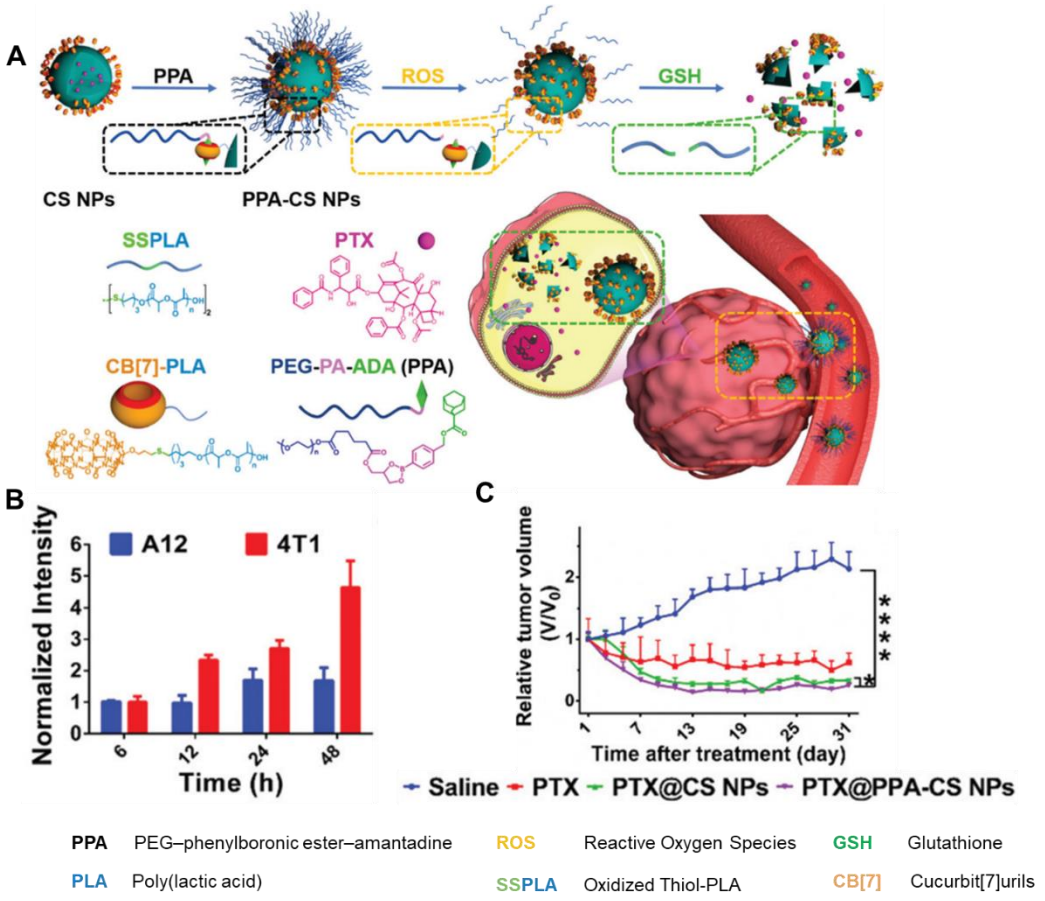


***Figure 1.2.3:*** *A) schematic image representing chemical structure and mode of operation of the anti-cancer supramolecular polymeric nanoparticles. B) Bar chart showing the penetration of the*

*proposed supramolecular polymeric particles into healthy mouse-derived hepatocytes (A12) and mouse-derived breast cancer cells (4T1), proving that the high oxidative environment of cancerous cells increases the drug penetration by de-PEGylation. C) The results of exposing a 4T1-bearing mouse to different treatment, including saline (blue), direct commercially available Paclitaxel drug (red), Paclitaxel drug loaded in cucurbit[7]uril functionalised particles without PEG functionality (green) and Paclitaxel-contained particles with the pegylated surface. Republished with permission of Royal Society of Chemistry, from Supramolecular Nanomedicine for Selective Cancer Therapy via Sequential Responsiveness to Reactive Oxygen Species and Glutathione, C. Sun, Z. Wang, Z. Wang, L. Yue, Q. Cheng, Z. Ye, Q. Zhang, R. Wang, 9, 2021; permission conveyed through Copyright Clearance Center, Inc.*

A similar systematic approach has also been proposed for protein delivery in which the intracellular glutathione and other amino acids are responsible for release of the encapsulated protein.[28] The proposed approach that can be used for protein therapies involves a template-induced production of protein-polyphenol particles. The assembly of these microcapsules are formed by loading of the protein of interest and tannic acid in mesoporous silica nano particles (the template); upon removal of the template the protein is encapsulated within a polyphenol network. The surface charge of the particles is dictated based on the extracellular pH (for transformation of the polyphenol hydroxy groups) as well as the isoelectric point of the protein. The negatively charged particles in extracellular medium (~ pH = 7.4) are able to enter the acidic endosome. As a result of the change in the pH of the medium (from extracellular to endosomic), the surface charge of the particles was altered, and the particles can then escape from the endosome into the cytosol. It was found that unlike the micellar extracellular proteins, endogenous oxidized glutathione (GSSD), glutathione (GSH) and small peptide and amino acids can trigger the disassembly of the protein particles and induce the protein release inside the target cell. In these instances, the polymeric particles serve as both the drug carrier and a shield to protect the drug from unwanted and off-target release during blood circulation, reducing hepatotoxicity and improving drug efficacy. This is important for delivering small molecule drugs, such as Bortezomib, since it is prone to rapid excretion before reaching the target site.[38] An additional approach to protect precious drug cargoes is to take advantage of amphiphilic supramolecular assemblies and create a globular structure with the drug located at the core. A notable example is the block copolymer containing poly(ethylene glycol) (PEG) and diethanolaminomethyl functionalised polystyrene synthesised by Nagasaki and co-workers.[38] Upon formation of the boric acid drug and diethanolamine conjugate, an amphiphilic polymer chain forms, which self-assemble into a globular structure with a hydrophobic (drug) core and a hydrophilic (PEG) shell. These supramolecular micelles are pH sensitive, and upon protonation the micelles break down and the drug released. The proposed amphiphilic particle formation and encapsulation of the boronic acid drugs offer a facile procedure for delivering small molecule drugs, particularly in boron neutron capture therapy (BNCT), expanding the range of agents that can be utilised, e. g. phenylboronic acid and *p*-phenylene-diboronic acid.

Supramolecular polymers have also been utilised to produce anti-kinking vascular grafts.[40] Vascular grafts are essential for patients suffering from kidney disease who rely on blood purification and do not have adaptable vasculature. Currently available vascular grafts are prone to lumen failure under bending stress or upon a sudden movement. In studies reported by Wu *et al.*, three-layered artificial vascular grafts were produced in which a layer of spiral reinforcement material was 3D printed and sandwiched between 2 layers of electrospun material. Two different material systems were used to realise the design, a polycarbonate bisurea reinforced by strands of PCL and a supramolecular system of chain extended Polycaprolactone - 2-ureido-4[1H]-pyrimidone (PCL-UPy) reinforced by UPy-dicapped PCL. Figure 1.2.4 A shows the structure and the morphology of these systems. The advantage of the supramolecular system is that the mechanical properties of the graft were found to be improved without compromising its flexibility. Although 3D printing of the spiral reinforcing scaffold improves the mechanical properties of the artificial graft regardless of the materials being used, the polycarbonate bisurea system could become problematic as a result of the difference in degradation mechanism of PCL and the hydrogen bonding bisurea shells (red system in Figure 1.2.4 A). In contrast, the layers of the fully supramolecular system (blue system in Figure 1.2.4 A) are comprised of a hydrogen bonding supramolecular network as well as a hydrogen bonding shell which therefore degrade at a similar rate and via the same mechanism. Therefore, the supramolecular vascular graft is safer and more durable, making its implementation more appealing and feasible.

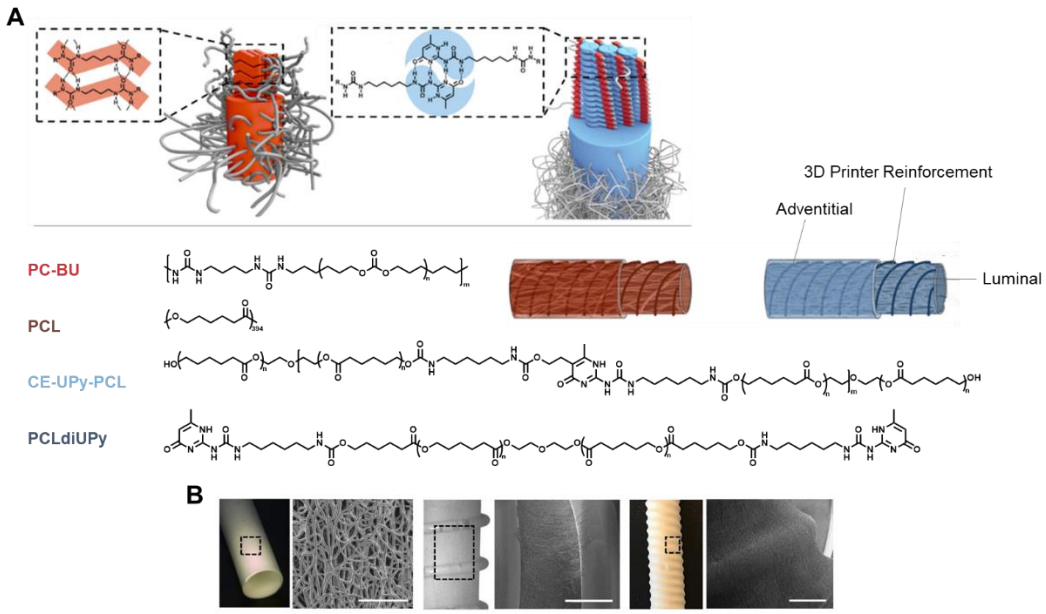


***Figure 1.2.4:*** *A) Schematic representation of the 3-layered artificial graft design and the related non/-supramolecular materials. B) microscopic images of the supramolecular anti kinking graft, left to right; first electrospun layer (luminal), scale bar = 100 µm, second 3D printed layer (reinforcement) and the third electrospun layer (adventitial). The scale bars represent 1 mm. Image reproduced with permission of Frontiers from reference 40.*

#### 1.2.1.2 Printing methods and application of supramolecular polymers in printing technology

Another exciting area that supramolecular polymers have found application in is printing[41,42] and additive manufacturing[43] which can be defined as the process of sequential deposition of material to create an image or object. The molecular recognition between the macromonomers in supramolecular polymers forms *pseudo* high molecular weight materials. The low energy interaction between these macromonomers can be dissociated by heat or another appropriate stimulus. Therefore, these polymers can be regarded as discrete macromonomers in the melt or under specific conditions (depending on their association constant), allowing for their exceptional processability compared to conventional polymers. Deposition of the lower molecular weight materials decreases the chance of nozzle blockage during the printing process, reducing the printers' downtime and maintenance cost. Similarly, the deposition of supramolecular materials can increase the printing speed. Their tunability allows for the facile and controllable introduction of customised functionality based on the final application in biomedical, pharmaceutical, and food areas. Although the mechanical properties of supramolecular polymer inks are generally inferior to conventional polymers, research is ongoing to propose applicable methods and strategies to produce robust and durable prints such as utilising appropriate fillers[44,45] or the introduction of UV curable motifs.[42] This section provides a brief overview of the 2D, 3D, and 4D printed supramolecular polymers, focusing on their applications to build a more advanced future world. However, since the focus of this thesis is on additive manufacturing, its methods and applications are discussed in more details.

##### 1.2.1.2.1 2D Printing

Exploiting supramolecular polymer inks allows for the production of functional 2D prints. The printing industry can be capable of producing more than merely a depiction of letters, numbers or figures. For instance, it can generate functional security inks,[46,47] food packaging labels[48], or produce coloured prints without using dyes.[41] For example, Schenning *et al.* have employed an ink formulation containing a UV-curable cholesteric liquid crystal and carboxylic acid hydrogen bonding motifs to print an optical battery-free humidity sensor for food and pharmaceutical packaging operating in the relative humidity range of 3 to 83%. The reported functional ink can be inkjet printed, which changes colour reversibly from red to green based on the absorbed water content. Since the cholesteric liquid crystal is chiral with a helical structure with hydrogen bonds, it is UV cross-linked after printing to retain the number of helical turns and the print thickness. By absorbing water, the printed polymer swells, increasing the helical pitch, reflecting light with a longer wavelength, and changing the

apparent colour. Although the reported mechanism of the action could permit advance and smart packaging, the quick reversibility of the colour change at temperatures above 0 °C could hinder monitoring the condition of the packages in transit and only represent the current status of the content. Furthermore, the incorporation of charge transfer complexes through supramolecular interactions have been reported to produced coloured inks.[41] Hayes and co-workers reported a two-component ink system that contains an electron-rich unit and an electron-deficient system, which produce colours upon supramolecular cross-linking by taking advantage of π-π stacking interaction between the components.[41,49] The reported synthesised π-electron-rich component possesses either pyrenyl or perylene terminal groups, and the π-electron-deficient component is a chain-folding naphthalene-diimide (Figure 1.2.5 A). Subsequent inkjet deposition of the ink component on various substrates, including glass, steel and polycarbonate films, gave rise to either red and green print upon forming a charge-transfer complex between naphthalene-diimide tweezer and pyrenyl or perylene, respectively (Figure 1.2.5 B). In addition, each component of ink contains low molecular weight constituents, which reduces the risk of inkjet nozzle blockage, although the printed ink crosslinks in a supramolecular manner and could exhibit the mechanical properties, durability and toughness similar to those of higher molecular weight polymers.[50] Additionally, the crosslinking of the ink's components is immediate and does not require any post-printing processing such as exposure to UV radiation or a chemical trigger.

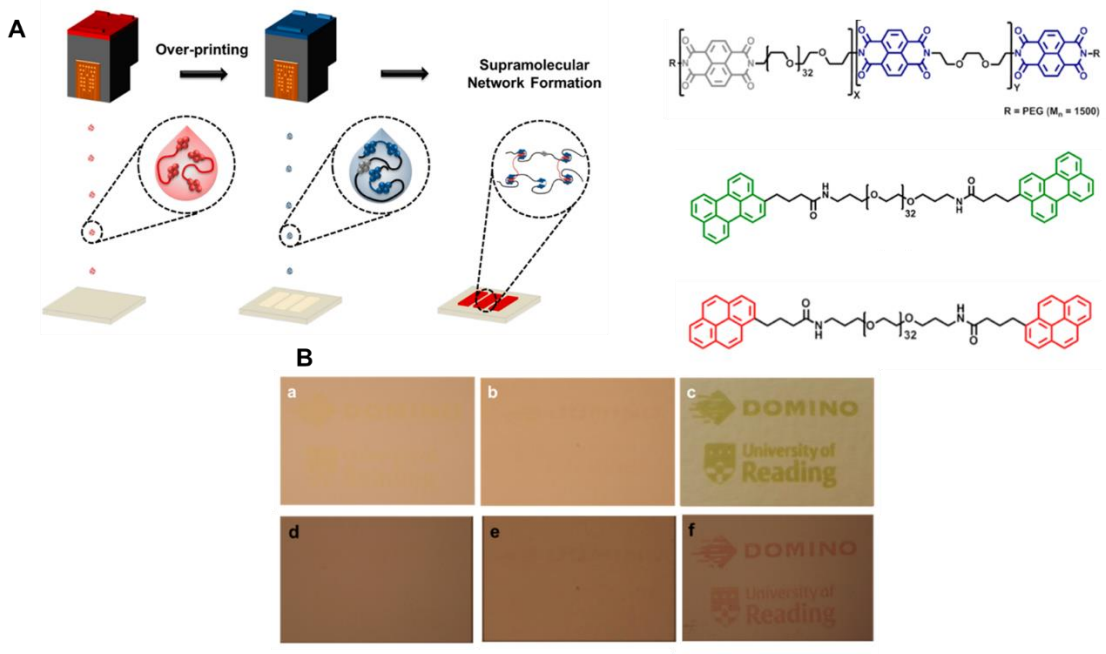


***Figure 1.2.5:*** *A) Schematic representation of the double-layer printing approach and the ink components' chemical structure (Blue: the π electron-deficient component and green and red: the π electron-rich components). B) (a,d) printed single component pyrenyl and perylene inks, (b,e) printed single component naphthalene-diimide ink (c,f) overprinting of the inks to create colour at ambient condition. Figure reproduced with kind permission from reference 41*

*(https://pubs.acs.org/doi/abs/10.1021/acsami.5b01569, further permission related to the material excerpted should be directed to the ACS) and republished with permission of Royal Society of Chemistry, from Molecular design of a discrete chain-folding polyimide for controlled inkjet deposition of supramolecular polymers, L. R. Hart, J. L. Harries, B. W. Greenland, H. M. Colquhoun and W. Hayes, 6, 2015]; permission conveyed through Copyright Clearance Center, Inc..*

Donor-acceptor and host-guest chemistries have also been reported to produce security inks enabling direct encrypted printing, which can be authenticated reversibly.[46,47] The fluorescent security ink reported by Stoddart *et al.*[47] is a rotaxane-based formulation capable of producing a pallete of finely tuned colours by varying each component's concentration in the formulation. This formulation consists of different host/guest moieties (for example, γ-cyclodextrin, adamantylamine), which compete with the formation of the complex between the rotaxanes pyrene and γ-cyclodextrin (CD) units. The rotaxane/γ-cyclodextrin complex was responsible for producing different fluorescent colour by changing the molar ratio of the bound γ-CD to the rotaxane (Figure 1.2.6).

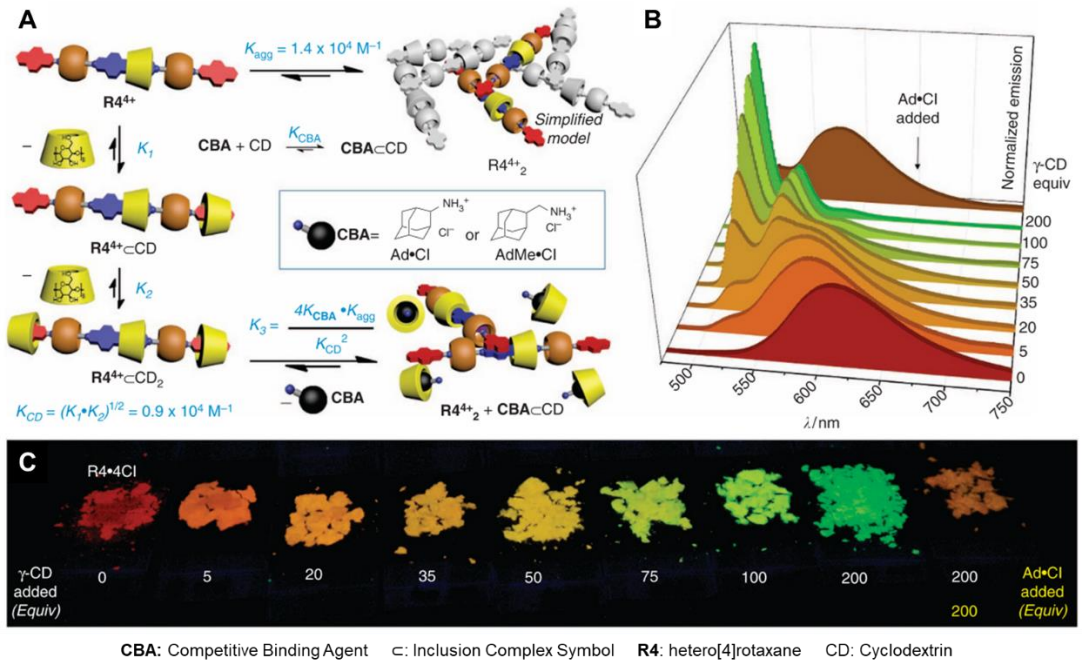


***Figure 1.2.6:*** *A) Graphical representation of the rotaxane ink's action mechanism reported[46] by Stoddart et al. and the competing guest species' role. B) Solid-state fluorescence spectra of the rotaxane ink with a different equivalence of γ-CD inclusion complex generated by λ excitation= 347 nm. C) The variety of colours produced by a mixture of the rotaxane ink containing different amount of the inclusion complex under UV light. Reproduced under Creative Commons Attribution 4.0 International License from https://www.nature.com/articles/ncomms7884?origin=ppub[47].*

#### 1.2.1.2.2 3D Printing

Sequential deposition of materials in multiple layers gives rise to customisable structures with high precision and resolution. As a result of the sequential deposition, additive manufacturing is another term used to describe this approach. 3D printing is a versatile method for

manufacturing structures which has seen rapid growth in recent years.[51-54] Some multi component structures such as interlinked sections are difficult or impossible to be constructed by conventional methods such as moulding, milling or casting. 3D printing is becoming an invaluable tool to rapidly manufacture new and improved replacement components. New designs can be rapidly realised using simple and accessible software: as the output of any 3D computer-aided design (CAD) package can be used as the input for a new 3D printed component.[55] Furthermore, it is possible to 3D scan, an existed component with sensors or probes and send the data to printer to reproduce it. For instance, such an approach can be used to manufacture a bone replacement individually for each patient with the exact dimensions as the original bone.[56] Therefore, this technology is also, of great value in prototyping and verify any characteristics of the sample part prior to investing on making moulds or other expensive mass production methods. As a result of low-cost approach toward producing new parts, industries benefit from assessing variety of new designs and ideas without having to invest substantially on a primitive plan. These advantages have led to additive manufacturing becoming a major industry in the last two decades. The global market has been forecasted to reach £69 billion by 2025.[57] The advantages of 3D printing parts are not limited to component manufacturing; pharmaceutical,[58] food and agrochemical companies as well as electronics manufacturers[59] and the aerospace industry[60] are investing is 3D printing technology. For example, in the pharmaceutical industry, 3D printing could be used to produce tablets that are customised for the patient's needs in terms of dosage levels or even formulating multiple medicines for a specific patient into a single dosage form. Despite the customisation advantage that come with 3D printing production method, there are some limitations associated with this method. For instance, the production speed is considerably lower than the conventional mass production methods such as injection moulding. Additionally, as a consequence of the layer-by-layer manufacturing procedure, the mechanical properties of a 3D printed part is naturally inferior to conventional production method. However, as a result of the high precision and customisability of 3D printing method, it brings a high value in production of moulds or realisation of a theoretical model.

Although there are numerous advantages for additive manufacturing there are some characteristics such as processability, printability and physical properties of the ink that affect the quality of the final structure.[55] In addition, the shrinkage of the printed structures during the drying process can make it difficult to produce highly complex parts with high precision. To address this, research is ongoing regarding the improvement of existing materials and the synthesis of novel materials to improve the speed and quality across all sections of the 3D printing industry.

To enable the printing of extremely complex topologies, it is possible to print a support structure which enables the construction of interlocked components. During post printing treatments, the scaffold can be removed to reveal the final object.[61] In addition, the ability to print several materials simultaneously has led to the possibility of printing more complex structures including core-shell components.[62] In these scenarios, printing the structure using removable scaffolds is an easier and more precise option. Furthermore, the material waste from 3D printing such structures would be minimal compared to conventional fabrication methods. Currently, various solid and liquid materials are commercially being used for ink in different 3D printers.[61] Materials that have been shown to be suitable for 3D printing range from pure metals and alloy to polymers and composites. From consideration of different techniques used for printing 3-dimensional objects, the suitability of an ink for a particular printing method will depend on the physical properties of the material such as its viscosity, melting point and mechanical properties. An ink formulation can be made prior to depositing and fed into printer, or the reaction can take place during depositing. High molecular weight polymers are desirable for production since high performance structures can result from their use, however, such materials can be challenging to print as a result of high viscosity and poor processability.[63] In particular, nozzle clogging is a common problem when attempting to print highly viscous materials. Implementation of supramolecular polymer as the ink for 3D printers can be beneficial as a result of the low energy demands required for their processing. Indeed, the applied energy to the material during a printing process is capable of dissociating the intermolecular interactions and therefor production of discrete macromonomer. The high shear and velocity involved in a 3D printing process facilitate the directing of the supramolecular motifs to align the microfibres or aid the microphase separation.[64] This is not easily and reproducibly achievable in other production methods such as drop casting or moulding.

There are a number of approaches available for 3D deposition of materials depending on their properties, for example: ink-jet printing, hot-melt extrusion, laser sintering and stereolithography. In relation to the objectives of this study, inkjet and extrusion printing are the deposition methods selected to be explored in more detail in the following sections.

#### 1.2.1.2.2.1 Inkjet 3D printing

Inkjet printers have been used for a long time in different scales for 2D printing. They have become commercially available and widely used since 1950s. This form of printing is based on the consecutive deposition of ink droplets, to typically form one-layer images. Printing these 2-dimentional layers on top of each other using appropriate ink produces a 3D structure. Figure 1.2.7 shows the process of 3D inkjet printing. In inkjet 3D printing, ink droplets can be

deposited in solution form or from the melt. Then upon solidification or evaporation of the solvent the layers are formed. The viscosity of the liquid being printed is the most important parameter to determine if a formulation is suitable for 3D printing. Regarding solution depositing, choosing the appropriate solvent is also of importance. In addition to solubility factors, the vapour pressure and viscosity of the solution should also be optimal. The ideal solvent would dry at a moderate pace in order to retain the structure resolution without generating bubbles in the deposited polymer. The thickness of each deposited layer depends on the dimension of the droplets and the distance between each drop (infill). However, the size of each droplet is also influenced by the viscosity of the ink solution and the nozzle dimensions.

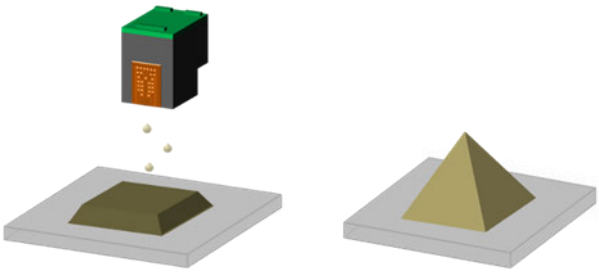

***Figure 1.2.7:*** *3D inkjet printing scheme. Image adapted with permission from L. R. Hart, S. Li, C. Sturgess, R. Wildman, J. R. Jones and W. Hayes, ACS Appl. Mater. Interfaces, 2016, 8, 3115–3122. Copyright 2016 American Chemical Society.*

Generally, there are two types of ink-jet printers; continuous or drop-on-demand (DOD).[64] In the continuous process there is a charged species in the ink which enables directing the droplets whether onto the substrate or back to the ink reservoir for recycling. However, in the DOD approach ink droplets are only generated when needed. DOD inkjet printers are more precise and produces higher quality images.[65]

Different deposition methods and apparatus have been suggested for 3D inkjet printers each of which needs appropriate ink to fabricate a high strength and high-resolution structures within their working capacity. One method is using a monomer or polymer powder bed, as a moveable substrate, in which a binder is printed onto the bed to unite, stiffen and bind the material in the desired sections. Upon completion of printing one layer, the moveable substrate descends to allow another layer of material powder covers the incomplete structure in order for the binder to continue being deposited and patterned next layer on top of the previous one. Figure 1.2.8 represents the stages of inkjet printing of a binder on a powder-filled print bed. The problem with this method of production is the limited variation in the chemical composition of the powder bed as well as the possibility of the unwanted dispersion of the binder in the powder bed which can affect the resolution of the final structure.[66] The density of the structure is highly dependent on the packing of the powder bed particles. While

a great amount of material in the powder bed is wasted, the density and consequently, the durability of the printed structure is not as satisfying as other inkjet printing methods as a result of the packing of the powder monomer. Meanwhile, by improving the packing *i.e.* increasing the density of the powder the flowability of the powder decreases and results in poor coverage of the top of the printed structure prior to printing the subsequent level. Consequently, the printing quality reduces as there would not be a packed powder for the next level for the ink to be printed on.

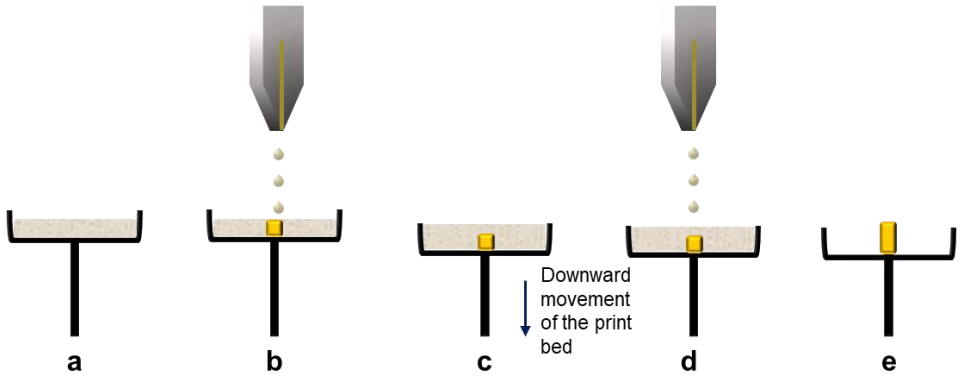


***Figure 1.2.8:*** *An illustration of the stages of an ink jet prints. a) the polymer powders loaded into the substrate, b) binder droplets jetting onto the bed, c) a new layer of polymer powder spread over the printed part by declining the polymer stage, d) binder printing the next layer and e) the structure is fully printed, and the excess polymer powder has been removed.*

The other method of inkjet printing is based on the direct deposition of the ink material on substrate. In this method, ink is dissolved in an appropriate solvent and the droplets of the solution deposited next to each other. The structure is ready for the next layer of deposition after evaporation of the solvent. Therefore, the viscosity of the solution and the drying time is of great importance. The ideal formulation is a scenario where the ink has a low viscosity in the minimum volume of solvent. However, an inherent issue with this approach is that dried image becomes wet as the subsequent layer is being printed. Although this can improve the layer adhesion, it may also lead to deformation of the previous layer and therefore the resolution of the image becomes diminished. Consequently, short drying times are highly desirable which require the use of relatively volatile solvents. Consideration of the shrinkage of material through drying and the type and amount of solvent as a carrier for these inks are key optimisations.

#### 1.2.1.2.2.2 Extrusion 3D printing

Extrusion or fused deposition modelling is a method of 3D printing in which a material is deposited in a continuous fashion (see Figure 1.2.9 for a general illustration). The cost-efficiency and its suitable design for domestic use have made them a very popular type

of 3D printers around the world.[51] In hot-melt extrusion process the material is fed into the extruder, which is behind the nozzle and is heated to above its viscoelastic temperature. As a consequence of the heating process, the material melts and its viscosity decreases enabling it to be forced to flow towards the deposition nozzle, often using a compressed gas. The printing material can then be directly deposited from the nozzle onto a substrate in sequential layers. The final topology of the product is achieved by moving either the substrate or the printhead vertically to allow space for next layer. In some printers the substrate could be heated, as well to help sticking the partially printed structure to the surface or to keep the material's viscosity low and increase the layers adhesion. However, close control of the melting temperature and solidifying time is required for this process. Thermoplastics and, more generally, heat-fuseable materials are particularly applicable to this method of printing.[61] However, the downside of this technique is the joint that is formed between the separate layers which results in a striped pattern on printed structure. Healable polymers and materials with relatively low glass transition temperatures could be beneficial to reduce this effect since warming the printed part during post-processing can smooth out the surface and reduce the printing pattern.

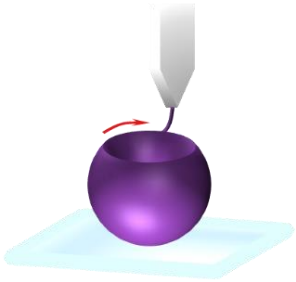

***Figure 1.2.9:*** *3D printing via extrusion.*

Melt extrusion additive manufacturing is a direct additive manufacturing technique that requires minimal chemical/physical alternation of the ink material to be deposited. Therefore, it is a highly desirable method for producing pharmaceuticals[17,67] and where the purity and non-toxicity of the material are of high importance. The development of new polymeric materials suitable for hot-melt extrusion is understudied, and currently, there are limited types of commercially available materials/filaments suitable to be used as inks, namely poly(lactic acid) (PLA) and acrylonitrile-butadiene-styrene copolymer (ABS). Supramolecular polymers are emerging in melt extrusion 3D printing as a result of the advantages they bring, such as lower processing temperature,[68] superior mechanical properties, better interlayer adhesion, rapid polymer solidification[24] and readily tuneable mechanical properties.[43] The combination of the tunability as a result of processability of the supramolecular polymers under 3D printing conditions as well as the readily customisable nature of the 3D printing production

methods have contributed considerably towards progression in different fields, especially the biomedical field.[29,68,69] The biomedical field is one of the industries which has benefited substantially from the combination of supramolecular polymers and 3D extrusion printing since this method of printing can be widely used in production of biomedical parts.[17]

For example, Long and co-workers have reported developing a segmented supramolecular polyurea exploiting ureido-cytosine with a quadruple hydrogen bonding as the molecular recognition motif.[24] The quadruple hydrogen bonding results in an outstanding toughness modulus of *ca.* 81 MPa in a printed supramolecular polyurea, which could be elongated to 1200% of its original length. A physically cross-linked network controls the mechanical properties of the material. In fact, upon a 50 °C increase in the temperature from 120 °C to 170 °C (around the dissociation temperature of the hydrogen bonds), the material's viscosity drops by three orders of magnitude which can be reversed rapidly upon cooling down. This substantial drop in viscosity and the ability to rapidly regain it made this supramolecular polyurea a suitable candidate for hot-melt extrusion 3D printing. It has been demonstrated that the rapid solidification of the material enabled the deposition of small single-walled geometries (Figure 1.2.10 A). Additionally, a similar segmented supramolecular polyurethane is reported in Chapter 2 as a way to print a customised drug-release implant at a lower temperature, allowing for the incorporation of a wider variety of drugs with lower decomposition temperature (Figure 1.2.10 B).[68]

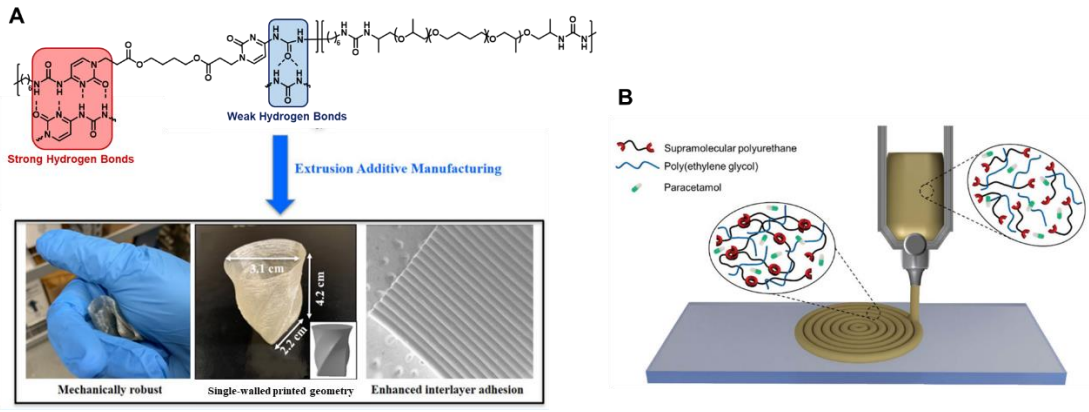


***Figure 1.2.10:*** *A) The segmented polyurea reported by Long et al. showing the chemical structure featuring the quadruple hydrogen bonding and the properties of the printed part featuring production of small single-walled structures as a result of the efficient interlayer adhesion originated from the low $T_g$ of polyether and the physical cross-linking from UCyt. Reprinted with permission from X. Chen, C. E. Zawaski, G. A. Spiering, B. Liu, C. M. Orsino, R. B. Moore, C. B. Williams and T. E. Long, ACS Appl. Mater. Interfaces, 2020, 12, 32006–32016. Copyright 2020 American Chemical Society.[24] B) Hot-melt printing process of the supramolecular printed implant reported by Hayes and co-workers Reproduced from Ref. 68 with permission from the Royal Society of Chemistry.*

Another variation of extrusion printing is termed “reactive extrusion”. This method is commonly used for bulk polymerisation where two reactants are stored in separate containers

and mixed in stoichiometric ratio while being fed into the extruder in absence of any solvents.[70] Reactants are heated and mixed in the extruder to generate the material that will be printed. A disadvantage of this technique is that for biomedical and food technology applications, the biocompatibility and cytotoxicity of the monomers and any reactant have to be considered since there may be residual monomers and unreacted chain ends in the final structure. Therefore, post curing and treatment to remove these components is an essential step in these cases.

#### 1.2.1.2.3 4D Printing

Implementation of responsive supramolecular materials as inks has permitted 4D printing. 4D printing is defined as 3D printing of a part that can undergo shape change in response to an appropriate stimulus after being printed.[71] Introducing a reversible shape change to this technology advances the field and enables the production of ever more complex structures which can perform a task. Ware *et al.* proposed an azobenzene liquid crystal supramolecular elastomer that can be 4D printed as a Braille-like actuator.[72] The proposed material comprises four key functionalities: mesogen to achieve crystallinity, azobenzene to induce shape change, Diels-Alder adduct to provide the processability needed for extrusion printing and 2-ureido-4[1H]-pyrimidinone (UPy) to lock the aligned structure after shape change using quadruple hydrogen bonds.[71] The printed Braille sheets consist of 6 dots, which can be raised accordingly upon temporary irradiation with UV light. The raised shape is stable for 24 hours and can be returned to the original flat structure by heating the image to 65 °C to adopt a new form (Figure 1.2.11 illustrates the process).

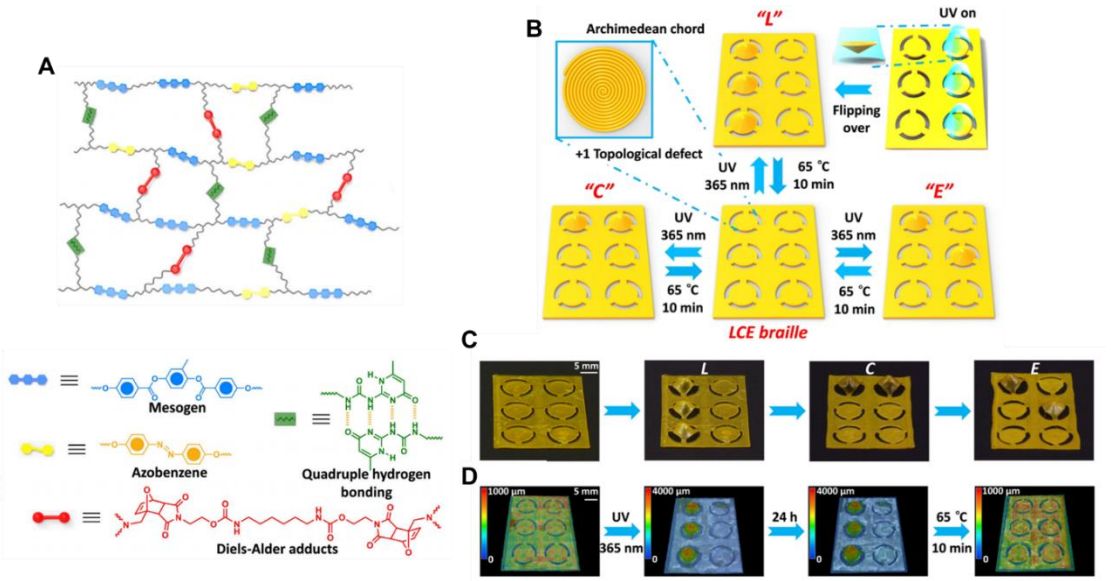


***Figure 1.2.11:*** *A) Schematic representation of the chemical structure of the azobenzene liquid crystalline supramolecular elastomer. B) Illustration of the 3D printed Braille-like sheet designs. C) Images of the printed Braille sheets showing letters "L", "C", and "E" 24 h after UV irradiation. D)*

*Micrograph topography of the printed Braille sheet during one cycle of the reversible shape change.[72] Reprinted with permission from X. Lu, C. P. Ambulo, S. Wang, L. K. Rivera-Tarazona, H. Kim, K. Searles and T. H. Ware, Angew. Chemie - Int. Ed., 2021, 60, 2–10. Copyright 2020 from John Wiley and Sons.*

Interestingly, Lu and co-workers reported a polyethyleneimine-co-poly(acrylic acid) synthesis that forms metallo-organic coordination with $Eu^{3+}$ ions to produce a range of luminescence colours.[72] A bilayer shape was printed consisting of a non-swellable polymer layer and a layer of the reported metallo-organic supramolecular hydrogel. The bilayer printed material showed luminescence colour change, opacity, and shape changes by tuning the ratio of coordinated and free $EU^{3+}$ ions and the degree of swelling in water. By taking advantage of these characteristics, successful printing of an underwater soft-grip actuator (which was invisible to marine life) was realised to grab and hold objects with a force of 0.16 N (Figure 1.2.12).

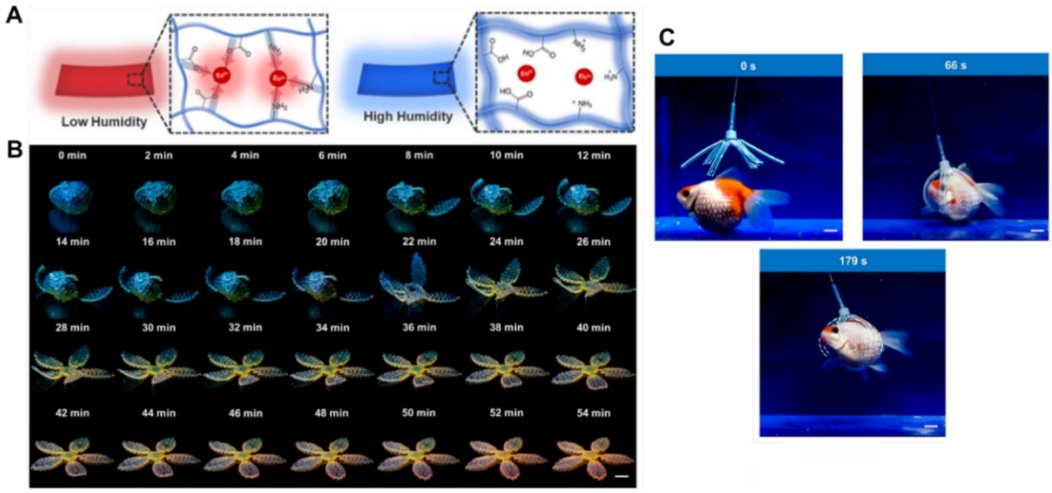


***Figure 1.2.12:*** *A) Mechanism of colour change by increasing the humidity. B) Progressive images of a fully swollen printed flower (at a relative humidity of 20%). The shape is drying slowly over time; thus, the material is becoming less swollen, and the flower is blossoming as a result. λexcitation = ~340 nm for colour change monitoring. C) Images of the soft-grip actuator in action. As the part is submerged in water becomes transparent (swollen and less phase-separated). Adapted with permission from L. R. Hart, S. Li, C. Sturgess, R. Wildman, J. R. Jones and W. Hayes, ACS Appl. Mater. Interfaces, 2016, 8, 3115–3122.Copyright 2020 American Chemical Society.*

From the brief survey of printing techniques presented above, it is clear that the printing material is of key importance in the quality of the final product. While the printability of the supramolecular polymers is compelling, their low stiffness is still a problem to tackle. This problem can be overcome by exploiting different methods such as introducing more efficient functional group in the polymer backbone or production of their nanocomposites. However, it has been shown that introduction of a recognition group with stronger association constant and higher concentration of supramolecular interactions could result in brittleness of the final material.[24-26]

### 1.2.2 Improvement of the mechanical properties of supramolecular polymers

Whilst the lower energy association of the supramolecular polymers and hence their reversibility is appealing, their mechanical properties are generally inferior to those of conventional polymers. The nanocomposite class of materials have attracted so much attention recently in different industries as a result of their high stiffness and toughness while maintaining the light weight and flexibility of the polymeric materials. In fact, a nanocomposite material exhibits the properties of its elastic network as well as the stiffness and toughness from the filler, synergistically.[74]

It is well-known that incorporating high modulus filler components into polymeric structures can dramatically improve the mechanical properties of the polymer including toughness and stiffness.[63,75] This mechanical property improvement can be in part attributed to the interfacial interaction between the particles and polymer network which results in higher supramolecular crosslinking. The presence of particles limits the movements of polymer molecules and increases the Ultimate Tensile Strength (UTS) of the material.[76] In addition, filler particles form an internal network within the polymer matrix which dissipate the applied stress among the fillers.[75,77]

The smaller fillers are more effective in reinforcing a polymer network as their efficacy as a result of their high aspect ratio outweighs the network disturbance they cause. However, filler particles smaller than 1 μm are difficult to disperse in a polymer matrix without aggregation. Generally, nanoparticles are likely to aggregate because of their high specific surface area as well as surface energy, unless they transferred into a medium that interacts with their surface effectively thus preventing aggregation.[74] Therefore, one of the important parameters in producing nanocomposites is achieving a homogenous dispersion of the filler in the polymer matrix and prevent the aggregation of the filler.[75] Homogenous dispersity of the particles increases the effective aspect ratio of the particles and can cause a better interfacial interactions between the fillers and the polymer molecules.[78] In this scenario the van der Waal's forces of attraction between the small particles make them more likely to aggregate.[79] Functionalisation of the fillers is one of the approaches that has attracted a lot of attention in this area.[80,82] Efficient functionalisation of the particles' surface can result in better interaction at the interface of polymer and filler which in turn can decrease the tendency for the particles to aggregate. Two different types of fillers have been exploited to reinforce a polymeric network *i.e.* organic and inorganic fillers each of which offers different advantages and application. These approaches are discussed in more detail in the following sections.

#### 1.2.2.1 Inorganic fillers

Introduction of inorganic fillers into the polymeric networks gives rise to composite materials. The fillers can be of different shapes and sizes; however, nano-sized fillers are the most popular. Nanocomposites can be defined as a polymeric system with one component at nanoscale size (1-100 nm).[83] Different nanoparticles have been reported to be used in polymeric systems to introduce additional functionality to the system or merely improving the mechanical properties. This includes gold,[84] silica[85-87] and iron oxide[20] nanoparticles, carbon nanotubes,[88-90] graphene oxide.[90,91] The addition of these nanoparticles can introduce different functionality to the polymeric network. For example, the nanocomposite reported by Mu and co-workers which contains graphene oxide and carbon nanotubes can be used as an artificial skin.[90] Introduction of these fillers resulted in the production of a force sensor in the reported artificial skin. In addition to introduction of a functionality, fillers are used to improve the mechanical properties and thermal resistance of the polymers.[92] Depending on the base material network the improvement could be to increase the strength and stiffness while maintaining the elasticity and ductility of the material.[93] Although, introduction of inorganic fillers enhances some properties of the material, the optimisation of its wt% is of high importance. By increasing the wt% of the fillers above a certain point the properties of the composite material tend to deteriorate.[92] This phenomenon is attributed to disturbance of the polymeric network by the particles and loss of efficient interaction between the polymer molecules. It can be concluded that the better the dispersion of the particles the higher the content of the fillers could be. Since the agglomeration of particles results in formation of bigger structures that results in disturbance of the polymer molecules interactions. On the other hand, by efficient dispersion of the fillers within the matrix, the polymers molecules are more likely to remain intact. Consequently, efficient dispersion of the fillers is desirable although in most cases this is difficult to achieve.

Different approaches to improve the dispersion of the fillers could be alternation of the preparation method or functionalisation of the fillers. Modification of the preparation method is the simpler approach, however, it might not be feasible within the scope of a laboratory or a production line. Additionally, introduction of chemical functionalities, however it is more difficult than physical alternation approaches, it could result in more homogenous mixture of the polymer and the filler. Indeed, by tuning the properties of the filler and the network such as the hydrophobicity/hydrophilicity it would be easier to produce nanocomposite with high dispersion of the fillers. Additionally, it would be beneficial to decrease the attractive interaction among the fillers themselves to facilitate the composite preparation process. Therefore, depending on the application and the properties of the components of the desired nanocomposites, a suitable approach can be selected. For example, graphene oxide and silica

particles are easier to functionalise as a result of their active surface when compared to carbon nanotubes.[91] Additionally, carbon nanotubes have a higher tendency to aggregate as a result of their morphology although as they offer a high aspect ratio, they can form a nanocomposite with enhanced properties. However, this property improvement is more likely to be anisotropic. In addition, a suitable functionalisation of the filler particles can result in the formation of a secondary crosslink network within the original polymer network that could substantially improves the mechanical properties.

To conclude, by careful introduction of inorganic fillers into a polymeric system enhancement of the mechanical or thermal properties can be enabled. This is done through the ability of the filler particles to absorb the applied energy or dissipate it within the network which results in maintaining an intact polymer network.

#### 1.2.2.2 Organic fillers

Another type of fillers that can be utilised in order to improve the mechanical properties of polymers, is organic fillers. These fillers normally reinforce the polymeric matrix through formation of a secondary network. This second network can eighter contain complementary interaction with the polymer molecules[94] or form a distinct new network.[95] The advantage of this method of improving the mechanical properties of the polymers over utilising inorganic fillers is that the tensile strength improves without compromising the toughness.[94] In fact, as a result of the formation of a secondary network, the ability of the material to absorb energy without failure increased. Therefore, this method can also be combined with the conventional composite making using inorganic fillers to introduce added functionality without compromising the toughness.[96]

In more detail, the formed secondary network is often a supramolecular network. This can be achieved through utilising low molecular weight gelators (LMWGs) or polymer gels.[97] LMWGs are small molecules capable of self-assembling and forming gel structure. Since both of these organic species (LMWG and polymer gels) features reactive functional groups, they can also be used to decorate the polymer backbone which consequently aid the homogenous dispersion of the gelator within the network and hence formation of a dual material with a homogenous mechanical property. In addition, gels are well-known for their superior rheological properties. Introduction of gels within the polymer network can therefore enhance its rheological properties such as viscosity as well as the mechanical properties.[97]

## 1.3 Project aims

The focus of this project has been on the optimisation of supramolecular polymers so that they are suitable and applicable in 3D printing as printers' ink. 3D printing and supramolecular polymers are relatively new field of research with potential broad real-world applications such as biomedical and wearable electronics. The combination of these dynamic materials and this manufacturing technique can potentially bring advantage to both fields. This project was undertaken as a part of an EPSRC-sponsored consortium project entitled "Formulation for 3D printing: creating a plug and play platform for a disruptive UK industry" with the focus on creating a library of materials suitable for 3D printing of materials for different industrial sectors. The main project partners involved in the studies reported in this PhD thesis were based in the Hayes group at the University of Reading and the Department of Chemical and Environmental Engineering at the University of Nottingham. The main obstacle in the uptake of 3D printers in industry is the limited range of commercially available materials that can be used in appropriate formulations in conjunction with the different modes of deposition (such as inkjet printing or hot-melt extrusion) in order to achieve printed objects that fulfil a desired need. By creating a sector-specific library of suitable polymers or their composites (plus combinations of these materials), can be selected and used by industry to "plug and play".

With the global target of creation of a library of new polymers for specific use in additive manufacturing, different methods have been proposed to improve supramolecular polymers and optimise them for 3D printing. A supramolecular polyurethane with a thermally dynamic nature was formulated with paracetamol and PEG. This formulation was suitable for hot-melt extrusion printing therefore a customisable drug release implant was printed. However, the printed implant undergoes a deformation upon release process (Chapter 2). In order to tackle this problem a small library of supramolecular polyurethane was reinforced with low molecular weight additives and their processability as well as their printability under hot-melt extrusion condition examined (Chapter 3).

Additionally, the reinforced supramolecular polyurethane contains different amount of low molecular weight additives synthesised and by taking advantage of a dual component reactive extrusion printer, a material with gradient mechanical properties was produced (Chapter 4). The method of production of the mechanical gradient polymers can be utilised to produce structures with established point of failure, elasticity or stiffness.

Inorganic fillers were incorporated into supramolecular polyurethane network in order to improve its mechanical properties (Chapter 5) and different methods such as functionalising the SiNP was utilised to improve the dispersion of the particles and study the dispersion effect

on the mechanical properties. In addition, iron oxide nanoparticles were incorporated into a supramolecular polyurethane to introduce an added functionality to the system. These magnetic particles respond to an oscillating magnetic field and in doing so create heat. The produced heat is able to generate enough energy needed to dissociate the supramolecular interaction and hence decrease the viscosity of the material thus affording a non-invasive way to address the polymer composite (Chapter 6).

## 1.4 References


1 Polymers Market-Forecast (2021-2026), https://www.industryarc.com/Report/18767/polymers-market, (accessed 22 August 2021).

2 L. Brunsveld, B. J. B. Folmer, E. W. Meijer and R. P. Sijbesma, *Chem. Rev.*, 2001, **101**, 4071–4098.

3 R. P. Sijbesma, F. H. Beijer, L. Brunsveld, B. J. B. Folmer, J. H. K. K. Hirschberg, R. F. M. Lange, J. K. L. Lowe and E. W. Meijer, *Science*, 1997, **278**, 1601–1604.

4 V. Simic, L. Bouteiller and M. Jalabert, *J. Am. Chem. Soc.*, 2003, **125**, 13148–13154.

5 V. Berl, M. Schmutz, M. J. Krische, R. G. Khoury and J. M. Lehn, *Chem. Eur. J.*, 2002, **8**, 1227–1244.

6 K. A. Houton and A. J. Wilson, *Polym. Int.*, 2014, **64**, 165–173.

7 P. Woodward, D. H. Merino, B. W. Greenland, I. W. Hamley, Z. Light, A. T. Slark and W. Hayes, *Macromolecules*, 2010, **43**, 2512–2517.

8 B. W. Greenland, S. Burattini, W. Hayes and H. M. Colquhoun, *Tetrahedron*, 2008, **64**, 8346–8354.

9 B. W. Messmore, J. F. Hulvat, E. D. Sone and S. I. Stupp, *J. Am. Chem. Soc.*, 2004, **126**, 14452–14458.

10 A. Feula, A. Pethybridge, I. Giannakopoulos, X. Tang, A. Chippindale, C. R. Siviour, C. P. Buckley, I. W. Hamley and W. Hayes, *Macromolecules*, 2015, **48**, 6132–6141.

11 J. B. Beck, J. M. Ineman and S. J. Rowan, *Macromolecules*, 2005, **38**, 5060–5068.

12 L. R. Hart, J. L. Harries, B. W. Greenland, H. M. Colquhoun and W. Hayes, *Polym. Chem.*, 2013, **4**, 4860–4870.

13 J. D. Dunitz and A. Gavezzotti, *Cryst. Growth Des.*, 2012, **12**, 5873–5877.

14 P. Su and H. Li, *J. Chem. Phys.*, 2009, **131**, 014102.

15 T. F. A. De Greef, M. M. J. Smulders, M. Wolffs, A. P. H. J. Schenning, R. P. Sijbesma and E. W. Meijer, *Chem. Rev.*, 2009, **109**, 5687–5754.

16 E. A. Appel, J. del Barrio, X. J. Loh and O. A. Scherman, *Chem. Soc. Rev.*, 2012, **41**, 6195–6214.

17 H. Patil, R. V. Tiwari and M. A. Repka, *AAPS PharmSciTech*, 2016, **17**, 20–42.

18 J. P. Benitez-Rangel, A. Domínguez-González, G. Herrera-Ruiz and M. Delgado-Rosas, *Polym. Plast. Technol. Eng.*, 2007, **46**, 721–727.

19 M. A. Repka, S. Shah, J. Lu, S. Maddineni, J. Morott, K. Patwardhan and N. N. Mohammed, *Expert Opin. Drug Deliv.*, 2012, **9**, 105–125.

20 S. Salimi, T. S. Babra, G. S. Dines, S. W. Baskerville, W. Hayes and B. W. Greenland, *Eur. Polym. J.*, 2019, **121**, 109264.

21 T. S. Babra, A. Trivedi, C. N. Warriner, N. Bazin, D. Castiglione, C. R. Siviour, W. Hayes and B. W. Greenland, *Polym. Chem.*, 2017, **8**, 7207–7216.

22 T. Aida, E. W. Meijer and S. I. Stupp, *Science (80-. ).*, 2012, **335**, 813–817.

23 WO 98/14504, 1998.

24 X. Chen, C. E. Zawaski, G. A. Spiering, B. Liu, C. M. Orsino, R. B. Moore, C. B. Williams and T. E. Long, *ACS Appl. Mater. Interfaces*, 2020, **12**, 32006–32016.

25 D. H. Merino, A. Feula, K. Melia, A. T. Slark, I. Giannakopoulos, C. R. Siviour, C. P. Buckley, B. W. Greenland, D. Liu, Y. Gan, P. J. F. Harris, A. M. Chippindale, I. W. Hamley and W. Hayes, *Polymer (Guildf).*, 2016, **107**, 368–378.

26 D. Hermida-merino, B. O. Driscoll, L. R. Hart, P. J. F. Harris, H. M. Colquhoun, A. T. Slark, C. Prisacariu, I. W. Hamley and W. Hayes, *Polym. Chem.*, 2018, **9**, 3406–3414.

27 J. H. K. K. Hirschberg, F. H. Beijer, H. A. van Aert, P. C. M. M. Magusin, R. P. Sijbesma and E. W. Meijer, *Macromolecules*, 1999, **32**, 2696–2705.

28 Y. Han, J. Zhou, Y. Hu, Z. Lin, Y. Ma, J. J. Richardson and F. Caruso, *ACS Nano*, 2020, **14**, 12972–12981.

29 X. Zhai, Y. Ma, C. Hou, F. Gao, Y. Zhang, C. Ruan, H. Pan, W. W. Lu and W. Liu, *ACS Biomater. Sci. Eng.*, 2017, **3**, 1109–1118.

30 H. Bai, Y. Zhao, C. Wang, Z. Wang, J. Wang, H. Liu, Y. Feng, Q. Lin, Z. Li and H. Liu, *Theranostics*, 2020, **10**, 4779–4794.

31 F. Guo, T. Xia, P. Xiao, Q. Wang, Z. Deng, W. Zhang and G. Diao, *Bioorg. Chem.*, 2021, **110**, 104764.

32 D. Dhumal, W. Lan, L. Ding, Y. Jiang, Z. Lyu, E. Laurini, D. Marson, A. Tintaru, N. Dusetti, S. Giorgio, J. L. Iovanna, S. Pricl and L. Peng, *Nano Res.*, 2020, **14**, 2247–2254.

33 X. Jiang, C. He and W. Lin, *Curr. Opin. Chem. Biol.*, 2021, **61**, 143–153.

34 J. Zhou, L. Rao, G. Yu, T. R. Cook, X. Chen and F. Huang, *Chem. Soc. Rev.*, 2021, 2839–2891.

35 I. I. Lungu, A. M. Grumezescu, A. Volceanov and E. Andronescu, *Molecules*, 2019, **24**, 1–21.

36 J. Shi, P. W. Kantoff, R. Wooster and O. C. Farokhzad, *Nat. Rev. Cancer*, 2017, **17**, 20–37.

37 C. Sun, Z. Wang, Z. Wang, L. Yue, Q. Cheng, Z. Ye, Q. Zhang and R. Wang, *Biomater. Sci.*, 2021, 9, 1355–1362.

38 W. Yang, X. Gao and B. Wang, *Med. Res. Rev.*, 2003, **23**, 346–368.

39 A. Kim, Y. Suzuki and Y. Nagasaki, *Acta Biomater.*, 2021, **121**, 554–565.

40 D. J. Wu, K. van Dongen, W. Szymczyk, P. J. Besseling, R. M. Cardinaels, G. Marchioli, M. H. P. van Genderen, C. V. C. Bouten, A. I. P. M. Smits and P. Y. W.

Dankers, *Front. Mater.*, 2020, **7**, 1–11.

41 L. R. Hart, J. L. Harries, B. W. Greenland, H. M. Colquhoun and W. Hayes, *ACS Appl. Mater. Interfaces*, 2015, **7**, 8906–8914.

42 J. S. Godleman, T. S. Babra, A. Afsar, A. Kyriacou, M. Thompson, J. L. Harries, H. M. Colquhoun and W. Hayes, *Prog. Org. Coatings*, 2021, **151**, 106105.

43 A. M. Pekkanen, R. J. Mondschein, C. B. Williams and T. E. Long, *Biomacromolecules*, 2017, **18**, 2669–2687.

44 L. R. Hart, S. Li, C. Sturgess, R. Wildman, J. R. Jones and W. Hayes, *ACS Appl. Mater. Interfaces*, 2016, **8**, 3115–3122.

45 H. Rupp, D. Döhler, P. Hilgeroth, N. Mahmood, M. Beiner and W. H. Binder, *Macromol. Rapid Commun.*, 2019, **40**, 1–6.

46 Z. Gao, F. Yan, S. Qiu, Y. Han, F. Wang and W. Tian, *Chem. Commun.*, 2020, **56**, 9214–9217.

47 X. Hou, C. Ke, C. J. Bruns, P. R. McGonigal, R. B. Pettman and J. F. Stoddart, *Nat. Commun.*, 2015, **6**, 1–9.

48 N. Herzer, H. Guneysu, D. J. D. Davies, D. Yildirim, A. R. Vaccaro, D. J. Broer, C. W. M. Bastiaansen and A. P. H. J. Schenning, *J. Am. Chem. Soc.*, 2012, **134**, 7608–7611.

49 L. R. Hart, J. L. Harries, B. W. Greenland, H. M. Colquhoun and W. Hayes, *Polym. Chem.*, 2015, **6**, 7342–7352.

50 WO 2014/111722 Al, *World Intellect. Prop. Organ.*, 2013.

51 S. C. Ligon, R. Liska, J. Stampfl, M. Gurr and R. Mülhaupt, *Chem. Rev.*, 2017, **117**, 10212–10290.

52 L. E. Murr, E. Martinez, K. N. Amato, S. M. Gaytan, J. Hernandez, D. A. Ramirez, P. W. Shindo, F. Medina and R. B. Wicker, *J. Mater. Res. Technol.*, 2012, **1**, 42–54.

53 C. Parra-Cabrera, C. Achille, S. Kuhn and R. Ameloot, *Chem. Soc. Rev.*, 2017, **47**, 209–230.

54 C. Alvarez-Lorenzo, C. A. García-González and A. Concheiro, *J. Control. Release*, 2017, **268**, 269–281.

55 P. Calvert and R. Crockett, *Chem. Mater.*, 1997, **9**, 650–663.

56 A. P. Nyaluke, D. An, H. R. Leep and H. R. Parsaei, *Comput. Ind. Eng.*, 1995, **29**, 345–349.

57 N. Strategy, *Additive Manufacturing UK*, 2018.

58 F. P. W. Melchels, J. Feijen and D. W. Grijpma, *Biomaterials*, 2010, **31**, 6121–6130.

59 S. J. Leigh, R. J. Bradley, C. P. Purssell, D. R. Billson and D. A. Hutchins, *PLoS One*, 2012, **7**, 1–6.

60 T. A. Campbell and O. S. Ivanova, *Nano Today*, 2013, **8**, 119–120.

61 J. P. Kruth, M. C. Leu and T. Nakagawa, *CIRP Ann. - Manuf. Technol.*, 1998, **47**, 525–540.

62 A. Kain, C. Mueller and H. Reinecke, *Procedia Chem.*, 2009, **1**, 750–753.

63 R. Vaiyapuri, B. W. Greenland, H. M. Colquhoun, J. M. Elliott and W. Hayes, *Polym. Int.*, 2014, **63**, 933–942.

64 N. A. Sather, H. Sai, I. R. Sasselli, K. Sato, W. Ji, C. V. Synatschke, R. T. Zambrotta, J. F. Edelbrock, R. R. Kohlmeyer, J. O. Hardin, J. D. Berrigan, M. F. Durstock, P. Mirau and S. I. Stupp, *Small*, 2021, **17**, 2005743.

65 B. de Gans, P. C. Duineveld and U. S. Schubert, *Adv. Mater.*, 2004, **16**, 203–213.

66 A. M. J. van den Berg, P. J. Smith, J. Perelaer, W. Schrof, S. Koltzenburg and U. S. Schubert, *Soft Matter*, 2007, **3**, 238–243.

67 M. Stanković, H. W. Frijlink and W. L. J. Hinrichs, *Drug Discov. Today*, 2015, **20**, 812–823.

68 S. Salimi, Y. Wu, M. I. E. Barreiros, A. A. Natfji, S. Khaled, R. Wildman, L. R. Hart, F. Greco, E. A. Clark, C. J. Roberts and W. Hayes, *Polym. Chem.*, 2020, **11**, 3453–3464.

69 T. Hu, X. Cui, M. Zhu, M. Wu, Y. Tian, B. Yao, W. Song, Z. Niu, S. Huang and X. Fu, *Bioact. Mater.*, 2020, **5**, 808–818.

70 R. M. Jeziórska, *Adv. Polym. Process. From Macro- to Nano-Scales*, 2009, 143–172.

71 C. Mendes-Felipe, J. Oliveira, I. Etxebarria, J. L. Vilas-Vilela and S. Lanceros-Mendez, *Adv. Mater. Technol.*, 2019, **4**, 1–16.

72 X. Lu, C. P. Ambulo, S. Wang, L. K. Rivera-Tarazona, H. Kim, K. Searles and T. H. Ware, *Angew. Chemie - Int. Ed.*, 2021, **60**, 2–10.

73 Y. Yao, C. Yin, S. Hong, H. Chen, Q. Shi, J. Wang, X. Lu and N. Zhou, *Chem. Mater.*, 2020, **32**, 8868–8876.

74 J. R. Capadona, O. Van Den Berg, L. A. Capadona, M. Schroeter, S. J. Rowan, D. J. Tyler and C. Weder, *Nat. Nanotechnol.*, 2007, **2**, 765–769.

75 J. Fox, J. J. Wie, B. W. Greenland, S. Burattini, W. Hayes, H. M. Colquhoun, M. E. Mackay and S. J. Rowan, *J. Am. Chem. Soc.*, 2012, **134**, 5362–5368.

76 S. Kumar and J. P. Kruth, *Mater. Des.*, 2010, **31**, 850–856.

77 S. J. Eichhorn, A.Dufresne, M. Aranguren, N. E. Marcovich, J. R. Capadona, S. . Rowan, C. Seder, W. Thielemans, M. Rowan, S. Renneckar, W. Gindl, S. Veigel, J. Keckes, H. Yano, K. Abe, M. Nogi, A. N. Nakagaito, A. Mangalam, J. Simonsen, A. S. Benight, A. Bismarck, L. A. Berglund and T. Peijs, *J. Mater. Sci.*, 2010, **45**, 1–33.

78 S. Meer, A. Kausar and T. Iqbal, *Polym. Plast. Technol. Eng.*, 2016, **55**, 826–861.

79 B. Utela, D. Storti, R. Anderson and M. Ganter, *J. Manuf. Process.*, 2008, **10**, 96–104.

80 A. Afsar, L. M. Harwood, M. J. Hudson, M. E. Hodson and E. J. Shaw, *Chem. Commun.*, 2014, **50**, 7477–7480.

81 D. Brühwiler, *Nanoscale*, 2010, **2**, 887–892.

82 J. W. Goodwin, R. S. Harbron and P. A. Reynolds, *Colloid Polym. Sci.*, 1990, **268**, 766–777.

83 H. Ishida, S. Campbell and J. Blackwell, *Chem. Mater.*, 2000, **12**, 1260–1267.

84 R. Vaiyapuri, B. W. Greenland, H. M. Colquhoun, J. M. Elliott and W. Hayes, *Polym. Chem.*, 2013, **4**, 4902–4909.

85 L. Wei, N. Hu and Y. Zhang, *Materials (Basel).*, 2010, **3**, 4066–4079.

86 H. Behniafar and M. K. Nazemi, *Polym. Bull.*, 2017, **74**, 3739–3749.

87 H. Zou, S. Wu and J. Shen, *chem. Rev.*, 2008, **108**, 3893–3957.

88 G. Otorgust, H. Dodiuk, S. Kenig and R. Tenne, *Eur. Polym. J.*, 2017, **89**, 281–300.

89 D. Pedrazzoli and I. Manas-Zloczower, *Polymer (Guildf).*, 2016, **90**, 256–263.

90 C. Mu, Y. Song, W. Huang, A. Ran, R. Sun, W. Xie and H. Zhang, *Adv. Funct. Mater.*, 2018, **28**, 1707503.

91 P. Katti, K. V. Kundan, S. Kumar and S. Bose, *Polymer (Guildf).*, 2017, **122**, 184–193.

92 J. R. C. Dizon, Q. Chen, A. D. Valino and R. C. Advincula, *MRS Commun.*, 2019, **9**, 209–217.

93 A. J. Clancy, D. B. Anthony and F. De Luca, *ACS Appl. Mater. Interfaces*, 2020, **12**, 15955–15975.

94 S. Salimi, L. R. Hart, A. Feula, D. Hermida-Merino, A. B. R. Touré, E. A. Kabova, L. Ruiz-Cantu, D. J. Irvine, R. Wildman, K. Shankland and W. Hayes, *Eur. Polym. J.*, 2019, **118**, 88–96.

95 L. Jin, H. Wang and Y. Yang, *Compos. Sci. Technol.*, 2013, **79**, 58–63.

96 V. R. Basrur, J. Guo, C. Wang and S. R. Raghavan, *Appl. Mater. interfaces*, 2013, **5**, 262–267.

97 D. J. Cornwell and D. K. Smith, *Mater. Horizons*, 2015, **2**, 279–293.

# Chapter 2

## A 3D Printed Drug Delivery Implant formed from a Dynamic Supramolecular Polyurethane Formulation

This chapter has been published as a peered review research article: S. Salimi, Y. Wu, M. I. E. Barreiros, A. A. Natfji, S. Khaled, R. Wildman, L. R. Hart, F. Greco, E. A. Clark, C. J. Roberts and W. Hayes, A 3D printed drug delivery implant formed from a dynamic supramolecular polyurethane formulation, *Polym. Chem.*, 2020, **11**, 3453–3464.

Note of Contribution: Y. Wu, M. I. E. Barreiros, Dr E. A. Clark and S. Khaled carried out the Formulation development, release study and the hot-melt extrusion of the material at the University of Nottingham under the supervision of Professor R. Wildman, and Professor C. J. Roberts. A. Natfji carried out the biocompatibility study at the University of Reading under the supervision of Dr F. Greco. S. Salimi carried out all of the other studies reported in this Chapter. Images in this Chapter reproduced from Ref. 66 with permission from the Royal Society of Chemistry.

### 2.1 Abstract

Using a novel molecular design approach, we have prepared a thermo-responsive supramolecular polyurethane as a matrix material for use in drug eluting implants. The dynamic supramolecular polyurethane (SPU) is able to self-assemble through hydrogen bonding and π-π stacking interactions, resulting in an addressable polymer network with a relatively low processing temperature. The mechanical properties of the SPU demonstrated the material was self-supporting, stiff, yet flexible thus making it suitable for hot-melt extrusion processing, inclusive of related 3D printing approaches. Cell-based toxicity assays revealed the SPU to be non-toxic and therefore a viable candidate as a biocompatible polymer for implant applications. To this end, the SPU was formulated with paracetamol (16 %w/w) and 4 wt% or 8 wt% poly(ethylene glycol) (PEG) as an excipient and hot melt extruded at 100 °C to afford a 3D printed prototype implant to explore the extended drug release required for an implant and the potential manipulation of the release profile. Furthermore, rheological, infra-red spectroscopy, powder X-ray diffraction and scanning electron microscopy studies revealed the chemical and physical properties and compatibility of the formulation components. Successful release of paracetamol was achieved from *in vitro* dissolution studies and it was predicted that the drug would be released over a period of up to 8.5 months with the hydrophilic PEG component able to influence the release rate. This extended release time

is consistent with applications of this novel dynamic polymer as a drug eluting implant matrix.

## 2.2 Introduction

Investigating new functional excipient materials for local or systemic delivery of drugs is of ongoing interest.[1] Such materials can lead to a range of benefits that can include improved efficiency of drug delivery, reduced toxicity and side effects and increased patient compliance.[2] A key consideration when designing implantable drug delivery devices is the mechanism(s) and hence kinetics by which the desired drug is released. For example, drug release can occur via physical degradation of a matrix, desorption from a matrix surface, diffusion of the drug from within a matrix, or cleavage of a chemical bond to liberate the free drug.[3] The ideal release time can range from hours to months depending on the disease being treated, the active ingredient plus the route of delivery such as oral or injection, and it is thus desirable that the release rate is relatively easily manipulated via any newly developed matrix material to adapt with range of applications and drugs.

Materials developed for potential drug delivery applications range from porous materials,[4] such as metal-organic frameworks,[5,6] to polymers and gels[7-11] which release the drug upon exposure to a suitable stimulus (e.g. pH and temperature).[108–110] The release of the drug can be through dissociation of the polymer network in drug-polymer blends or by cleavage of the drug to excipient bond (covalent or non-covalent in nature). Polymer systems used successfully in this application include polyurethanes,[15] poly(caprolactone) (PCL),[16] poly(dimethylsiloxane),[17] poly(lactic acid)[18] and more extensively polyethylene glycol (PEG).[13,19-22] Additionally, blends of different classes of polymers have been used[22-24] and are employed to modify or tune release rates and profiles through a combination of the individual components properties such as the level of hydrophobicity and hydrophilicity. For example, PCL is prone to hydrolysis *in-vivo* which results in drug release, however, as a consequence of its hydrophobicity the process is remarkably slow in order of months. In the majority of polymeric drug delivery implant systems, release occurs upon degradation (surface or bulk) of the polymer matrix, resulting in increased surface area and subsequent drug release.[25] A prominent example of this process is the slow hydrolysis of carbamate motifs within polyurethanes which makes them suitable for long-term drug release in implants.[21] This rate of bond cleavage and hence drug release can be tuned by blending polymers with different degradation rates. A similar approach has been reported previously[119] by taking advantage of hydrophilicity of PEG to induce hydrolysis of the whole system and to increase the rate of drug release.

One new approach being investigated to produce different types of solid dosage forms is to deposit the formulation using additive manufacturing processes such as 3D printing. Exploiting 3D printing approach enabling customisation in production of solid dosage forms to patients based on their specific need. This could be performed in different ways such as printing solutions via ink-jet technologies[26] and solids by extrusion techniques.[27] The later has shown promise in the 3D printing of well-known pharmaceutical materials, owing to similarities with traditional processing methods such as hot-melt extrusion.[28] The absence of solvent to process the ink in this method is considered beneficial which especially favours biocompatibility of the printed part, since the majority of organic solvents show a level of toxicity to human body.[29] However, in order to be able to extrude the majority of conventional polymeric materials with high molecular weight, high temperature is required to reduce the viscosity of the polymer and prompt printing. The high processing temperature (≥180 °C) involved in this method, constrain the components that can be used to formulate pharmaceuticals, especially for the low temperature resistive drugs.[30,31] A new approach to the formation of a solid implant from extrusion-based techniques at relatively mild temperatures could be by taking advantage of dynamic supramolecular polyurethanes (SPU). The SPU reported in this chapter is able to self-assemble through hydrogen bonding and π-π stacking interactions,[32] giving rise to thermally reversable material properties.[33-35] The thermally addressable nature of the SPU makes it an ideal candidate for hot-melt extrusion, inclusive of 3D printing approaches, as the melt viscosity is in a suitable range for printing and a stiff, yet flexible structure is rapidly produced upon cooling.[36] The relatively low temperature required to dissociate the supramolecular interactions, and thus deposit the material, may also widen the range of actives available to be formulated as a result of the mild processing conditions preventing thermal degradation of the Active Pharmaceutical Ingredient (API). This lower operating temperature could address one of the main obstacles regarding extrusion of pharmaceutical formulations. Additionally, the release profile of the drug (here paracetamol as a model drug) can be modulated and enhanced by co-formulating with PEG,[37,38] which is a regulatory approved and commonly used excipient in pharmaceutical and personal care applications. As a widely used pain-killer, it may be advantageous to incorporate paracetamol into an implant (e.g. for knee and joint replacement applications). The extrusion 3D printing of SPU-PEG-paracetamol formulations to produce robust constructs which demonstrated suitable mechanical performance as well as biocompatibility is reported in this chapter. Drug release from the printed formulations was evaluated via *in vitro* studies and the extrapolation of this data predicted that a release duration of 5 to 8.5 months would be achievable with the formulations; a timescale range that is consistent with many implant applications. There is clear potential to alter release rates further through modification of the formulation by varying the percentage of PEG or its molecular weight.

## 2.3 Results and discussion

In order to create a prototype biomedical implant-style device which can be fabricated by hot-melt extrusion 3D printing, a thermally reversible polymer with a melting point below 140 °C (as dictated by the printer being used) was required. By harnessing the reversible nature of the supramolecular recognition motifs, the disassembly of the polymer network could be thermally triggered in the print-head before being extruded onto the substrate surface (Figure 2.3.1). Upon cooling, the recognition motifs are able to reassemble, yielding a mechanically robust polymer network and object. Furthermore, polyurethanes often afford flexible materials which may be of benefit for patient comfort and welfare which is specifically desirable in long-term deployment such as implants. Paracetamol was selected as a model drug and PEG was incorporated into the formulation to generate different release rates.

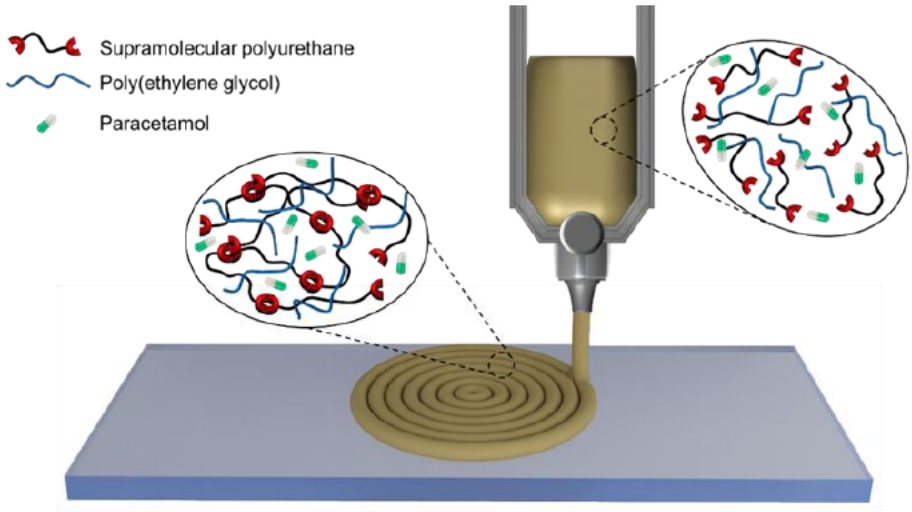


***Figure 2.3.1:*** *Schematic representation of the 3D printing of the prototype drug-release implant comprising of a dynamic self-assembling polyurethane, PEG and model drug (paracetamol).*

### 2.3.1 Polymer Synthesis

To realise an implantable and potentially personalisable drug delivery device, an appropriate supramolecular recognition motif was required. To this end, a hydrogen bonding and π-π stacking end-group, namely *N*-(4-methoxybenzyl)-1-(4-nitrophenyl)methanamine[32] **2.1** was identified as a suitable assembly motif and was synthesised via the formation of the imine and subsequent reductive amination as previously reported (Scheme 2.3.1).[32]

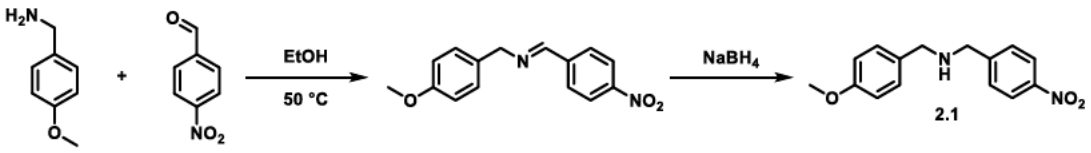


***Scheme 2.33.1:*** *Synthesis steps of the recognition motif 2.1 via imine formation.*

To prepare the supramolecular polymer, an apolar hydrogenated polybutadiene (Krasol HLBH-P2000, molecular weight as received = 2 kg.mol$^{-1}$) diol **2.2** (a viscous liquid) was end-capped with 4,4'-methylene diphenyl diisocyanate (4,4'-MDI) **2.3** at 80 °C in the bulk[39,40] to afford the pre-polymer **2.4**. The prepolymer was then terminated in solution (anhydrous THF) with the recognition motif **2.1** (Scheme 2.3.2). The purified supramolecular polyurethane **SPU1** was then isolated after multiple precipitations into methanol from concentrated solutions (where THF was the solvent), *i.e.* the synthesised polymer was dissolved in minimum amount of THF and slowly poured into methanol and the precipitate was collected.

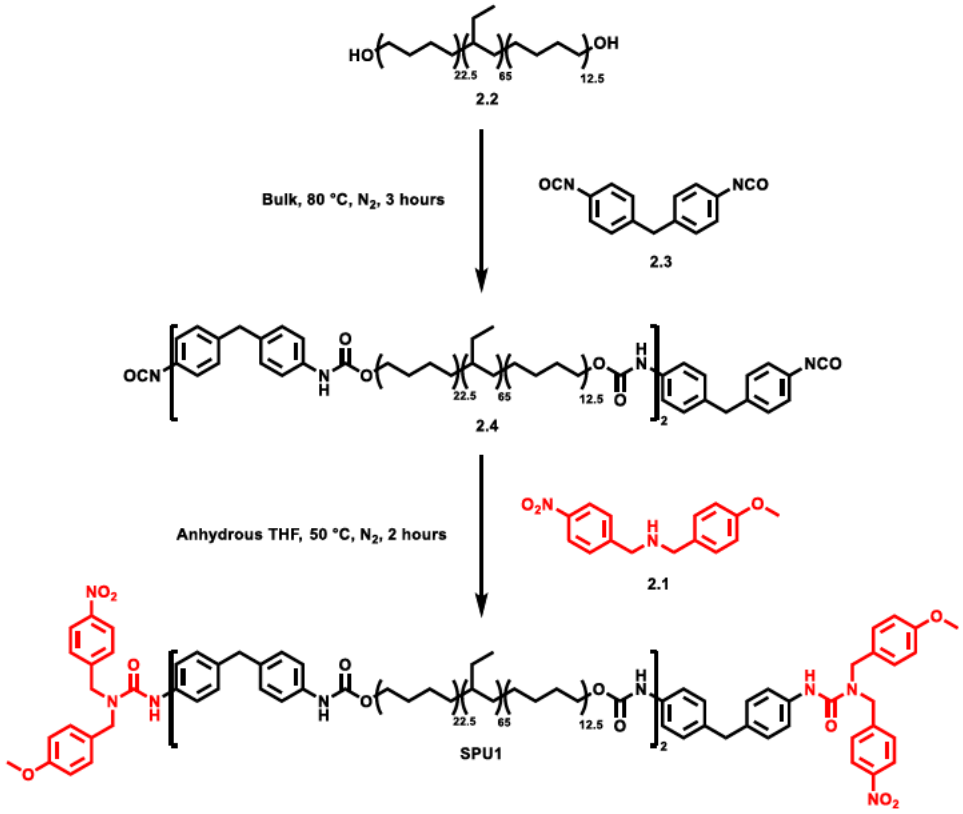


***Scheme 2.3.2:*** *Synthesis of the supramolecular polyurethane* ***SPU1*** *by chain-extension of the polyol* ***2.2*** *with diisocyanate* ***2.3*** *to yield the pre-polymer* ***2.4*** *which was subsequently terminated with recognition motif* ***2.1****.*

To confirm the successful synthesis of **SPU1**, NMR spectroscopy was undertaken. $^{1}$H NMR spectroscopy revealed the downfield shift of the characteristic diol chain terminal methylene resonances (4.15 ppm) adjacent to the newly formed urethanes and the end-group **2.1** methylene adjacent to the newly formed urea (4.70 and 4.45 ppm) (Figure 2.3.2). In addition, urea and urethane carbonyl resonances were observed at 159.6 ppm and 155.8 ppm by $^{13}$C NMR spectroscopy. Also the downfield shift of the protons of the methylene bridge in 4,4'-MDI after formation of the urea bond was observed (Marked as red and orange in Figure 2.3.2). IR spectroscopic analysis confirmed the disappearance of the characteristic isocyanate stretch at 2340 cm$^{-1}$ and the appearance of carbonyl stretches at 1708 cm$^{-1}$ and 1646 cm$^{-1}$

corresponding to the newly formed urethane and urea bonds, respectively. Additionally, N-O stretches were observed at 1512 $cm^{-1}$ and 1462 $cm^{-1}$, assigned to the nitro group in the self-assembly motif and thus further confirming the incorporation of the end-group in the supramolecular polyurethane.

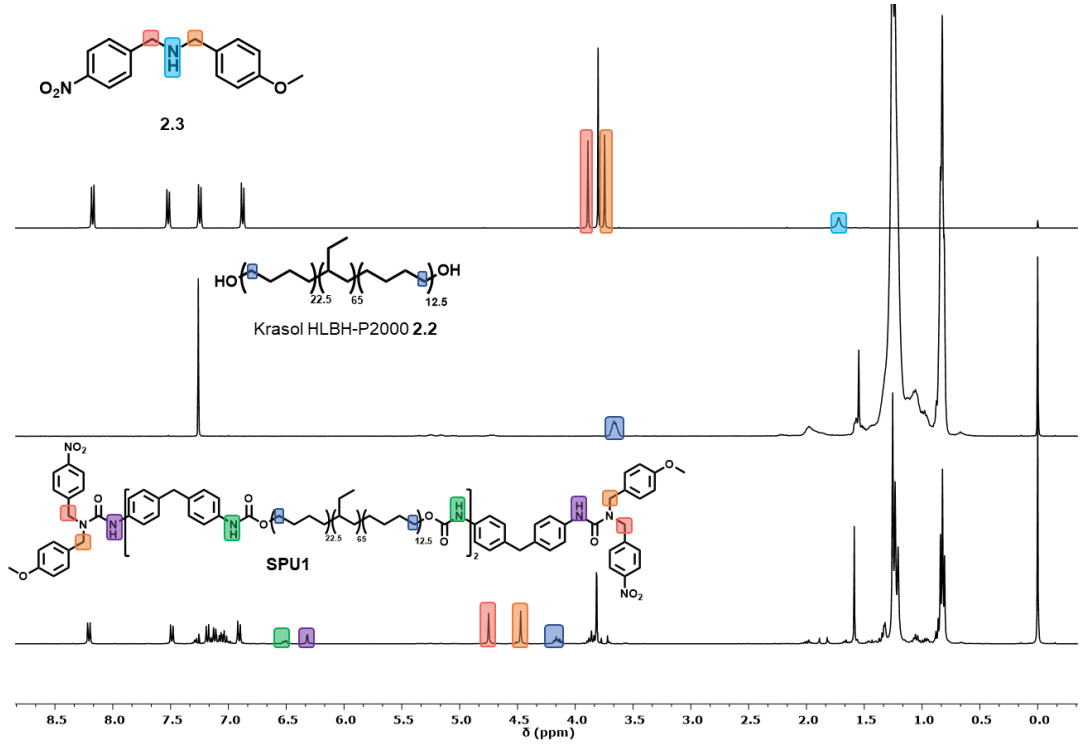


***Figure 2.3.2:*** *Stacked $^{1}H$ NMR spectra of the end-group (N-(4-Methoxybenzyl)-1-(4-nitrophenyl)methanamine **2.1**, polymer **2.2**, and **SPU1**, confirming the formation of the urethane and urea linkages in $CDCl_3$.*

Analysis of **SPU1** by GPC (Figure 2.3.3 A and B) revealed a bimodal distribution, attributed to chain extension within the polyurethane, with a $M_n$ of 6100 Da and $Đ$ = 2.06, corresponding to approximately 2 repeat units per polymer chain.[35] This is in close agreement with the analysis of the integrals from the $^{1}H$ NMR spectroscopic data. Comparison of the GPC eluograms of **SPU1** and the diol backbone revealed an increase in the polymer molecular weight confirming the formation of new bonds. The small elution band at 17.9 min represents the formation of bisurea compound (Figure 2.3.3 C) from the reaction of the diisocyanate **2.3** and the recognition motif **2.2**. The majority of it was separated from the desired product **SPU1** during the precipitation into methanol, however, there could be some remaining that has formed strong hydrogen bonding with the polymer hard segments and is not solubilising in methanol, consequently.

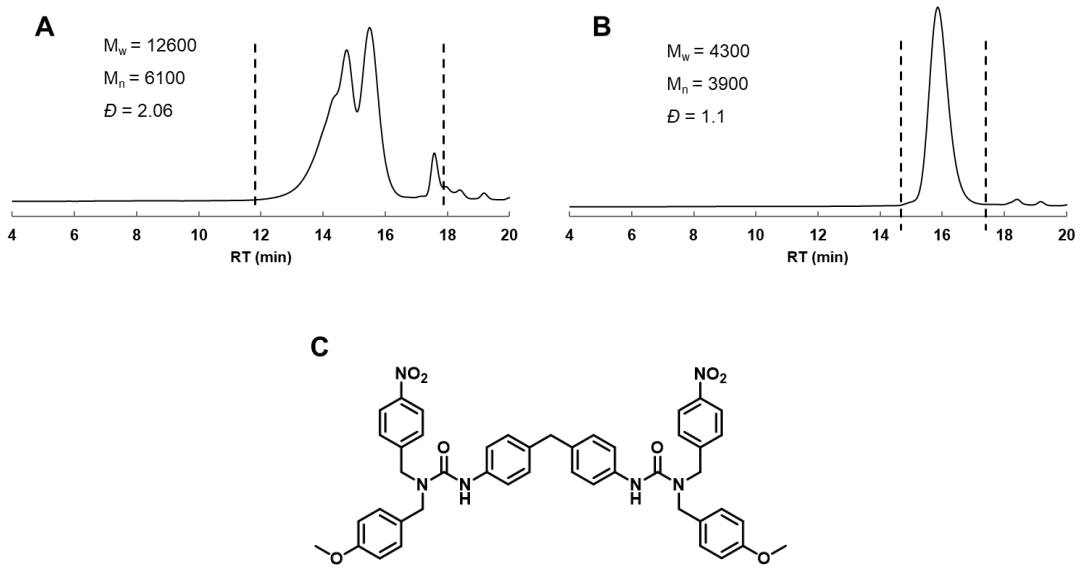


***Figure 2.3.3:*** *GPC eluograms of* ***A) SPU1*** *and* ***B)*** *Krasol HLBH-P2000* ***2.2****. The regions used for molecular weights calculations are shown between the hashed lines. Analysis was carried out in THF against PS standards. The small elution bands above 18 minutes are system peaks.*[132]

The thermal characteristics of the polymer were also probed using differential scanning calorimetry (DSC) (Figure 2.3.4). The experiment was repeated for 3 cycles at 20 °C $min^{-1}$ (displayed is the second cycle). The thermogram revealed a $T_g$ at -47.85 °C, which can be attributed to the soft domain of the phase separated supramolecular polymer, comprising of the hydrogenated polybutadiene. A second, less pronounced, $T_g$ was observed at 19.45 °C which relates to the hard domains formed from hydrogen bonding motifs. These results are in good agreement with structurally related SPUs which exhibit two thermal transitions.[32,33,35] Furthermore, the temperature range of $T_g$ values of the bulk and self-assembled components indicated that the polymer was relatively malleable at room temperature and appropriate for use as a biomedical device produced by hot-melt extrusion printing. This low $T_g$ is beneficial in such an application as it indicate that the material is sturdy enough inside body and it does not soften to change shape.

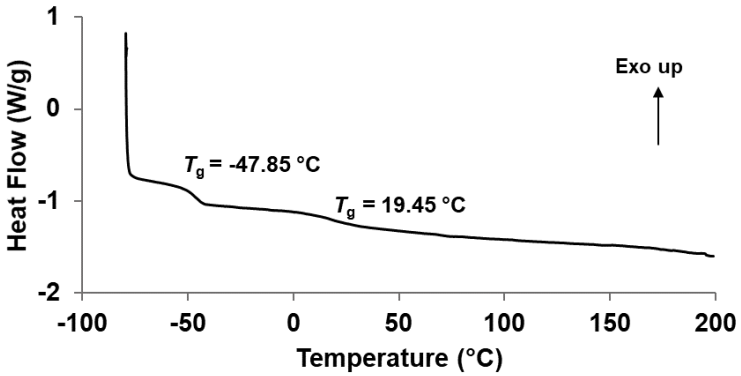


***Figure 2.3.4:*** *DSC thermogram of SPU1.*

In order to assess the suitability of the supramolecular polymer for use in a biomedical device, films were required for analysis prior to 3D printing. To achieve this, the polymer was dissolved in the minimum amount of THF before drop casting onto PTFE moulds. The solution was left to dry under ambient conditions for 24 hours before drying under vacuum at 80 °C for a further 48 hours. Critically, **SPU1** afforded a malleable and self-supporting elastomeric material (Figure 2.3.5) in contrast to the viscous hydrogenated polybutadiene precursor **2.2** as a result of the self-assembly of hydrogen bonding motifs and phase separation.[42-46]

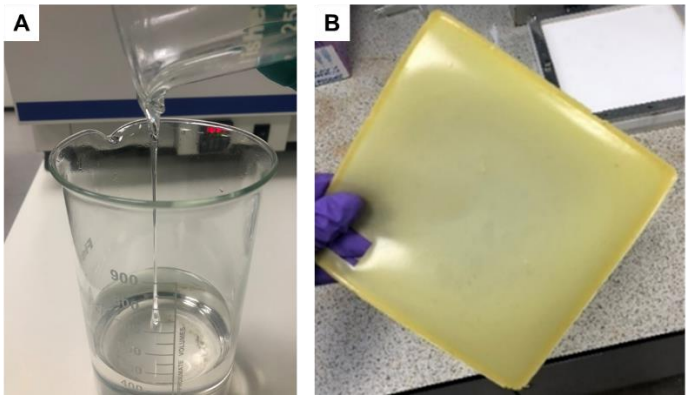


***Figure 2.3.5: A)*** *The image of the unreacted hydrogenated polybutadiene* ***2.2*** *with low viscosity at room temperature.* ***B)*** *An image of the self-supporting drop-cast polyurethane* ***SPU1*** *film from THF.*

### 2.3.2 Biocompatibility Studies

To fabricate a safe drug delivery device, it is essential that the polymer be biocompatible. Several studies[47,48] have focused on the biocompatibility of polyurethanes, and as a consequence this class of polymer has been shown to be promising substrates for the design of drug delivery systems or biomedical devices. Recently, it has been demonstrated by the Hayes group that a structurally related polyurethane with morpholine end groups was biocompatible with human fibroblasts.[33] In fact, the terminal group was modified in order to

improve the supramolecular interactions and obtain a polymeric material with desirable physical and mechanical characteristics to enable it to be used to produce a drug release implant exploiting hot-melt extrusion printing. As a first step in establishing the potential of **SPU1** in this regard, the cytotoxicity of the polyurethane film was evaluated. Liquid extracts (obtained as explained in Section 2.5.5) from the polymeric films were used to determine the biocompatibility of the polymeric films by an MTT assay (ISO 10993). To achieve this, mouse fibroblasts (L929), were exposed to the liquid extracts of the polymer. In this experiment, 0.1 w/w% zinc diethyldithiocarbamate was added to **SPU1** as positive control and polyethylene was used as the negative control. The polyurethane was found to be non-toxic, as cell viability was in excess of 94% after exposure to undiluted (100%) liquid extracts from the polymer (Figure 2.3.6) which is considerably above the 70% cell viability limit which is assigned by FDA (ISO 10993). Additionally, the experiment was repeated with 75%, 50% and 25% dilution of the polymer extract to examine the effect of concentration on cell viability. Importantly this is not significantly different from the negative control and hence **SPU1** was proved safe as potential candidate for 3D printing of a biomedical device within the time scale of the experiment. However longer term biocompatibility and cytotoxicity experiments are needed to be certain for the final application. Essentially, the exchange of the end groups, from morpholine to N-(4-methoxybenzyl)-1-(4-nitrophenyl)methanamine did not affect the cytotoxicity of the polyurethane. These results are in good agreement with previously reported data, in which a poly(caprolactone)-derived supramolecular polyurethane with the analogues *N*-(4-methoxybenzyl)-1-(4 nitrophenyl)methanamine end groups was found to be non-toxic.[49]

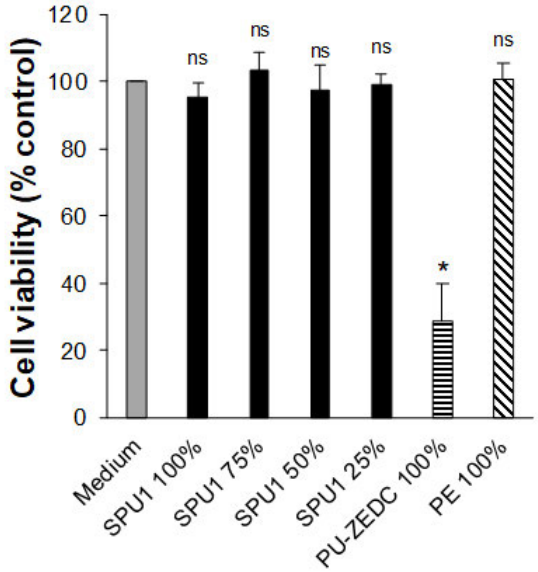


***Figure 2.3.6:*** *Cytotoxicity of liquid extracts from the medium, supramolecular polyurethane (**SPU1**) at different dilutions (100%, 75%, 50%, 25%), positive control (PU-ZEDC) and negative control (PE), both at 100%. Data are presented as mean ± s.e.m. Statistical significance with respect to untreated*

*cells (medium) was determined by ANOVA followed by Bonferroni post hoc test (* = TBC - P < 0.05; ns = non-significant).*

### 2.3.3 Polymer Formulations and Analysis

In order to formulate a drug delivery device with effective rates of release in addition to good processability, a formulation was developed comprising of the supramolecular polyurethane and PEG. A commercially available PEG ($M_w$ as received = 20 kg.mol$^{-1}$) was selected as an excipient to modify the rate of release of the active from the formulation and further tune the extrusion characteristics of the polymer blend.[50] Previous studies have revealed that less than 8 wt% of PEG is able to modify the release rate of a dosage form whilst also having a positive contribution to the printability of the formulation.[51] Herein, paracetamol was selected as the model drug to examine the drug release rate from the proposed implant form and formulated at 16 wt%. Paracetamol is used commonly in a number of 3D printed pharmaceutical forms as a model drug, illustrating an ability to achieve formulations that meet Pharmacopeia standards of manufacture, e.g. weight uniformity, hardness, friability etc.[52-54]

Formulations for 3D printing were prepared by blending **SPU1** and PEG (20 kg.mol$^{-1}$) in ethyl acetate (0.15 mL.g$^{-1}$) prior to the addition of paracetamol to yield a homogeneous mixture (Table 2.3.1). The solvent was then removed *in vacuo* and the printing 'ink' was ready to be loaded into the printer cartridge.

***Table 2.3.1****: Composition of the formulations **F1** and **F2**.*

| | SPU1 (wt%) | PEG (wt%) | Paracetamol (wt%) |
|---|---|---|---|
| **F1** | 80.00 | 4.00 | 16.00 |
| **F2** | 76.00 | 8.00 | 16.00 |

To explore the thermal responsive nature of the supramolecular polyurethanes, variable temperature IR spectroscopic analysis (VT-FTIR) was conducted (Figure 2.3.7 A) between 20 °C and 160 °C.[55-56] A strong absorbance for both free (1730 cm$^{-1}$) and hydrogen-bonded (1710 cm$^{-1}$) carbonyl units relating to the urethane groups was observed, in addition to the ordered hydrogen bonded urea carbonyl moieties (1655 cm$^{-1}$) and bound NH groups (3313 cm$^{-1}$) in **SPU1** at room temperature. Indeed, the intensity of the urethane, urea and NH absorbance bands were seen to weaken and/or shift with increased temperature,[40] as a result of dissociation of the hydrogen bonds which was consummate with a new absorbance at 3440 cm$^{-1}$, indicative of free NH bonds. Most notably, the absorbance corresponding to hydrogen bonded urethanes (~1710 cm$^{-1}$) could be seen to diminish and coalesce with the adjacent free carbonyl (~1735 cm$^{-1}$) signal.

In order to probe the effect of PEG on the thermo-responsiveness of the supramolecular polyurethane, VT-FTIR spectroscopic analysis of **F1** and **F2** was also conducted between 20 °C to 160 °C (Figure 2.3.7 B, C). The formulations **F1** and **F2** demonstrated significant decreases in absorbances associated with hydrogen bonding (bound NH ~ 3313 $cm^{-1}$ and urethane carbonyls ~ 1710 $cm^{-1}$) and a concurrent increase in free urethane (1740 $cm^{-1}$) and free NH (3440 $cm^{-1}$) absorbances. Additionally, the stretch at 1655 $cm^{-1}$, corresponding to ordered hydrogen bonded urea carbonyl units proceeded to shift to a higher wavenumber (1670 $cm^{-1}$) upon heating, indicating dissociation of hydrogen bonding of the urea moieties.[57] Additionally, upon cooling, the intensity of signals relating to hydrogen bonding motifs were fully restored, demonstrating the thermally dynamic character of the polymer network.

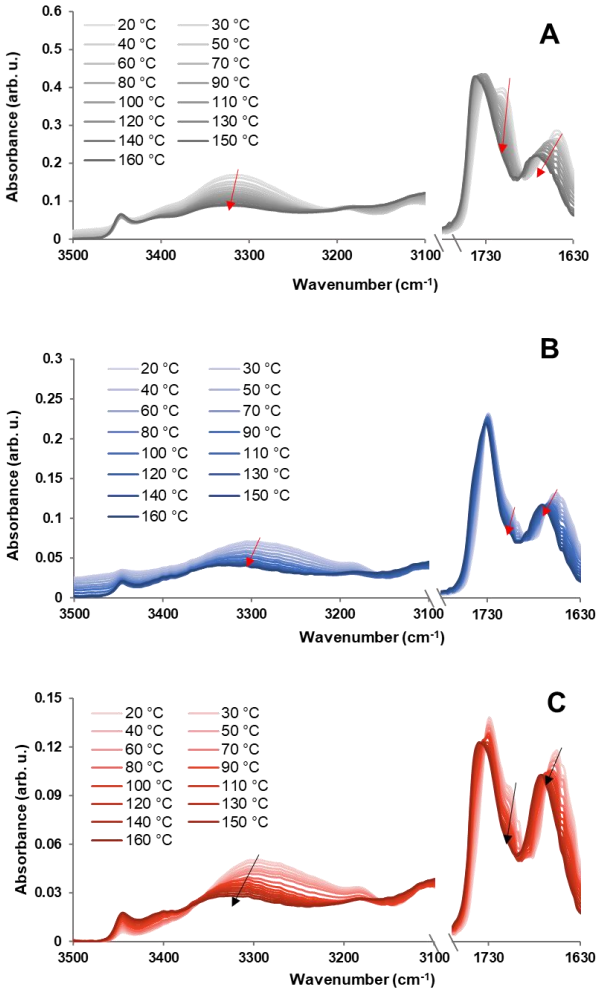


***Figure 2.3.7:*** *Partial FTIR spectra of A)* ***SPU1*** *B)* ***F1*** *and C)* ***F2*** *in the temperature range of 20 °C – 160 °C, showing the carbonyl and NH regions.*

To study the physical properties of the polymer formulations as related to assessing their suitability for printing and potential long-term stability as implants, films were prepared as previously described with the addition of the relevant weight percentage of PEG. The polymer films were then annealed in the oven for 72 hours at 80 °C until dry. To assess the thermal characteristics of the polyurethane **SPU1** and formulations **F1** and **F2** rheological analysis of films were undertaken (Figure 2.3.8). In all instances, the physical properties of the polymer were governed by the elastic character of the materials, in the low temperature regime (*ca*. 0 °C - 35 °C), as demonstrated by the storage modulus (G') exceeding the loss modulus (G"). Upon further heating, G' and G" gradually decreased as a result of the dissociation of the supramolecular polyurethane network and shift in equilibrium towards the unbound state at which the material losses its stiffness. In contrast, the rheological behaviour of the hydrogenated polybutadiene **2.2** is dominated by the viscous character of the polymer through all temperature regimes, as exemplified by a constant phase angle of *ca*. 90° upon heating (Figure 2.3.8 A). When considering **SPU1** alone (Figure 2.3.8 B), the phase angle is initially less than 45° at low temperatures, indicating the material properties are predominantly elastic in nature. At 38.1 °C, the phase angle crosses 45° and therefore viscous behaviour governs the properties of polyurethane at temperatures that are in excess of this value. By increasing the PEG content, the temperature at which the cross-over between G' and G" occurred was observed to increase as a result of the PEG excipient retarding the transition from elastic to viscous behaviour within the system (Figure 2.3.8 C and 2.3.8 D). Additionally, in F1 and F2 the G' and G" cross over occurs in a region compared to **SPU1** that an exact point is observed. This can also be attributed to the presence of PEG (not homogeneous within the **SPU1** network) which results in a prolonged melting procedure. Therefore, the incorporation of PEG in the formulation increased the temperature of the cross-over point, shifting this away from core body temperature (37 °C). In doing so, this may contribute to the control mechanism of drug release using the PEG as well as making the resulting implant more mechanically robust under normal operating temperatures within the body. However, the higher temperature might impose the need for higher temperature in order to be able to extrude the formulation.

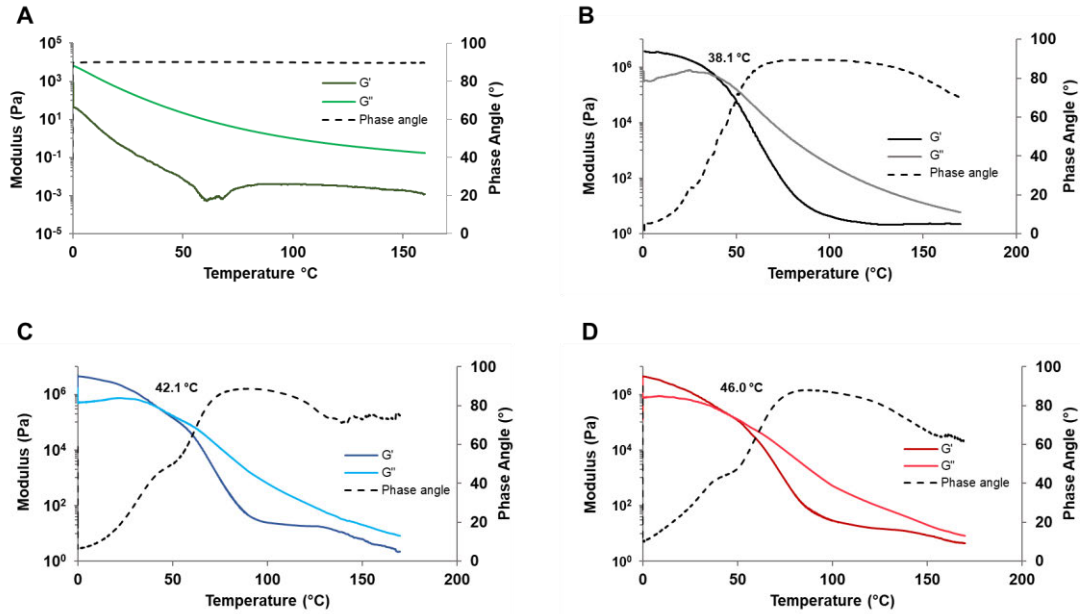


***Figure 2.3.8*** *Rheological behaviour of A) Krasol HLBH-P 2000 B)* ***SPU1****, C)* ***F1*** *and D)* ***F2*** *with respect to temperature.*

To further explore the morphology of the supramolecular polyurethane **SPU1** and the phase behaviour of the PEG in Formulations **F1** and **F2**, SAXS analysis was conducted (Figure 2.3.9). **SPU1** exhibits typical microphase separation behaviour as confirmed by the Bragg peak centred at 73.6 Å which arises from immiscibility of the polar hard (self-assembling) and apolar soft (polymer backbone) domains. PEG displayed Bragg peaks at 154.6 Å and 84.9 Å, respectively, whilst the addition of PEG to the supramolecular polyurethane to yield formulations **F1** and **F2** resulted in shifts to lower domain spacing (**F1** = 66.9 Å, **F2** = 69.3 Å). Interestingly, no apparent diffraction peaks attributed to PEG were observed in the formulations. This data suggests that the PEG within the formulation was either mixed thoroughly into the phase separated polyurethane architecture through incorporation into the polar hard domains or the concentration is too low for the SAXS to be detected. Furthermore, this data is supported by the VT-FTIR spectroscopic analysis (see Figure 2.3.7) which suggests that PEG is incorporated into the self-assembling polyurethane matrix as demonstrated by weakening of the hydrogen bonding carbonyl absorbances relative to the neat **SPU1**.

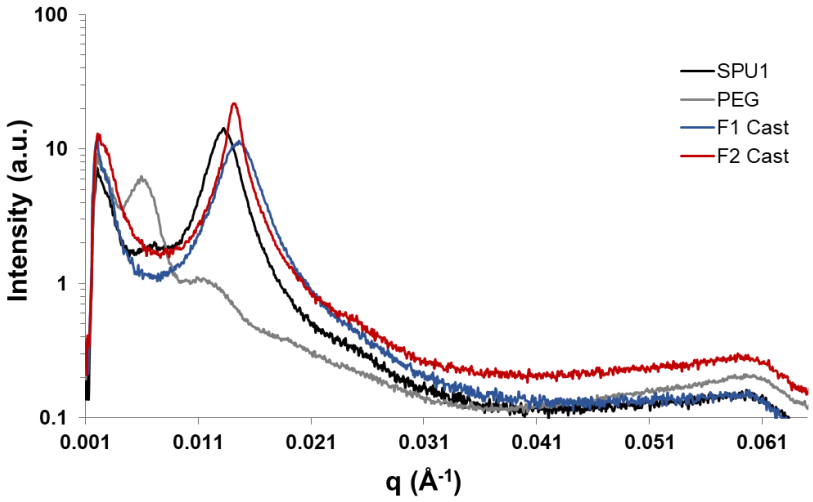


***Figure 2.3.9:*** *SAXS patterns of cast films of the* ***SPU1****, PEG (20 kDa),* ***F1*** *and* ***F2****.*

Tensile testing was carried out to further understand the mechanical characteristics of the polymer formulations (Figure 2.3.10). From the cast films, strips of polymer (*ca*. 40 mm × 5 mm × 1 mm) were cut for analysis, by extended to failure, the stress-strain graphs were recorded and by applying relevant calculations the corresponding mechanical properties were calculated from the individual stress–strain curves (Table 2.3.2). Ultimate tensile strength calculated as the maximum stress recorded in the graph which represents the maximum force that a unit cross-section of the specimen can tolerate before permanent deformation. Similarly, Young's modulus is defined as the slope of the first linear section of the stress *vs.* strain graph and provides an indication of the flexibility of the material. The higher the Young's modulus the material is considered more brittle. Another component of mechanical properties which can be extracted from a tensile test is the toughness of the material. Toughness is defined as the total energy that a unit volume of the specimen can absorb before failure and is calculated as the area under the stress *vs.* strain graph.

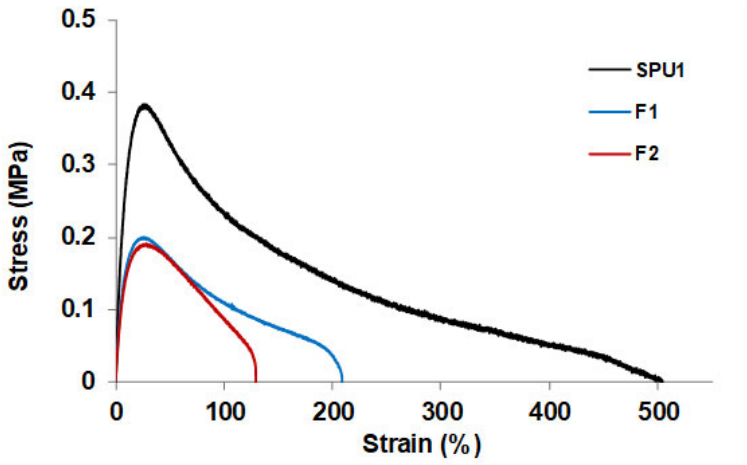


***Figure 2.3.10:*** *Stress/strain curves for drop-cast films of the supramolecular polyurethane (**SPU1**) and formulations for 3D printing (**F1** & **F2**) as cast from solution.*

The supramolecular polyurethane **SPU1** exhibited the greatest ultimate tensile strength (0.37 MPa), Young's modulus (2.34 MPa), modulus of toughness (0.67 MPa) and elongation at break (500 %). In agreement with rheological studies, the incorporation of 4 wt% PEG to the formulation (**F1**) dramatically reduced the mechanical properties of the formulation. A loss of approximately 50 % of the ultimate tensile strength (0.20 MPa), 20 % of the Young's modulus (1.87 MPa) and 69 % of the modulus of toughness (0.21 MPa) was observed. Furthermore, the elongation at break was observed to have decreased to 210 %, a reduction of 290 % when compared to **SPU1**. The decrease in mechanical performance was attributed to the PEG excipient interrupting the hydrogen bonding network and thus reducing self-assembly between the hydrogen bonding motifs in addition to disrupting any phase separation between soft and hard segments of the **SPU1**. This was corroborated by SAXS data (Figure 2.3.9) collected from films of the formulation which suggested that PEG was thoroughly mixed into the phase separated polymer matrix, signified by the omission of diffraction peaks relating to PEG. It is likely that the polar PEG molecules would have migrated to the polar self-assembling hard domains, thus interrupting the self-assembly. Similar reductions in mechanical performance were also observed in **F2**. Whilst a reduction in the mechanical properties were observed through the addition of PEG to the supramolecular polymer matrix, the resulting properties were still within the printable parameters range for hot-melt extrusion 3D printing of a geometrically well-defined object that could be considered for future development into an implant and therefore this material was utilised in the development of test structures.

***Table 2.3.2*** *Tensile data for the neat supramolecular polyurethane (**SPU1**) and formulations containing PEG (**F1** & **F2**).*

| | Ultimate Tensile Strength (MPa) | Young's Modulus (MPa) | Modulus of Toughness (MPa) |
|---|---|---|---|
| **SPU1** | 0.37 ± 0.02 | 2.34 ±0.27 | 0.67 ± 0.05 |
| **F1 (4% PEG)** | 0.20 ± 0.01 | 1.87 ± 0.10 | 0.21 ±0.08 |
| **F2 (8% PEG)** | 0.20 ± 0.03 | 1.52 ± 0.13 | 0.24 ± 0.06 |

### 2.3.4 3D Printing and Analysis of Prototype Implants

To produce a prototype implant, a bar geometry (30 mm × 3 mm × 2.5 mm), similar to that used for some contraceptive implants, was designed using computer aided design (CAD) before being converted into layers ready for 3D printing. The 3D design was transported to Heartware - the software of the Cellink INKREDIBLE printer - to generate a sliced pattern readable by the printer. The process of hot-melt extrusion printing is described in more details in Chapter 4. The formulations were loaded into an aluminium extrusion printing cartridge and placed in a Cellink INKREDIBLE printer. The formulations were subsequently deposited with control over parameters such as the applied pressure, temperature, printing layer height, printing speed and material infill. Bar samples were then printed to evaluate the spatial definition and composition of the materials (Figure 2.3.11). Drug-free formulations were also printed as controls using the same conditions for materials testing.

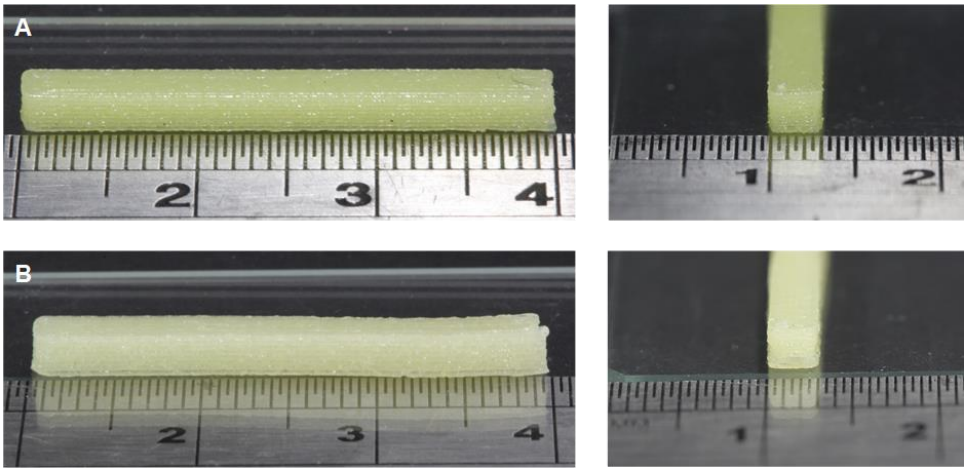


***Figure 2.3.11:*** *Side-on and end-on view images of the 3D printed bars of A) **F1** (4% PEG) and B) **F2** (8% PEG).*

The dimensions and masses of the prototype implants (N = 10 bars) were then analysed (Table 2.3.3) to assess the resolution and reproducibility of the printing process. Less than 2% deviation was observed in the length and thickness for both **F1** and **F2**, indicating good

printability of the polymer formulations. The widths of the printed bars were also analysed and were revealed to be slightly more variable (**F1** = ± 4%, **F2** = ± 2%), however, this still demonstrated good reproducibility of the extruded prototype implants which is lower than 0.5 mm, the average spatial resolution of the most commercial imaging systems.[146] The weight of individual printed bars was also measured (Table 2.3.3) and analysis showed that the printed implants made using **F1** comply with the United States Pharmacopeia (USP) specification (±7.5% deviation).[59] Larger variations up to 10.1% were noted for the bars printed from **F2** which may relate to the increased PEG content and its effect on printability, but this remains to be determined. It is not unfeasible that the reassembly of the supramolecular network was hindered by incorporation of PEG which could increase the solidification time and consequently reduce the reproducibility.

***Table 2.3.3*** *A summary of the dimensions, print parameters and masses of printed bar implants (n = 10 for all measurements).*

| | F1 | F2 |
|---|---|---|
| **3D Model Geometry** | Bar | |
| **3D Model Dimension (mm)** | 30 (L) × 3 (W) × 2.5 (H) | |
| **Length (L)*** | 29.58 ± 0.19 | 29.59 ± 0.14 |
| **Width (W)*** | 3.11 ± 0.06 | 3.17 ± 0.03 |
| **Thickness (H)*** | 2.54 ± 0.02 | 2.71 ± 0.01 |
| **Mass (g)*** | 0.224 ± 0.0036 | 0.212 ± 0.0108 |

To confirm the incorporation of the drug in the formulation and assess its stability during the printing process, IR spectroscopy (Figure 2.3.12 A) was conducted on the pure components (**SPU1**, PEG, and paracetamol) and the printed formulations (**F1** and **F2**) for comparison. From the cast film of **SPU1**, both urethane (1709 $cm^{-1}$) and urea (1645 $cm^{-1}$) carbonyl stretches were observed.[32] Sharp absorptions at 1516 $cm^{-1}$ and 1462 $cm^{-1}$ were attributed to the $NO_2$ asymmetrical and symmetrical stretches, respectively, arising from the nitro functionalised aryl group of the terminal self-assembly motif in the polymer. A characteristic N-H stretch from the urea was also identified at 3323 $cm^{-1}$, and C-H stretch were identified at 2921 $cm^{-1}$. An out of plane aromatic C-H bend was also observed around 770 $cm^{-1}$. Two strong absorptions, centred at 2871 $cm^{-1}$ and 1097 $cm^{-1}$ were observed in PEG and were attributed to C-H stretching and the C-O stretching within the polymer, respectively.[60] Finally, an N-H stretch (3323 $cm^{-1}$), out of plane C-H bend (836 $cm^{-1}$), carbonyl adsorption bands (1654 $cm^{-1}$) and N-H out of plane bending (wagging) at 1563 $cm^{-1}$ were observed in paracetamol in addition to the expected O-H stretch at 3320 $cm^{-1}$.[61]

IR spectroscopy of the 3D printed formulations (**F1** and **F2**) were then analysed to assess the stability of the components. Indeed, N-H stretches were observed at 3323 $cm^{-1}$ for **F1** and 3315 $cm^{-1}$ for **F2**, comparable to that seen in pure **SPU1** and paracetamol. A carbonyl stretch was observed at 1654 $cm^{-1}$ in both **F1** and **F2** relating to paracetamol in addition to an adsorption at 1709 $cm^{-1}$ which was attributed to the carbonyl moiety from **SPU1**. Additionally, N-O stretches were observed at 1516 $cm^{-1}$ and 1462 $cm^{-1}$, further confirming the presence of the supramolecular polymer in formulations **F1** and **F2**. The O-H stretch of paracetamol was not apparent in **F1** and **F2**, possibly as a result of hydrogen bonding between paracetamol and the polymer matrix.

Powder X-ray diffraction (PXRD) of the pure components and the two printed formulations were also performed in order to examine the state of the dispersed drug in the final formulations (Figure 2.3.12 B). The **SPU1** diffraction pattern exhibits a broad halo, indicating that the polymer is amorphous. This is in accordance with DSC data in which **SPU1** did not show any melting point to show any crystallinity within the polymer network (Figure 2.3.4). In contrast, the diffraction pattern of the PEG excipient suggests that this material is at least in-part crystalline, as indicated by the two broad diffraction signals. The PXRD pattern of pure paracetamol matches that of crystalline form I previously reported.[150] After formulation and printing, there wasn't evidence of a phase transformation of paracetamol in the formulations, **F1** and **F2**. Owing to the low percentage composition of PEG in **F1** and **F2**, nothing definitive can be said about the crystallinity of PEG in these formulations after printing, based on the PXRD data alone. However, as there is no evidence of any change in the crystalline form of the paracetamol in the printed formulations **F1** and **F2**, this suggests that the printing process does not alter or damage the constituent components of the formulations.

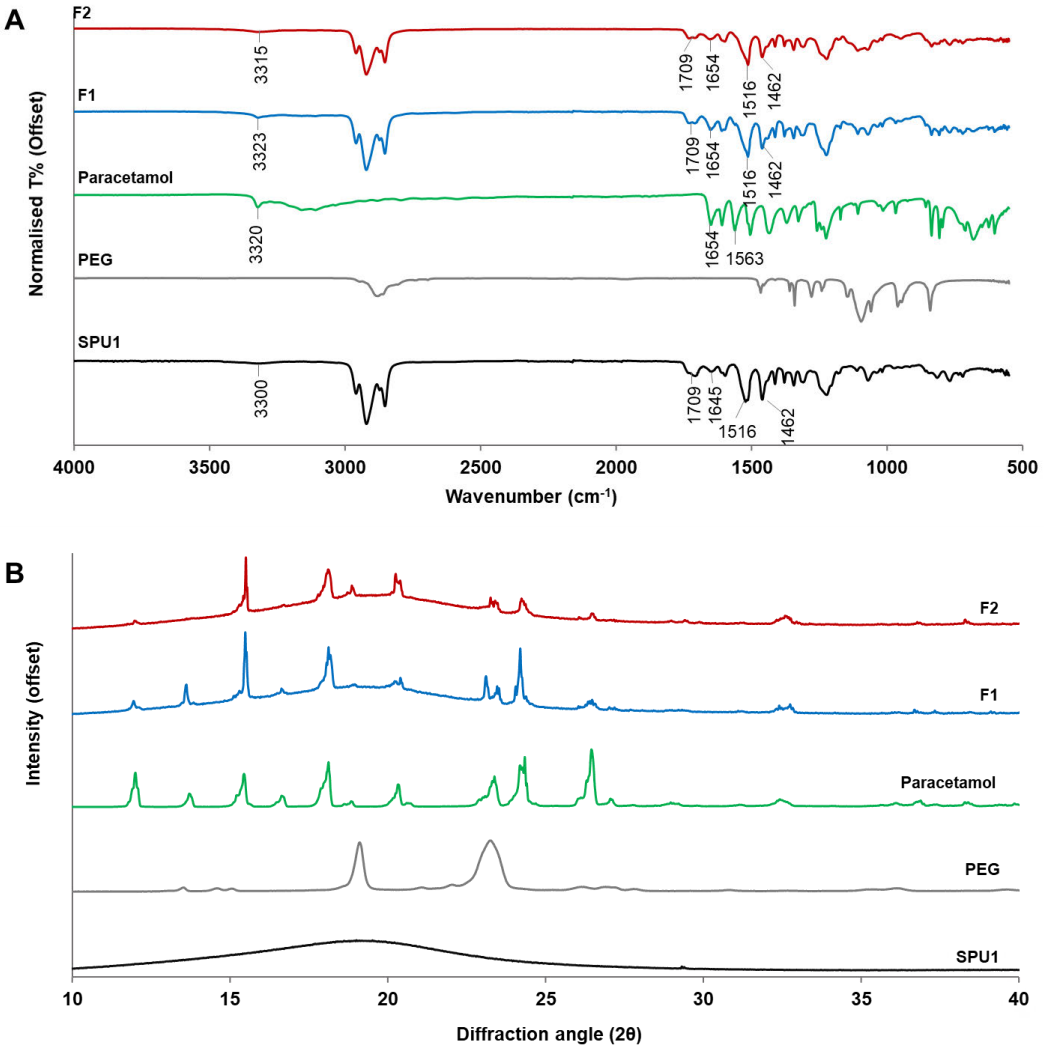


***Figure 2.3.12*** *A) FTIR spectra and B) PXRD patterns of pure* ***SPU1****, PEG 20 kg mol$^{-1}$, paracetamol and the printed bars of* ***F1*** *and* ***F2****.*

The possible effect of heat and shear involve in printing process on the formulation's constituents was further studied by DSC analysis of **SPU1**, **F1** and **F2** (Figure 2.3.13). Printed and cast formulations were subjected to DSC analysis to study the effect of 3D printing on thermal properties of the material. Two glass transitions at *ca*. -47 °C and *ca*. 0 °C, typical of phase separated polyurethane are noted in both formulations at either method of preparation.[34,63] Although, no meaningful changes in thermal transition temperatures were observed, a less intense melting peak at *ca*. 57 °C that corresponds to PEG was present in the thermograms of the printed formulations. These results suggest that the high shear and temperature experienced by the formulation in the hot-melt extrusion 3D printing process lead to a more efficient blending of **SPU1** and PEG and therefore, a loss in PEG crystallinity.

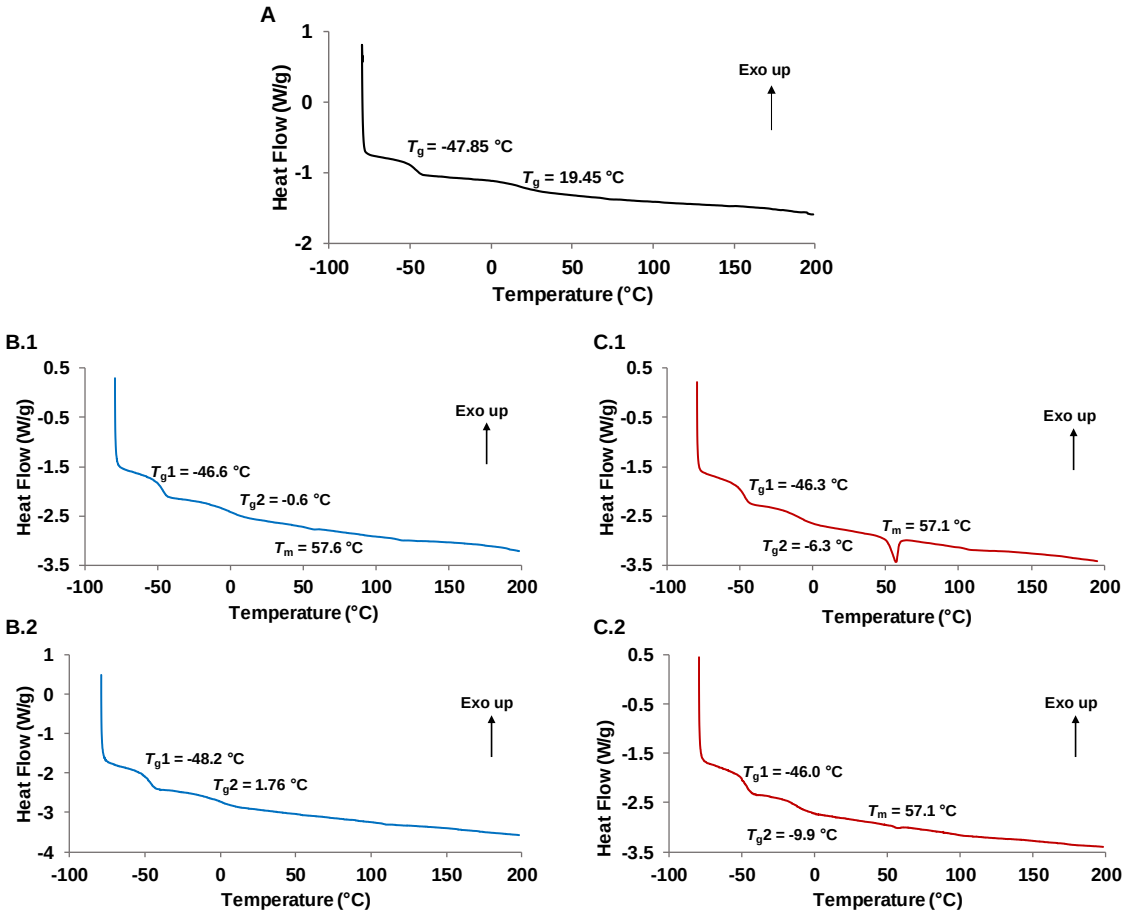


***Figure 2.3.13:*** *Differential Scanning Calorimetry of A)* ***SPU1****, B)* ***F1*** *1: cast and 2: printed, C)* ***F2*** *1: cast and 2: printed showing all thermal transitions. Shown in the graphs are the second cycle of the 3 cycles experiment.*

To explore the effect of 3D printing on the formulation, additional SAXS experiments were conducted. Scattering patterns were collected of the printed formulations, **F1** and **F2**, and compared to the cast analogues (Figure 2.3.14). An increase in domain sizes (*ca.* 4 Å shift) was observed in both formulations which contribute to bigger microphase separation as a consequence of the 3D printing process. Although a small change, this may be as a result of the thermal and shear processes associated with 3D hot-melt extrusion printing annealing the polymer formulation and more efficient penetration of PEG within the **SPU1** matrix. PEG polymer chains permeate to the hard segments of the **SPU1** resulting in bigger aggregation within the network between hard and soft segments.

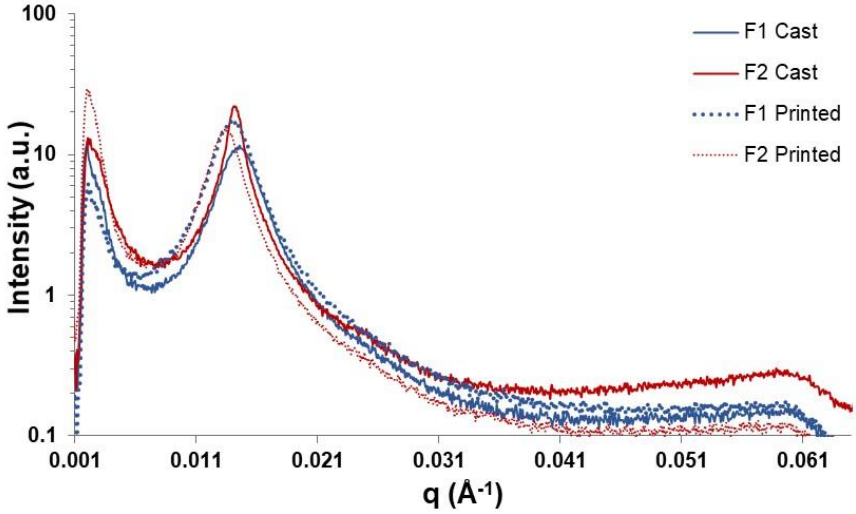


***Figure 2.3.14:*** *A comparison of SAXS patterns from cast and 3D printed formulations* ***F1*** *and* ***F2****.*

It was noted that after a week, the surface of the printed prototype implant appeared to smoothen slightly (Figure 2.3.15), and visually the layers appeared to become more homogeneous as a result of creep. This was also attributed the low $T_g$ of the material. Since the $T_g$ of the formulations is lower than the ambient temperature, the material is not totally solid and the polymer chains receive enough thermal energy to perform small motions to achieve thermal equilibrium.

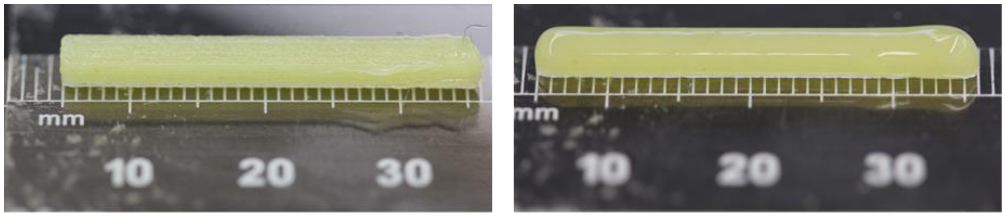


***Figure 2.3.15:*** *Images of the printed formulation* ***F1*** *showing creep over 7 days.*

To monitor the effects of creep on the mechanical properties of drug-free formulations, 3D printed samples were aged under ambient conditions for 7 days. To study the effect on rheological behaviour, a frequency sweep at 25 °C was performed in the linear viscoelastic region and between 0.01 Hz and 100 Hz (Figure 2.3.16). It was noted that in the very low frequencies region the viscous and elastic moduli in both **F1** and **F2** are close and by increasing the frequency, G' becomes considerably dominant. Additionally, the initial modulus at the starting frequency ($10^{-2}$ Hz) did not show any meaningful difference between the pristine and aged samples. After studying the effect of creep and aging on the rheology profile of the formulations, attention turned to investigate the rheological properties of the 3D printed samples over time compared with a sample prepared by drop-casting (Figure 2.3.17).

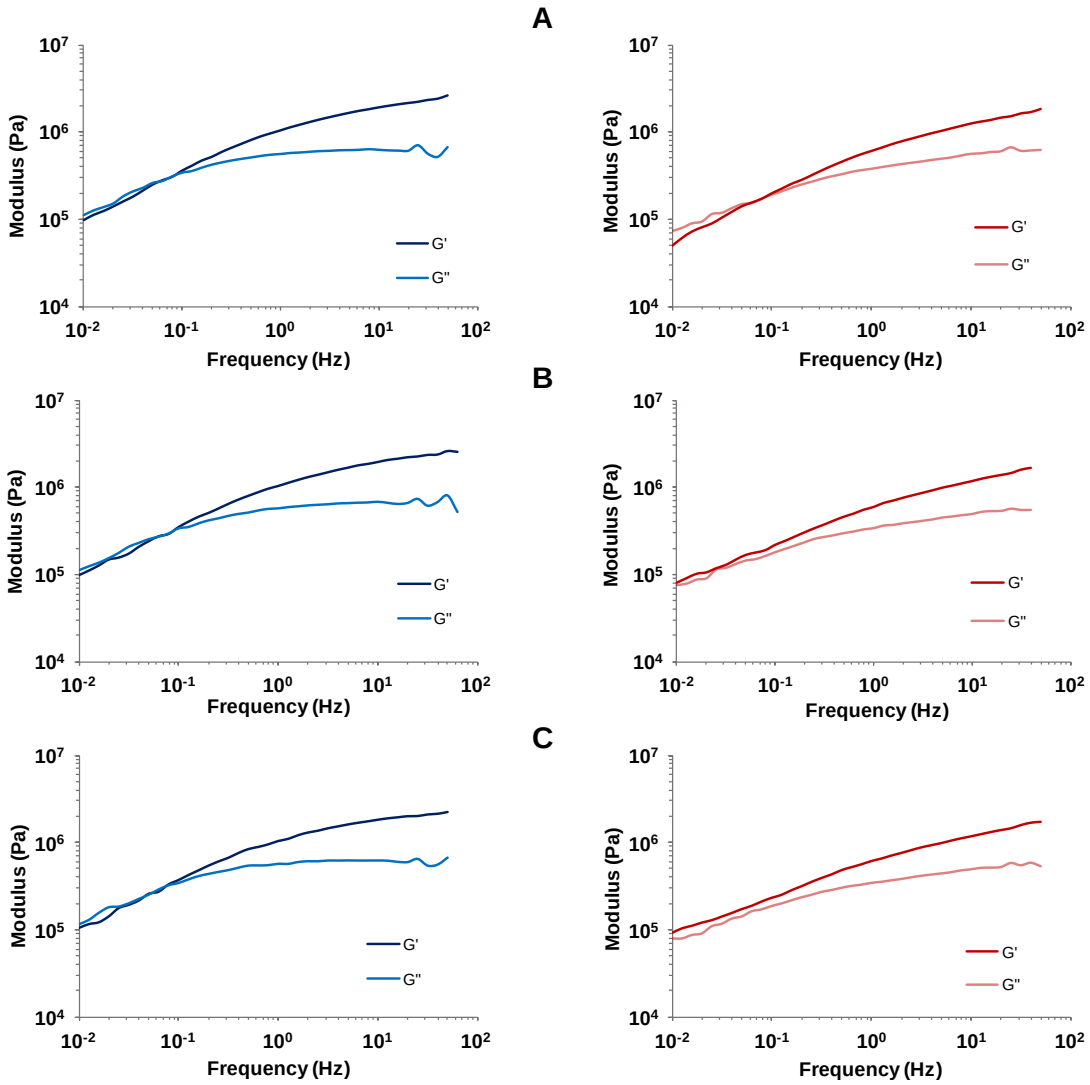


***Figure 2.3.16:*** *Variation of moduli with frequency for **F1** (left) and **F2** (right) over A) 0, B) 3 and C) 7 days aging period at ambient condition.*

Interestingly, the printed objects exhibited a modest increase in modulus when compared to the cast specimen (cast = $4.5\times10^4$ Pa, printed = $1\times10^5$ Pa). It is believed that the elevated temperature, combined with high sheer forces imparted on the polar PEG and apolar **SPU1** components of the formulation during printing resulted in improved microphase separation in hard/soft domains (and hence stiffer) when compared to the drop cast sample.

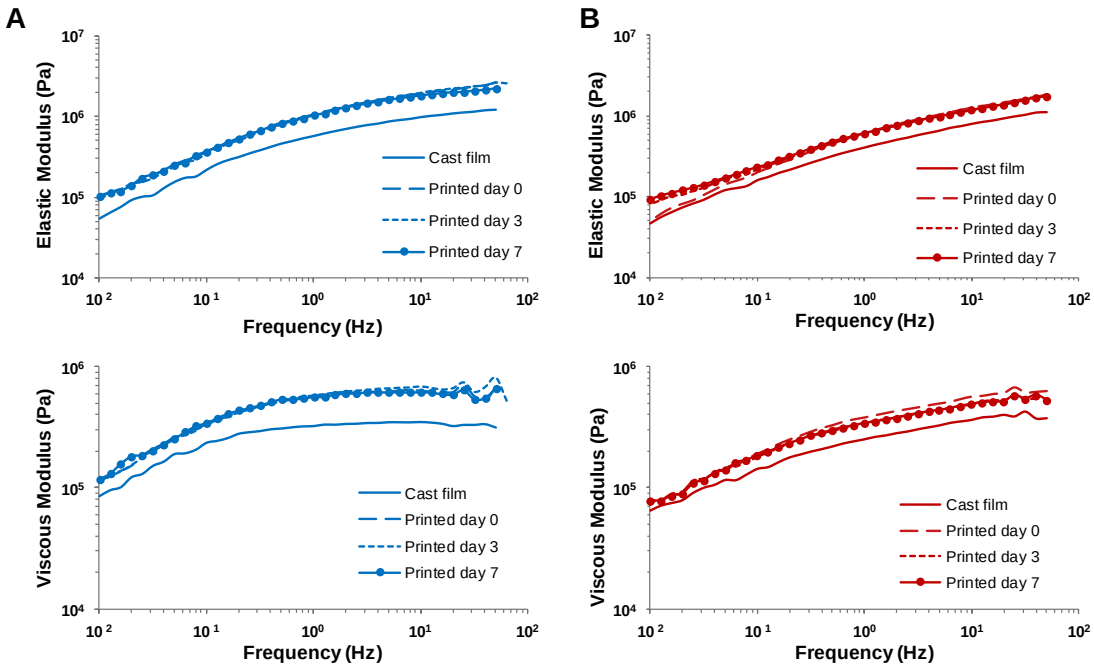


***Figure 2.3.17:*** *Variation of elastic and viscous modulus vs. frequency at 25 °C for drop cast and 3D printed disks in A)* ***F1*** *and B)* ***F2****.*

To further examine the effects of creep on the mechanical properties of the 3D printed drug-free formulations, the printed bars (ca. 40 mm × 5 mm × 0.7 mm) were elongated to break, and stress/strain profiles recorded (Figure 2.3.18).

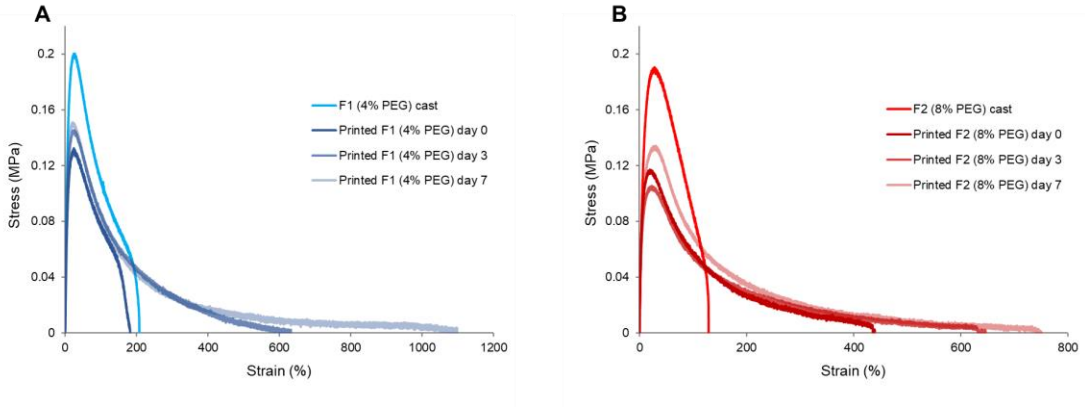


***Figure 2.3.18****: Representative stress/strain graphs of drop-cast film, pristine and aged printed samples of A) formulation 1 (****F1****) and B) formulation 2 (F2).*

The experiment was repeated three times for each aging time and the tensile characteristics calculated as the average of these three repeats (Figure 2.3.19). Interestingly, the ultimate tensile strength (Figure 2.3.19 A) of the printed material was seen to reduce by approximately 20% in **F1** and 45% in **F2** when compared to the pure polymer film prepared by drop-casting (Figure 2.3.19 C), indicating that 3D printing does not fully translate the materials ability to withstand loads as a result of voids and poor interlayer adhesion compared to the

homogeneous drop-cast films. Furthermore, although interlayer contact appears to improve visually over time, the ultimate tensile strength remains approximately constant between printing and day 7 for both formulations (**F1** and **F2**). The Young's modulus (Figure 2.3.19 B) was approximately equivalent when comparing 3D printed and drop-cast data for formulations **F1** and **F2** (Figure 2.3.19 C), revealing that along the axis of printing and elongation, the polymers properties were unaffected by formulation and processing. An overall upward trend was observed in Young's modulus over time which was attributed to the dynamic nature of the supramolecular polymer within the printed formulation. During the aging process, the printed layers undergo minor deformation as a consequence of thermal relaxion and reassembly of the supramolecular polymer in a lower energy regime.[64] Thus, the printed objects which have undergone creep over time demonstrate a moderate increase in stiffness and are therefore more resistant to permanent deformation. This relationship was most pronounced in **F1** where the percentage composition of PEG lower, allowing for better network reorientation over time.

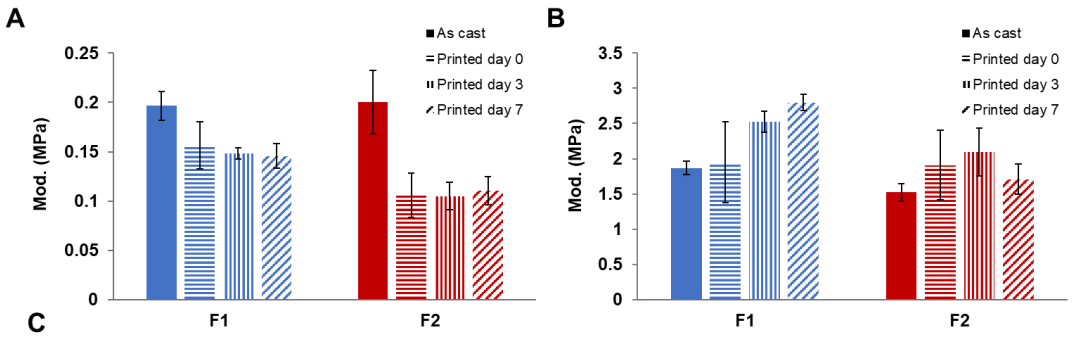


C

| | F1 | | | | F2 | | | |
|---|---|---|---|---|---|---|---|---|
| | Cast | Day 0 | Day 3 | Day 7 | Cast | Day 0 | Day 3 | Day 7 |
| Young's Modulus (MPa) | 1.87 ± 0.10 | 1.95 ± 0.57 | 2.52 ± 0.15 | 2.80 ± 0.11 | 1.52 ± 0.13 | 1.91 ± 0.50 | 2.09 ± 0.34 | 1.71 ± 0.22 |
| Ultimate Tensile Strength (MPa) | 0.20 ± 0.01 | 0.16 ± 0.02 | 0.15 ± 0.01 | 0.14 ± 0.01 | 0.20 ± 0.03 | 0.11 ± 0.02 | 0.10 ± 0.01 | 0.11 ± 0.01 |

***Figure 2.3.19:*** *Bar charts comparing the **A)** ultimate tensile strength and **B)** Young's modulus of printed formulations **F1** and **F2** over 7 days.*

Although a slight decrease in the resolution of the printed object may occur, the deformation may result in enhanced mechanical properties by virtue of improved interlayer adhesion and increased contact area between printed layers. Mechanical analysis of creep by rheology and tensile testing can be correlated with rheological analysis of the cast materials (**SPU1**, **F1** and **F2:** Figure 2.3.8) where the temperature at which G' and G" was observed to cross (phase angle = 45°) is close to ambient temperature in all instances, thus allowing the dynamic supramolecular polymer to disassemble and reassemble slowly over extended timeframes.

### 2.3.5 Drug Release from the Printed Prototype Implants

The initial rate of paracetamol release from the printed formulations was determined using HPLC analysis. To that aim, a typical standard calibration curve was produced using a paracetamol stock solution (160 ppm) in 5 mL methanol and diluting to volume with pH 6.8 dissolution media in a 250 mL volumetric flask (Figure 2.3.20). The standard solutions were subjected to HPLC analysis and the HPLC UV diode array detector signal related to paracetamol at 1.6 min was recorded.

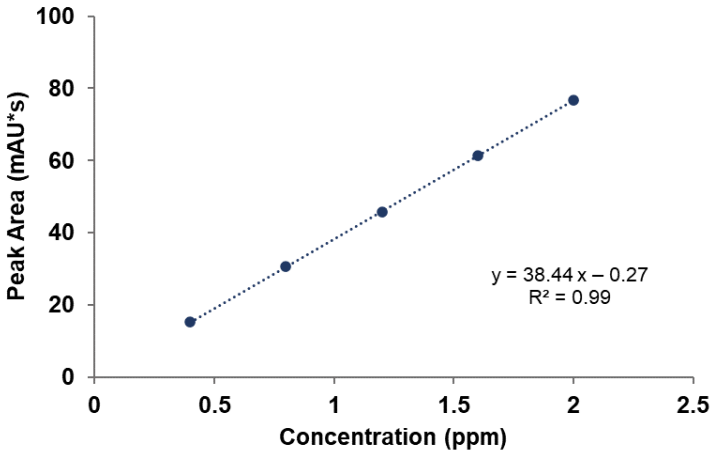


***Figure 2.3.20:*** *HPLC calibration curve for paracetamol in 0.05 M phosphate buffer (pH 6.8).*

Samples were then taken from the release media and was subjected to HPLC analysis to determine the amount of paracetamol released from each formulation within the specified time intervals. The printed implants were found to exhibit similar release rates, with up to 2.5% paracetamol and 2% paracetamol released over one week for formulations, **F1** and **F2**, respectively (Figure 2.3.21).

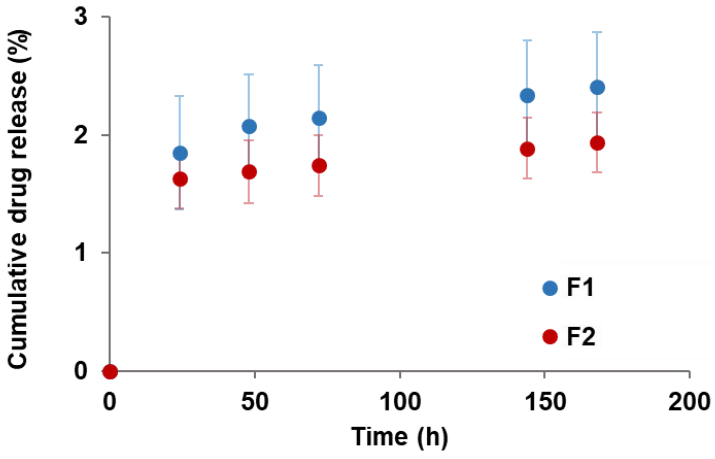


***Figure 2.3.21:*** *Release behaviour of paracetamol over 7 days from the printed formulations, **F1** and **F2**. Data shown are average of 5 repetitions.*

With such low levels of release of API, fitting models to such data to predict long-term release should be done with some caution. Therefore, the release profile data was fit to zero-order equation (eq 2.1), first-order equation (eq 2.2) and Korsmeyer-Peppas model (eq 2.3) to find the best fit.[65]

$$C_t = C_0 + k_0 t$$

**Equation 2.1:** Zero order equation of model drug release.

$$log\ C_0 - log\ C_t = \frac{k_1 t}{2.303}$$

**Equation 2.2:** First order equation of model drug release.

$$F = \left(\frac{M_t}{M}\right) = K_m . t^n$$

**Equation 2.3:** Korsmeyer-Peppas equation of model drug release.

$C_0$ is the initial concentration of API released, $k$ is a constant number, $M$ is the mass of API released and $K_m$ is kinetic constant. With this in mind, a first order release model was implemented to approximate the behaviour of the implants beyond 168 hours (Table 2.3.4).

***Table 2.3.4:*** *The predicted paracetamol release behaviour from the implants based on fitting the dissolution data to Zero order, First order and Korsmeyer-Peppas release models.*

| | F1 | | | | F2 | | | |
|---|---|---|---|---|---|---|---|---|
| **Model** | **Predicted time to 100% release (month)** | **$R^2$** | **Slope** | **y-intercept** | **Predicted time to 100% release (month)** | **$R^2$** | **Slope** | **y-intercept** |
| **Zero-Order** | 3.99 | 0.9285 | $3.46 \times 10^{-3}$ | 1.84 | 6.54 | 0.9975 | $2.11 \times 10^{-3}$ | 1.58 |
| **First-Order** | **8.48** | 0.9062 | $7.02 \times 10^{-4}$ | $2.68 \times 10^{-1}$ | **4.91** | 0.999 | $1.18 \times 10^{-3}$ | $4.64 \times 10^{-1}$ |
| **Korsmeyer-Peppas** | $1.33 \times 10^{12}$ | 0.9901 | $1.31 \times 10^{-1}$ | $8.82 \times 10^{-2}$ | $2.88 \times 10^{18}$ | 0.9604 | $9.00 \times 10^{-2}$ | $1.87 \times 10^{-1}$ |

**F1** and **F2** are predicted to fully release the active over 8.5 months and 5 months, respectively. This is, at the very least, indicative that suitable timescales for applications of these materials as implants will be achievable and that composition variations, such as PEG amount as here, can be used to tune release rate. Interestingly, **F1** with lower percentage of PEG exhibited higher release rate of paracetamol compared to **F2**. This could be attributed to the phase separation of the material which also observed in the SAXS experiment (Figure 2.3.14) and the inhomogeneity of the formulation. In order for the material to be suitable for implant applications, it should robustly retain its designed shape. It should be noted that deformation of the implants (Figure 2.3.22) was observed after dissolution testing – this

preliminary result implies that further optimisation of the material may be needed. This deformation could be resulted from the difference in the dissolution rate of PEG and **SPU1**. The quick diffusion of PEG into the aqueous media results in deformation of the printed implant and to left voids behind. The process of diffusion of PEG is especially facilitated considering the temperature of the dissolution media (37 °C) and its closeness to the moduli cross-over temperature (Figure 2.3.8) Essentially, the deformation and the void formation are more substantial in **F2** in which there is more wt% of PEG present.

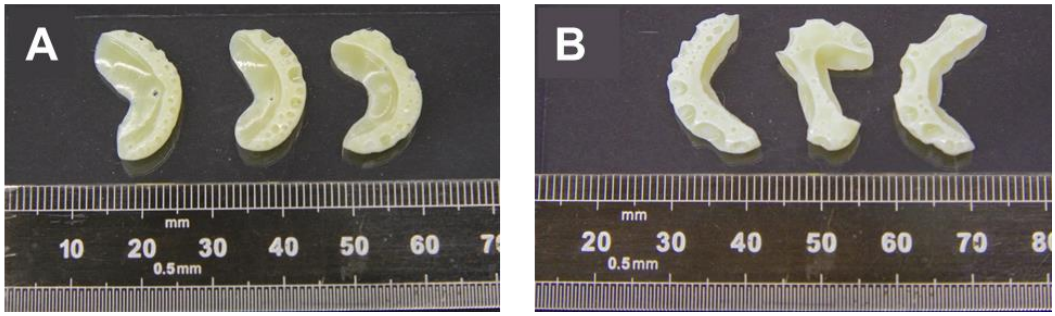


***Figure 2.3.22:*** *Images of the printed paracetamol bars,* ***F1*** *(A) and* ***F2*** *(B), after dissolution testing (7 days) at 37 °C.*

SEM was used to characterise the morphology of the printed formulations (**F1** and **F2**). Hot melt extrusion of both formulations gave rise to well dispersed paracetamol within the polyurethane matrix as demonstrated by the absence of agglomerates and crystallites. To examine the effects of drug release on morphology, analysis was also carried out after 7 days of dissolution studies. A stark contrast in the structure of the printed formulations was observed after treatment with the dissolution media (Figure 2.3.23), resulting in a micro-porous network which was attributed to the leaching of the PEG excipient. As expected, the pores were more prominent in the **F2** as a consequence of the increased loading of PEG in the formulation. Clearly, the size of these pores cannot be the only contributing factor to drug release as on the time-scales observed in our dissolution studies there is not a direct correlation with this microscopic observation and drug release. Many factors are likely to contribute to drug release, including pore connectivity, pore size distribution and exposed surface area and these remain a matter for future formulation optimisation studies. Whether these features would affect the integrity of the implant over longer timescales should also be considered and may also explain the deformation of the implants (Figure 2.3.22).

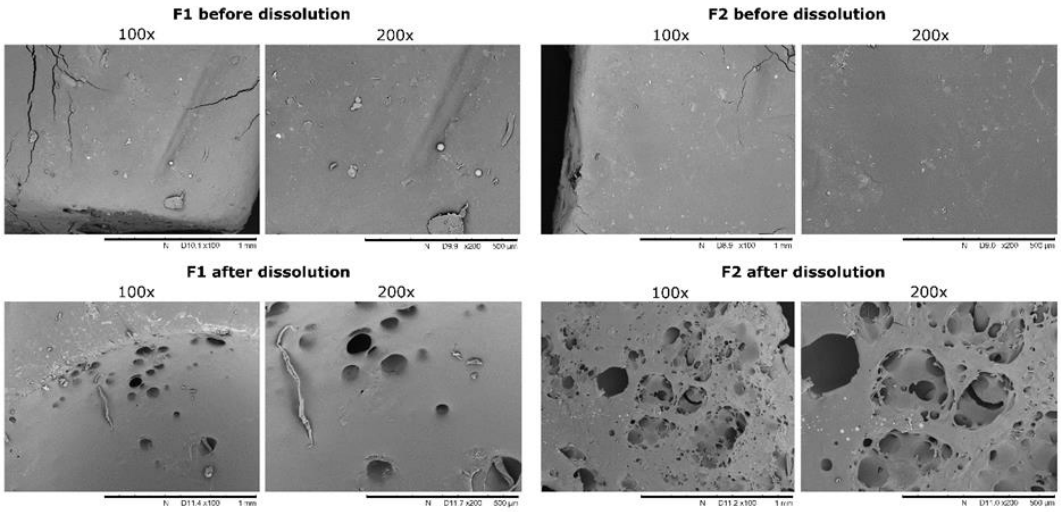


***Figure 2.3.23*** *SEM images of sample cross-section before and after the dissolution tests.*

## 2.4 Conclusions and Future Perspectives

Through molecular design, a thermo-responsive supramolecular polyurethane has been prepared that is able to dissemble and assemble over a specific transition temperature range and evaluated for its potential biocompatibility and cytotoxicity. The mechanical properties of the **SPU1** showed that the material is self-supporting and stiff, yet flexible. Additionally, the supramolecular nature of the material offers lower processing temperature compared to conventional high molecular weight polymers which enables the extrusion of the material and relatively lower temperatures. The material was therefore investigated as a candidate for 3D printed implant applications. In order to investigate the release characteristics, paracetamol (16 wt%) was dispersed into the **SPU1** formulated with 4 wt% or 8 wt% PEG excipients to investigate the ability to manipulate drug release profile. Bar implants were then designed, and the formulations successfully 3D printed using a hot-melt extrusion printer from melt at 100 °C. This lower printing temperature offers the possibility of incorporation and 3D deposition of a wider range of pharmaceuticals with lower thermal stability using hot-melt extrusion method.

The mechanical characteristics of the formulations were analysed which indicated that the material was a suitable matrix for hot-melt extrusion printing. The paracetamol in the printed implants was identified as the monoclinic stable (form 1) by PXRD and there were no adverse effects observed in printing the active in the formulations after extrusion. HPLC analysis was used to quantify the drug release from the prototype implants. From initial dissolution experiments, the release profiles were fitted to a first-order drug release model. This approximation indicates that 36 mg of paracetamol would be released within up to 8.5 months depending on PEG loading. However, further formulation optimisation is ideal to ensure the

homogeneity of PEG within the proposed excipient. This slow and potentially controllable release profile is consistent with timescales desired and needs for optimisation for drug eluting implants. However, it was noted that the implants deform over course of dissolution characterization. Finally, SEM was used to examine the morphology of the printed implants before and after drug release. The transition temperatures of the **SPU1** may need to be further considered and optimised for long term release applications. However, other reinforcement strategies that do not interrupt the biocompatibility or processability of the formulation could also be considered. In addition, by tuning the excipient formulation and utilising 3D printing technique, production of multi material customised implants can be realised which are capable of releasing multiple drugs at different rates.[66]

## 2.5 Experimental

### 2.5.1 Materials

All reagents were purchased from Sigma Aldrich or Alfa Aesar and used as received with the exception of Krasol HLBH-P2000 ($M_w$ as received = 2 kg $mol^{-1}$) [hydrogenated poly(butadiene)] which was supplied by TOTAL Cray Valley. Solvents were purchased from Fisher Scientific and used as received. Tetrahydrofuran (THF) was distilled from sodium and benzophenone prior to use, where anhydrous THF was needed. For cytotoxicity studies, polyurethane containing 0.1% (w/w) zinc diethyldithiocarbamate (PU-ZDEC) and polyethylene (PE) were obtained from Hatano Research Institute, Food and Drug Safety Center, Japan. Fetal bovine serum and streptomycin were purchased from Gibco™.

### 2.5.2 Instrumentation and Analysis

$^1$H NMR spectroscopy (400 MHz) and $^{13}$C NMR spectroscopy (400 MHz) were recorded with either a Bruker Nanobay 400, or Bruker DPX 400, using an appropriate deuterated solvent. Data was processed using MestReNova version 11.0.3-18688. Chemical shifts (δ) are reported in ppm with respect to TMS (δ 0.00 ppm) in $CDCl_3$ or the solvent residue (δ 2.50 ppm) in the case of DMSO-$d_6$ as solvents. Infrared spectra were collected using a Perkin Elmer Frontier FTIR-ATR spectrometer between 4000 $cm^{-1}$ and 550 $cm^{-1}$ with a scan resolution of 2 µm and a step size of 0.5 $cm^{-1}$. Variable temperature infrared spectra were recorded with Perkin-Elmer Spectrum 100 FTIR spectrometer equipped with Specac variable temperature cell holder and temperature controller. To carry out the experiment, KBr disks containing 1 wt% of each sample were prepared as follows: 3.00 mg of each analyte was dissolved in the minimum volume of THF and mixed with 300 mg KBr powder. The mixture was then dried completely under vacuum and ground to achieve a fine powder which was

then pressed to produce a translucent KBr disk. A KBr disk was also generated following the same preparative method without the addition of the sample in order to acquire the background spectra which was subtracted from the sample's IR spectra. The PXRD patterns of pure paracetamol, excipients (**SPU1**, and PEG) and the printed formulations (**F1** and **F2**) were obtained at room temperature using a Bruker D8 Advance with DaVinci XRD instrument, setup in divergent beam mode running in Bragg-Brentano geometry and a Lynxeye 1D detector. A generator voltage of 40 kV was set, with a current of 40 mA. Samples were scanned over 2 theta range of 10° to 40° in a step size of 0.02° and time per step of 1 second. Small angle X-ray scattering (SAXS) data were collected using a Bruker Nanostar instrument with an Incoatec microfocus X-ray copper source (1.54 Å wavelength) operating at 45 kV. Scattering patterns were collected using a Vantec area detector (2048 × 2048 pixels) using silver behenate (d-spacing of 58.3 Å) as a calibrant. The data obtained was analysed by DIFFRAC.SAXS software version 4.1.62. The imaging and calibration software used was Image J, version 1.4.3.67. Gel permeation chromatography (GPC) analysis was obtained by an Agilent Technologies 1260 Infinity systems in THF calibrated with polystyrene standards. Data was analysed using the Agilent GPC/SEC software. For each experiment, 2 mg/mL solution of polymer was prepared in BHT stabilised THF - taken from the mobile phase - and subjected to two Agilent PLgel 5 µm MIXED-D 300 × 7.5 mm columns connected in series at flow rate of 1.0 $mL.min^{-1}$. Differential Scanning Calorimetry (DSC) thermograms were obtained using a TA DSC Q2000 adapted with a TA Refrigerated Cooling System 90, using aluminium TA Tzero pans and lids. Thermal transitions were recorded using heating and cooling rates of 10 and 20 $°C.min^{-1}$, respecively for 3 cycles from 80 °C to 200 °C. For each of these analyses 5 - 8 mg of sample was used. TA Universal Analysis version 4.5A and Microsoft Excel 365 were used for data analysis of this thermal data.

Scanning Electron Microscope (SEM) images was carried out on a Hitachi SEM TM3030 Tabletop on a tilt stage. The microscope was equipped with a Bruker Scan generator, X Flash SDD detector, Bruker Nano MinSVE processor, Deben USB Chamberscope and Deben Sprite HR Stage controller joystick. Images of the printed prototype implants were collected by cooling the printed bars to -80 °C in freezer and were cross sectioned using a scalpel. The samples were then mounted on double-sided conductive carbon tape and sputter coated with gold with an Agar Sputter Coater.

Tensile tests were carried out using AML instruments™ single column tensile tester with vise grips equipped with rubber jaws. From each film 3 strips (5 mm × 40 mm × 1 mm) were cut, and individual samples were located between the grips of tensile instrument and elongated at

a rate of 10 mm.min$^{-1}$ and the stress *vs.* strain curve recorded. Data analysed using Microsoft Excel 365. The modulus of toughness was calculated by integrating the recorded plot to give the area under the curve. The trapezium rule was applied to calculate the area between zero strain to strain at break for each sample. The error reported is the standard deviation between the calculated areas of three repeats for each sample. Rheological experiments were carried out using a Malvern Panalytical Kinexus Lab+ fitted with a peltier plate cartridge and 8 mm parallel plate geometry. Data were analysed using rSpace for Kinexus version 1.75.2326 and Microsoft Excel 365. Cast samples were first heated to 60 °C applying 1 N of force to obtain good contact between the sample and geometry/plate. An amplitude sweep (between 0.1 - 16 % at 1 Hz) and frequency sweep (0.01 - 100 Hz) was then conducted to determine the linear viscoelastic regime as determined by the software. The sample was then heated from 0 °C to 170 °C whilst recording the storage (G') and loss moduli (G") in oscillatory mode. To carry out rheology experiments on printed samples, samples were loaded on the instrument at 25 °C and the amplitude and frequency sweep experiments were conducted at the same temperature.

### 2.5.3 Synthesis of 2.1

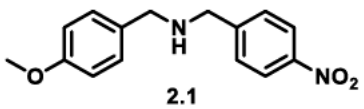


**2.1**

*N*-(4-Methoxybenzyl)-1-(4-nitrophenyl)methanamine **2.1** was synthesised in accordance to the previously reported procedure.[32] Briefly, to a stirred solution of 4-nitrobenzaldehyde (4.00 g, 26.45 mmol) in ethanol (50 mL) was added 4-methoxybenzylamine (4.38 g, 31.92 mmol) and resulting mixture stirred at 50 °C for 18 h. Ethanol was removed *in vacuo* before the crude solid was passed through silica plug using ethyl acetate as the eluant. The resultant imine intermediate was then dissolved in methanol (50 mL) and stirred with sodium borohydride (39.68 mmol, 1.5 eq., 1.50 g) for 4 h at room temperature. The solvent was subsequently removed *in vacuo* after which water was added and the product isolated by extraction with ethyl acetate (3 × 50 mL) to yield an orange oil (7.18 g, 84%). IR (ATR) ν (cm$^{-1}$): 3098, 3024, 3008, 2963, 2932, 2913, 2835, 1676, 1639, 1605, 1600, 1580, 1510, 1443, 1440, 1417, 1378, 1340, 1298, 1295, 1245, 1219, 1179, 1144, 1106; $^{1}$H NMR (400 MHz, $CDCl_3$) $\delta$ ppm: 8.18 (2H, appt.d, AA'XX' system, CCHC**H**CNO$_2$), 7.52 (2H, appt.d, AA'XX' system, CC**H**CHCNO$_2$), 7.24 (2H, appt.d, AA'XX' system, CCHC**H**COCH$_3$), 6.89 (2H, appt.d, AA'XX' system, CC**H**CHCOCH$_3$), 3.89 (2H, s, NHC**H$_2$**ArNO$_2$), 3.80 (3H, s, ArOC**H$_3$**), 3.75 (2H, s, NHC**H$_2$**ArOCH$_3$), 1.72 (s, br, N**H**), $^{13}$C NMR (100 MHz; $CDCl_3$) $\delta$

ppm: 158.8, 148.2, 147.0, 131.9, 129.3, 128.7, 123.6, 113.9, 55.3, 52.7, 52.2. ESI-MS: calcd for $M^+$ ($C_{15}H_{17}O_3N_2$): 273.1234 Da, m/z found: 273.1230 Da

### 2.5.4 Synthesis of SPU1[32]

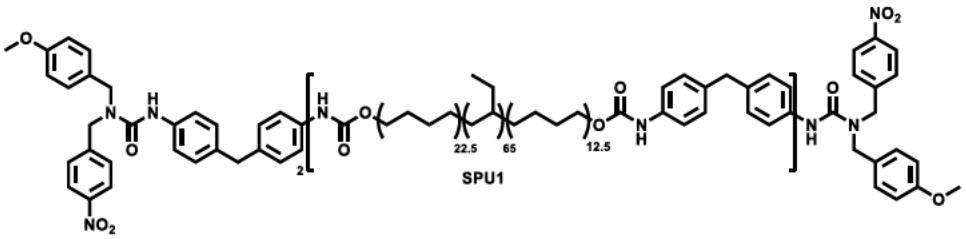


The polyol Krasol HLBH-P 2000 was dried in a vacuum oven at 120 °C under partial vacuum for 1 hour prior to use. Krasol HLBH-P 2000 **2.2** (20 g, 9.5 mmol) was mixed with 4,4′-methylenebis(phenyl isocyanate) **3** (5.02 g, 20.1 mmol) in the bulk for 3 h at 80 °C under $N_2$. The resulting mixture was then dissolved in anhydrous THF (150 mL) and cooled to room temperature. To the pre-polymer **2.4** was added *N*-(4-methoxybenzyl)-1-(4-nitrophenyl)methanamine **2.1** (5.57 g, 20.46 mmol) and the solution stirred for 2 hours at 50 °C. The solution was concentrated *in vacuo* and the product isolated with repeated precipitations from THF in methanol (3 × 1 L) to yield the product **SPU1** as a light orange coloured solid (22.6 g, 75%). IR (ATR) ν ($cm^{-1}$): 3331, 2957, 2921, 2851, 1708, 1646, 1596, 1512, 1462, 1412, 1342, 1304, 1241, 1174, 1108, 1031, 972, 813, 777, 735, 700 $^1$H NMR (400 MHz, $CDCl_3$) $\delta$ 8.20 (4H, appt.d, AA'XX', CCHC**H**CNO$_2$), 7.50 (4H, appt.d, AA'XX', CC**H**CHCNO$_2$), 7.17 (4H, appt.d, AA'XX', CCHC**H**COCH$_3$), 7.14–6.98 (16H, m, Ar), 6.89 (4H, appt.d, AA'XX', CCHC**H**COCH$_3$), 6.50 (2H, br, N**H**C(O)O), 6.32 (2H, N**H**C(O)N**H**), 4.75 (5H, s, NC**H$_2$**ArNO$_2$), 4.47 (5H, s, NC**H$_2$**ArOCH$_3$), 4.20 - 4.10 (4H, m, CH$_2$C**H$_2$**OC(O)NH), 3.86 (4H, m, ArC**H$_2$**Ar), 3.81 (6H, s, ArOC**H$_3$**), 2.03–0.65 (407H, m, ((C**H$_2$**)$_4$)$_n$. $^{13}$C NMR (400 MHz, $CDCl_3$) $\delta$ 159.6, 155.8, 147.4, 145.5, 136.4, 135.9, 129.4, 128.4, 128.1, 127.8, 124.0, 120.2, 114.7, 67.9, 55.4, 50.7, 40.5, 38.9, 38.4, 37.9, 36.1, 33.2, 30.7, 30.2, 29.8, 26.8, 25.9, 10.9; GPC (THF): $M_n$ = 6100 Da, $M_w$ = 12600 Da, $Đ$ = 2.06; DSC: $T_g$ = -47.8 °C, 19.45 °C.

### 2.5.5 Biocompatibility Studies

*In vitro* cell culture studies were performed using a mouse fibroblast cell line (L929, ECACC). Cells were cultured in Dulbecco's modified eagle's medium (high glucose) supplemented with 2 mM of L-glutamine, 10 % fetal bovine serum, penicillin (100 units $mL^{-1}$) and streptomycin (0.1 $mg.mL^{-1}$). Cells were maintained in a 5% $CO_2$ humidified atmosphere at 37 °C. Potential *in vitro* cytotoxicity effects of **SPU1** were evaluated as

follows. The polymeric films were incubated with tissue culture medium (3 $cm^2.mL^{-1}$, for 24 h) as previously reported.[33] Polyurethane containing 0.1% (w/w) zinc diethyldithiocarbamate (PU-ZDEC) and polyethylene (PE) were used as positive and negative controls, respectively. After incubation, the polymeric films were removed and their liquid extracts (the culture media containing any materials leached from the polymeric films during the incubation) were either applied or diluted, where required, using the tissue culture medium prior to their application onto the cells. Cells were seeded in a 96 well plate at $1 \times 10^4$ cells per mL in tissue culture medium and allowed to adhere for 24 hours. The medium was then replaced with 100 µL of either: (a) the tissue culture medium, (b) liquid extracts from **SPU1** at different dilutions (100, 75, 50, 25%) (c) liquid extracts of the positive control (PU-ZDEC) at (100%) or (d) liquid extracts of the negative control PE at (100%) (Figure 2.3.6), and cells incubated with the extracts for 48 hours. All diluted liquid extracts were sterile filtered prior to their application onto the cells. After 43 hours incubation, a 3-[4,5-dimethylthiazol-2-yl]-2,5-diphenyltetrazolium bromide (MTT) solution (5 mg $mL^{-1}$ in PBS) was added to the wells (20 µL per well) and cell viability assessed as previously reported.[33]

### 2.5.6 Formulations' 3D printing and Analysis

Drug containing formulations for 3D printing were prepared in accordance with Table 2.3.1. Briefly, **SPU1** and PEG (20 kg $mol^{-1}$) were dispersed in ethyl acetate (0.15 $mL.g^{-1}$) and the formulation heated to 100 °C until homogenous. Paracetamol (acetaminophen) was then added to the translucent and yellow formulations and stirred under continued heating until evenly dispersed to yield pale yellow and opaque materials with 4 wt% PEG (**F1**) and 8 wt% PEG (**F2**), respectively. The solvent was then removed *in vacuo* at 70 °C for 24 h until constant mass was obtained. The formulations for 3D printing were loaded into an aluminium extrusion printing cartridge fitted with a sterile precision conical nozzle (I&L Biosystems Ltd., Seer Green, UK) with an inner diameter of 0.609 mm (21G). A Cellink INKREDIBLE printer was used to print the formulations. The extrusion pressure and temperature were set as 3.0 bar (300 kPa), 100 °C and 3.1 bar (310 kPa), 105 °C for formulation **F1** and **F2** respectively, a printing layer height of 0.3 mm, printing speed of 10 mm $s^{-1}$ and a rectilinear infill of 100%. A bar geometry (30 mm × 3 mm × 2.5 mm) was designed using Blender computer graphics software. G-codes were then generated with Slic3r (version 1.3.0) with the optimised printing parameters stated above.

### 2.5.7 Release Studies

Dissolution testing of the printed implants was carried out using a Copely Scientific Dissolution Tester DIS 8000 with rotating USP I baskets according to USP specifications for

paracetamol. Briefly, 0.05 M potassium phosphate dissolution media was prepared with potassium dihydrogen phosphate in ultra-pure water (18.2 MΩ.cm) and adjusted to pH 6.8 with a 50 wt% sodium hydroxide solution. Testing was carried out at constant volume at 37 °C in 900 mL of media. Five millilitre sample aliquots were removed at predetermined times (24, 48, 72, 144, 168 h, respectively) and replaced with five millilitres of media at 37 °C and filtered with a (0.45 µm Millex PTFE hydrophilic filter). Samples were then analysed with an Agilent HPLC Series 1260 Infinity system, equipped with a UV diode array detector. A probe wavelength of 243 nm was used to quantify the absorbance of the paracetamol. The mobile phase compositions were 80% ultrapure water and 20% HPLC grade methanol. An ACE C18-AR analytical column (100 mm × 4.6 mm) with 5 µm particle size was used to separate the samples at 30 °C using flowrate of 0.5 $mL.min^{-1}$. A 5µL injection volume was implemented for the samples; sample runtimes were 5 minutes, and the paracetamol retention time was 1.62 min. Paracetamol stock solutions (160 ppm) were prepared by dissolving paracetamol (nominally 40 mg) in 5 mL methanol and diluting to volume with pH 6.8 dissolution media in a 250 mL volumetric flask. Standards were prepared with 160 ppm paracetamol stock solution and dissolution media. A typical standard calibration curve is shown in Figure 2.3.20.

## 2.6 References


1 A. S. Narang and S. H. S. Boddu, *Excipient Applications in Formulation Design and Drug Delivery*, Springer, Cham, 1st edn., 2015.

2 S. P. Chaudhari and P. S. Patil, *Int. J. Adv. Pharmacy, Biol*. Chem., 2012, **1**, 21–34.

3 S. Pundir, A. Badola and D. Sharma, *Int. J. Drug Res. Technol*., 2013, **3**, 12–20.

4 M. vallet-Regi, F. Balas and D. Arcos, *Angew. Chem. Int. Ed*., 2007, **46**, 7548–7558.

5 Y. Cui, B. Li, H. He, W. Zhou, B. Chen and G. Qian, *Acc. Chem. Res*., 2016, **49**, 483–493.

6 J. Della Rocca, D. Liu and W. Lin, *Acc. Chem. Res*., 2011, **44**, 957–968.

7 R. Duncan, *Nat. Rev. Drug Discov.*, 2003, **2**, 347–360.

8 M. A. C. Stuart, W. T. S. Huck, J. Genzer, M. Müller, C. Ober, M. Stamm, G. B. Sukhorukov, I. Szleifer, V. V. Tsukruk, M. Urban, F. Winnik, S. Zauscher, I. Luzinov and S. Minko, *Nat. Mater*., 2010, **9**, 101–113.

9 W. B. Liechty, D. R. Kryscio, B. V. Slaughter and N. A. Peppas, *Annu. Rev. Chem. Biomol. Eng*., 2010, **1**, 149–173.

10 K. Y. Lee and D. J. Mooney, *Chem. Rev.*, 2001, **101**, 1869–1879.

11 P. Gupta, K. Vermani and S. Garg, *Drug Discov. Today*, 2002, **7**, 569–579.

12 O. S. Fenton, K. N. Olafson, P. S. Pillai, M. J. Mitchell and R. Langer, *Adv. Mater*., 2018, **30**, 1705328.

13 O. Pillai and R. Panchangnula, *Curr. Opin. Chem. Biol*., 2001, **5**, 447–451.

14 K. E. Uhrich, S. M. Cannizzaro, R. S. Langer and K. M. Shakesheff, *Chem. Rev*., 1999, **99**, 3181–3198.

15 W. N. Sivak, J. Zhang, S. Petoud and E. J. Beckman, *Acta Biomater*., 2009, **5**, 2398–2408.

16 G. V. Salmoria, P. Klauss, K. M. Zepon and L. A. Kanis, *Int. J. Adv. Manuf. Technol*., 2013, **66**, 1113–1118.

17 J. Intra, J. M. Glasgow, H. Q. Mai and A. K. Salem, *J. Control. Release*, 2008, **127**, 280–287.

18 R. Chen, G. Li, A. Han, H. Wu and S. Guo, *J. Biomater. Sci. Polym. Ed*., 2016, **27**, 529–543.

19 D. Q. M. Craig, *Drug Dev. Ind. Pharm*., 1990, **16**, 2501–2526.

20 G. Fontana, M. Licciardi, S. Mansueto, D. Schillaci and G. Giammona, *Biomaterials*, 2001, **22**, 2857–2865.

21 A. L. Acton, C. Fante, B. Flatley, S. Burattini, I. W. Hamley, Z. Wang, F. Greco and W. Hayes, *Biomacromolecules*, 2013, **14**, 564–574.

22 W. J. Jia, Y. C. Gu, M. Gou, M. Dai, X. Li, B. Kan, J. L. Yang, Q. F. Song, Y. Q. Wei and Z. Y. Qian, *Drug Deliv*., 2008, **15**, 409–416.

23 T. Patrício, M. Domingos, A. Gloria, U. D'Amora, J. F. Coelho and P. J. Bártolo, *Rapid Prototyp. J.*, 2014, **20**, 145–156.

24 Y. Zhang and R. X. Zhuo, *Biomaterials*, 2005, **26**, 6736–6742.

25 G.-H. Son, B.-J. Lee and C.-W. Cho, *J. Pharm. Investig*., 2017, **47**, 287–296.

26 Y. Gu, X. Chen, J. H. Lee, D. A. Monteiro, H. Wang and W. Y. Lee, *Acta Biomater.*, 2012, **8**, 424–431.

27 J. Yu, Y. Xu, S. Li, G. V. Seifert and M. L. Becker, *Biomacromolecules*, 2017, **18**, 4171–4183.

28 H. Patil, R. V. Tiwari and M. A. Repka, *AAPS PharmSciTech*, 2016, **17**, 20–42.

29 D. R. Joshi and N. Adhikari, *J. Pharm. Res. Int*., 2019, **28**, 1–18.

30 A. Goyanes, F. Fina, A. Martorana, D. Sedough, S. Gaisford and A. W. Basit, *Int. J. Pharm.*, 2017, **527**, 21–30.

31 S. A. Khaled, M. R. Alexander, R. D. Wildman, M. J. Wallace, S. Sharpe, J. Yoo and C. J. Roberts, *Int. J. Pharm*., 2018, **538**, 223–230.

32 A. Feula, A. Pethybridge, I. Giannakopoulos, X. Tang, A. Chippindale, C. R. Siviour, C. P. Buckley, I. W. Hamley and W. Hayes, *Macromolecules*, 2015, **48**, 6132–6141.

33 A. Feula, X. Tang, I. Giannakopoulos, A. M. Chippindale, I. W. Hamley, F. Greco, C. Paul Buckley, C. R. Siviour and W. Hayes, *Chem. Sci*., 2016, **7**, 4291–4300.

34 D. H. Merino, A. Feula, K. Melia, A. T. Slark, I. Giannakopoulos, C. R. Siviour, C. P. Buckley, B. W. Greenland, D. Liu, Y. Gan, P. J. F. Harris, A. M. Chippindale, I. W. Hamley and W. Hayes, *Polym. (United Kingdom)*, 2016, **107**, 368–378.

35 S. Salimi, L. R. Hart, A. Feula, D. Hermida-Merino, A. B. R. Touré, E. A. Kabova, L. Ruiz-Cantu, D. J. Irvine, R. Wildman, K. Shankland and W. Hayes, *Eur. Polym. J*., 2019, **118**, 88–96.

36 R. J. Wojtecki, M. A. Meador and S. J. Rowan, *Nat. Mater.*, 2011, **10**, 14–27.

37 J. S. Maximilien, in *Handbook of Pharmaceutical Excipients*, eds. R. C. Rowe, P. J. Sheskey and M. E. Quinn, Pharmaceutical Press, 6th edn., 2009, pp. 522–524.

38 A. A. D'souza and R. Shegokar, *Expert Opin. Drug Deliv.*, 2016, **13**, 1257–1275.

39 P. Woodward, A. Clarke, B. W. Greenland, D. Hermida Merino, L. Yates, A. T. Slark, J. F. Miravet and W. Hayes, *Soft Matter*, 2009, **5**, 2000.

40 P. Woodward, D. H. Merino, B. W. Greenland, I. W. Hamley, Z. Light, A. T. Slark and W. Hayes, *Macromolecules*, 2010, **43**, 2512–2517.

41 D. Held and F. Gores, Tips & Tricks GPC/SEC: System Peaks or Ghost Peaks in GPC/SEC, http://www.chromatographyonline.com/tips-tricks-gpcsec-system-peaks-or-ghost-peaks-gpcsec, (accessed 29 March 2020).

42 R. P. Sijbesma, F. H. Beijer, L. Brunsveld, B. J. B. Folmer, J. H. K. K. Hirschberg, R. F. M. Lange, J. K. L. Lowe and E. W. Meijer, *Science*, 1997, **278**, 1601–1604.

43 P. Cordier, F. Tournilhac, C. Soulié-Ziakovic and L. Leibler, *Nature*, 2008, **451**, 977–980.

44 V. Simic, L. Bouteiller and M. Jalabert, *J. Am. Chem. Soc.*, 2003, **125**, 13148–13154.

45 S. Sivakova, D. A. Bohnsack, M. E. Mackay, P. Suwanmala and S. J. Rowan, *J. Am. Chem. Soc.*, 2005, *127*, 18202–18211.

46 K. Hackethal, F. Herbst and W. H. Binder, *J. Polym. Sci. Part A Polym. Chem.*, 2012, **50**, 4494–4506.

47 J. Yang, H. Chen, Y. Yuan, D. Sarkar and J. Zheng, *Front. Chem. Sci. Eng.*, 2014, **8**, 498–510.

48 B. S. G. Valdés, C. S. B. Gomes, P. T. Gomes, J. R. Ascenso, H. P. Diogo, L. M. Gonçalves, R. G. dos Santos, H. M. Ribeiro and J. C. Bordado, *Polymers (Basel).*, 2018, **10**, 1170.

49 L. R. Hart, S. Li, C. Sturgess, R. Wildman, J. R. Jones and W. Hayes, *ACS Appl. Mater. Interfaces*, 2016, **8**, 3115–3122.

50 RC Rowe, P Sheskey and M. Quinn, *Handbook of Pharmaceutical excipients*, Libros Digitales-Pharmaceutical Press, 2009.

51 S. A. Khaled, J. C. Burley, M. R. Alexander, J. Yang and C. J. Roberts, *Int. J. Pharm.*, 2015, **494**, 643–650.

52 S. A. Khaled, M. R. Alexander, R. D. Wildman, M. J. Wallace, S. Sharpe, J. Yoo and C. J. Roberts, *Int. J. Pharm.*, 2018, **538**, 223–230.

53 S. A. Khaled, M. R. Alexander, D. J. Irvine, R. D. Wildman, M. J. Wallace, S. Sharpe, J. Yoo and C. J. Roberts, *AAPS PharmSciTech*, 2018, **19**, 3403–3413.

54 F. Fina, A. Goyanes, C. M. Madla, A. Awad, S. J. Trenfield, J. M. Kuek, P. Patel, S. Gaisford and A. W. Basit, *Int. J. Pharm.*, 2018, **547**, 44–52.

55 D. H. Merino, A. T. Slark, H. M. Colquhoun, W. Hayes and I. W. Hamley, *Polym. Chem.*, 2010, **1**, 1263–1271.

56 D. J. Skrovanek, S. E. Howe, P. C. Painter and M. M. Coleman, *Macromolecules*, 1985, **18**, 1676–1683.

57 B. Nie, J. Stutzman and A. Xie, *Biophys. J.*, 2005, **88**, 2833–2847.

58 E. George, P. Liacouras, F. J. Rybicki and D. Mitsouras, *Radiographics*, 2017, **37**, 1424–1450.

59 *USP 40 - NF 35 The United States Pharmacopeia and National Formulary 2017*, United States Pharmacopeial Convention, 2016.

60 I. S. Khattab, A. Nada and A. A. Zaghloul, *Drug Dev. Ind. Pharm.*, 2010, **36**, 893–902.

61 M. K. Trivedi, S. Patil, H. Shettigar, K. Bairwa and S. Jana, *Chem. Sci. J.*, 2015, **6**, 100098.

62 M. Haisa, S. Kashino, R. Kawai and H. Maeda, *Acta Crystallogr. Sect. B Struct. Crystallogr. Cryst. Chem*, 1976, **32**, 1283–1285.

63 I. Yilgor and E. Yilgor, *Polym. Rev.*, 2007, **47**, 487–510.

64 S. Burattini, H. M. Colquhoun, B. W. Greenland and W. Hayes, *Faraday Discuss.*, 2009, **143**, 251–264.

65 A. Lisik and W. Musiał, *Materials (Basel).*, 2019, **12**, 730.

66 1 S. Salimi, Y. Wu, M. I. E. Barreiros, A. A. Natfji, S. Khaled, R. Wildman, L. R. Hart, F. Greco, E. A. Clark, C. J. Roberts and W. Hayes, *Polym. Chem.*, 2020, **11**, 3453–3464.

# Chapter 3

## Property Enhancement of Healable Supramolecular Polyurethanes

*This chapter has been published as a peered review research article: S. Salimi, L.R. Hart, A. Feula, D. Hermida-Merino, A. B. R. Touré, E. A. Kabova, L. Ruiz-Cantu, D. J. Irvine, R. Wildman, K. Shankland and W. Hayes, Property Enhancement of Healable Supramolecular Polyurethanes, Eur. Polym. J., 2019,* ***118****, 88–96.*

*Note regarding contributions to this study: S. Salimi, L.R. Hart and A. Feula performed design, synthesis and characterisation of the materials under the supervision of W. Hayes and E. A. Kabova gave support on performing powder X-ray diffraction under the supervision of K. Shankland at the University of Reading. D. Hermida-Merino carried out the SAXS and WAXS analysis at The European Synchrotron Radiation Facility (ESRF), Grenoble, France. A. B. R. Touré carried out the AFM analysis with the support from L. Ruiz-Cantu for interpretation of the AFM results under the supervision of D. J. Irvine and R. Wildman at the University of Nottingham.*

*Synthesis and characterisation of* ***SPU 3.1 (PropDiol****) and* ***RSPU (PropDiol)-15%*** *was carried out by Abdullah Alwahaibi under the supervision of S. Salimi and W. Hayes at the University of Reading.*

### 3.1 Abstract

Low molecular weight additives which can cooperatively self-assemble with supramolecular polyurethanes via complementary hydrogen bonding interactions offer an attractive route to enhancing the properties of addressable polymer networks which are capable of demonstrating substantial physical change by introducing modest energy into the system. Here, the design, synthesis, characterisation and mechanical properties of a series of supramolecular polyurethanes with varied loadings of a low molecular weight bis-urea additive is presented. These additives are able to self-assemble with analogous recognition motifs within the supramolecular polyurethanes to form polar 'hard' domains, promoting phase separation within the bulk material and, crucially, increasing the strength of the polymer network. In addition, the bis-urea additive is a by-product within the polymerisation and thus can be synthesised *in situ*, without the need for complex purification or blending. The mechanical properties of these reinforced polymers were enhanced when compared to the pristine supramolecular polyurethane alone, as a result of higher degrees of order within the polymer matrix. Furthermore, a formulation comprising the small molecule blended with the supramolecular polyurethane was produced to examine the effect of material preparation and filler dispersion within the polymer matrix. Interestingly, the mechanical performance of a

blended material was diminished as a result of modest dispersion and incorporation within the polymer matrix. These findings thus demonstrate a facile, one-pot, method that does not require purification to produce reinforced supramolecular polyurethanes. This methodology may find use in industrial applications in which enhancements to the physical and mechanical properties can be easily achieved through the *in situ* synthesis of low molecular weight additives within the polymerisation.

## 3.2 Introduction

Supramolecular polymers[1,2] are a class of stimuli responsive materials which are able to self-assemble into dynamic arrays as a result of highly directional and specific non-covalent interactions. These materials are comprised typically of low-molecular weight species which are able to form a *pseudo* high molecular weight polymer network with attractive physical properties.[3,4] The switchable nature of supramolecular polymers has been investigated for a wide range of potential applications including adhesives, surface-coatings and healable materials.[4-6] As a consequence of the highly addressable assembly motifs, supramolecular polymers offer a route to novel materials and properties which can be easily processed at relatively low temperatures [7] Narrow processing windows are afforded through dissociation and subsequent reassociation of recognition motifs when subjected to external stimulus such as heat, light or pressure.[8-10] However, supramolecular polymers currently only have limited industrial use, especially in real-world structural applications, as the mechanical properties require further refinement.

One approach to enhancing the mechanical properties of supramolecular polymers is utilising additives which provide reinforcement of the polymer matrix.[11-15] Supramolecular polymer composites are known to improve the mechanical properties of the bulk polymer matrix. In an attempt to optimize the interface between additives and the polymer matrix, Bose *et al.* reported a graphene oxide functionalized with PEEK to facilitate good dispersion within an epoxy matrix.[16] Fox *et al.* reinforced a relatively weak but thermally responsive polymer supramolecular polymer blend with rigid, biosourced cellulose nanocrystals to afford healable nanocomposite materials.[17] The tensile modulus of the material increased from 8 MPa to 261 MPa as the proportion of filler increased up to 10 wt% and films were found to heal upon exposure to elevated temperatures of 85 °C. This increase in the tensile modulus means the material can absorb more energy before deforming, plastically, therefore a more durable material is made. In addition, supramolecular polymers that assemble via hydrogen bonding units with high association constant motifs such as ureidopyrimidinone have been shown to enhance the fracture toughening of carbon fiber composites whilst retaining the healing capability,[18] form robust composites[19,20] with nanosilica and reinforce a styrene-butadiene

rubber.[21] In 2010, Shokrollahi *et al.* reported an approach in which both the polymer (functionalized polycaprolactone) and filler (hydroxyapatite) featured hydrogen bonding motifs to enhance the mechanical properties of the blend.[22] Additionally, specific molecular recognition between a healable supramolecular polymer blend material and functionalized gold nanoparticles featuring complementary surface groups has also been reported by Vaiyapuri *et al.*.[23] This healable composite highlighted the requirement for structural refinement of both the polymer and filler to realise a composite with efficient healing characteristics.

An alternative approach to creating reinforced materials is the addition of organic small molecules to the polymer matrix that structurally complement the receptor units within the phase separated bulk polymer.[24] Low molecular weight organic nucleating agents have previously been employed to great effect to induce phase separation and form hard domains within soft polymer matrices.[13,25,26] Furthermore, phase separation has been shown to increase the mechanical strength of the polymer network. In the light of the possible advantages of creating reinforced polymers from organic additives, in addition to previous studies in the Hayes research group on addressable and healing supramolecular polymers,[27-31] this Chapter reports the facile route to enhancing the mechanical properties by reinforcing supramolecular polyurethanes with low molecular weight additives. A known[32] elastomeric supramolecular polyurethane (SPU) was doped with a complementary low molecular weight additive (LMWA) that can reinforce the hard segment by cooperatively forming hydrogen bonds to form supramolecular arrays with the polymer's hard segment. This is analogous to other approach reported in the literature in which hard segment content is increased through the incorporation of covalently bonded chain-extenders to enhance phase separation in polyurethanes.[33-37] Crucially, purification was not required to form the self-assembled polymer networks as the additive was formed *in situ*. The effect of increasing the weight percentage of the LMWA, and thus the relative hard domain content was studied systematically, and the material properties assessed. The polymer with the most promising mechanical properties was then selected and an analogous composition formulated by blending the constituent components from isolated intermediates at the equivalent weight ratio. The mechanical properties of the reinforced polyurethanes prepared *in situ* or formulated were then compared to assess the importance of polymer preparation. Finally, the healability of the reinforced materials were probed to assess the effect of the LMWA on the healing efficiency of the polymer matrix.

The effect of various end groups on the properties of the final polyurethane have been studied previously within the Hayes research group to introduce different functionality to the polyurethane.[27,32,38] It was shown that by adjusting the molar ratio of the isocyanate and the

end group mechanical and *in situ* introduction of LMWA properties of the SPU can be improved considerably.[39] By taking the same approach a small library of the reinforced SPUs was produced. This library included five different SPUs, comprised of identical hydrogenated poly(butadiene) and isocyanate (4,4′-MDI) and a distinct end group, each of which offers unique mechanical properties. The printability and processability of these materials using hot-melt extrusion 3D printing technique for potential biomedical applications was then investigated. The advantage of these materials is their relatively low processing temperature. The materials soften upon dissociation of the low energy supramolecular interactions which assemble the hard segments, and the end-groups results in a decrease in viscosity of the material. Therefore, these materials can theoretically be extruded at relatively low temperature, and upon solidification present enhanced mechanical properties.

## 3.3 Results and Discussion

The effective self-assembly of polyurethanes is a key parameter which defines the physical and mechanical characteristics of the material.[32] Organic, low molecular weight additives (LMWA) which can cooperatively add to the supramolecular array (Figure 3.3.1) may provide a route to reinforcing the polymer network through highly directional and specific hydrogen bonding interactions, as well as further improving the phase separation.[40-42] In addition, the highly directional interaction between polyurethanes and the LMWA may improve the dispersion of the additives within the polymer matrix. A combination of these factors may result in an improvement to the mechanical properties of the parent polymers.

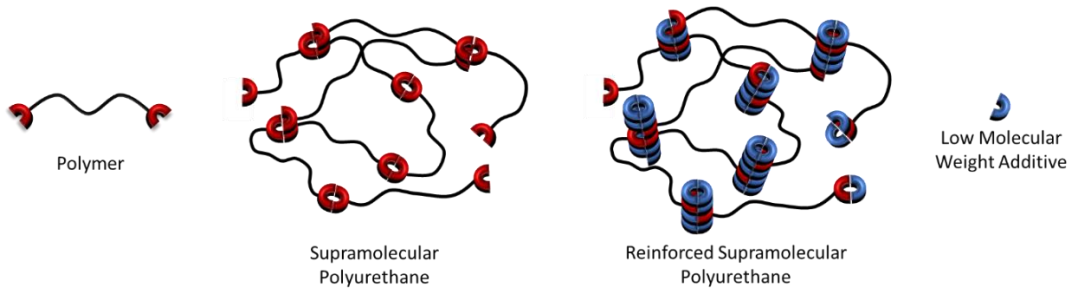


***Figure 3.3.1:*** *An illustration of the self-assembly of the supramolecular polyurethane and cooperative self-assembly of the SPU with low molecular weight additive to produce a reinforced supramolecular polyurethane.*

### 3.3.1 Synthesis and Characterisations of RSPUs

To achieve reinforced supramolecular polyurethanes (RSPUs), a facile one pot, two-step procedure was first employed to synthesise SPU **3.1** (**AmMorph**) from Krasol HLBH-P2000 **2.2**, 4,4'-Diphenylmethane diisocyanate **2.3** and 4-(2-aminoethyl)morpholine **3.3**.[32] Through careful synthetic design, the procedure was modified (Scheme 3.3.1) to prepare the LMWA

**3.2** (**AmMorph**) *in situ* as a by-product during the synthesis of SPU **3.1 (AmMorph)** and successfully yield a series of hydrogen bonding RSPUs.

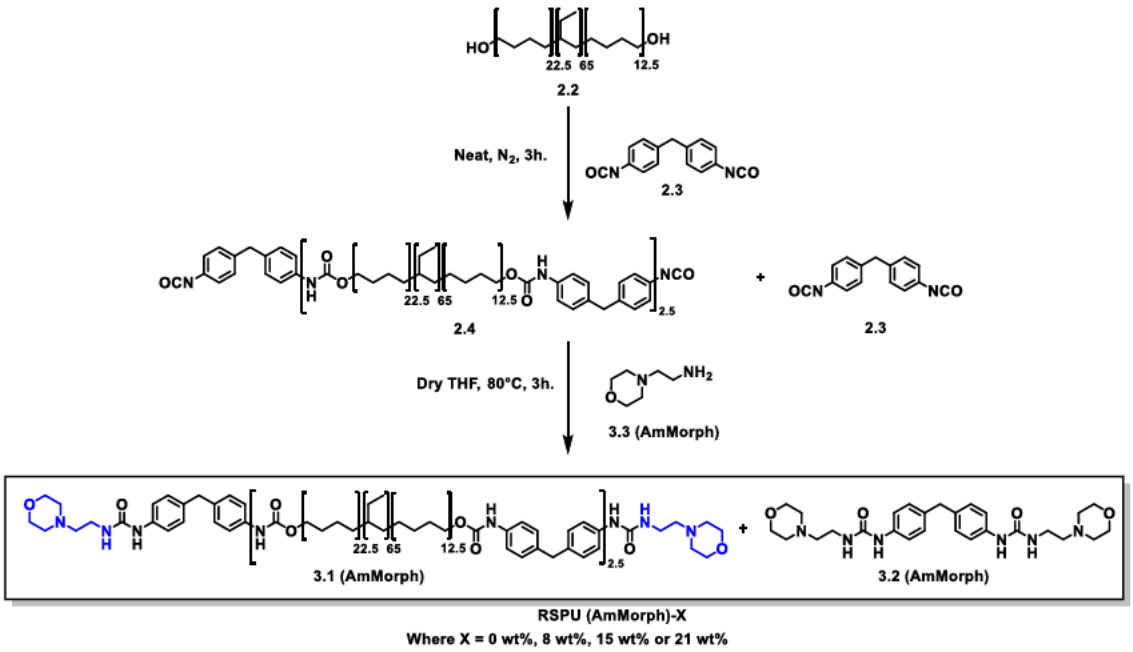


***Scheme 3.3.1**: Synthesis of the supramolecular polyurethane (SPU **3.1**) and the in-situ preparation of LMWA **3.2** to yield reinforced supramolecular polyurethanes (RSPUs).*

To synthesise the supramolecular polyurethanes, hydrogenated poly(butadiene) **2.2** (Krasol-HLBH-P2000) (molecular weight as received = 2000 g $mol^{-1}$) was first reacted with 4,4'-MDI **2.3** in the bulk to afford the pre-polymer **2.4**, which was subsequently end-capped with the hydrogen-bonding moiety (4-(2-aminoethyl)morpholine) **3.3 (AmMorph)**. As a control material, the SPU **3.1 (AmMorph)** was purified by repeated precipitations into methanol to remove any LMWA **3.2 (AmMorph)**. The LMWA **3.2 (AmMorph)** content (produced *in situ*) for the reinforced supramolecular polyurethanes **RSPUs** was controlled by modifying the feed ratios (Table 3.3.1) of the diisocyanate **2.3** and the hydrogen-bonding end-group **3.3 (AmMorph)** with respect to the polymer **2.2**. The **RSPU (AmMorph)-0%** was produced using the same reagent stoichiometry as **3.1 (AmMorph)** but without purification, with the assumption that the polymerisation would continue to completion and LMWA **3.2 (AmMorph)** would not be afforded. Additionally, the absence of a purification step for all reinforced polymers allowed for the LMWA **3.2 (AmMorph)** to be retained in the bulk. A final composite was formulated by selecting the material with the most promising physical and mechanical characteristics and blending the appropriate weight ratios of SPU **3.1 (AmMorph)** and **LMWA 3.2 (AmMorph)**, after isolation to yield the equivalent reinforced polymer blend **RSPU (AmMorph)-15% (Blend)**.

***Table 3.3.1:*** *The conditions and stoichiometry of starting materials used in the preparation of the SPU and RSPU samples, and the molecular weight data of the resulting polymers ($M_n$ of Krasol HLBH-P 2000 by GPC = 3400 g.mol$^{-1}$). The percentage values are calculated based on the stochiometric excess values of **2.3** and **3.3** compared to **2.2**.*

| (AmMorph) RSPU | Reagent Stoichiometry [(2.2) : (2.3) : (3.3)] | Preparation Method | Molecular Weight ($M_n$, g.mol$^{-1}$) | Polydispersity (Đ) |
|---|---|---|---|---|
| **SPU 3.1** | 1:2:2 | One-pot & purification | 9100 | 1.4 |
| **RSPU-0%** | 1:2:2 | One-pot | 8800 | 1.4 |
| **RSPU-8%** | 1:2.5:3 | One-pot | 7800 | 1.3 |
| **RSPU-15%** | 1:3:4 | One-pot | 7250 | 1.3 |
| **RSPU-21%** | 1:3.5:5 | One-pot | 7000 | 1.2 |
| **RSPU-15% (Blend)** | 1:3:4 | One-pot Blended | 8050 | 1.3 |

The successful synthesis of SPU **3.1** was first confirmed by $^1$H NMR spectroscopy which revealed a resonance at 4.16 ppm, characteristic of methylene residue adjacent to newly formed urethanes in the polymer core. Furthermore, the installation of the hydrogen bonding motif to the pre-polymer **2.4** was confirmed by a triplet at 3.33 ppm, assigned to the methylene adjacent to the newly formed urea. $^{13}$C NMR spectroscopy was also used to confirm the establishment of urea (156.2 ppm) and urethane (153.8 ppm) linkages, respectively, in the supramolecular polymer. As an additional conformation of the formation of urethane/urea linkages in the supramolecular polyurethane **3.1 (AmMorph)**, infra-red spectroscopy revealed the complete consumption of isocyanates functionalities as observed by the disappearance of the vibration at 2270 cm$^{-1}$. Furthermore, new absorbances at 1642 cm$^{-1}$ and 1706 cm$^{-1}$ were attributed to the carbonyl stretches in the newly formed urethane/urea bonds, respectively.[35,43-45] Finally, GPC analysis was employed to confirm the extent of chain extension in the polyurethane, with an average of 2 hydrogenated poly(butadiene) residues per supramolecular polymer ($M_n$ = 9100 g.mol$^{-1}$). This data is in close agreement with integration analysis of the $^1$H NMR spectroscopic data. The low molecular weight additive **3.2** was prepared by mixing 4,4'-MDI **2.3** with the hydrogen bonding end-group **3.3** in anhydrous THF and maintaining under reflux for 3 hours before isolating via filtration and subsequent washing with THF.

The presence of additional LMWA **3.2 (AmMorph)**, formed *in situ* in all of these RSPUs, was established by $^1$H NMR spectroscopy (Figure 3.3.2 A).[46] Figure 3.3.2 shows the partial

$^{1}$H NMR spectra of the materials containing varied concentration of LMWA **3.2**. The colour of protons in the chemical structure corresponds to the related resonance marked with a circle of the same colour on top. An increase in additive **3.2** concentration was confirmed by comparing the integration of resonances from the polymer core (4.14 ppm, light blue) relative to those from the methylene bridge of 4,4′-MDI residues at 3.89 ppm (orange) - the ratio between polymer and small molecule could thus be determined. To further confirm this relationship, the integrals of the resonances arising from the polymer core can be compared to those from the α-protons to the urea (3.33 ppm, red) of the hydrogen bonding end-group. Both analyses demonstrate an increase in the concentration of LMWA **3.2 (AmMorph)** in the reinforced supramolecular polyurethanes as the feed ratio was increased.

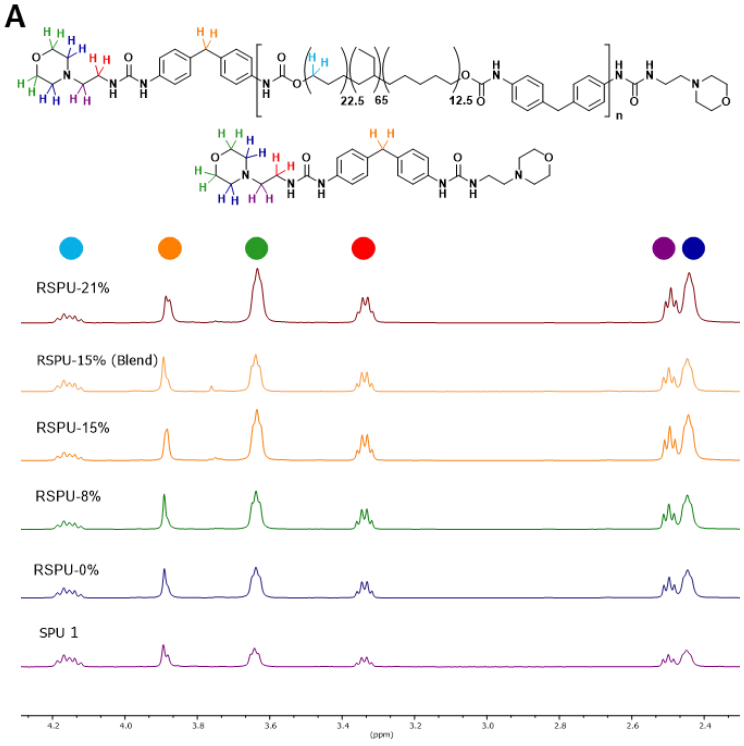

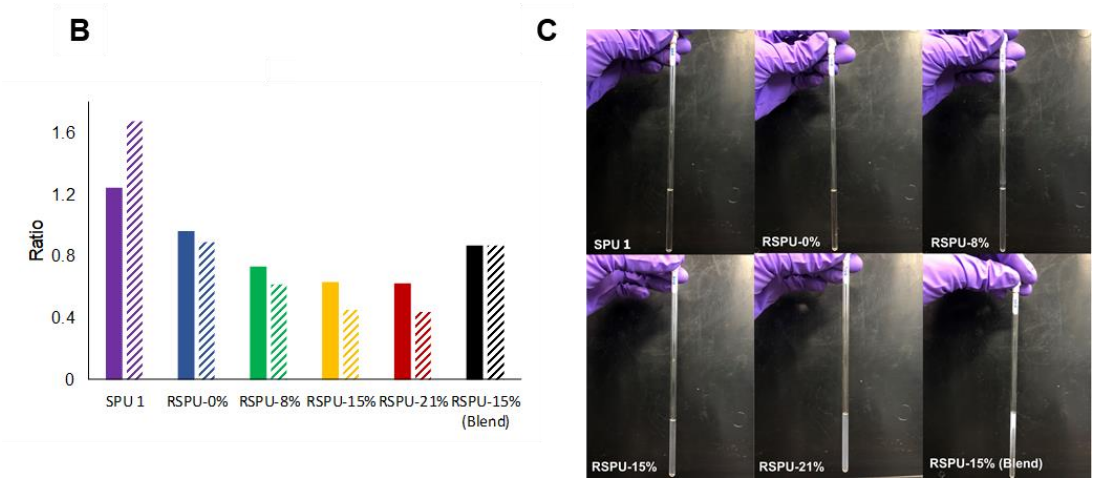


***Figure 3.3.2:*** *A) stacked partial $^{1}$H NMR spectra of* ***SPU 3.1*** *and RSPUs. B) Bar chart illustrating ratios of polyurethane and LMWA* ***3.2*** *component based on integration of the $^{1}$H NMR spectroscopic data. Hashed-bars represent the ratio of the integrals of resonances at 4.17 ppm (poly(butadiene)) and those at 3.33 ppm (solid bars), which correlate to end-capping motifs. C) Pictures of the NMR tubes showing the increase in LMWA* ***3.2*** *aggregate.*

In order to illustrate the increase in the concentration of the LMWA **3.2** in the reinforced polyurethanes, the ratios of the integrals of key resonances from $^{1}$H NMR spectroscopy were analysed (Figure 3.3.2 B). The solid bars show the ratio between the integrals of the resonances at 4.17 ppm corresponding to the protons from poly(butadiene) backbone adjacent to the urethane and the resonance at 3.89 ppm corresponding to methylene bridge of the 4,4'-MDI moiety. In addition, hashed-bars represent the ratio of the integrals of resonances at 4.17 ppm (poly(butadiene)) and those at 3.33 ppm, which correlate to end-capping motifs. These data (Figure 3.3.2 B) show a downward trend in the ratio between these resonances and thus demonstrates an increase in 4,4′-MDI and end-capping moiety containing molecules. In **RSPU (AmMorph)-15%** and **RSPU (AmMorph)-21%** this trend is no longer apparent. This could be attributed to the sparing solubility (Figure 3.3.2 C) of LMWA **3.2** in deuterated chloroform. In the case of **RSPU (AmMorph)-15% (blend)** this insolubility is more apparent, suggesting that the LMWA **3.2** may aggregate and therefore the concentration in solution is lower.

In addition, GPC analysis (Figure 3.3.3) of the reinforced supramolecular polyurethanes revealed an increase in the elution profile of the LMWA **3.2** ($M_n$ = ~ 400 g.mol$^{-1}$) component as the stoichiometry of the diisocyanate **2.3** and hydrogen bonding end-group **3.3 (AmMorph)** was increased with respect to hydrogenated poly(butadiene) **2.2** ($M_{n(GPC)}$ = 3400 g.mol$^{-1}$). The **RSPU (AmMorph)-0%** was shown to contain approximately 4.5% LMWA **3.2 (AmMorph)** by $^{1}$H NMR spectroscopy and GPC analysis**.** Further analysis of the bimodal signal in the chromatogram attributed to the reinforced polymers revealed a decrease in molecular weight ($M_n$) with increased filler concentration (SPU **(AmMorph) 3.1** = 9100

g.mol$^{-1}$, **RSPU (AmMorph)-21%** = 7000 g.mol$^{-1}$). In addition, a decrease in polydispersity index (SPU **(AmMorph) 3.1** Đ = 1.4, **RSPU (AmMorph)-21%** Đ = 1.2) was also observed, indicating the extent of chain extension decreases with increased concentration of LMWA **(AmMorph) 3.2**. The reduction in molecular weight was rationalised by considering the stoichiometry of the diisocyanate **2.3**, which increases with respect to polymer **2.2**, thus reducing the probability for chain-extension.

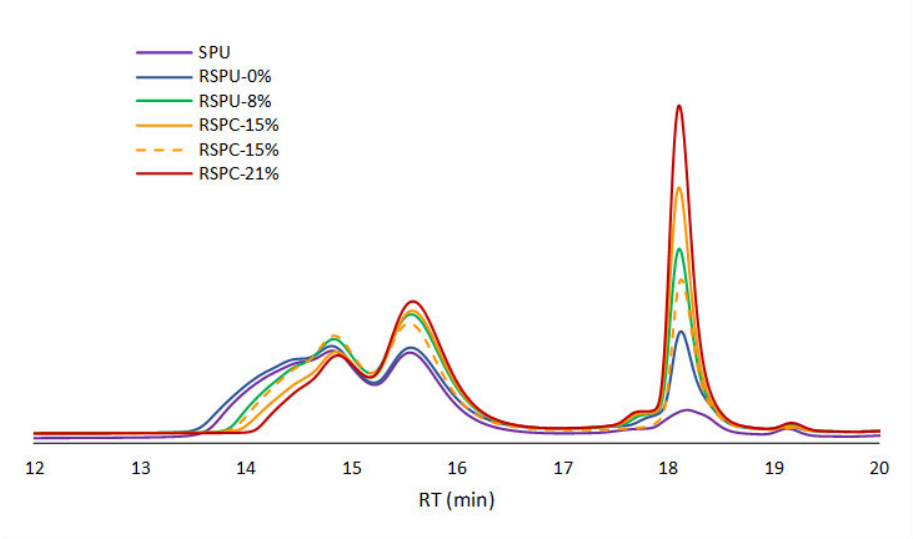


***Figure 3.3.3:*** *GPC eluograms of SPU* ***(AmMorph) 3.1*** *and RSPUs showing the changes in the content of LMWA.*

The thermal properties of the supramolecular polyurethanes were also probed to assess the effect of the LMWA **3.2** on the supramolecular polymer array. The addition of LMWA **3.2** showed no effect on the glass transition temperature ($T_g$) of the soft phase of the RSPUs (Figure 3.3.4) when compared to that of SPU **(AmMorph) 3.1**, which remained constant at -47 °C. This is also correct about the second $T_g$ of *ca.* 20 °C corresponding to the hard segment of phase separated polyurethanes. In contrast, the melting point ($T_m$) was observed to increase in temperature and intensity in the RSPUs, from 140 °C in **RSPU (AmMorph)-0%** to 171 °C in **RSPU (AmMorph)-21%** as a consequence of the LMWA **3.2 (AmMorph)** reinforcing the polyurethane network and increasing the concentration of the supramolecular interactions. Interestingly, **RSPU (AmMorph)-15% (Blend)** exhibited a melting point at 191 °C, which is approximately equivalent to that of LMWA **3.2 (AmMorph)** alone, revealing the additive is not able to fully penetrate the hydrogen bonding network of the polyurethane and it is solely exhibiting the melting point of the aggregated LMWA **3.2**.

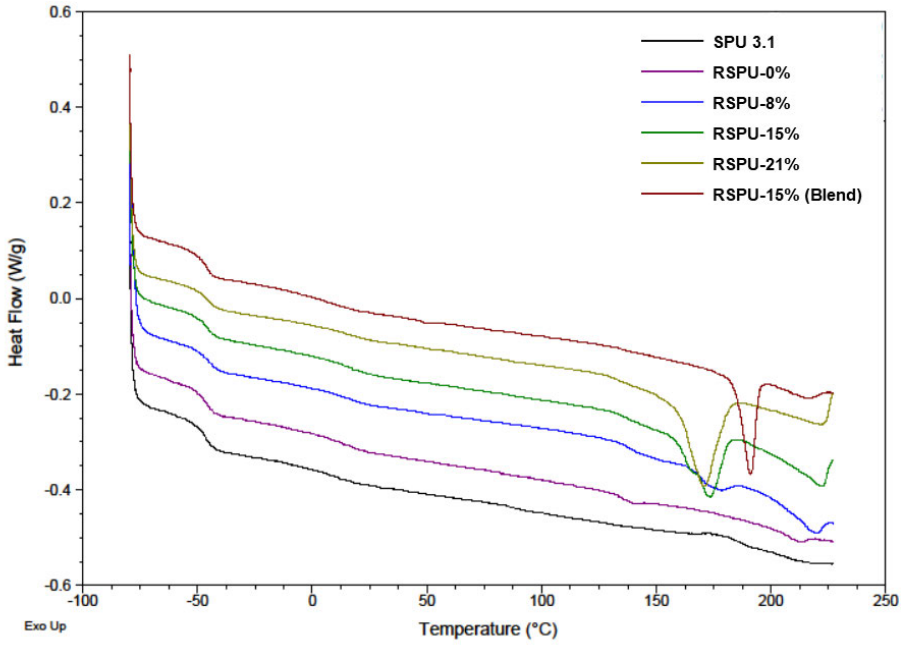


***Figure 3.3.4:*** *DSC thermograms of the synthesised RSPUs and the* ***SPU (AmMorph) 3.1*** *showing changes in the melting point as a result of the change in the concentration of LMWA* ***3.2****.*

To assess the ability of the additive **3.2 (AmMorph)** to strengthen the polymer network and affect its mechanical properties, tensile testing was selected as the most appropriate method to evaluate the phase separated polymers. To facilitate this, drop-cast films were produced of the supramolecular polymer **3.1 (AmMorph)** and its reinforced analogues RSPUs. The polymer solutions were dried under vacuum at 70 °C to afford malleable and elastomeric films.

### 3.3.2 Mechanical Properties of the Synthesised RSPU (AmMorph) 3.1

The generated polymer films were cut into strips (dimensions = 40 mm × 5 mm × 1 mm) and elongated to break to assess their tensile properties. The test revealed that the presence of the additive **3.2 (AmMorph)** (formed *in situ*) in the reinforced polymer improves the mechanical properties of the materials when compared to the purified supramolecular polymer (Figure 3.3.5). Indeed, a clear trend was observed between the weight percentage of LMWA and properties such as the modulus of toughness and ultimate tensile strength (Table 3.3.2). The polymer **RSPU (AmMorph)-21%** gave rise to the largest improvement in stiffness. A 3400 % increase in the Young's modulus was observed (135.2 MPa), whilst the ultimate tensile strength increased by approximately 800 % (2.5 MPa). However, a decrease in elasticity (strain at break = 3 %) and modulus of toughness (0.1 MPa) was evident as a result of the increased additive weight percentage, resulting in an extremely brittle material, possibly as a result of aggregation of the LMWA within the polymer matrix. Although the polymer **RSPU (AmMorph)-15%** gave rise to more modest mechanical properties (Young's

modulus = 43.2 MPa, Ultimate tensile strength = 1.4 MPa, modulus of toughness = 0.49 MPa), the material was easy to handle and thus offered the best balance between mechanical properties and processability.

Additionally, to identify if the method of formulation and preparation had a significant effect on the mechanical properties of the reinforced polyurethanes, a polymer blend was prepared by mixing the isolated SPU **3.1 (AmMorph)** with the LMWA **3.2 (AmMorph)** in solution before casting a polymer film. **RSPU (AmMorph)-15%** was selected as a candidate for this study as a result of the optimum mechanical properties and physical characteristics (Figure 3.3.5 hashed line). In brief, to formulate the polymer blend, polyurethane **3.1** and bis-urea additive **3.2** were synthesised and isolated before mixing the two components (15 wt% of LMWA **3.2 (AmMorph)**) in THF under reflux to afford **RSPU (AmMorph)-15% (Blend)**. The resulting solution was then drop-cast, and the resulting film was also analysed. Surprisingly, a discernible difference was noted for the mechanical properties of **RSPU (AmMorph)-15%** and **RSPU (AmMorph)-15% (Blend)** (Figure 3.3.5). The reinforced polymer formulated by blending revealed a decrease in Young's modulus (18% reduction), ultimate tensile strength (34 % weaker) whilst a small decrease in toughness (12 % less robust) was also observed which is essentially invariant when considering the error within the three repeat analyses. Interestingly, an increase in elongation to break was noted for the blended RSPU. This could be rationalised by agglomeration of the bis-urea additive **3.2 (AmMorph)** which results in a less homogeneous film and thus the polymers properties are dictated by those of SPU **3.1 (AmMorph)**, gives rise to an increase in elongation when compared to **RSPU (AmMorph)-15%** and reduction in overall mechanical properties. Essentially, the bis-urea additive **3.2** interrupts the supramolecular network instead of reinforcing it as a result of aggregates formed within the network.

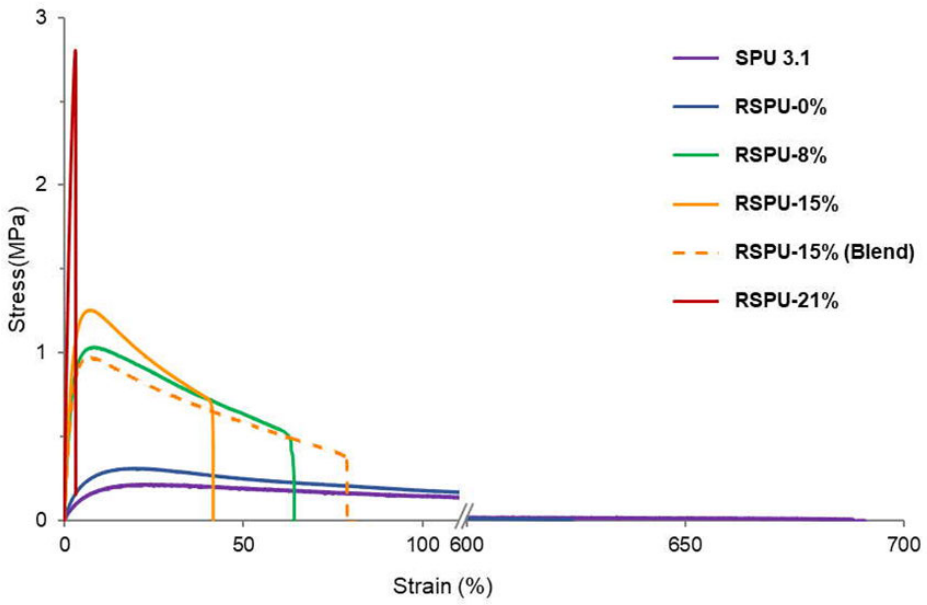


***Figure 3.3.5:*** *Stress-strain curves of the supramolecular polyurethane* ***3.1 (AmMorph)*** *and reinforced supramolecular polyurethanes RSPUs with increasing weight loading of the low molecular weight additive* ***3.2****.*

***Table 3.3.2:*** *Mechanical properties of the SPU* ***3.1 (AmMorph)*** *and* ***RSPUs (AmMorph)*** *extracted from tensile tests (values shown are the average of 3 repeats).*

| Polyurethane | Young's Modulus (MPa) | Ultimate Tensile Strength (MPa) | Toughness (MPa) | Strain at Break (%) |
|---|---|---|---|---|
| **SPU 3.1** | 3.9 ± 1.4 | 0.3 ± 0.1 | 0.6 ± 0.1 | 617 ± 73.0 |
| **RSPU-0%** | 4.4 ± 1.4 | 0.3 ± 0.0 | 0.6 ± 0.0 | 608 ± 16.0 |
| **RSPU-8%** | 36.8 ± 4.2 | 1.0 ± 0.1 | 0.4 ± 0.1 | 66 ± 12.0 |
| **RSPU-15%** | 43.2 ± 4.4 | 1.4 ± 0.1 | 0.5 ± 0.1 | 46 ± 8.0 |
| **RSPU-21%** | 35.4 ± 1.7 | 0.9 ± 0.0 | 0.4 ± 0.1 | 80 ± 10.0 |
| **RSPU-15% (Blend)** | 135.2 ± 18.1 | 2.5 ± 0.3 | 0.1 ± 0.0 | 3 ± 1.0 |

To further assess the mechanical characteristics of the reinforced polyurethanes, rheological analysis (Figure 3.3.6) was undertaken to explore the viscoelastic nature of the polymers and determine the effect of the LWMA on the thermally addressable materials. Temperature sweeps (Appendix Figure A1) were performed in oscillatory shear, revealing that the rubbery properties of the materials dominate in the low temperature regime (0 - 40 °C). In this range, the characteristic of the supramolecular polymer is predominant, resulting in an elastomeric but stiff material, and is not affected by the incorporation of the bis-urea additive **3.2 (AmMorph)**. Increasing the temperature further resulted in a decrease in the storage and loss modulus in all materials. The rate of change accelerating between 40 °C and 80 °C owing

to the dissociation of the supramolecular interactions and the material properties are defined by the viscoelastic properties of the polymers at elevated temperatures. Increasing the weight percentage of **3.2** in the composite retards this effect and thus the material remains stiffer at elevated temperatures. The storage modulus, G′, decreased by no more than an order of magnitude in polyurethanes reinforced with more than 8 wt% LMWA **3.2 (AmMorph)**, whereas a decrease of 3 orders of magnitude was observed in the pure supramolecular polymer and **RSPU (AmMorph)-0%**. In agreement with tensile testing, **RSPU (AmMorph)-21%** does not behave elastically under load and thus does not exhibit a significant loss in storage modulus over the temperature range.[182] These results correlate well with visual inspection of the materials when heated, in which **RSPU (AmMorph)-8%** and **RSPU (AmMorph)-15%** appear to soften slightly but retain their physical integrity at elevated temperatures, whereas **RSPU (AmMorph)-21%** remained stiff and brittle in nature over the same temperature regime and therefore was not able to be examined under comparable analytical conditions on the rheometer. This phenomenon can be attributed to the reduction in soft polymer content in the phase separated material, decreasing the flexible component of the polyurethane. Furthermore, the notable increase in storage modulus of the **RSPUs (AmMorph)** is a clear indicator of increased hydrogen bonding interactions in the polymer network.

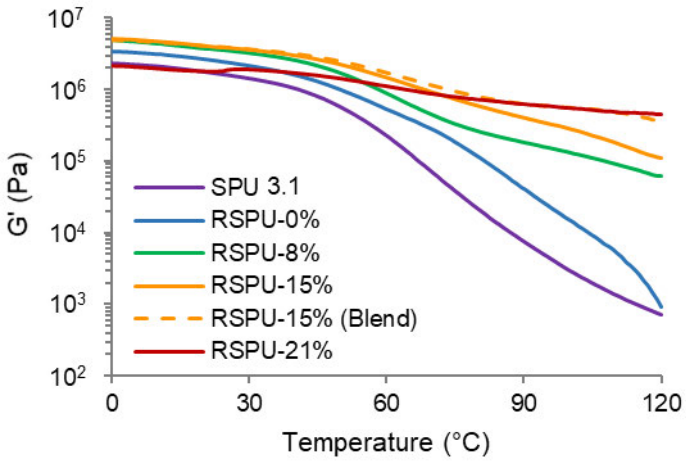


***Figure 3.3.6:*** *Changes in storage modulus (G') of the SPU* ***3.1 (AmMorph)*** *and* ***RSPUs (AmMorph)*** *between 0 and 120 °C.*

### 3.3.3 Morphology of the Synthesised RSPUs (AmMorph) 3.1

In order to further understand the morphology of the reinforced polymers, small angle X-ray scattering (SAXS) (Figure 3.3.7 A) and wide-angle X-ray scattering (WAXS) (Figure 3.3.7 B) analysis was employed. The WAXS scattering pattern revealed an amorphous halo with spacings centred on 4.9 Å suggesting the presence of stacked urea moieties within the

supramolecular array. Crystalline features are seen to emerge, as evidenced by distinct signals which grow in intensity with respect to increased weight percentages of the LMWA **3.2 (AmMorph)**. The SAXS scattering patterns for the supramolecular polyurethane **3.1 (AmMorph)** and reinforced polymers RSPUs formed *in situ* all showed a domain spacing of 66.1 Å, suggesting a microphase-separated morphology arising from the immiscibility of the hard hydrogen bonding end-groups with the soft polymer backbone. Crucially, the composite formulated by blending **RSPU (AmMorph)-15% (Blend)** revealed a domain spacing of 56.0 Å, indicating that a different assembly mode was present. This provides further evidence of aggregation between the LMWA **3.2 (AmMorph)** and a less homogeneous polymer network, indicating composite formulation is paramount.

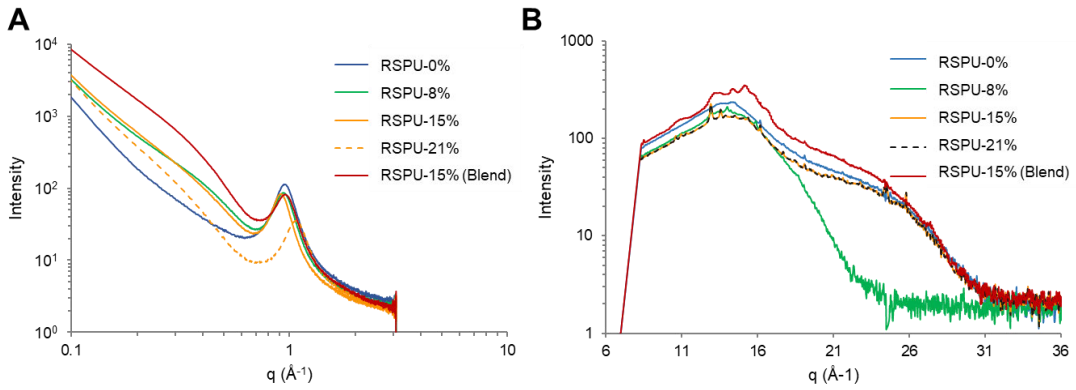


***Figure 3.3.7:*** *A) SAXS and B) WAXS diffraction pattern of* ***RSPUs (AmMorph)*** *at room temperature.*

To probe the thermal responsive nature of the supramolecular networks, variable temperature SAXS analysis was also undertaken (Figure 3.3.8). Upon heating from -60 °C to approximately 30 °C, no significant change was observed in the morphology of the polymer composites. Increasing the temperature further resulted in a decrease in the domain spacing at 66.1 Å **RSPU (AmMorph)-15%** and 56.0 Å **RSPU** (**AmMorph**)**-15%** (**Blend**), respectively, caused by efficient phase mixing between the hard and soft domains. This is in good agreement with rheological data, which demonstrated a decrease in storage modulus at equivalent temperatures. On cooling the materials, microphase-separation was restored in the polymer network by reassociation of hydrogen bonding motifs. Similar trends were observed for all polyurethanes (Figure 3.3.8), demonstrating that the addition of the bis-urea additive **3.2 (AmMorph)** does not disrupt the thermal reversibility of the supramolecular polymers. However, among all of the synthesised materials, the change in the intensity was minimal in the case of **RSPU (AmMorph)-21%** which is suggestive of the least response to thermal changes.

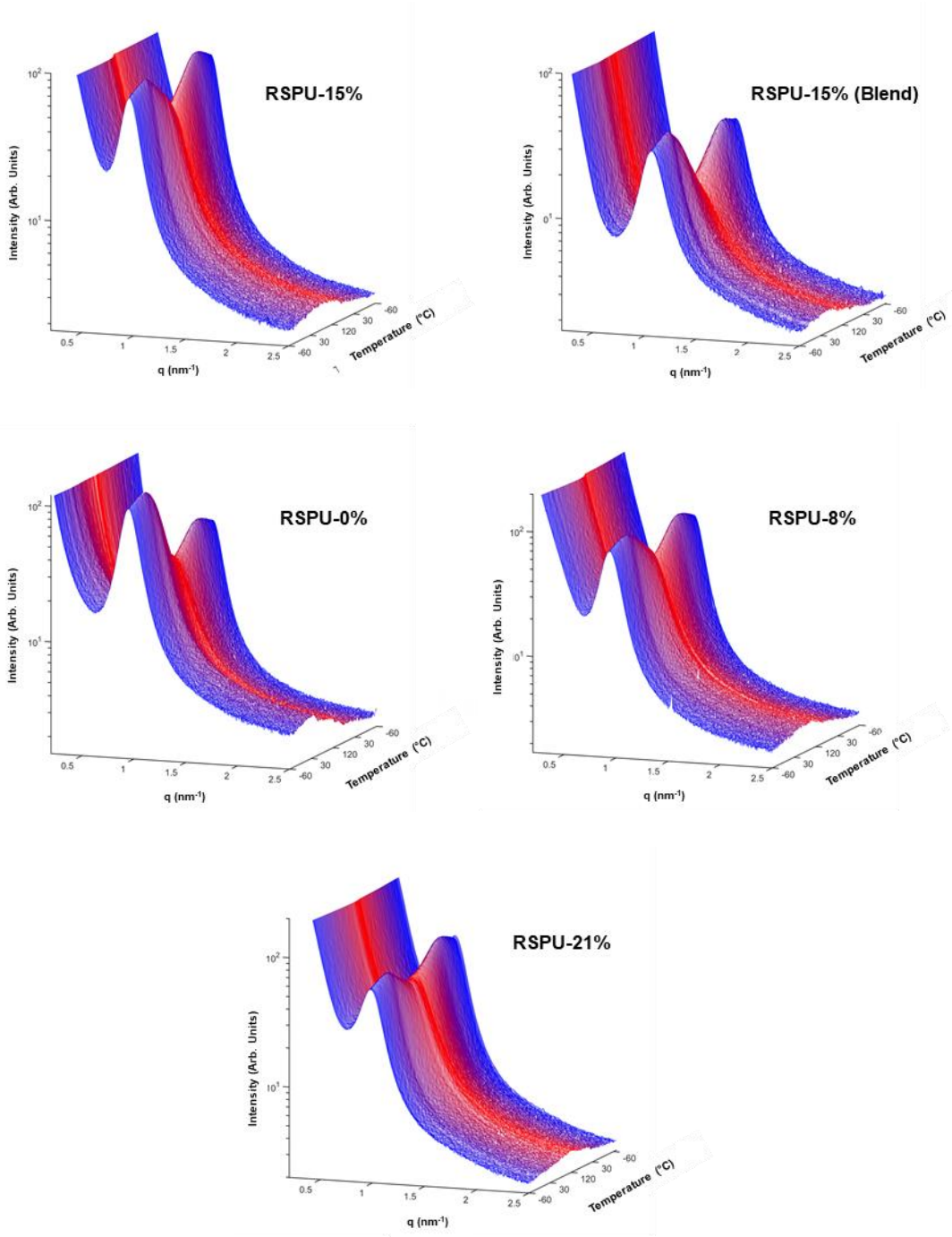


***Figure 3.3.8:*** *Variable temperature SAXS analysis of* ***RSPUs (AmMorph)*** *confirming the thermally reversible nature of the materials.*

Furthermore, variable temperature FT-IR spectroscopic analysis was conducted on the SPU **3.1 (AmMorph)** and **RSPUs (AmMorph)** and revealed a thermo-responsive behaviour similar to structurally related polyurethanes.[35,44,48,49] Figure 3.3.9 shows the changes in the integration of the NH stretching band by increasing the temperature in RSPUs. A strong absorbance for hydrogen bonded N-H absorbances was observed, centred at approximately 3320 $cm^{-1}$, arising from urethane and urea moieties. The intensity of the absorbance band

(calculated by integration between 3400 - 3100 $cm^{-1}$) was seen to diminish with increased temperature (20 °C - 120 °C) for all polyurethanes as a result of dissociation of the hydrogen bonding interaction within the polymer network.

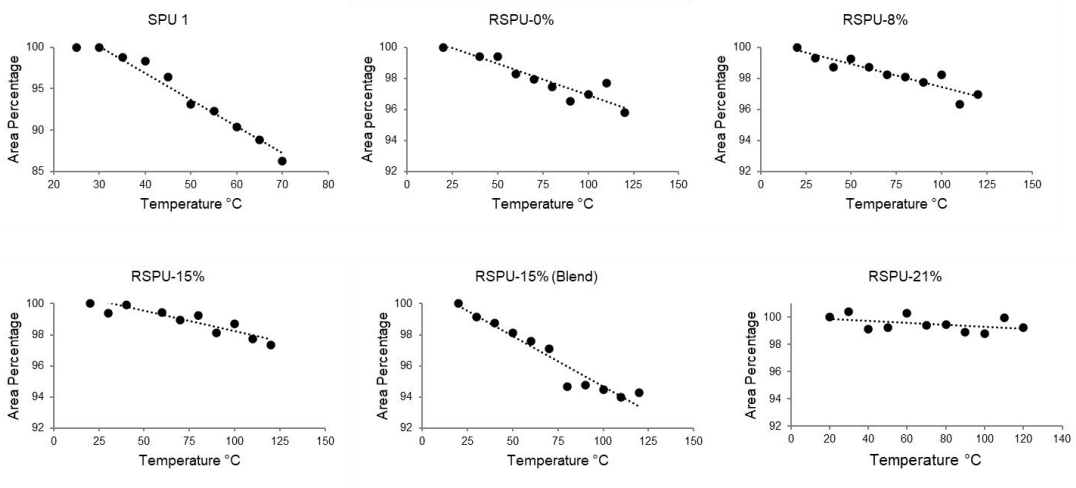


***Figure 3.3.9:*** *Graphs showing the change in integration of NH stretching band at ca. 3320 $cm^{-1}$ by heating **RSPUs (AmMorph)** over a range of temperatures (25 °C – 125 °C for the RSPUs).*

Powder X-ray diffraction data provided further insight to the role of the LMWA **3.2 (AmMorph)** in the reinforced polymers. The diffraction pattern of LMWA **3.2 (AmMorph)** was compared (Figure 3.3.10) to the polymer prepared *in situ* **RSPU (AmMorph)-15%** and the formulation prepared by blending **RSPU (AmMorph)-15% (Blend)**. It was apparent that the powder patterns for **3.2** and both **RSPU (AmMorph)-15%** and **RSPU (AmMorph)-15% (Blend)** shared many common diffraction peaks, suggesting that the additive was able to agglomerate into crystallites, however, the noticeable differences in reflection intensities attributable to LMWA **3.2 (AmMorph)** in both polymer samples suggest a marked difference in the distribution of crystallites in the two samples. Unfortunately, owing to the broad nature of the powder patterns of the polyurethanes, the crystalline phases were not able to be indexed.

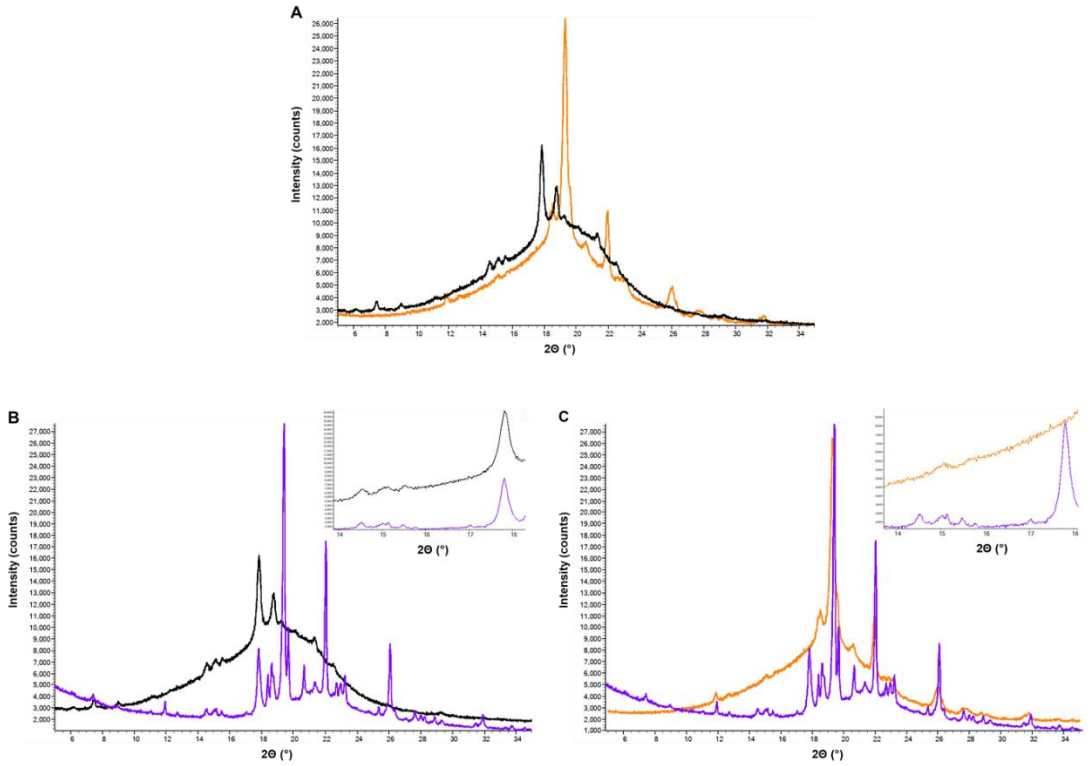


***Figure 3.3.10:*** *Powder X-ray diffraction patterns in the range 5-35 °2θ (λ=1.54056 Å) for A)* ***RSPU (AmMorph)-15%*** *(orange) and* ***RSPU (AmMorph)-15% (Blend)*** *(black) B)* ***RSPU (AmMorph)-15% (Blend)*** *and LWMA* ***3.2*** *(purple) and C)* ***RSPU (AmMorph)-15%*** *and LMWA* ***3.2****. Insets show change in bulk phase of LMWA* ***3.2 (AmMorph)*** *in each RSPU****.***

In addition, DSC analysis (Figure 3.3.11) was performed to further study the crystallinity within the polymer network and the effect of LMWA incorporation on the thermal properties of the materials. The DSC thermograms obtained confirmed the presence of multiple polymorphs in the LMWA **3.2 (AmMorph)** (Figure 3.3.11 A) further complicating any attempts at indexing PXRD analysis. DSC thermograms of the polymeric materials were also collected and revealed that by increasing the content of LMWA a melting point appears. Indeed, the purified and the **RSPU (AmMorph)-0%** exhibit a totally amorphous morphology. However, upon introduction of LMWA a distinct melting point emerge representing formation of a crystalline structure within the network. Meanwhile, regarding **RSPU (AmMorph)-15% (Blend)** the melting point is higher and closer to the main melting point of the pure LMWA **3.2 (AmMorph)** sample, indicating inefficient mixing of the LMWA with the polymer network.

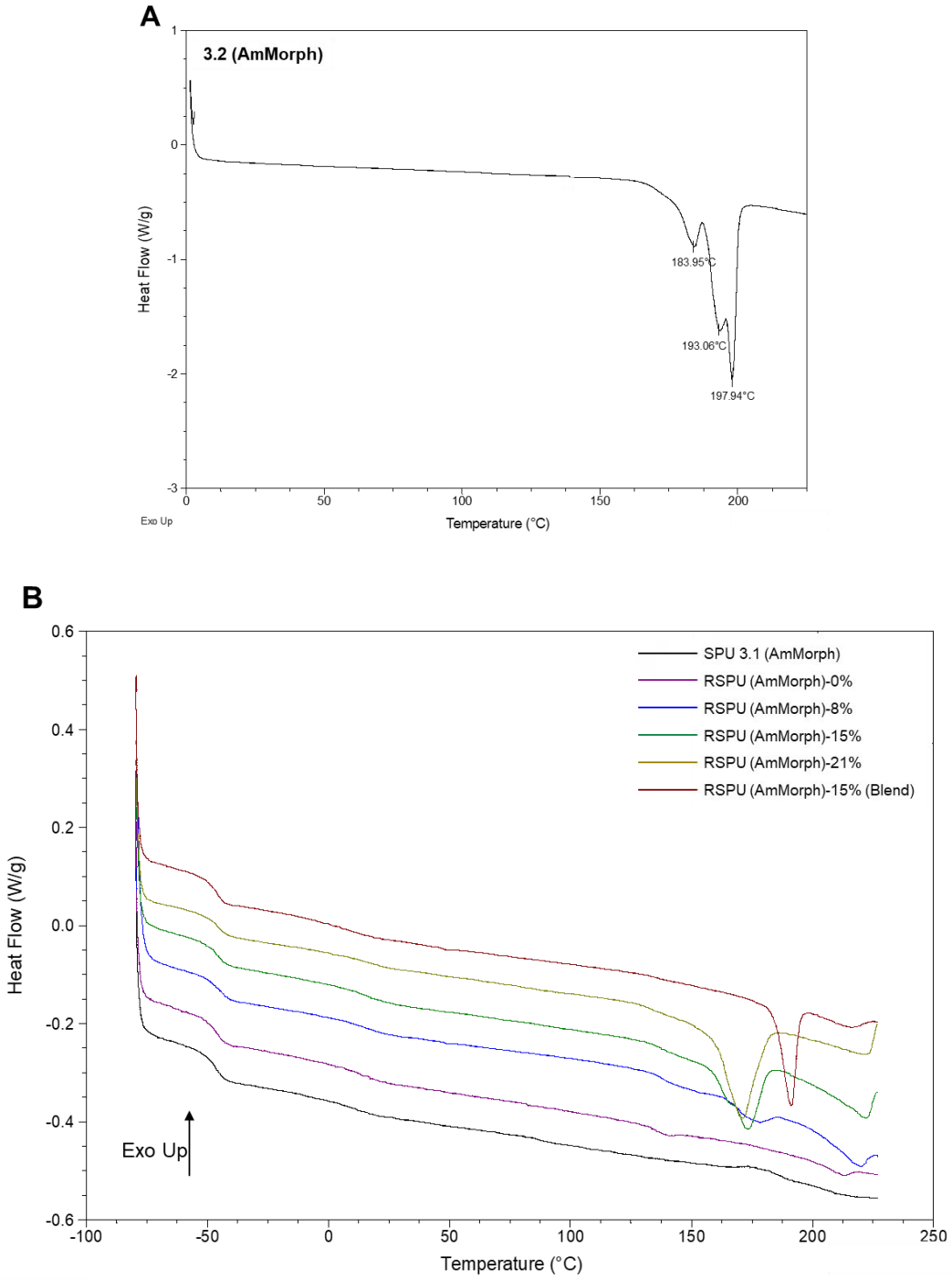


***Figure 3.3.11:*** *DSC thermograms of A) LMWA* ***3.2 (AmMorph)*** *revealing the presence of polymorphism in the sample and B) synthesised SPU* ***3.1 (AmMorph)*** *and corresponding RSPUs.*

To further analyse the self-assembly of the SPU **3.1 (AmMorph)** and RSPUs, AFM studies (Figure 3.3.12) were carried out to visualise the changes in the morphology attained by the addition of the LMWA **3.2 (AmMorph)** at increasing mole percentages and the effect of *in situ* preparation as opposed to blending. As expected, micro-phase separation was observed in SPU **3.1 (AmMorph) (**Figure 3.3.12) as a consequence of the assembly of hydrogen bonding

motifs and the ordered stacking of the MDI linkers which promote the packing of both urethane and urea moieties. Interestingly, phase separation became more apparent with increased loading of LMWA **3.2 (AmMorph)**, whilst remaining at the same length scale as supported by SAXS analysis (Figure 3.3.7 A). This increase in intensity also correlates well with both WAXS (Figure 3.3.7 B) and powder diffraction analysis (Figure 3.3.10), in which the diffraction signals increased in both d-spacing and magnitude with increased content of LMWA **3.2 (AmMorph)**. Furthermore, a correlation between the morphology observed in the AFM micrographs (Figure 3.3.12) and the $^{1}$H NMR spectral data was noted. A shoulder was observed in the proton resonance at *ca.* 3.90 ppm (Figure 3.3.2 A) attributed to the methylene bridge of the MDI residues in the LMWA **3.2 (AmMorph)**. Thus, it is proposed that there is an optimum additive concentration that leads to an improvement in polymer toughness and increased uniformity in the phase separation. For example, in the case where a multiplet is observed at 3.90 ppm (**RSPU (AmMorph)-8%**, and **RSPU (AmMorph)-15% (Blend)**), aggregation of the hard segments is apparent. However, when these two resonances are coincident (**RSPU (AmMorph)-15%**) an even phase separated morphology is observed. When comparing the **RSPUs (AmMorph)** prepared *in situ* or blended, it is apparent that a homogeneous and defined phase separated morphology is present in both samples, however, **RSPU (AmMorph)-15% (Blend)** revealed additional aggregation of hard domains, presenting a similar topography to **RSPU (AmMorph)-8%**, which can be attributed to poor mixing and intercalation of the LMWA **3.2 (AmMorph)** into the polymer network and hydrogen bonding array.

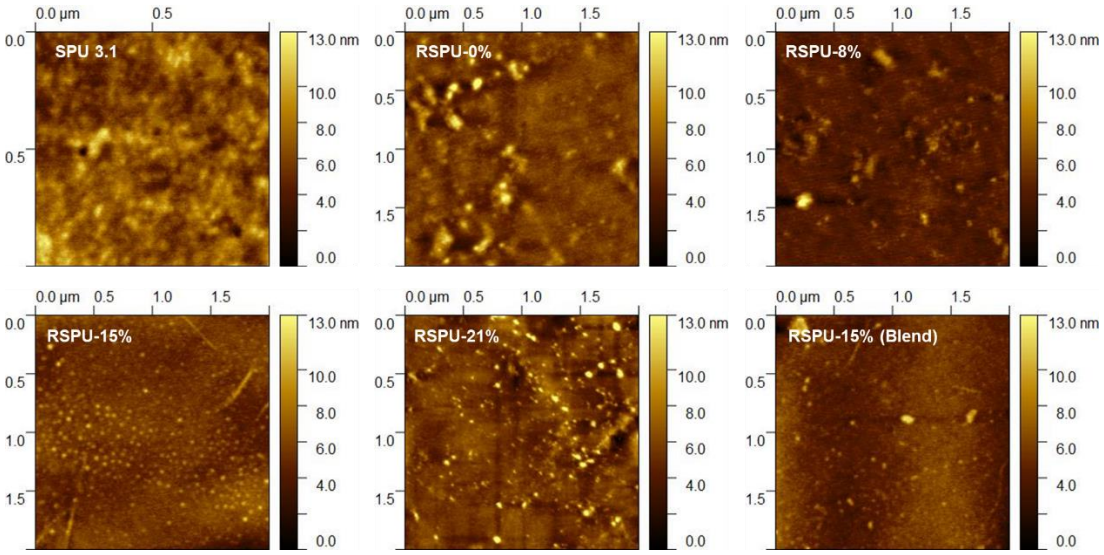


***Figure 3.3.12:*** *Atomic force microscopy images of the SPU **3.1 (AmMorph)** and RSPUs showing the micro phase separation between LMWA **3.2 (AmMorph)** and the polyurethane matrix.*

Furthermore, analysis of the average diameters and distribution size of the hard domains for both **RSPU (AmMorph)-15%** and **RSPU (AmMorph)-15% (Blend)** within the microphase

separated morphology demonstrated that the one-pot synthesis was able to better control the hard to soft domain ratio by reducing both the diameter (30.4 ± 0.4 nm, *vs.* 58.4 ± 1.4 nm) and distribution size (45 nm *vs.* 145 nm ) of the hard domain (Figure 3.3.13 and Figure 3.3.14). Therefore, the one-pot synthesis method ultimately provides a more homogenous and well-defined phase separated structure.

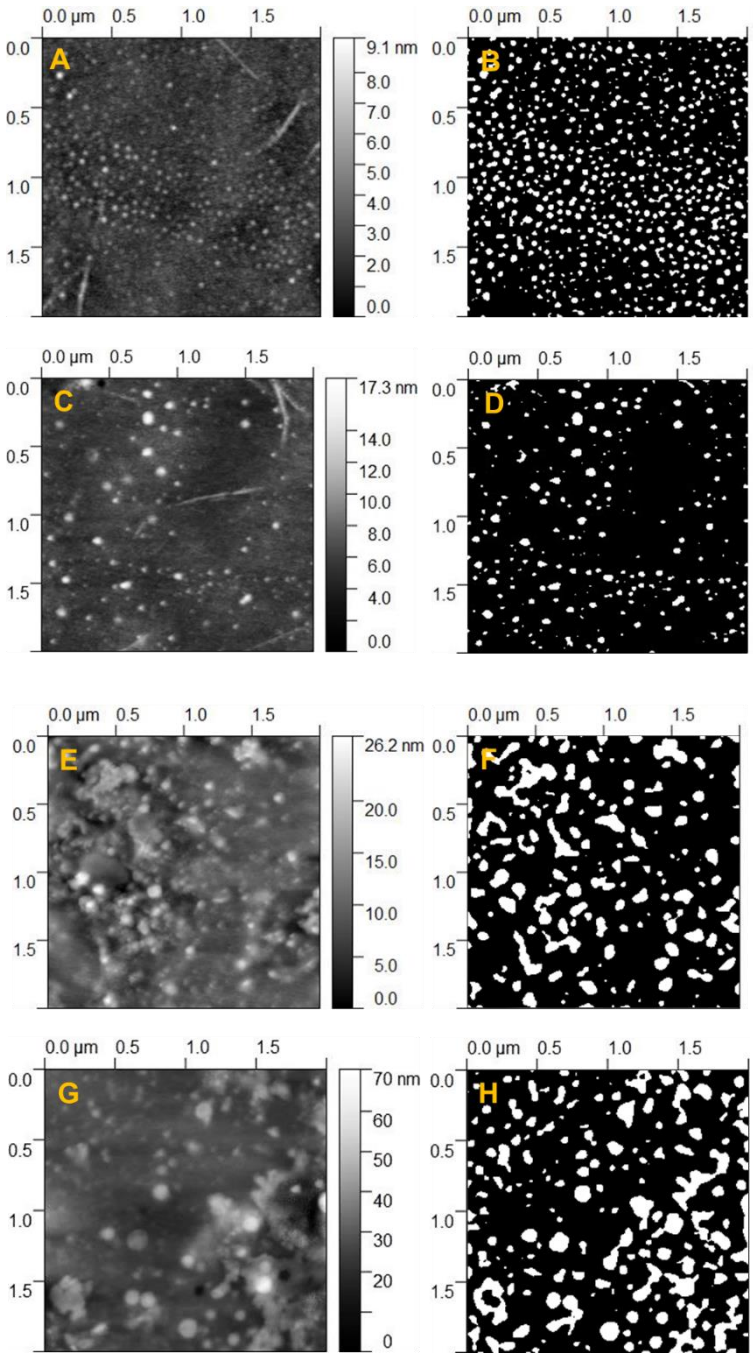


***Figure 3.3.13**: AFM Images of **RSPU (AmMorph)-15%** (A and C) and **RSPU (AmMorph)-15% (Blend)** (E and G) with the corresponding phase separation shown for **RSPU (AmMorph)-15%** (B and D) and **RSPU (AmMorph)-15% (Blend)** (F and H). Images on the left-hand column are the AFM images and on the right-hand column are the processed ones in ImageJ.*

Particle size analysis was conducted using ImageJ. The AFM images were scaled, threshold and particle size analysis was performed to quantify the micro-phase separations observed in **RSPU (AmMorph)-15%** and **RSPU (AmMorph)-15% (Blend)**. The scale was not homogenised for all of the samples in order to keep a suitable contrast for the particle analysis function (Figure 3.3.13 right-hand column). In order to carry out micro-phase separation analysis, polar 'hard' domains were assimilated to particles and characterise by their diameters. The particle analysis provided the diameter of the observed phase separations. Data were collected using AFM images for both samples. Statistical analysis of the diameters was then performed (Figure 3.3.14). Data from both **RSPU (AmMorph)-15** and **RSPU (AmMorph)-15%** (**Blend**) composition were plotted in a box plot in order to visualise the distribution of the diameter and consequently assess the effect of preparation *in situ vs.* blending (Figure 3.3.14). All the data concerning the diameter size were gathered and plotted for both compositions to gain better understanding of the overall diameter size distribution. As it can be seen from the below box plot, the distribution of size of the hard domain is considerably smaller in **RSPU (AmMorph)-15** compared to when the **LMWA** is blended with the SPU after synthesis. This could be attributed to more efficient dispersion of **LMWA** within the SPU network.

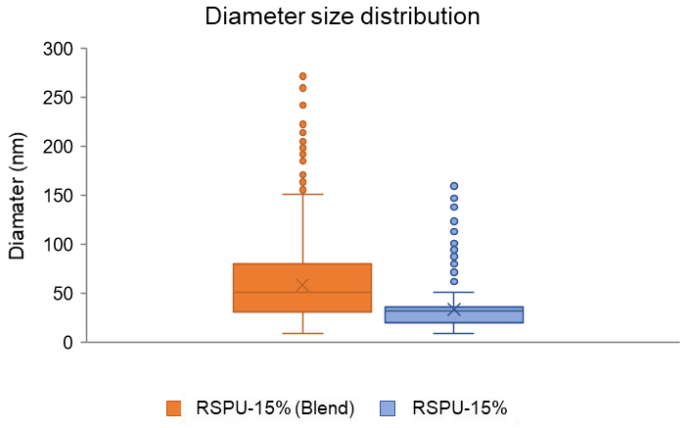


| | Average diameter (nm) | Percentage of outliers and extremes (%) |
|---|---|---|
| **RSPU-15%** | 30.4 ± 0.4 | 0.9 |
| **RSPU-15%-Blend** | 58.4 ± 1.4 | 1.5 |

***Figure 3.3.14:*** *Averages, standard error of the mean and percentage of extreme and outliners in diameter and distribution calculation of the* ***RSPU (AmMorph)-15%*** *and* ***RSPU (AmMorph)-15% (Blend)****.*

### 3.3.4 Healing Properties of RSPU (AmMorph)

Our previous studies have shown that the pristine supramolecular polyurethane **3.1 (AmMorph)** is healable[32] as a consequence of addressable and thermally responsive hydrogen bonding interactions. Therefore, understanding the effect that the LMWA **3.2 (AmMorph)** may have on the healing properties of the polyurethanes was interesting. Therefore, healability of the **RSPUs (AmMorph)** first assessed by variable temperature optical microscopy. Specimens of the polymer films were damaged using a scalpel blade, cutting through the entire thickness of the film (*ca.* 1 mm) and placed onto a glass slide. The damaged specimens were then heated at 10 °C $min^{-1}$ and healing assessed visually. As an exemplar, **RSPU (AmMorph)-15%** and **RSPU (AmMorph)-15% (Blend)** (Figure 3.3.15 A & B) are seen to begin healing at approximately 60 °C, and show complete closure of the damaged area at temperatures in excess of 90 °C. All polymers, with the exception of **RSPU (AmMorph)-21%**, demonstrated optical healing in excess of 95% (Figure 3.3.15 C, D & E). Indeed, the temperature required to induce healing increased with the increased weight percentage of bis-urea additive **3.2** from 40 °C in SPU **3.1 (AmMorph)** to 90 °C **RSPU (AmMorph)-15%**, as expected from rheological analysis of the materials.

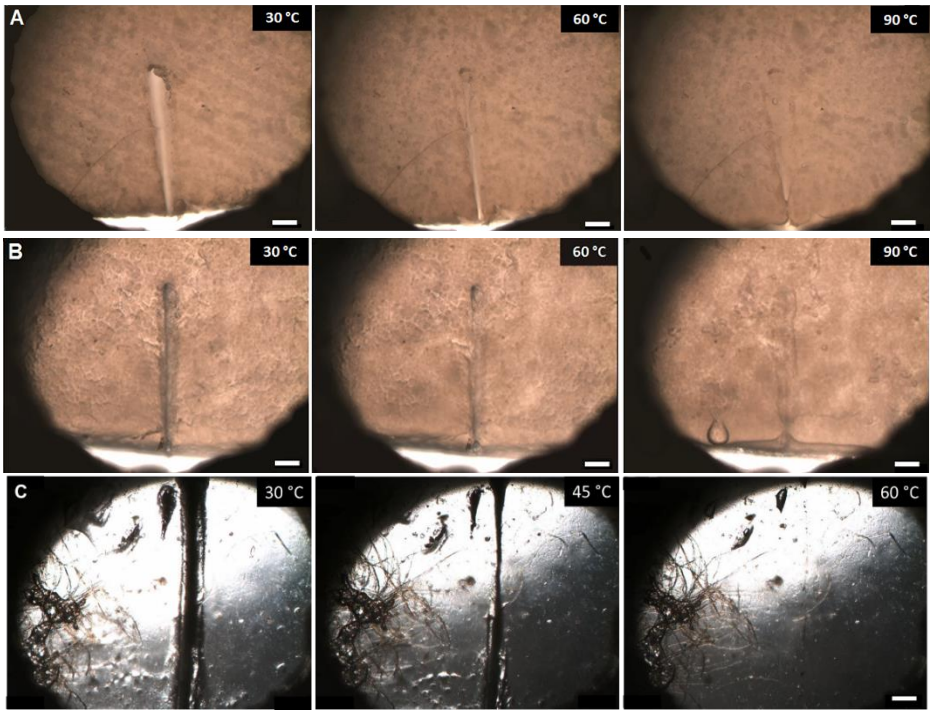

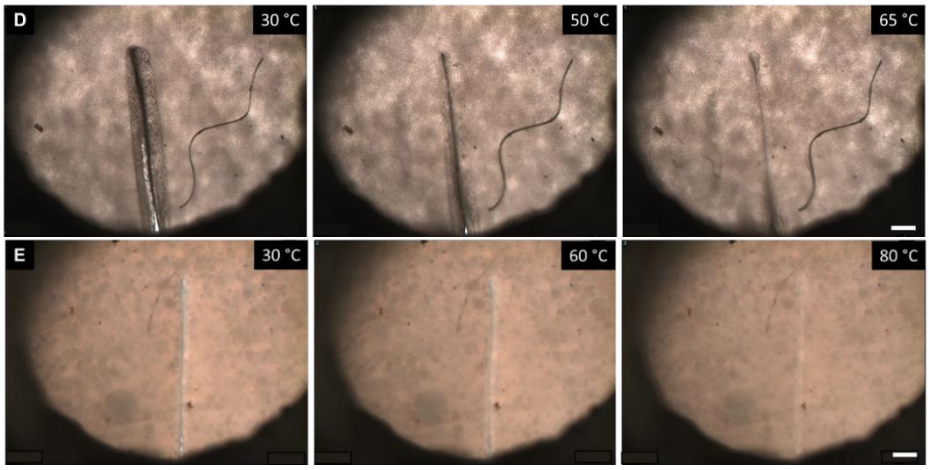


***Figure 3.3.15****: Progress of healing in A)* ***RSPU (AmMorph)-15%*** *and B)* ***RSPU (AmMorph)-15% (Blend)*** C) SPU **(AmMorph) 3.1**, D) **RSPU *(AmMorph)*-0%** and E) **RSPU *(AmMorph)*-8%**. *Images were taken using an optical microscope equipped with a hot stage. The scale bar is representing 50 μm.*

Finally, to examine the recovery of the mechanical properties after healing, tensile testing (Figure 3.3.16) was performed on polymer films cut into strips (dimensions = 40 mm × 5 mm × 1 mm). The pristine polymer strips were cutting into two pieces from the middle and the damaged surfaced placed in contact with each other on a warmed PTFE plate. The strips were placed into an oven for 1 hour at appropriate temperature derived from the rheological data and microscopy images for each polyurethane (Figure 3.3.15 and Appendix Figure A1) before cooling to room temperature and carefully pealing from the PTFE plate. Promisingly, healing was observed in **RSPU (AmMorph)-15%** and **RSPU (AmMorph)-15% (Blend)**. Healing efficiencies in excess of 98 % with respect to Young's modulus were observed for both reinforced polymers; however, slight reductions in the ultimate tensile strength (**RSPU (AmMorph)-15%** = 77 % recovery, **RSPU (AmMorph)-15% (Blend)** = 65 % recovery) were apparent which is comparable to the pristine samples. Low healing efficiencies were seen in total amount of energy adsorbed (modulus of toughness, **RSPU (AmMorph)-15%** = 12 % recovery, **RSPU (AmMorph)-15% (Blend)** = 9% recovery) as a result in diminished elongations to break reducing the integration of the stress/strain curves.

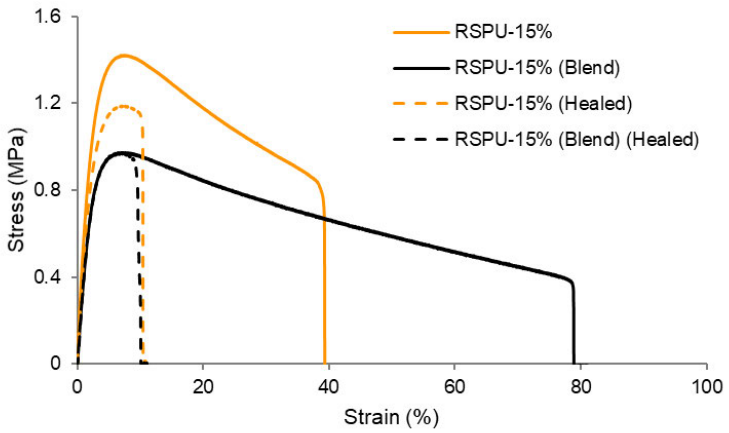


***Figure 3.3.16**: Tensile data for polymer composites **RSPU (AmMorph)-15%** and **RSPU (AmMorph)-15% (Blend)** showing their properties pre- and post-healing.*

Similar trends were observed for all RSPUs (Appendix Figures A2) revealing excellent recovery of the Young's modulus, moderate recovery of the ultimate tensile strength, and low healing efficiencies in modulus of toughness. This reduction in modulus of toughness when healed is in keeping with data reported for other supramolecular polymers which exhibit healability.[3,4] Full tensile properties of the pristine and healed materials extracted from their tensile graphs can be found in Table 3.3.3.

***Table 3.3.3:** Tensile properties of pristine and healed materials.*

| (AmMorph) RSPU | Young's modulus | | UTS | | Toughness | |
|---|---|---|---|---|---|---|
| | Pristine (MPa) | Healed (MPa) | Pristine (MPa) | Healed (MPa) | Pristine (MPa) | Healed (MPa) |
| **SPU 3.1** | 3.9 ± 1.4 | 1.3 ± 0.3 | 0.3 ± 0.1 | 0.1 ± 0.0 | 0.6 ± 0.1 | 0.1 ± 0.0 |
| **RSPU-0%** | 4.4 ± 1.3 | 4.0 ± 0.4 | 0.3 ± 0.0 | 0.4 ± 0.1 | 0.5 ± 0.0 | 0.7 ± 0.1 |
| **RSPU-8%** | 36.8 ± 4.2 | 35.5 ± 2.6 | 1.0 ± 0.1 | 1.1 ± 0.0 | 0.4 ± 0.1 | 0.1 ± 0.1 |
| **RSPU-15%** | 43.2 ± 4.4 | 42.5 ± 2.5 | 1.4 ± 0.1 | 1.1 ± 0.1 | 0.5 ± 0.1 | 0.1 ± 0.0 |
| **RSPU-15% (Blend)** | 35.4 ± 1.7 | 37.2 ± 2.2 | 0.9 ± 0.0 | 0.6 ±0.0 | 0.4 ± 0.1 | 0.0 ± 0.0 |
| **RSPU-21%** | 135.2 ± 18.1 | - | 2.4 ± 0.3 | - | 0.0 ± 0.0 | - |

When comparing these data to the healability of the supramolecular polyurethane **3.1(AmMorph)**,[32] it is evident that healing efficiency is reduced though the addition of additives to the supramolecular polymer network. However, despite the reduction in healing efficiency, the utilisation of this synthetic approach in industrial applications may provide a facile route to increasing the mechanical performance of functional supramolecular polymers through a one-pot no-purification synthesis method.

### 3.3.5 Synthesis and Characterisation of Reinforced SPU with a Stronger Recognition Motif

In order to better understand the effect of LMWA on the properties of the material and validating the reinforcing *in situ* synthesis method, a stronger recognition motif was selected to be incorporated into the reinforced system. (±)-3-Amino-1,2-propanediol **(PropDiol)** was selected as a strong hydrogen bonding motif. This hydrogen bonding recognition motif has been shown to form stronger network as a result of its chirality which helps with ordering the of the hydrogen bonding species *i.e.* ureas, urethanes as well as the end group.[184] However, the same synthesis procedure described for synthesis of reinforced supramolecular polyurethane detailed in Section 3.3.1 was employed in order to *in situ* generate reinforcing species. In brief, polydiol **2.2**, was mixed with 4,4′-MDI **2.3**. The mixture was subsequently heated to 80 °C under inert condition and constant stirring for 3 hours. The prepolymer **2.4** mixture then dissolved in anhydrous THF and cooled to room temperature. The end group, (±)-3-amino-1,2-propanediol **3.3 (PropDiol)** was then added to the mixture and heated to 80 °C under nitrogen and constant stirring for 18 hours. The resulting products was purified (via centrifuge and filtration) to remove insoluble by-product LMWA **3.2 (PropDiol).** This pure supramolecular polyurethane will be referred to from here on as SPU **3.1 (PropDiol)**. Additionally, a reinforced analogous material contains 15 wt% of LMWA **3.2 (PropDiol)** was also synthesised following the same procedure without purification and is called **RSPU (PropDiol)-15%**.

In order to prove the successful formation of the desired polymeric systems spectroscopy analysis were performed. The disappearance of the characteristic intense IR stretching at ~ 2230 $cm^{-1}$, corresponding to the isocyanate residues, was indicative of the consumption of the 4,4′-MDI **2.3** isocyanate moieties through reaction with the poly(butadiene) diol **2.2** and the hydrogen bonding end group **3.3 (PropDiol)**. Additionally, the shift of proton resonance at 3.66 ppm, corresponding to the α-protons of the polydiol **2.2** (i.e. adjacent to terminal hydroxy groups), to 4.16 ppm confirms the formation of urethane functionality (Appendix Figure A3). After confirming the formation of the desired materials samples were cast into PTFE moulds and dried to obtain self-supporting films. A solvent mixture of 35% v/v DMF in THF was used to cast the materials from. A mixture was utilised in order to help with dissolution of the different contents *i.e.* DMF dissolved the polar LMWA **3.2 (PropDiol)** and THF dissolved the polymer which is consisting mainly of an apolar aliphatic chain. High loading of LMWA **3.2 (PropDiol)** resulted in visual difference between the pure and reinforced samples and formed a brittle film of the reinforced sample (Figure 3.3.17). This was attributed to the increased content of LMWA **3.2 (PropDiol)** and consequently the higher concentration of the assembled hard domain within the matrix which reduces the film's

transparency. In addition, the increase in the concentration of LMWA **3.2 (PropDiol)** results in a decrease in the content of soft segment. Consequently, the flexibility of the material decreases, and the material became brittle when compared to SPU **3.1 (PropDiol)** (Figure 3.3.17). In conclusion, the *in situ* addition of 15 wt% LMWA **3.2 (PropDiol)** increases the hard segment composition such that the material is unable to form a continuous film which can be processed and analysed. Therefore, mechanical analysis (which requires a flat film) such as tensile testing or rheology was not possible for these materials.

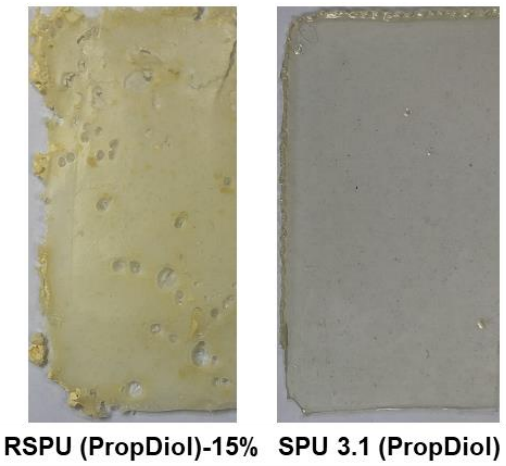


***Figure 3.3.17:*** *Solution cast films of the synthesised materials from a 35% v/v mixture of THF and DMF.*

In order to further characterise the synthesised materials and better understand the structure-property relationships, GPC analysis was of interest. To that aim, a solution of 2 $mg.mL^{-1}$ of SPU **3.1 (PropDiol)** in THF was prepared and left overnight to fully dissolved. The solution was then filtered and injected into the GPC instrument. Figure 3.3.18 shows the achieved eluogram. The multimodal eluograms represents that a chain extended polymer has formed. This is a natural result of uncontrolled synthesis with a difunctional linker (4,4′-MDI **2.3**). Additionally, the presence of peak 2 (Figure 3.3.18) which is attributed to the unwanted formation of LMWA **3.2 (PropDiol)**, further proves this phenomenon. In fact, it is apparent that the theoretical 1:1 reaction between the polyol and 4,4′-MDI **2.3** has not occurred and each polyol **2.2** has possibly reacted with more than one 4,4′-MDI **2.3**. In fact, the presence of LMWA **3.2 (PropDiol)** in the purified samples indicates that the centrifuge and the filtration do not completely remove the LMWA species as a result of its low solubility as well as strong interaction with the hard domain of the polymer. In addition, **RSPU (PropDiol)-15%** was not soluble in either DMF or THF alone as a result of high content of the bis urea **3.2** moiety. *i.e.* THF is capable of mainly dissolving the soft segment, however, the hard domain is more soluble in DMF. Therefore, collection of GPC analysis of **RSPU (PropDiol)-15%** proved impossible within the capability of the analytical facilities available to this study.

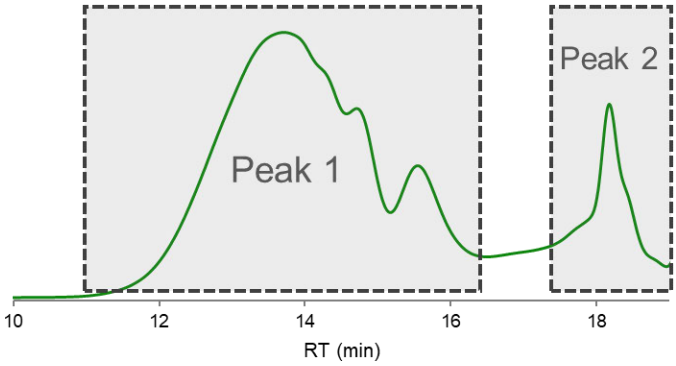


| Analyte | $M_n$ (g.mol$^{-1}$) | $M_w$ (g.mol$^{-1}$) | Đ |
|---|---|---|---|
| **SPU 3.1 (PropDiol)** | 14580 | 32100 | 2.20 |
| **LMWA 3.2 (PropDiol)** | 665 | 770 | 1.15 |

***Figure 3.3.18****: GPC eluograms of SPU* ***3.1 (PropDiol)*** *with THF as the eluent as well as the calculated molecular weights for each peak. Boxes specifies the areas at which the calculation applied.*

Subsequently, after the difficulties in characterisation of the reinforced material associated with the strong self-assembly of the hard segment and LMWA **3.2 (PropDiol)**, attention turned to study the supramolecular interactions in more details. Preliminary computational modelling using Chem 3D enabled the generation of a viable dimer assembly of LMWA **3.2 (PropDiol)**. Molecular dynamics refinements were performed to acquire the model (Figure 3.3.19). From the model, the presence of multiple hydrogen bonds as well as π- π stacking interactions between the benzene rings, can be observed. The hydrogen bonds length and the system energy were calculated to 2.01 Å - 2.09 Å and -86.37 kJ.mol$^{-1}$ which is indicative of a system with medium to strong hydrogen bonding with electrostatic and some covalent nature.[154]

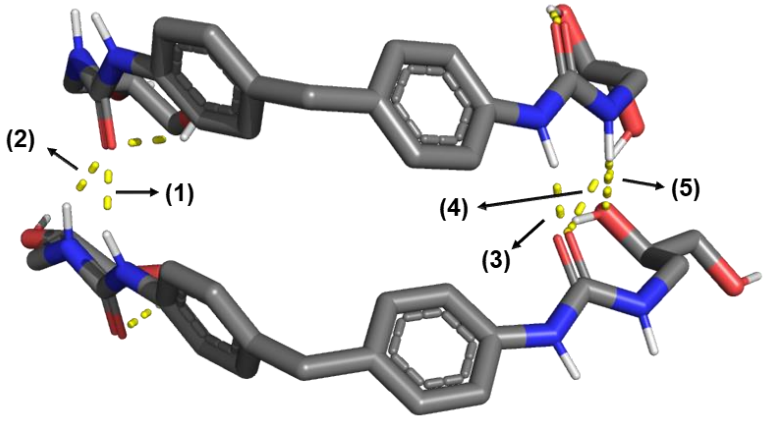

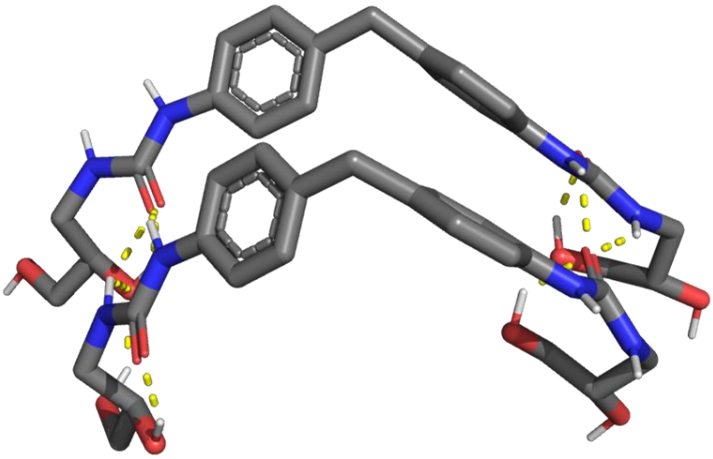

***Figure 3.3.19****: Preliminary computational models showing hydrogen bond interactions between two* ***LMWA (PropDiol)*** *molecules.*

Additionally, the bond angles obtained from this preliminary modelling study reinforce the assessment of the hydrogen bonds strength (Table 3.3.4). In brief hydrogen bonds with angles between 130° - 180° and 1.5 Å - 2.2 Å are considered moderately strong bonds featuring mainly electrostatic nature.[154] The hydrogen bonds from this study were bifurcated between the urea or a single bond between the -OH of the neighbouring **3.2** (**PropDiol)**. The involvement of the recognition motif in formation of these moderate hydrogen bonds serve to explain the difference in the mechanical properties of the materials with different concentration of the LMWA **3.2 (PropDiol)**.

***Table 3.3.4:*** *Properties of the intermolecular hydrogen bonds forms in a LMWA* ***3.2 (PropDiol)*** *dimer.*

| Hydrogen bond type | Bond Angle (°) | Bond length (Å) |
|---|---|---|
| **(1) N-H····O** | 133.0 | 2.06 |
| **(2) N-H····O** | 144.5 | 2.09 |
| **(3) N-H····O** | 136.1 | 2.06 |
| **(4) N-H····O** | 145.1 | 2.08 |
| **(5) O-H····O** | 149.0 | 2.01 |

Another key factor in determining the efficiency of hydrogen bonds in a system is the association constant ($K_a$). In this case $K_a$ indicates whether the species tend to form supramolecular assemblies, or the free form is preferred. Based on the bond angle and length from the modelling studies outlined above, the hydrogen bonds form between LMWA

**3.2 (PropDiol)** were likely to be moderate-strong nature, it is also important to understand how likely they are to form. To that aim, an $^{1}$H NMR titration study was carried out on solutions of LMWA **3.2 (PropDiol)** in a mixture of deuterated chloroform and hexafluoro-2-propanol (HFIP) (8:2, $CDCl_3$:HFIP, v/v) with various concentration (0.0050 M, 0.010 M, 0.015 M, 0.02 M, 0.03 M and 0.04 M). Two main resonances of interest were located at 6.48 ppm (*Ar*-N***H***-C(O)) and 5.28 ppm (C(O)-N***H***-CH2) which are attributed to the hydrogen bonding NH donors. It was observed that by increasing the concentration, both hydrogen bonding donors exhibited a downfield shift *i.e.* the higher concentration of LMWA **3.2 (PropDiol)** the higher concentration of hydrogen bonds in the system. Figure 3.3.20 shows the shift to lower fields in the chemical shifts of interest.

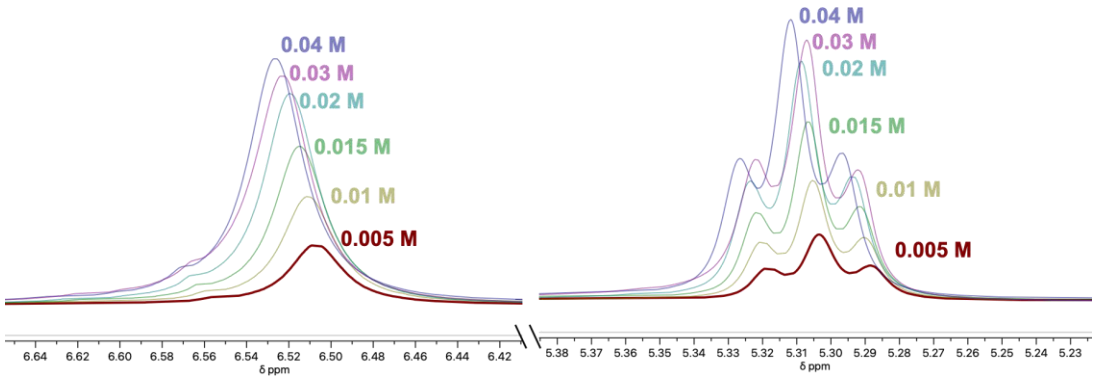


***Figure 3.3.20:*** *$^{1}$H NMR shift of LMWA **3.2 (PropDiol)** resonances with varying concentrations in 8:2 $CHCl_3$:HFIP (v/v) solution.*

The observed changes in the chemical shifts of these two protons as well as the concentration data were analysed using the DynaFit[51] algorithm and fitted (Figure 3.3.21) using least-squares minimisation based on trust region algorithm to find the association constant in solution.[27,52]

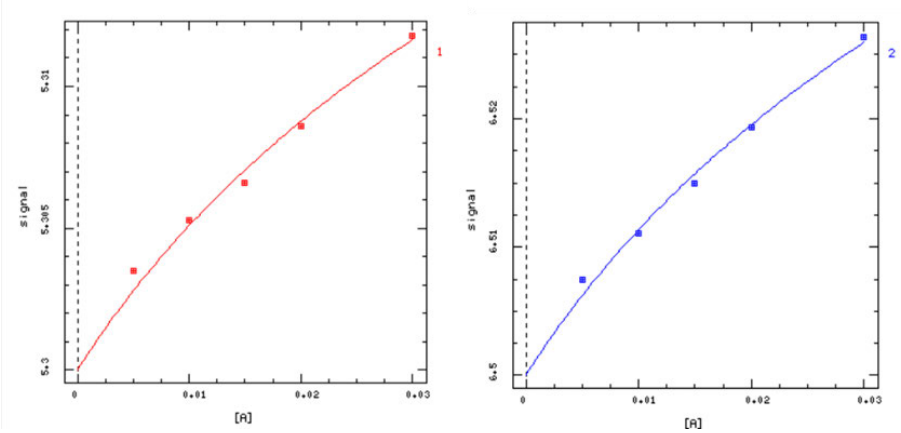


***Figure 3.3.21****: Plots showing points of $^{1}$H NMR spectroscopic chemical shifts vs. concentration and the fitted plot generated by DynaFit.*

Disappointingly, from these calculations the association constant was found to be $K_a$ = 8.2 ± 2.2 $M^{-1}$. The relatively high error can be attributed to the limited number of points that was inputted which resulted from the difficult solubility of LMWA **3.2 (PropDiol)** into the solvent system. Although, the achieved association constant is relatively low compare to other reported hydrogen bonding systems,[2] it is comparable with the $K_a$ values of similar bis urea/urethane moieties that have been reported and the exhibited mechanical properties are comparable with polyurethanes of higher molecular weight, perhaps as a result of efficient molecular ordering resulting from its chirality.[43,48]

To conclude, data revealed that the association constant of the **PropDiol**-based LMWA is within a range of the previously studied supramolecular bis-urea/urethane such as a 4-(2-aminoethyl)morpholine (**AmMorph**)-based LMWA with $K_a$ = 9.7 $M^{-1}$ [48] However, since the nature of the formed hydrogen bonds are considered moderately strong[1] the introduction of LMWA improved the mechanical properties of the material considerably. Therefore, it necessitates the optimisation of the concentration of LMWA based on the association motif and the desired final application of the material.

### 3.3.6 Synthesis and Characterisation of a library of RSPUs

After fully understanding the properties of the RSPU materials and the effect of LMWA on the mechanical properties of the pristine **SPU 3.1**, 3D printing of these reinforced materials was proposed. Essentially, it is desirable to enhance the mechanical properties of supramolecular polyurethane to increase their durability under various environmental conditions. For instance, as mentioned previously in Chapter 2, Section 2.3.5, by improving the mechanical properties of the **SPU1** used in 3D printing of a drug-release implant, the deformation of the implant after releasing the drug might be avoided. In this Chapter, it has been shown that by adjusting the molar ratio of the isocyanate linker and the end group in polyurethane syntheses, the mechanical properties of the afforded supramolecular polyurethane can be improved considerably.[39] Consequently, the same approach was taken to produce a small library of the reinforced SPUs by *in situ* introduction of the corresponding LMWA (Scheme 3.3.2). The effect of the structure of the end groups on the properties of the supramolecular polyurethanes have been studied previously within the Hayes research group.[27,32,38] Based on these previous studies, five different end-capping groups with different association ability was selected to be incorporated into the system. This library includes five different SPUs, made up of an identical diol **2.2** and isocyanate (4,4′-MDI) **2.3** and a distinct end group, each of which offers unique mechanical properties. The library was made in order to investigate the printability and processability of these materials using hot-melt extrusion 3D printing technique for potential biomedical applications.

Corresponding RSPUs were synthesised following the same procedure outlined in Section 3.3.1. However, a compromise between a low-temperature processability and improved mechanical properties was made and the reagents stochiometric ratio of polydiol:isocyanate:end group was set to 1:2.25:2.5 (theoretical 4%) to produce LMWAs *in situ*. Therefore, the molar ratio of the produced LMWA was constant in all RSPUs. Synthesis of RSPUs with 4% LMWA was selected for this study in order to be able to maintain the percentage across all materials with different recognition motifs. *E.g.* materials consist of stronger end group would become too brittle to form a film upon introduction of high content of LMWA. The materials synthesised with this ratio are named **RSPU′** within this thesis. As described previously, Krasol HLBH-P200 **2.2** was mixed with (4,4′-MDI) **2.3** for 3 hours in neat under inert condition. The formed prepolymer **2.4** dissolved in anhydrous THF and after cooling to room temperature, the appropriate self-assembly motif **3.3** was added to the mixture. Upon completion of the reactions, the solvent was removed, and the polymer used as recovered.

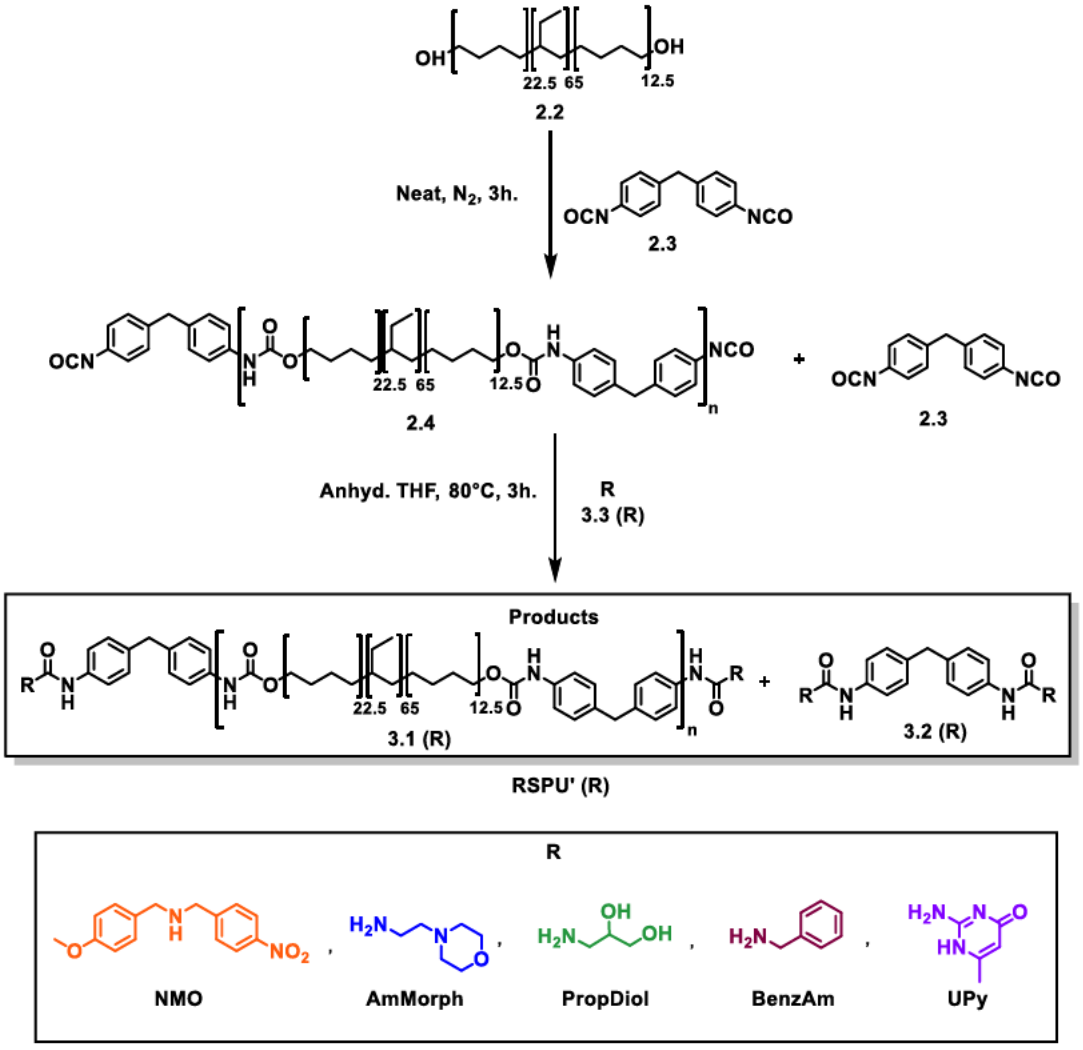


***Scheme 3.3.2:*** *Reaction scheme illustrating the production of the reinforced SPUs.*

Without further purification, the synthesised materials were solution cast into a PTFE mould. The films were then dried in an oven and prepared for subsequent analysis. However, as a result of the high concentration of supramolecular interactions and low energy of film preparation method (stirrer bar mixing), the prepared films were found not to be homogenous and macrophase separation occurred. Shown below in Figure 3.3.22 are the structures and sample codes of the reinforced SPUs used for printing.

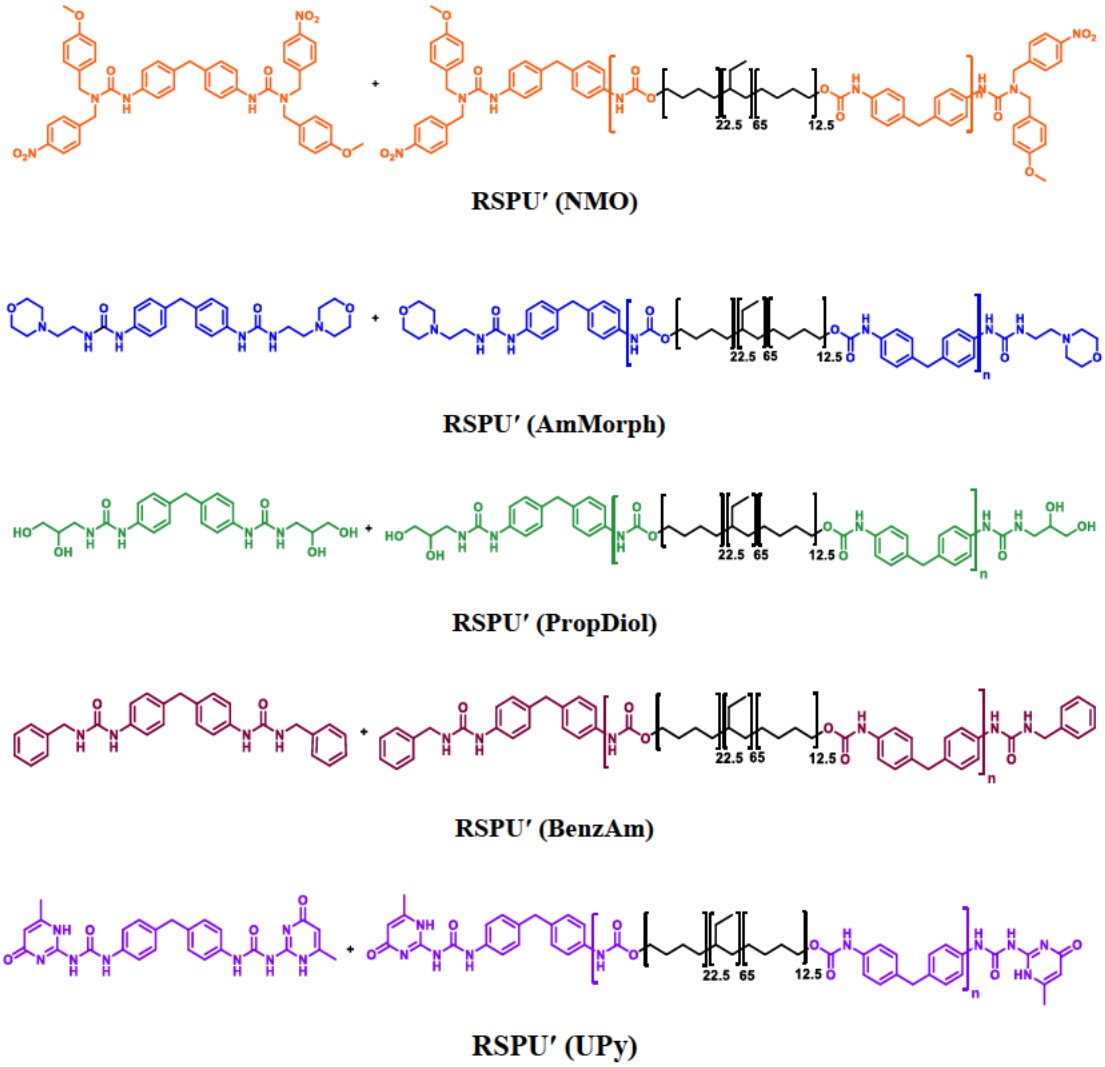


***Figure 3.3.22:*** *Structures and sample codes of the small library of reinforced SPUs.*

In order to find out the molecular weight of the synthesised RSPU′s, they were subjected to GPC analysis with THF as the mobile phase with the chromatograph equipped with a refractive index (RI) detector. The resultant eluograms are shown in Figure 3.3.23. The grey rectangle illustrates the area of integration for molecular weight analysis. Although most of the synthesised RSPU′s demonstrate similar molecular weight distribution, SPU **3.1 (UPy)** was poorly soluble in the mobile phase and therefore GPC analysis under these conditions

was inconclusive. Similarly, the LMWAs of **3.2 (PropDiol)** and **3.2 (UPy)** were not soluble in THF or DMF and hence filtered out from the solution.

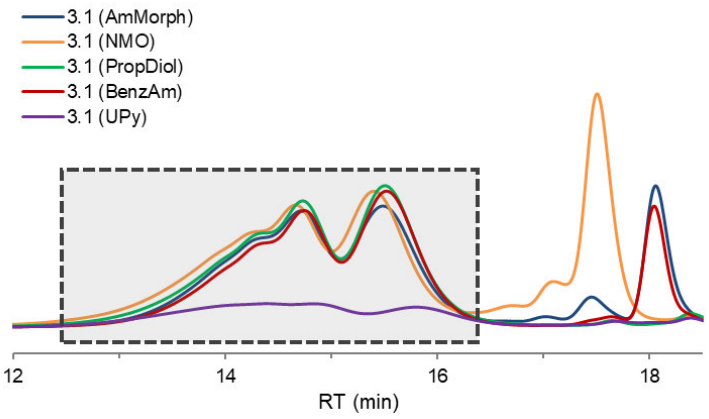


***Figure 3.3.23:*** *GPC eluograms of the synthesised RSPUs showing a bimodal distribution of the polymer as well as the formed LMWAs. The rectangle displays the area of integration for molecular weight calculations.*

However, the collected eluograms were utilised to calculate the molecular weights of the synthesised RSPU′s without taking into account the peak related to the LMWAs. Molecular weight calculation results are presented in Table 3.3.5. In brief, GPC analysis confirmed that the synthesised RSPU′s have comparable molecular weight and polydispersity and therefore, further validating the stoichiometrically-controlled reinforcement of supramolecular polyurethanes method.

***Table 3.3.5:*** *Calculated molecular weights of the synthesised RSPU's using the GPC analysis.*

| RSPU' | $M_n$ (g.mol$^{-1}$) | $M_w$ (g.mol$^{-1}$) | Đ |
|---|---|---|---|
| **RSPU' (AmMorph)** | 8460 | 13016 | 1.54 |
| **RSPU' (NMO)** | 9450 | 15500 | 1.64 |
| **RSPU' (PropDiol)** | 8380 | 13650 | 1.63 |
| **RSPU' (BenzAm)** | 8020 | 12260 | 1.53 |
| **RSPU' (Upy)** | Insoluble | Insoluble | Insoluble |

Once the molecular weight characteristics of the RSPUs had been established, the focus then switched to determining their thermal properties to elucidate if they were suited for 3D printing. As a consequence of the nature of the end-capping groups **3.3**, the RSPU′s were anticipated to possess different thermal properties. The RSPU′s were subjected to DSC analysis and heated from -80 °C to 200 °C at the rate of 10 °C min$^{-1}$ for three cycles. Figure

3.3.24 presents the collected thermograms of the samples. In brief, every sample exhibits a $T_g$ of *ca.* -46 °C arising from the soft segment of the polyurethane. In addition, the thermogram of **RSPU′ (BenzAm)** reveals a melting point at *ca.* 73°C. Furthermore, **RSPU′ (PropDiol)** has a second $T_g$ of -3.8 °C as well as a *pseudo*-melting point ($T_m$) of 187.0 °C. However, the observed $T_m$ is relatively broad, with lower heat flow and did not represent commonly seen melting point transition curve of crystalline or semi-crystalline materials. This was attributed to several factors which include the polymorphic nature of the material. The phenomenon is also promoted by the different possible packing and hydrogen bonding arrays within the material which can be explained by the use of a racemic mixture of the chiral end group **3.3 (PropDiol)**. In conclusion, the materials have similar thermal properties, however the **RSPU′ (PropDiol)** is expected to cause problems for printing as it presents high melting point.

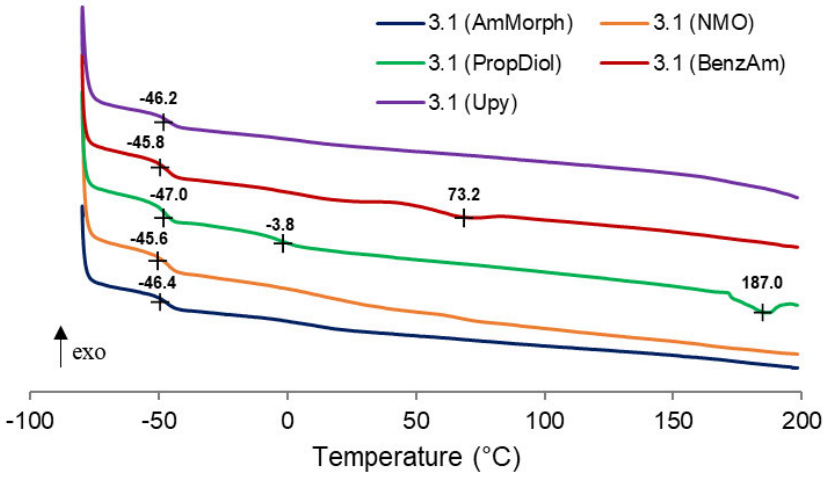


***Figure 3.3.24**: DSC thermograms of the synthesised RSPU's.*

### 3.3.7 Hot-Melt Extrusion 3D Printing of the RSPU′s Library and its characterisations

Hot-melt extrusion 3D printing was selected as the suitable technique to deposit the reinforced supramolecular polyurethanes. This method is solvent free, and hence it is used most extensively for biomedical and pharmaceutical applications. To this aim, a CELLINK INREDIBLE+ (Figure 3.3.25) 3D bioprinter was utilised. This printer works by heating the cartridge to decrease the viscosity of the contained ink and upon application of compressed air the material can be deposited in a controlled manner to afford well-defined images.

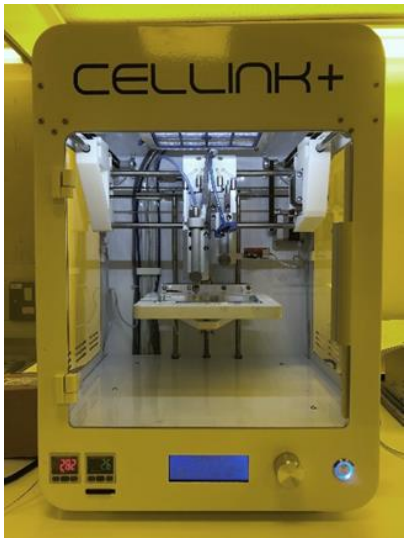


***Figure 3.3.25****: The hot-melt 3D extrusion printer used to deposit the library of RSPUs.*

Different target shapes of the materials were required in order to meet requirements of subsequent analysis. The required shapes have to be designed in a format that is readable by the printer system. Indeed, to be able to print a design, it needs to be converted into a computer programming language to correctly control and direct the printhead. The most widely used computer language by 3D printers is GCode. GCode contains the printing parameters and the layer-by-layer shape of the design. GCode is the language of 3D printers which usually generated automatically by the printer's software and can be edited, if needed, in any simple text-editing programme by knowing the related commands. To that aim, GCode files of a 5 × 40 × 0.6 mm bar and a 20 × 20 × 0.6 mm square and 10 × 10 × 0.6 mm square was created using AutoCAD TINKERCAD online.[53] The online software enables generation of any 3D design. These files were then imported to the printer software (HeartWare) to generate the appropriate slicing (as the ink is applied in a layer-by-layer fashion) and the GCode based on the suitable setting for each material (Table 3.3.6). Then the material was loaded into an aluminium cartridge equipped with a 25 G nozzle and heated to desired temperature for 15 minutes prior to extrusion. By applying the appropriate pressure, 4 bars, 1 big square and 1 small square was printed with 100% infill for tensile testing, rheology and biocompatibility studies, respectively. The high pressure and temperature as well as the shear applied to extrude these materials resulted in a more homogeneous printed parts compared to the cast film by virtue of more efficient mixing of LMWA **3.2 (R)** and the corresponding polymer network

The next sections include printing parameters and a discussion about the properties of each printed material individually. Table 3.3.6 shows the parameters required for extrusion 3D printing of each material.

***Table 3.3.6:*** *Printing parameters for the hot-melt extrusion printing.*

| RSPU' | Pressure (kPa) | T (°C) | Layer height (mm) | Speed ($mm.s^{-1}$) | Bed Temperature (°C) |
|---|---|---|---|---|---|
| **RSPU' (NMO)** | 283 | 110 | 0.35 | 1 | 30 |
| **RSPU' (AmMorph)** | 330 | 120 | 0.35 | 1 | 50 |
| **RSPU' (PropDiol)** | 410 | 120 | 0.35, 0.25 | 0.5 | 50 |
| **RSPU' (BenzAm)** | 340 | 110 | 0.35 | 1 | - |
| **RSPU' (Upy)** | - | - | - | - | - |

It has to be noted that although the initial attempt to extrude **RSPU′ (BenzAm)** was carried out successfully and a filament produced upon applying pressure, after a short while, the nozzle became blocked, and the material stopped extruding regardless of the pressure and temperature applied (within the printer's operational limits). This result could be attributed to the high melting point and strong association between the LMWA **3.2 (BenzAm)**. Since the LMWA **3.2 (BenzAm)** is strongly associated therefore the *in situ* blending with the polymer has been inefficient. Figure 3.3.26 shows a picture of the cast film revealing phase separation in the cast film illustrating the aggregation of LMWA **3.2 (BenzAm)**. Therefore, within the printing temperature window the LMWA **3.2 (BenzAm)** did not dissociate, and aggregation of the material eventually blocked the nozzle and made continuous printing impossible. Upon removal of the stuck material from the nozzle the aggregates of the LMWA **3.2 (BenzAm)** (similar to the aggregates seen on the cast film) were evident visually confirming the assumption that the LMWA **3.2 (BenzAm)** is responsible for the nozzle blockage. This could be addressed by decreasing the content of LMWA **3.2 (BenzAm)** within this formulation.

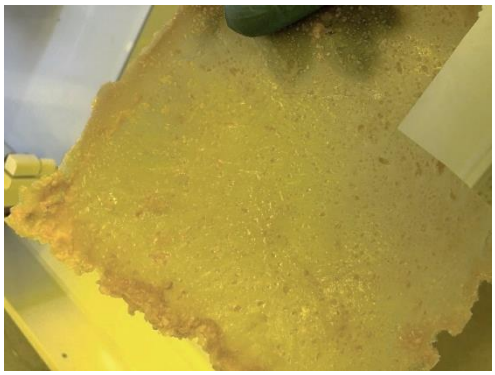

***Figure 3.3.26:*** Picture of ***RSPU′ (BenzAm)*** film, showing high phase separation between the polymer and the corresponding LMWA. *The yellow hue of the picture is from the yellow lighting of the lab and the polymer is of creamy white colour.*

Additionally, **RSPU′ (UPy)** features UPy as the end group which is well-known for its high association constant ($6 \times 10^7$ $M^{-1}$ in $CDCl_3$)[2] (Figure 3.3.27). The temperature capacity of the printer (130 °C) could not provide enough energy required to dissociate the complementary hydrogen bonding network to decrease the viscosity of the material suitable for extrusion by the CELLINK printer.

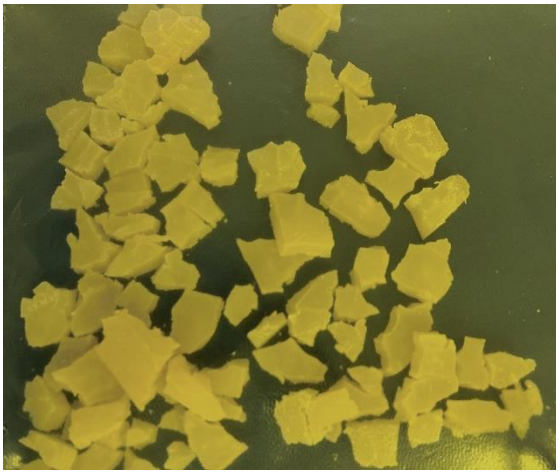

***Figure 3.3.27**: Picture of **RSPU′ (UPy)** after casting. As a result of high association constant of the UPy end group, the material was found to be very brittle and unable to form a continuous film.*

Figure 3.3.28 shows the bars being printed for tensile testing from each printable material namely, **RSPU′ (NMO)**, **RSPU′ (AmMorph)** and **RSPU′ (PropDiol)**. In order to examine the reproducibility of the prints, the dimensions of the printed bars were measured using a micrometer and the weight of each specimen was recorded. Table 3.3.7 - 9, exhibit the results of these measurements for reinforced SPUs. The results show that for the individual material, the dimensions of all four printed parts are within a small error from each other and the designed size, except for the thickness. The thickness of the specimens is within a range from each other, however, there was a big error from the original design size. This could be explained based on the slicing and the swelling of the material. HeartWare slices the 3D design based on the size of the nozzle (25 G, 0.44 mm) and the defined layer thickness. Therefore, 0.6 mm is less than 2 layers but more than 1 layer. Considering printing 2 layers of the material (0.88 mm theoretically) and factor in the swelling of the material upon heating, this thickness error from the original size can be explained and corrected if needed. In the case of **RSPU′ (AmMorph)** (Table 3.3.8), the thickness possessed a smaller error as the material exhibited less swelling. Regarding **RSPU′ (PropDiol)** (Table 3.3.9), the thickness of the printed sample was corrected by changing the thickness of the second printing layer. However, this approach was only suitable for **RSPU′ (PropDiol)**, since the viscosity of the melt was higher than the other two materials at the printing temperature and therefore the print did not deform by decreasing the layer height.

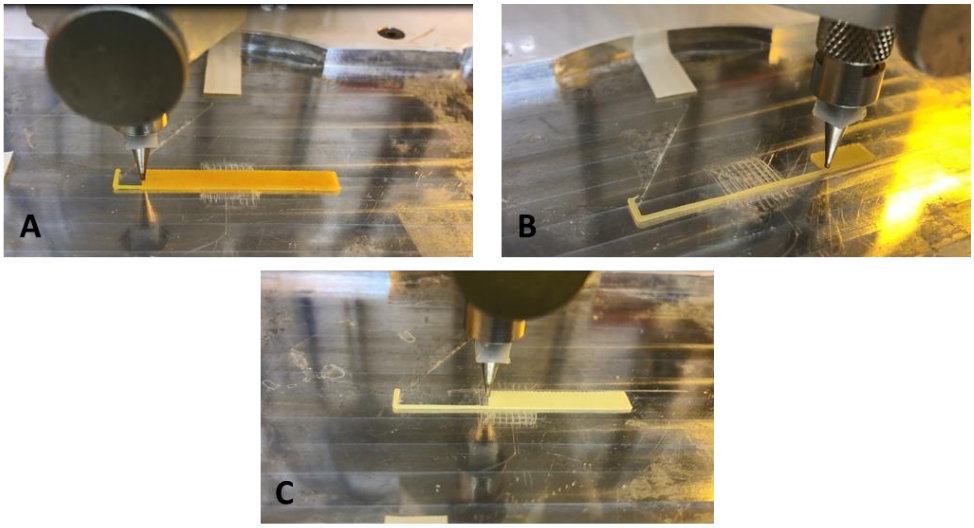


***Figure 3.3.28:*** *Pictures of A)* ***RSPU' (NMO)****, B)* ***RSPU' (AmMorph)*** *and C)* ***RSPU' (PropDiol)*** *being printed.*

***Table 3.3.7:*** *Weight and dimension distribution of the printed bars of* ***RSPU' (NMO).***

| | L (40 mm) | Width (5 mm) | Thickness (0.6 mm) | Weight (g) |
|---|---|---|---|---|
| **Bar 1** | 40.28 | 4.80 | 1.13 | 0.172 |
| **Bar 2** | 40.16 | 4.80 | 1.09 | 0.171 |
| **Bar 3** | 40.15 | 4.80 | 1.06 | 0.190 |
| **Bar 4** | 40.10 | 4.70 | 1.10 | 0.172 |
| **Average** | 40.17 ± 0.07 | 4.78 ± 0.04 | 1.10 ± 0.02 | 0.176 ± 0.008 |

***Table 3.3.8:*** *Weight and dimension distribution of the printed bars of* ***RSPU' (AmMorph)****.*

| | L (40 mm) | Width (5 mm) | Thickness (0.6 mm) | Weight (g) |
|---|---|---|---|---|
| **Bar 1** | 40.21 | 4.88 | 0.93 | 0.165 |
| **Bar 2** | 40.19 | 4.81 | 0.80 | 0.142 |
| **Bar 3** | 40.27 | 4.82 | 1.04 | 0.169 |
| **Bar 4** | 40.12 | 4.77 | 1.07 | 0.176 |
| **Average** | 40.20 ± 0.05 | 4.82 ± 0.04 | 0.96 ± 0.10 | 0.163 ± 0.013 |

***Table 3.3.9:*** *Weight and dimension distribution of the printed bars of* ***RSPU' (PropDiol)****.*

| | L (40 mm) | Width (5 mm) | Thickness (0.6 mm) | Weight (g) |
|---|---|---|---|---|
| **Bar 1** | 40.28 | 4.65 | 0.67 | 0.159 |
| **Bar 2** | 40.33 | 5.05 | 0.75 | 0.113 |
| **Bar 3** | 40.19 | 4.62 | 0.70 | 0.131 |
| **Bar 4** | 40.29 | 4.94 | 0.92 | 0.117 |
| **Average** | 40.27 ± 0.05 | 4.82 ± 0.18 | 0.76 ± 0.10 | 0.130 ± 0.018 |

In order to compare the mechanical properties of the printed samples, the printed bars were mounted on the tensile testing instrument and tested at a rate of 10 mm.min$^{-1}$. The changes in stress by changes in strain was recorded. Figure 3.3.29 presents the representative tensile graphs of each printed bar.

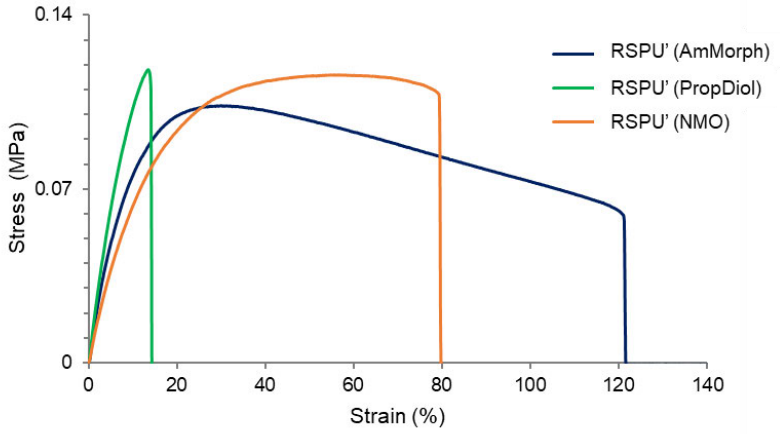


***Figure 3.3.29:*** *Stress-strain graphs of the printed bars from different* ***RSPU's.***

The experiment was repeated four times for each material and the average calculated parameters are presented in Table 3.3.10.

***Table 3.3.10:*** *Mean tensile properties of the printed bars from three different* ***RSPU's.*** *Calculated from 4 repeat experiments.*

| Polyurethane | Young's Modulus (MPa) | Ultimate Tensile Strength (MPa) | Toughness (MPa) | Strain at Break (%) |
|---|---|---|---|---|
| **RSPU' (AmMorph)** | 0.84 ± 0.11 | 0.10 ± 0.01 | 0.09 ± 0.03 | 101.96 ± 30.48 |
| **RSPU' (PropDiol)** | 1.42 ± 0.22 | 0.13 ± 0.01 | 0.01 ± 0.00 | 15.35 ± 3.13 |
| **RSPU' (NMO)** | 0.75 ± 0.03 | 0.12 ± 0.00 | 0.07 ± 0.01 | 75.055 ± 8.27 |

It can be concluded that the **RSPU′ (PropDiol)** is the stiffest material presenting the highest Young's modulus of three with a sharp increase in stress upon applying stress. On the other hand, **RSPU′ (AmMorph)** is capable of absorbing the most energy before fracturing and failure which can be supported by the strain at break (9 and 2.6 times more energy absorbance capability compared to **RSPU′ (PropDiol)** and **RSPU′ (NMO)**, respectively). Furthermore, all of the three materials exhibited similar ultimate tensile strength within the error. This is defined as the maximum resistance of the material before deforming plastically. Tensile results show a clear relationship between the degree of the supramolecular interactions formed from **LMWA 3.2** and the **SPU 3.1** hard segments. It is evident that by increasing the

supramolecular interactions the material become stiffer as a result of the hard segment dominating the properties of the material. In contrast, the tensile properties are mainly influenced by the soft segments and the polymer backbone properties when the association of the LMWA **3.2** and the end-capping group of the polymer is weaker. It must be noted that, the reported supramolecular polyurethanes exhibited low mechanical properties compared to commercially available thermoplastic polyurethanes with tensile strength of 1 or 2 order of magnitude.

In addition, rheological properties of the printed materials were also studied. To fulfil that purpose, circular samples (D = 8 mm) were cut from the printed squares for testing in rheometer. The linear visoelastic region (LVER) was determined by performing a strain sweep experiment. Next, a frequency sweep experiment was performed to measure the changes in the moduli. This experiment was carried out at a constant temperature at 25 °C to maintain the print lines and the layered structure intact and study the possibility of failure of the structure as a result of production method. All three of the printed materials exhibited an almost parallel pattern between the storage and loss moduli within the experiment frequency range. Additionally, the storage modulus was dominant in all samples at room temperature indicating that the properties of the materials are governed by elastic properties and follows the order of **RSPU′ (AmMorph)** > **RSPU′ (NMO)** > **RSPU′ (PropDiol)** from the stiffest (Figure 3.3.30). Finally, based on the determined LVER a suitable frequency was selected and applied to perform an oscillatory experiment with a constant frequency. The samples were heated from 0 °C to 150 °C to investigate the changes in the moduli by increasing the temperature. The experiment revealed that all material shows a cross-over point at elevated temperature at above which the viscous property of the material dominates. It is evident from the results that **RSPU′ (PropDiol)** requires more energy and therefore higher temperature to reach the cross-over point. This could be explained by the stronger supramolecular association between its molecules arising mainly from the hydrogen bonds between LMWA **3.2 (PropDiol)**. Additionally, as expected, RSPU' (NMO) shows a *ca.* 28 °C increase in cross-over temperature compare to its pristine form reported in Chapter 2 (**SPU1**, Fig 2.3.8 B)

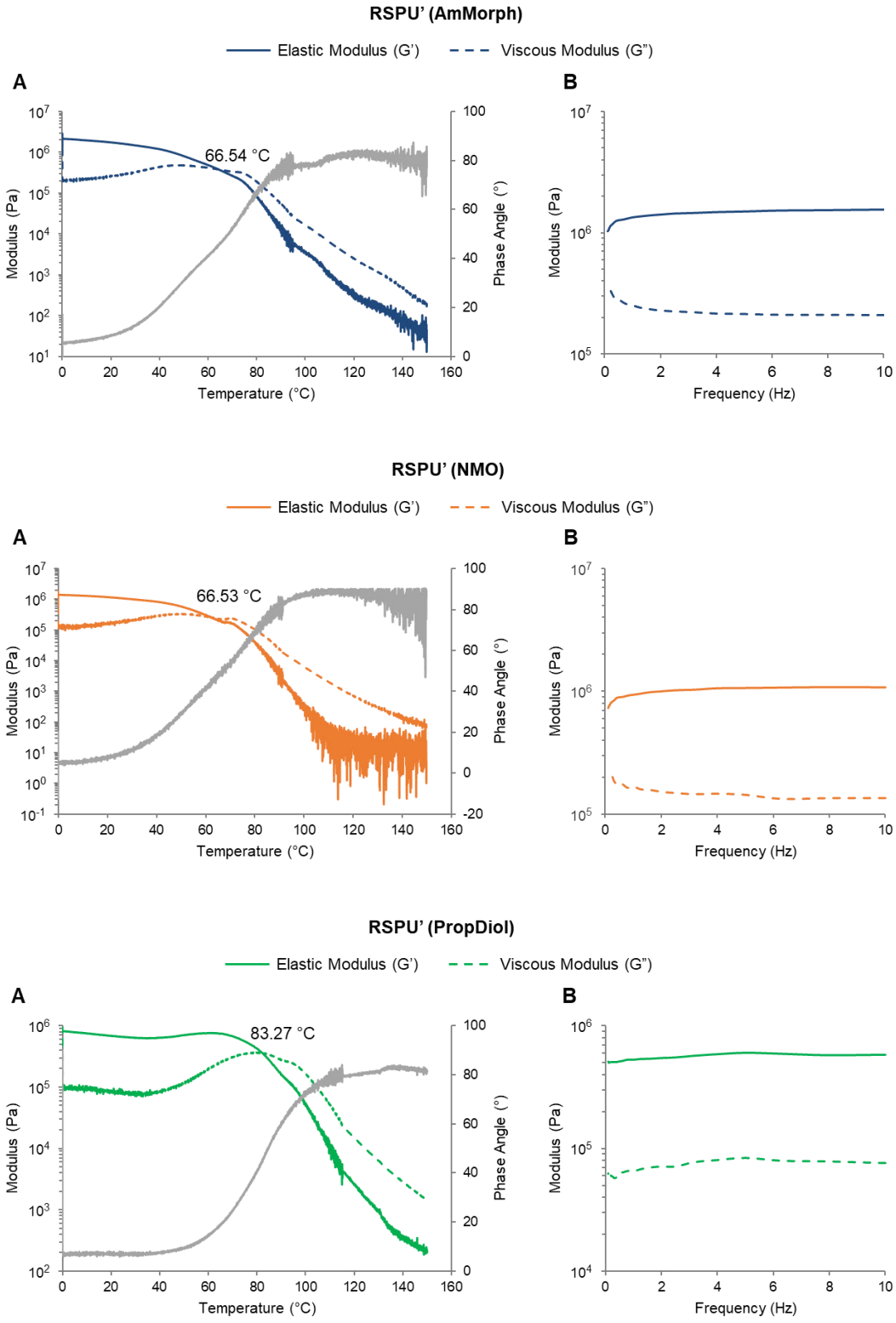


***Figure 3.3.30:*** *The result of oscillatory rheological analysis of the printed materials in constant A) temperature and B) frequency.*

To better understand the morphology of the materials and compare the morphology of cast *vs.* printed materials SAXS analyses were performed at room temperature. The RSPU′s materials which contain excess bis-urea LMWAs moieties can potentially exhibit higher degrees of

phase separation within the network by forming additional interactions with the hard segment of the polymer (Figure 3.3.31).

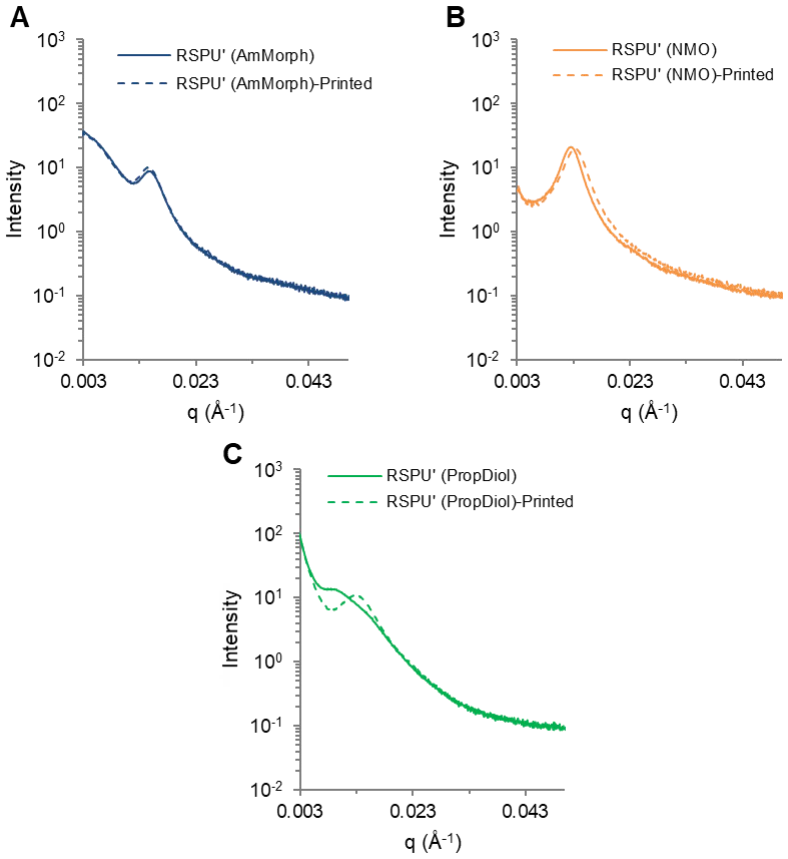


***Figure 3.3.31**: Comparison of the SAXS diffraction patterns of the printed and cast RSPU's.*

The SAXS analysis revealed that, based on the strength of the intermolecular interactions that each end-group can form, the d-spacing of the cast material differs. For example, **RSPU′ (AmMorph)** and **RSPU′ (NMO)** exhibited spacing of 62.5 Å and 76.9 Å, respectively. In contrast, although the cast **RSPU′ (PropDiol)** showed a broad indistinct peak at 105.3 Å, it represents the inefficiency of the production method (solution casting). In brief, as an effective mixing of the LMWA **3.2 (PropDiol)** with the polymer network does not occur, a distinct spacing was not observed. Upon extrusion of the materials in lower viscosity by passing through a static mixer, more efficient mixing occurs in all cases and a shift to smaller spacing was evident. This phenomenon was less pronounced in the systems that possessed end-groups with weaker interactions *i.e.* **RSPU′ (AmMorph) < RSPU′ (NMO) < RSPU′ (PropDiol)** with spacings of 66.67 Å, 71.43 Å and 71.42 Å after printing, respectively.

Next, in order to study the suitability of these materials for biomedical/pharmaceutical applications, attention turned to understanding the behaviour of *in vitro* production of

LMWAs and the possible leaching of it from the polymeric system into the related medium. Within the scope of drug delivery application, the leaching of the LMWA is of high importance since it can influence the biocompatibility of the material and therefore it has to be investigated as one of the main inspections of the suggested material. As a primary study, smaller squares of 10 × 10 × 0.6 mm from each printable material were produced. These samples were then placed in a sample vial containing PBS buffer at pH = 7.4 which is considered the subcutaneous pH. This pH was selected based on the potential application of these materials as drug release implants. The sample vials were then put in a water bath at 37 °C and stirred with a magnetic stirrer bar. Aliquots of the samples (500 µL) were taken from each vial daily and replaced with fresh buffer solution to keep the volume constant. After 15 days, collected samples were loaded onto a quartz plate and loaded into the plate microreader to collect the UV-vis spectra of the samples (Figure 3.3.32). The data obtained revealed that in all cases there was leaching of the LMWAs from the samples into the buffer solution. However, since the LMWA was not directly soluble in the buffer, producing a calibration curve and identification of the nature of the released species with this technique was not possible. Interestingly, although some leaching of LMWAs was observed in the medium the printed square did not change shape after 15 days in the buffer (Figure 3.3.33) unlike the printed formulations of pure **SPU1** which showed deformation after the release experiment as reported in Chapter 2, Figure 2.3.22. Maintaining the physical shape is of high importance as the material is to be used as drug implants and therefore, the printed image needs to be stable for a few months under the skin condition as the standard timescale for drug release implants. However, these are primary experiments and need to be repeated upon eluting of a drug over a longer period of time. Consequently, to better understand the nature of the released species in the medium and its effect on the biocompatibility of the materials, a new set of samples were utilised to study *in vitro* behaviour of the materials in a cell line.

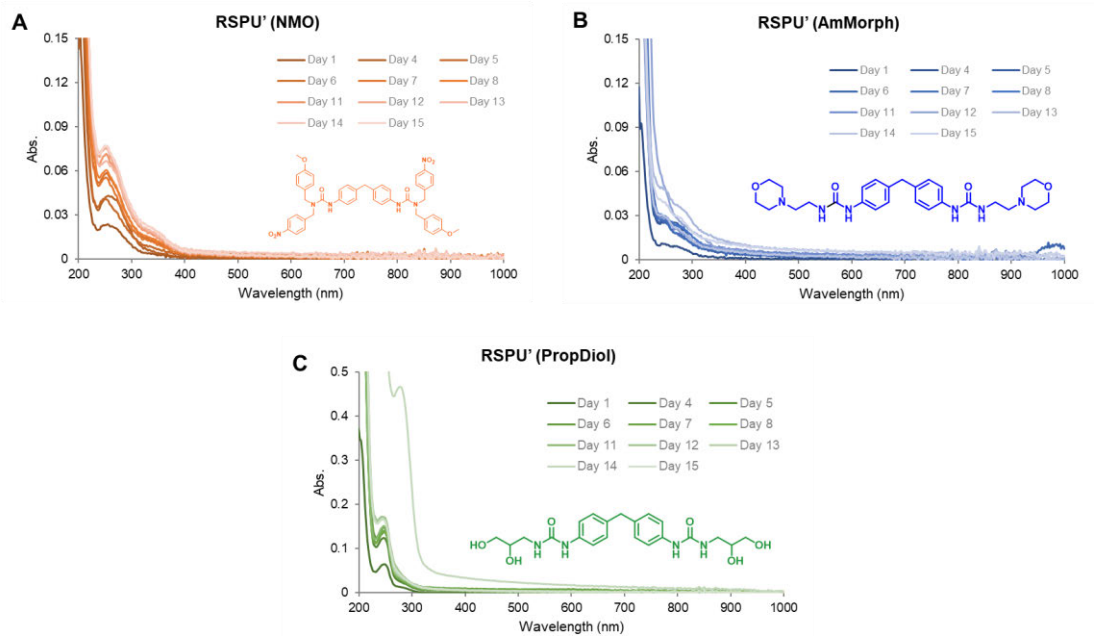


***Figure 3.3.32****: UV-vis spectra of the medium in contact with RSPU's for 15 days. The absorbance was corrected by a fresh buffer solution.*

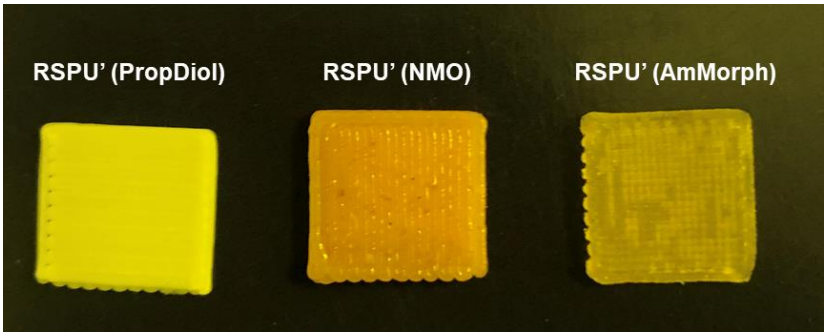


***Figure 3.3.33:*** *Picture of the printed RSPU's after 15 days in buffer pH = 7.4.*

To understand the cell viability and therefore biocompatibility of the materials, biocompatibility test was performed. The NIH3T3 cell line which derived from mouse embryonic fibroblasts was employed in this experiment. Three sets of control media were produced *i.e.* incubated media (negative control 1), fresh media (negative control 2) and the media cells killed with Industrialised methylated spirit (IMS) as the Positive control. Additionally, three pieces of each material were sterilized with UV radiation and were placed in the media inside an incubator. Finally, cell viability was assessed with Presto blue at day 1 and day 7. Figure 3.3.34 shows the results from the experiment. **RSPU′ (AmMorph)** and **RSPU′ (PropDiol)** proved to be biocompatible within the experiment time scale with more than 70% cell viability. However, **RSPU′ (NMO)** is considered moderately biocompatible with 50% to 70% cell viability after 7 days. Since the sample were cut from the cast film, the

inhomogeneity arises from the phase separation between the samples could results in the large error seen in the graph for day 7.

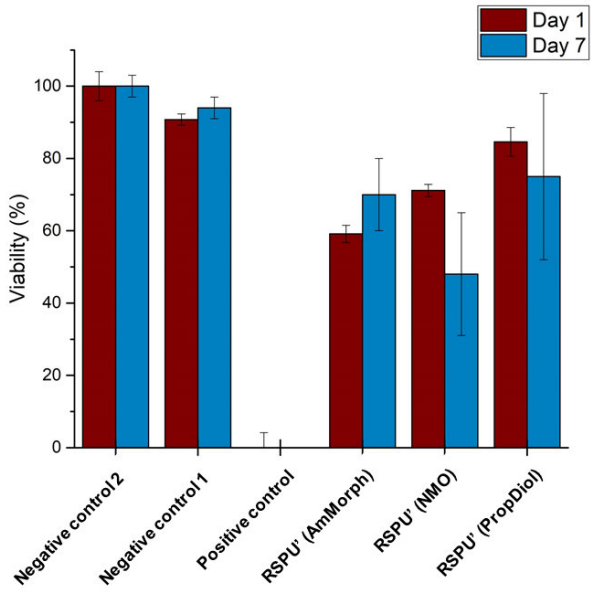


***Figure 3.3.34:*** *The biocompatibility graph of the RSPU's showing the cell viability in contact at day 1 and day 7.*

After the basic investigation of the printing capabilities and properties of these materials, printing of a more complex structure was attempted. This was done in order to examine the printing performance of these materials to generate a complicated 3D structure. To that aim an interlocked 3D structure (Figure 3.3.35) was selected and modified.

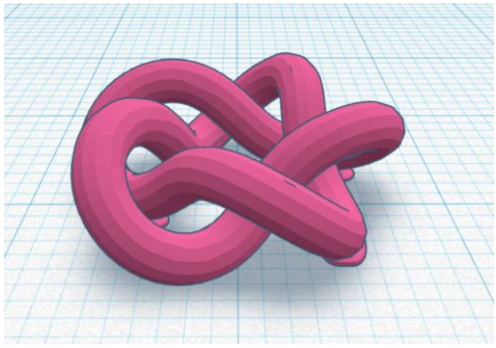

***Figure 3.3.35:*** *The 3D design of the interlocked structure.*

The design file was then loaded input into HeartWare in order to be sliced accordingly and to generate an appropriate GCode to be sent to the 3D printer (Figure 3.3.36). Slicing is defined as the production of the layer-by-layer image of a 3D design along the z axis using the defined printing parameters.

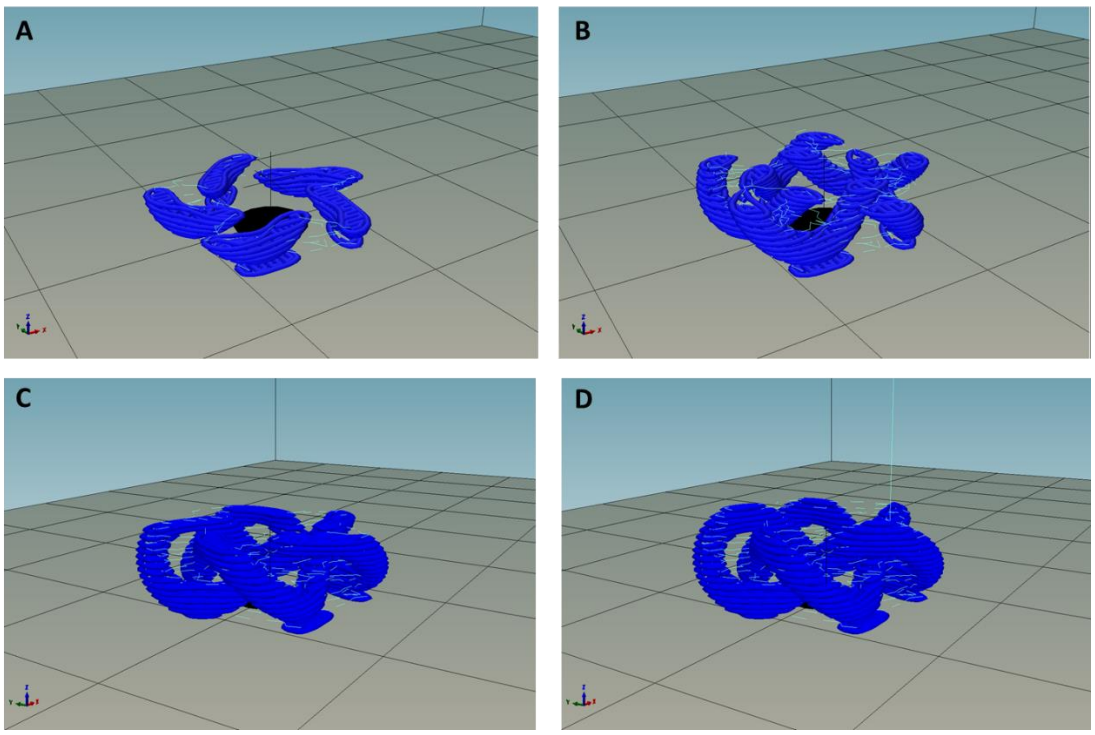


***Figure 3.3.36:*** Images of the sliced 3D image generated in HeartWare. A to D show different layer ranges at different heights.

Figure 3.3.36 C shows the slicing where the bridging happens in this design. Generally, bridges and overhangs are complicated features to be generated by 3D printing. These are the layers that deposited where there is no material underneath it in the previous layer as a support structure. Conventionally, these layers printed on a support structure which needs to be removed upon completion of the print. The removal of the support structure can cause problem in the final finish of the part. It could also result in destruction of the print if it is located near the delicate features of the print. Therefore, recently, development of materials which are capable of holding a shape without sagging (by solidifying quickly after deposition), without requiring support structure, have been seen as desirable.

Herein, the focus of printing the complex structure (Figure 3.3.35) was to examine the ability of **RSPU′s** to print the bridges in this design. Figure 3.3.37 shows the results of printing the complex structure using each different RSPU′s. It can be seen in this figure that encouragingly the **RSPU′ (NMO)** and **RSPU′ (AmMorph)** generated perfect bridges without sagging. In contrast, in the case of **RSPU′ (PropDiol)**, as it is obvious in the bottom image, the bridging is not perfect, and some degree of sagging can be seen near the edge. However, the failure in generating a perfect bridge does not solely result from the material properties. Extra care must be taken in producing the slicing, especially in bridges layers.

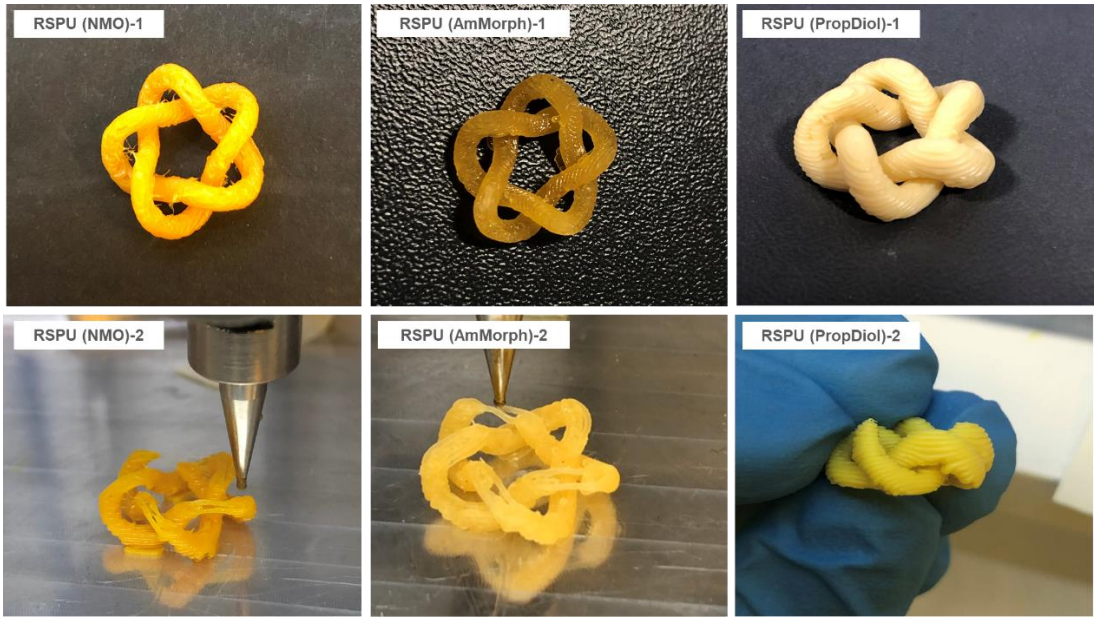


***Figure 3.3.37:*** *Pictures of the printed complex structure with different RSPU's.*

Accordingly, by changing the layer height within the acceptable range, considering the material and the nozzle diameter, the layers may be constructed differently. Figure 3.3.38 illustrates the effect of changing the layer height on the slicing of a 3D design at the bridging height. In this instance, Figure 3.3.38 C generates the best bridging quality in comparison. The red circle in Figure 3.3.38 A indicates the point where sagging is highly likely to appear upon printing. In brief, Figure 3.3.38 A and B were created with the layer height of 0.35 mm and the first layer height of 0.35 and 0.25, respectively. In contrast, the structure shown in Figure 3.3.38 C has the first layer height of 0.35 and 0.30 for subsequent layers.

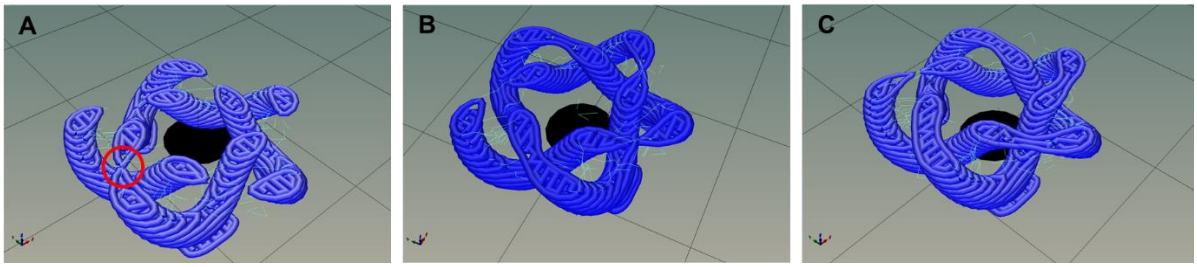


***Figure 3.3.38:*** *Shows the complex structure that is sliced by different layer heights to illustrates the difference in layers shape.*

In conclusion, although all three materials showed promising result in terms of printability, the quality of the structure they formed were different. The printing tracks on the part printed using **RSPU′ (PropDiol)** was the deepest of all three as a result of the high viscosity of the material in melt. However, for the same reason, the ability of the material to print and hold complex structure was higher.

## 3.4 Conclusions

The mechanical strength of an industrially relevant supramolecular polyurethane has been enhanced using low molecular weight additives. Using a facile and accessible methodology, the bis-urea additive **3.2** was synthesised *in situ* and can cooperatively self-assemble with the thermally addressable supramolecular network via complementary hydrogen bonding interactions. Furthermore, the polymers can be prepared without the need for complex purification or blending. By the addition of as little as 8 wt% of the LMWA **3.2 (AmMorph)**, a significant increase in both the Young's modulus and ultimate tensile strength is achieved, 840 % and 230 %, respectively, when compared to the phase separated pristine polyurethane **3.1 (AmMorph)** in addition to retention of the modulus of toughness. Furthermore, increasing the loading of the additive **3.2 (AmMorph)** continues to improve these properties up to a loading of 15 wt%. Additionally, additive loadings of 21 wt% gave rise to an increasingly stiff but brittle material which was difficult to handle. A formulation comprising of the additive (15 wt%) blended with the neat polyurethane was also produced to examine the effect of material preparation and filler dispersion within the polymer matrix. The mechanical performance of the reinforced polyurethane formulated by blending was diminished when compared to the analogous polymer with *in situ* generated LMWA **3.2 (AmMorph)**. Finally, the effect of the LMWA **3.2 (AmMorph)** on the healability of the reinforced polyurethanes was examined. Healing was observed in reinforced polyurethanes with up to 15 wt% additive loading, with healing efficiencies in excess of 98 % observed in the case of the Young's modulus. These findings demonstrate a facile, one-pot, purification-less methodology to produce industrially relevant supramolecular polyurethanes with improved physical and mechanical properties when compared to the pristine polymer alone. The method was further validated by exploiting a chiral hydrogen bonding motif with stronger supramolecular interactions. It was shown that, since the strength of assembly of the end-group plays a crucial role in phase separation of the material and hence, the mechanical properties, the percentage of LMWA needed for desirable properties must be optimised. Further development and refinement of polymer blends of this type are required to produce materials which have desirable mechanical properties for real-world applications.

Additionally, a series of *in situ* reinforced materials with optimised content of relative LMWA **3.2** featuring different self-assemble motifs as end-groups was synthesised (**RSPU′**s). The printability and processability of the small library were studied and extrusion of the materials containing end-groups with strong assembly (**UPy**, **BenzAm**) proved impossible within the capability of the extrusion 3D printer. The reproducibility of the prints was studied by printing bars of 5 × 40 × 0.6 mm. These samples were then used to perform mechanical

property analysis of the printed parts and to study the effect of printing on the properties of the reinforced materials. The cell viability of the materials was also measured, and it was shown that they are relatively safe for pharmaceutical/biomedical final applications, however, the content of LMWA seemed to adversely affect the biocompatibility. In addition, the ability of RSPU′s to generate complex structure by extrusion 3D printing without the need of a support structure was also examined and proved promising.

The future work involves producing a drug release profile for each material and to further investigate the application of these materials as a potential excipient for personalised drug release implants.

## 3.5 Experimental

### 3.5.1 Materials and Instrumentation

All reagents and solvents were purchased from Alfa Aesar, Fisher Scientific or Sigma Aldrich with the exception of Krasol HLBH-P 2000 [hydrogenated poly(butadiene)] which was supplied by TOTAL Cray Valley and used as received. Additionally, tetrahydrofuran (THF) was distilled from sodium and benzophenone prior to use. All the materials and characterisation instrumentation used in this Chapter is reported in Chapter 2, Section 2.5, unless otherwise specified.

Rheology analysis of **RSPUs** was performed using an Anton-Paar Physica MCR301 Rheometer, in oscillatory shear. For data collection strain was set to 0.1% and samples were heated at a ramp rate of 2 ˚C/min. Tensile tests were carried out using an AML instruments single column universal tester, equipped with a 1 kN load cell and vise grips. Samples were analysed at a strain rate of 10 $mm.min^{-1}$. Small-Angle X-ray Scattering (SAXS) and Wide-Angle X-ray Scattering (WAXS) experiments were performed on beamline BM26B (DUBBLE) at ESRF, Grenoble, France. Samples, as films, were placed in aluminium DSC pans with mica windows and mounted in a brass block for temperature control. The sample-to-detector (SAXS) distance was 3.9 m, the sample-to-detector (WAXS) distance was 27.9 cm, and the X-ray energy was 12 keV. The $q = 4\pi \sin\theta/\lambda$ range was calibrated using silver behenate. Data processing (background subtraction, radial averaging) was performed using Bubbles software. SAXS data of the RSPU′s was collected for 10 minutes using a copper source (wavelength 1.54 Å) and calibrated the data using silver behenate at 58.3 Å. The powder X-ray diffraction pattern for LMWA **3.2** was collected on a Bruker D8 Advance operating in transmission capillary mode, whilst the data for films of **RSPU (AmMorph)-15%** and **RSPU (AmMorph)-15% (Blend)** were collected on a Bruker D8 Advance operating in reflection flat-plate mode. All data were collected in the range 5-35° 2θ, with a

step size 0.017° and 2 seconds/step count time. Atomic force microscopy (AFM) measurements were conducted using a Dimension FastScan Bio AFM (Bruker Nano Surfaces Division) equipped with a motorised x-y-stage. Measurements were operated with a Nanoscope controller operated in a PeakForce Quantitative NanoMechanics (QNM) mode in air using a silicon tip with a resonant frequency of approximately 150 kHz and a force constant of approximately 6 N/m (RTESPA-150, Bruker Nano Inc.). Rectangular samples (0.5 × 0.5 cm) were glued onto a glass slide and placed on the motorised stage. The microscope was focused onto each sample. The peak force set point, amplitude setpoint, drive amplitude and gains were adjusted during imaging. 5 μm × 5 μm surface area scans were performed on the samples. Gwyddion software (version 2.22) was used for data analysis.

In order to cast films of the reinforced supramolecular polyurethanes (**RSPUs (AmMorph)**), the THF volume was reduced to approximately 30 mL directly after synthesis and the solution was poured into a 150 mm ×150 mm PTFE mould. In the case of SPU **3.1 (AmMorph)**, the purified solution was dissolved in THF (30 mL) and poured into a 150 mm ×150 mm PTFE mould. All films were left at room temperature for 2 hours before drying overnight in an oven at 70 °C under reduced pressure.

### 3.5.2 Synthesis of Supramolecular Polyurethane 3.1 (AmMorph)

Hydrogenated poly(butadiene) **2.2**, molecular weight as supplied = 2000 g.mol$^{-1}$, was dried under vacuum in oven at 120 ˚C for 1 hour. In the bulk, hydrogenated poly(butadiene) **2.2** (10.00 g, 5 mmol) was mixed with 4,4′-MDI **2.3** (2.50 g, 10 mmol) at 80˚C under $N_2$ for 3 hours with gentle stirring. The colourless pre-polymer **2.4** thus obtained was then dissolved in dry THF (100 mL) and allowed to cool to room temperature. 4-(2-Aminoethyl)morpholine **3.3** (1.30 g, 10 mmol) was then added to the solution and this was maintained under reflux for 18 hours under $N_2$. The solvent was then removed *in vacuo* and the supramolecular polymer **3.1** purified by dissolving in chloroform (30 mL) and repeated precipitation from methanol (× 3). 10.9 g, 80 %; IR (ATR) (cm$^{-1}$): 3311, 2939, 2921, 2852, 1651, 1599, 1537, 1460, 1413, 1379, 1309, 1220, 1116, 1068; $^1$H NMR (δ; 400 MHz; $CDCl_3$) 7.33-7.04 (20H, *m*), 6.63-6.51 (2H, *br*) 5.32-5.20 (2H, *br*), 4.19-4.12 (4H, *m*), 3.89 (4H, *s*), 3.64 (4H, *m*), 3.33 (2H, *q*, *J* = 5.6), 2.50 (2H, *t*, *J* = 6.0), 2.45 (4H, *m*), 2.07-0.58 (392H, *m*); $^{13}$C NMR (δ; 100 MHz; $CDCl_3$) 156.1, 153.7, 136.5, 136.2, 129.6, 129.4, 121.7, 118.9, 66.9, 57.8, 53.3, 40.6, 38.9, 37.9, 36.1, 33.4, 33.2, 30.7, 30.2, 29.8, 26.8, 25.9, 10.8; GPC (THF) $M_n$ = 9100 g mol$^{-1}$, $M_w$ = 12500 g mol$^{-1}$, Đ = 1.37.

### 3.5.3 Synthesis of LMWA 3.2 (AmMorph)

4,4'-MDI **2.3** (1.00 g, 4.0 mmol) and 4-(2-amino ethyl)morpholine (1.09 g, 8.4 mmol) **3.3** were dissolved in dry THF (40 mL) which was brought to and maintained under reflux under $N_2$ for 3 hours. The resulting white solid was filtered and washed with THF to yield the title compound: 1.97 g, 99 %; $MP_{(DSC)}$ = 184-198 °C; IR (ATR) ($cm^{-1}$) 3302, 1634, 1575, 1514, 1242, 1115, 1007, 913. $^1$H NMR (δ; 400 MHz; DMSO-$d_6$): 8.54 (2H, *s*), 7.28 (4H, *d*, *J* = 8.0 Hz), 7.06 (4H, *d*, *J* = 8.0 Hz), 6.03 (2H, t, *J* = 4.0 Hz), 6.02 (2H, *t*, *J* = 8.0 Hz), 3.76 (2H, *s*), 3.60 (8H, *t*, *J* = 4.0 Hz), 3.20 (4H, *quart*, *J* = 8.0 Hz), 2.38 (12H, *m*); $^{13}$C NMR (δ; 100 MHz; DMSO-$d_6$) 155.1, 138.4, 134.1, 128.7, 117.6, 66.1, 57.8, 53.2, 35.9; ESI-MS: calcd for $M^+$ ($C_{27}H_{39}N_6O_2$): 511.3033 Da, m/z found: 511.3017 Da.

### 3.5.4 Synthesis of Reinforced Supramolecular Polyurethanes (RSPUs) (AmMorph)

All reinforced polyurethanes were synthesised following the procedure for **SPU 3.1 (AmMorph)** (Section 3.5.2) but without purification; the masses and stoichiometry of each reagent used for each RSPU (prepared *in situ*) is shown in Table 3.5.1.

***Table 3.5.1****: Mass of each reagent used in the synthesis of the reinforced supramolecular polymer.*

| **Polyurethane (AmMorph)** | Polymer (**2.2**) (g) | 4,4'-MDI (**2.3**) (g) | End-group (**3.3**) (g) |
|---|---|---|---|
| **SPU 3.1** | 10.00 | 2.38 | 1.25 |
| **RSPU-0%** | 10.00 | 2.38 | 1.25 |
| **RSPU-8%** | 10.00 | 2.98 | 1.87 |
| **RSPU-15%** | 10.00 | 3.57 | 2.50 |
| **RSPU-21%** | 10.00 | 4.17 | 3.12 |

**RSPU (AmMorph)-0%**: 13.63 g, >99%. IR (ATR) ($cm^{-1}$); 3311, 2939, 2921, 2852, 1703, 1651, 1599, 1537, 1513, 1460, 1413, 1379, 1309, 1220, 1116, 1068. $^1$H NMR (δ; 400 MHz; $CDCl_3$) 7.33-7.04 (24H, *m*), 6.63-6.51 (2H, *br*) 5.36-5.20 (2H, *br*), 4.19-4.12 (4H, *m*), 3.89 (4H, *s*), 3.64 (8H, *m*), 3.33 (4H, *q*, *J* = 5.6), 2.50 (4H, *t*, *J* = 6.0), 2.45 (8H, *m*), 2.07-0.58 (371H, *m*); $^{13}$C NMR (δ; 100 MHz; $CDCl_3$) 156.1, 153.7, 136.5, 136.2, 129.6, 129.4, 121.7, 118.9, 66.9, 57.8, 53.3, 40.6, 38.9, 37.9, 36.1, 33.4, 33.2, 30.7, 30.2, 29.8, 26.8, 25.9, 10.8. (DSC) Tg = -45.35 °C. GPC (THF) $M_n$ = 8800 g $mol^{-1}$, $M_w$ = 12450 g $mol^{-1}$, Đ = 1.41.

**RSPU (AmMorph)-8%:** 14.85 g, >99%. IR (ATR) ($cm^{-1}$); 3311, 2939, 2921, 2852, 1703, 1651, 1599, 1537, 1513, 1460, 1413, 1379, 1309, 1220, 1116, 1068. $^1$H NMR (δ; 400 MHz;

$CDCl_3$) 7.33-7.04 (30H, *m*), 6.63-6.51 (2H, *br*) 5.36-5.20 (4H, *br*), 4.19-4.12 (4H, *m*), 3.89 (6H, *s*), 3.64 (13H, *m*), 3.33 (7H, *q*, *J* = 5.6), 2.50 (7H, *t*, *J* = 6.0), 2.45 (13H, *m*), 2.07-0.58 (398H, *m*); $^{13}$C NMR (δ; 100 MHz; $CDCl_3$) 156.1, 153.7, 136.5, 136.2, 129.6, 129.4, 121.7, 118.9, 66.9, 57.8, 53.3, 40.6, 38.9, 37.9, 36.1, 33.4, 33.2, 30.7, 30.2, 29.8, 26.8, 25.9, 10.8. (DSC) Tg = -43.66 °C, Tm = 178.00 °C. GPC (THF) $M_n$ = 7800 g mol$^{-1}$, $M_w$ = 10288 g mol$^{-1}$, Đ = 1.31.

**RSPU (AmMorph)-15%:** 16.07 g, >99%. IR (ATR) (cm$^{-1}$); 3311, 2939, 2921, 2852, 1703, 1643, 1588, 1558, 1513, 1460, 1413, 1379, 1309, 1220, 1116, 1068. $^1$H NMR (δ; 400 MHz; $CDCl_3$) 7.33-7.04 (35H, *m*), 6.63-6.51 (2H, *br*) 5.46-5.27 (4H, *br*), 4.19-4.12 (4H, *m*), 3.88 (6H, *s*), 3.64 (18H, *m*), 3.33 (9H, *q*, *J* = 5.6), 2.50 (10H, *t*, *J* = 6.0), 2.45 (17H, *m*), 2.07-0.58 (398H, *m*); $^{13}$C NMR (δ; 100 MHz; $CDCl_3$) 156.1, 153.7, 136.5, 136.2, 129.6, 129.4, 121.7, 118.9, 66.9, 57.8, 53.3, 40.6, 38.9, 37.9, 36.1, 33.4, 33.2, 30.7, 30.2, 29.8, 26.8, 25.9, 10.8. (DSC) Tg = -46.80 °C, Tm = 173.16 °C. GPC (THF) $M_n$ = 7250 g mol$^{-1}$, $M_w$ = 9300 g mol$^{-1}$, Đ = 1.28.

**RSPU (AmMorph)-21%:** 17.29 g, >99%. IR (ATR) (cm$^{-1}$); 3311, 2939, 2921, 2852, 1703, 1643, 1588, 1558, 1513, 1460, 1413, 1379, 1309, 1220, 1116, 1068. $^1$H NMR (δ; 400 MHz; $CDCl_3$) 7.04-7.33 (34H, *m*), 6.51-6.63 (2H, *br*) 5.27-5.46 (4H, *br*), 4.12-4.19 (4H, *m*), 3.89 (7H, *s*), 3.63 (18H, *m*), 3.33 (9H, *q*, *J* = 5.6), 2.50 (10H, *t*, *J* = 6.0), 2.45 (18H, *m*), 0.58-2.07 (403H, *m*); $^{13}$C NMR (δ; 100 MHz; $CDCl_3$) 156.1, 153.7, 136.5, 136.2, 129.6, 129.4, 121.7, 118.9, 66.9, 57.8, 53.3, 40.6, 38.9, 37.9, 36.1, 33.4, 33.2, 30.7, 30.2, 29.8, 26.8, 25.9, 10.8. (DSC) Tg = -46.35 °C, Tm = 171.06 °C. GPC (THF) $M_n$ = 7000 g mol$^{-1}$, $M_w$ = 8650 g mol$^{-1}$, Đ = 1.24

### 3.5.5 Preparation of Blended Reinforced Polyurethane (RSPU(AmMorph)-15% (Blend))

SPU **3.1 (AmMorph)** (8.22 g, 85 wt%) was dissolved in THF (40 mL) followed by the addition of LMWA **3.2 (AmMorph)** (1.46 g, 15 wt%). The mixture was brought to and maintained under reflux for 24 hours while stirred before cooling to room temperature. The solvent volume was reduced, and the blended reinforced polymer was cast from solution. IR (ATR) (cm$^{-1}$); 3311, 2939, 2921, 2852, 1703, 1643, 1588, 1558, 1513, 1460, 1413, 1379, 1309, 1220, 1116, 1068. $^1$H NMR (δ; 400 MHz; $CDCl_3$) 7.33-7.04 (24H, *m*), 6.63-6.51 (2H, *br*) 5.46-5.27 (3H, *br*), 4.19-4.12 (4H, *m*), 3.89 (4H, *s*), 3.64 (9H, *m*), 3.33 (9H, *q*, *J* = 5.6), 2.50 (5H, *t*, *J* = 6.0), 2.45 (17H, *m*), 2.07-0.58 (385H, *m*); $^{13}$C NMR (δ; 100 MHz; $CDCl_3$) 156.1, 153.7, 136.5, 136.2, 129.6, 129.4, 121.7, 118.9, 66.9, 57.8, 53.3, 40.6, 38.9, 37.9, 36.1,

33.4, 33.2, 30.7, 30.2, 29.8, 26.8, 25.9, 10.8. (DSC) Tg = -46.01 °C, Tm = 191.12 °C. GPC (THF) $M_n$ = 8050 g mol$^{-1}$, $M_w$ = 10400 g mol$^{-1}$, Đ = 1.29.

### 3.5.6 Synthesis of SPU 3.1 (PropDiol)

Krasol HLBH-P2000 **2.2** (5.00 g, 2.4 mmol) was dried in oven at 120 °C under reduced pressure for one hour. It was then mixed with 4,4'-MDI **2.3** (1.19 g, 4.8 mmol) under $N_2$ and constant gentle stirring at 80 °C for three hours. The colourless pre-polymer **2.4** was then dissolved in anhydrous THF (50 mL) then left to cool to room temperature. (±)-3-Amino 1,2 propanediol **3.3 (PropDiol)** (0.44 g, 4.8 mmol) was added to the mixture which was then heated to 80 °C and maintained under reflux for 18 hours. The reaction mixture was cooled down and the precipitate removed by centrifugation four times. The remaining cloudy solution was further purified by filtering through Celite™ and washing with THF. The resultant **SPU 3.1 (PropDiol)** was dried under vacuum. A rubbery material obtained: 5.05 g, 76 %; IR (ATR) (cm$^{-1}$): 3326, 2958, 2920, 2852, 1707, 1597, 1524, 1460, 1413, 1379, 1311, 1223, 1070. $^1$H NMR (δ ppm; 400 MHz; $CDCl_3$): 7.28 (14H, *m*), 6.50 (1H, s), 5.39 – 5.10 (2H, *m*), 4.68 (1H, s), 4.15 (4H, dt, J = 12.8, 7.0 Hz), 3.88 (2H, s), 3.78 – 3.28 (3H, *m*), 2.25 – 0.49 (380H, *m*). $^{13}$C NMR (δ ppm; 100 MHz; $CDCl_3$): 129.4, 38.9, 38.4, 36.1, 33.5, 33.3, 30.7, 30.2, 29.8, 29.8, 26.8, 26.6, 26.1, 25.9, 10.9, 10.7. (DSC) $T_g$ = 47 °C, GPC (THF) $M_n$ = 14580 g.mol$^{-1}$, $M_w$ = 32100 g.mol$^{-1}$, Đ = 2.20.

### 3.5.7 Synthesis of RSPU (PropDiol)-15%

Preheated and dried Krasol HLBH-P200 **2.2** (5.00 g, 2.4 mmol) was stirred with 4,4'-MDI **2.3** (1.79 g, 7.2 mmol) for 3 hours at 80 °C under inert atmosphere ($N_2$). The resultant prepolymer was dissolved in anhydrous THF (50 mL) and the mixture was cooled to room temperature. (±)-3-Amino 1,2 propanediol **(PropDiol)** (0.87 g, 9.7 mmol) was added to the mixture which was heated under reflux for 18 hours under nitrogen. Cloudy solution was dried to give a brittle material with a yellow hue. 7.53 g, 98%; $^1$HNMR: Insoluble, IR (ATR) (cm$^{-1}$): 3319, 2958, 2921, 2852, 1632, 1596, 1541, 1512, 1460, 1410, 1305, 1225, 1106, 1067, 1018, 774. (DSC) $T_g$: -48 °C. GPC (THF): insoluble.

### 3.5.8 Synthesis of RSPU′s (R) for 3D printing

All reinforced polyurethanes were synthesised following the procedure for SPU **3.1 (AmMorph)** (Section 3.5.2) but without purification. In brief, Krasol HLBH-P2000 (**2.2**) (15.00g, 1 equivalent) was dried in vacuum oven. Then 4,4′-MDI **2.3** (4.22 g, 2.25equivalent) was added to it and stirred at 80 ˚C for 3 hours. The reaction mixture was dissolved in dry THF (150 mL) and cooled to room temperature. The desired end-capping

group **3.3 (R)** (2.5 equivalent) was then added to the solution and the mixture brought to and maintained under reflux while stirring overnight. Reaction solution was then dried *in vacuo* and solution cast from chloroform. The masses of the **3.3 (R)** used in the reactions are shown in Table 3.5.2.

***Table 3.5.2:*** *Masses of the recognition motifs used in synthesising the RSPU (R).*

| Polyurethane | End-group (**3.3 (R)**) (g) |
|---|---|
| **RSPU (AmMorph)** | 2.44 |
| **RSPU (NMO)** | 5.11 |
| **RSPU (PropDiol)** | 1.71 |
| **RSPU (BenzAm)** | 2.01 |
| **RSPU (Upy)** | 2.35 |

**RSPU′ (AmMorph):** 21.66 g, >99%. IR (ATR) ($cm^{-1}$); 3310, 2960, 2920, 2860, 2850, 1700, 1650, 1600, 1540, 1510, 1460, 1410, 1380, 1310, 1220, 1140, 1120, 1070, 1020, 914, 857, 814, 767, 719. $^{1}$H NMR (δ; 400 MHz; $CDCl_3$) 6.95-7.33 (23H, *m*), 6.52-6.74 (2H, *br*) 5.7 (1H, *br*), 5.5 (1H, *br*), 4.10-4.22 (4H, *m*), 3.88 (3H, *s*), 3.81 (2H, *s*), 3.62 (10H, *m*), 3.33 (6H, *m*), 2.35-2.50 (18H, *m*), 0.57-2.04 (361H, *m*); $^{13}$C NMR (δ; 100 MHz; $CDCl_3$) 156.5, 156.3, 153.8, 136.9, 136.7, 136.4, 136.1, 129.6, 129.4, 121.5, 121.0, 119.0, 66.8, 57.9, 53.4, 40.6, 38.5, 37.9, 36.8, 36.2, 33.5, 33.2, 30.7, 30.2, 29.7, 26.8, 26.6, 26.0, 25.9, 10.9, 10.6. (DSC) Tg = -46.42 °C, GPC (THF) $M_n$ = 8460 $g.mol^{-1}$, $M_w$ = 13016 $g.mol^{-1}$, Đ = 1.54

**RSPU′ (NMO):** 24.33 g, >99%. IR (ATR) ($cm^{-1}$); 3310, 2960, 2920, 2860, 2850, 1710, 1640, 1600, 1510, 1460, 1410, 1380, 1340, 1300, 1230, 1210, 1170, 1110, 1070, 1030, 1020, 969, 945, 834, 814, 767, 735, 721, 719. $^{1}$H NMR (400 MHz, $CDCl_3$) $\delta$ 8.17 (5H, appt.d), 7.50 (5H, appt.d), 6.95-7.32 (30H, *m*), 6.89 (7H, appt.d), 6.48-6.6 (2H, br), 6.36-6.46 (2H, *s*), 4.72 (5H, *s*), 4.46 (5H, *s*), 4.06 - 4.23 (4H, *m*), 3.67-3.92 (15H, *m*), 2.09–0.58 (354H, *m*,). $^{13}$C NMR (δ; 100 MHz; $CDCl_3$) 159.5, 155.9, 147.4, 145.5, 136.6, 136.4, 129.4, 129.2, 128.4, 128.1, 127.9, 123.9, 120.3, 118.9, 114.7, 55.4, 50.6, 40.5, 38.9, 38.4, 36.1, 33.5, 33.2, 30.6, 30.2, 29.7, 26.8, 26.5, 25.8, 10.9, 10.7, (DSC) Tg = -45.65 °C. GPC (THF) $M_n$ = 9450 $g.mol^{-1}$, $M_w$ = 15500 $g.mol^{-1}$, Đ = 1.64

**RSPU′ (PropDiol):** 20.93 g, >99%. IR (ATR) ($cm^{-1}$); 3320, 2940, 2920, 2860, 2850, 1720, 1700, 1630, 1590, 1570, 1520, 1460, 1410, 1380, 1310, 1220, 1200, 1140, 1110, 1060, 1040, 1010, 914, 864, 816, 772, 718. $^{1}$H NMR (δ; 400 MHz; $CDCl_3$) 7.04 – 7.34 (14H, *m*), 6.83 (8H, *br*), 5.02 – 5.35 (1H, *m*), 4.09 – 4.25 (4H, *br*), 3.85 – 3.96 (4H, *m*), 3.78 – 3.28 (3H, *m*),

0.43 – 2.07 (353H, *m*). $^{13}$C NMR (δ; 100 MHz; $CDCl_3$) 130.3, 128.9, 68.8, 68.5, 40.7, 38.9, 38.5, 37.8, 36.1, 33.5, 33.2, 30.7, 30.2, 29.8, 26.8, 26.6, 26.1, 25.8, 10.9, 10.6. (DSC) Tg = -47.03 °C, $T_{m1}$ = -3.8 °C, $T_{m2}$ = 187.0 °C. GPC (THF) $M_n$ = 8380 g.mol$^{-1}$, $M_w$ = 13650 g.mol$^{-1}$, Đ = 1.63

**RSPU′ (BenzAm):** 21.23 g, >99%. IR (ATR) (cm$^{-1}$); 3300, 2940, 2920, 2860, 2850, 1720, 1700, 1630, 1590, 1570, 1520, 1460, 1410, 1380, 1300, 1220, 1200, 1100, 1070, 1020, 912, 856, 814, 769, 745, 718, 696. $^1$H NMR (δ; 400 MHz; $CDCl_3$) 7.04-7.33 (34H, *m*), 6.51-6.63 (2H, *br*) 5.27-5.46 (4H, *br*), 4.12-4.19 (4H, *m*), 3.89 (7H, *s*), 3.63 (18H, *m*), 3.33 (9H, *q*, *J* = 5.6), 2.50 (10H, *t*, *J* = 6.0), 2.45 (18H, *m*), 0.58-2.07 (403H, *m*); $^{13}$C NMR (δ; 100 MHz; $CDCl_3$) 156.1, 153.7, 136.5, 136.2, 129.6, 129.4, 121.7, 118.9, 66.9, 57.8, 53.3, 40.6, 38.9, 37.9, 36.1, 33.4, 33.2, 30.7, 30.2, 29.8, 26.8, 25.9, 10.8. (DSC) Tg = -45.8 °C, $T_m$ = 73.2 °C. GPC (THF) $M_n$ = 8020 g.mol$^{-1}$, $M_w$ = 12260 g mol$^{-1}$, Đ = 1.53.

**RSPU′ (UPy):** 21.23 g, >99%. IR (ATR) (cm$^{-1}$); 3290, 3070, 2910, 2920, 2860, 2850, 1700, 1650, 1580, 1540, 1510, 1460, 1410, 1410, 1380, 1320, 1240, 1220, 1210, 1030, 1020, 962, 913, 857, 809, 763, 762, 735, 718. $^1$H NMR (δ; 400 MHz; $CDCl_3$) 7.37 (3H, *d*), 7.03-7.22 (8H, *m*), 6.39-6.75 (2H, *br*), 5.99 (1H, *br*), 4.98-5.34 (1H, *m*), 4.06-4.29 (4H, *br*), 3.83-3.99 (3H, *m*), 2.97-3.16 (2H, *d*), 2.36 (3H, *s*), 2.19 (1H, *s*), 0.50-2.08 (370H, *m*). $^{13}$C NMR (δ; 100 MHz; $CDCl_3$) 129.4, 121.04, 40.6, 39.1, 38.8, 38.4, 37.9, 36.1, 33.5, 33.2, 30.7, 30.2, 29.8, 26.8, 26.6, 26.4, 26.0, 25.9, 20.3, 19.2, 10.9, 10.6, 10.5. (DSC) Tg = -46.24 °C. GPC (THF): insoluble

### 3.5.9 UV-vis plate reader

Samples of dimension 10 × 10 × 0.6 mm from all three printable reinforced polyurethane material **RSPU′**s were assessed. These samples were then placed in a sample vial containing PBS buffer at pH = 7.4. The sample vials were then put in a water bath at 37 °C and stirred with a magnetic stirrer bar. Aliquots of the samples (500 µL) were taken from each vial daily and replaced with 500 µL fresh buffer solution to keep the volume constant. After 15 days, collected samples were loaded into a quartz plate and loaded into the plate microreader to collect the UV-vis spectra of the samples. Samples loaded onto a Hellma 96ft Quartz plate and loaded into a Tecan Microplate Reader Spark. The absorbance was recorded using the SparkControl software V2.3 and plotted in Excel 365.

## 3.6 References

1 J. W. Steed and J. L. Atwood, *Supramolecular Chemistry*, John Wiley & Sons Ltd, Chichester, Second., 2009.

2 L. Brunsveld, B. J. B. Folmer, E. W. Meijer and R. P. Sijbesma, *Chem. Rev*., 2001, **101**, 4071–4098.

3 S. Burattini, B. W. Greenland, D. Chappell, H. M. Colquhoun and W. Hayes, *Chem. Soc. Rev.*, 2010, **39**, 1973.

4 L. R. Hart, J. L. Harries, B. W. Greenland, H. M. Colquhoun and W. Hayes, *Polym. Chem.*, 2013, **4**, 4860–4870.

5 S. Burattini, H. M. Colquhoun, B. W. Greenland and W. Hayes, in *Supramolecular Chemistry: From Molecules to Nanomaterials*, John Wiley & Sons Ltd., 2012.

6 F. Herbst, D. Döhler, P. Michael and W. H. Binder, *Macromol. Rapid Commun*., 2013, **34**, 203–220.

7 J. Li, C. L. Lewis, D. L. Chen and M. Anthamatten, *Macromolecules*, 2011, **44**, 5336–5343.

8 C. Heinzmann, S. Coulibaly, A. Roulin, G. L. Fiore and C. Weder, *ACS Appl. Mater. Interfaces*, 2014, **6**, 4713–4719.

9 M. W. Urban, *Prog. Polym. Sci*., 2009, **34**, 679–687.

10 J. Li, J. A. Viveros, M. H. Wrue and M. Anthamatten, *Adv. Mater.*, 2007, **19**, 2851–2855.

11 S. Meer, A. Kausar and T. Iqbal, *Polym. Plast. Technol. Eng*., 2016, **55**, 826–861.

12 H. Zheng, J. Zhang, S. Lu, G. Wang and Z. Xu, *Mater. Lett*., 2006, **60**, 1219–1223.

13 L. Jin, H. Wang and Y. Yang, *Compos. Sci. Technol*., 2013, **79**, 58–63.

14 Y. Wang, J. Niu, J. Hou, Z. Wang, J. Wu, G. Meng, Z. Liu and X. Guo, *Polymer (Guildf).*, 2018, **135**, 16–24.

15 S. Hackelbusch, T. Rossow, P. Van Assenbergh and S. Seiffert, *Macromol. Symp.*, 2013, **46**, 6273–6286.

16 P. Katti, K. V. Kundan, S. Kumar and S. Bose, *Polymer (Guildf).*, 2017, **122**, 184–193.

17 J. Fox, J. J. Wie, B. W. Greenland, S. Burattini, W. Hayes, H. M. Colquhoun, M. E. Mackay and S. J. Rowan, *J. Am. Chem. Soc*., 2012, **134**, 5362–5368.

18 F. Lin, R. Wang, L. Liu, B. Li, L. W. Ouyang and W. J. Liu, *Express Polym. Lett*., 2017, **11**, 690–703.

19 V. Kostopoulos, A. Kotrotsos, S. Tsantzalis, P. Tsokanas, T. Loutas and A. W. Bosman, *Compos. Sci. Technol*., 2016, **128**, 84–93.

20 V. Kostopoulos, A. Kotrotsos, A. Baltopoulos, S. Tsantzalis, P. Tsokanas, T. Loutas and A. W. Bosman, *Express Polym. Lett*., 2016, **10**, 914–926.

21 X. Tan, Y. Zhao, M. Shang, G. R. Hamed and L. Jia, *Polymer (Guildf).*, 2017, **122**, 242–248.

22 P. Shokrollahi, H. Mirzadeh, O. A. Scherman and W. T. S. Huck, *J. Biomed. Mater. Res. A*, 2010, **95A**, 209–221.

23 R. Vaiyapuri, B. W. Greenland, H. M. Colquhoun, J. M. Elliott and W. Hayes, *Polym. Chem.*, 2013, **4**, 4902–4909.

24 B. C. Baker, I. German, G. C. Stevens, H. M. Colquhoun and W. Hayes, *RSC Adv*., 2018, **8**, 41445–41453.

25 D. J. Cornwell and D. K. Smith, Mater. *Horizons*, 2015, **2**, 279–293.

26 T. F. A. De Greef, M. M. L. Nieuwenhuizen, R. P. Sijbesma and E. W. Meijer, *J. Org. Chem.*, 2010, **75**, 598–610.

27 B. C. Baker, I. M. German, A. M. Chippindale, C. E. A. McEwan, G. C. Stevens, H. M. Colquhoun and W. Hayes, *Polymer (Guildf).*, 2018, **140**, 1–9.

28 B. C. Baker, C. L. Higgins, D. Ravishankar, H. M. Colquhoun, G. C. Stevens, F. Greco, B. W. Greenland and W. Hayes, *ChemistrySelect*, 2016, **1**, 1641–1649.

29 B. C. Baker, A. L. Acton, G. C. Stevens and W. Hayes, *Tetrahedron*, 2014, **70**, 8303–8311.

30 D. M. Wood, B. W. Greenland, A. L. Acton, F. Rodríguez-Llansola, C. A. Murray, C. J. Cardin, J. F. Miravet, B. Escuder, I. W. Hamley and W. Hayes, *Chem. Eur. J.*, 2012, **18**, 2692–2699.

31 F. Rodríguez-Llansola, B. Escuder, J. F. Miravet, D. Hermida-Merino, I. W. Hamley, C. J. Cardin and W. Hayes, *Chem. Commun.*, 2010, **46**, 7960–7962.

32 A. Feula, X. Tang, I. Giannakopoulos, A. M. Chippindale, I. W. Hamley, F. Greco, C. Paul Buckley, C. R. Siviour and W. Hayes, *Chem. Sci.*, 2016, **7**, 4291–4300.

33 I. Yilgör, E. Yilgör and G. L. Wilkes, *Polymer (Guildf).*, 2015, **58**, A1–A36.

34 I. Yilgor and E. Yilgor, *Polym. Rev.*, 2007, **47**, 487–510.

35 D. Hermida-merino, B. O. Driscoll, L. R. Hart, P. J. F. Harris, H. M. Colquhoun, A. T. Slark, C. Prisacariu, I. W. Hamley and W. Hayes, *Polym. Chem.*, 2018, **9**, 3406–3414.

36 C. Prisacariu, E. Scortanu, I. Stoica, B. Agapie and V. Barboiu, *Polym. J.*, 2011, **43**, 613–620.

37 R. M. Versteegen, R. P. Sijbesma and E. W. Meijer, *Macromolecules*, 2005, **38**, 3176–3184.

38 A. Feula, A. Pethybridge, I. Giannakopoulos, X. Tang, A. Chippindale, C. R. Siviour, C. P. Buckley, I. W. Hamley and W. Hayes, *Macromolecules*, 2015, **48**, 6132–6141.

39 S. Salimi, L. R. Hart, A. Feula, D. Hermida-Merino, A. B. R. Touré, E. A. Kabova, L. Ruiz-Cantu, D. J. Irvine, R. Wildman, K. Shankland and W. Hayes, *Eur. Polym. J.*, 2019, **118**, 88–96.

40 K. A. Houton and A. J. Wilson, *Polym. Int.*, 2014, **64**, 165–173.

41 A. J. Wilson, *Soft Matter*, 2007, **3**, 409–425.

42 S. Sivakova, D. A. Bohnsack, M. E. Mackay, P. Suwanmala and S. J. Rowan, *J. Am. Chem. Soc.*, 2005, **127**, 18202–18211.

43 P. Woodward, A. Clarke, B. W. Greenland, D. Hermida Merino, L. Yates, A. T. Slark, J. F. Miravet and W. Hayes, *Soft Matter*, 2009, **5**, 2000–2010.

44 D. H. Merino, A. Feula, K. Melia, A. T. Slark, I. Giannakopoulos, C. R. Siviour, C. P. Buckley, B. W. Greenland, D. Liu, Y. Gan, P. J. F. Harris, A. M. Chippindale, I. W. Hamley and W. Hayes, *Polymer (Guildf).*, 2016, **107**, 368–378.

45 V. Simic, L. Bouteiller and M. Jalabert, *J. Am. Chem. Soc.*, 2003, **125**, 13148–13154.

46 S. Iqbal, F. Rodríguez-Llansola, B. Escuder, J. F. Miravet, I. Verbruggen and R. Willem, *Soft Matter*, 2010, **6**, 1875–1878.

47 H. Kautz, D. J. M. Van Beek, R. P. Sijbesma and E. W. Meijer, *Macromolecules*, 2006, **39**, 4265–4267.

48 P. Woodward, D. H. Merino, B. W. Greenland, I. W. Hamley, Z. Light, A. T. Slark and W. Hayes, *Macromolecules*, 2010, **43**, 2512–2517.

49 S. Burattini, B. W. Greenland, D. H. Merino, W. Weng, J. Seppala, H. M. Colquhoun, W. Hayes, M. E. Mackay, I. W. Hamley and S. J. Rowan, *J. Am. Chem. Soc*., 2010, **132**, 12051–12058.

50 D. Hermida-Merino, L. R. Hart, P. J. Harris, A. T. Slark, I. W. Hamley and W. Hayes, *Polym. Chem*., 2021, **12**, 16–19.

51 P. Kuzmic, *anal. Biochem*, 1996, **237**, 260–273.

52 K. Melia, B. W. Greenland, D. Hermida-Merino, L. R. Hart, I. W. Hamley, H. M. Colquhoun, A. T. Slark and W. Hayes, *React. Funct. Polym*., 2018, **124**, 156–161.

53 AUTODESK TINKERCAD, https://www.tinkercad.com/, (accessed 8 November 2020).

# Chapter 4

## Additive Manufacturing and physical assessment of a simple structure from a nanocomposite formulation whose composition was graduated across the 3D image in a structured fashion

*Note regarding contributions to this study: The DIC analysis was performed at the University of Oxford with the help of Peihao Song and Aaron Graham under the supervision of Clive Siviour. The printing experiments were done at the centre for additive manufacturing at the University of Nottingham with the help of Yuyang Wu. All other experiments including the design and synthesis of the materials was done by Sara Salimi by the help of Lewis Hart under the supervision of Wayne Hayes.*

### 4.1 Abstract

3D Printing techniques such as inkjet or reactive extrusion printing potentially offer the ability to control the formulation of composite inks and their mechanical properties in addition to controlling where the ink is actually deposited. In this way, 3D structures can be generated whereby the mechanical properties of the material within that printed image are not uniform across its form. This approach offers route to device generation in which the mechanical properties can be tailored in order to address a specific need. Generation of mechanical gradient polymers (MGPs) offers a new level of functionality to the polymers.[1] MGPs can be defined as a polymeric part within which the mechanical properties change gradually. The advantage of this type of material is that the added functionality can be introduced through the method of production rather than the molecular level. By production of MGP the mechanical properties of the part such as stiffness and flexibility can be tuned along the specimen based on the intended application. Previously, *in situ* production of the bis-urea low molecular weight additive has been proved to be an effective method of reinforcing supramolecular polyurethane which also enables tuning of the mechanical properties by differing the content of LMWA in the system (Chapter 3).[2] By increasing the content of LMWA in the elastomer SPU, material becomes stiffer and less elastomeric. In this Chapter, in order to produce a continuous material featuring different mechanical properties along one axis, a reinforcement method utilising LMWA was combined with the two-component reactive extrusion (REX) 3D printing. The REX printer requires two input materials which are then mix based on a specified ratio prior to deposition. In order to

produce a gradient printed specimen, the input material was selected to be a purified supramolecular polyurethane and a reinforced supramolecular polyurethane with high content of the LMWA. These two materials were then mixed in specified ratios (the ratio was varied during deposition) and a material with a range of mechanical properties was produced. The produced material could potentially be used advantageously in the production of customised skin sensors with higher elasticity and possessing enhanced flexibility at the point of flexion (e.g. knuckle and finger joints) offering improved durability and higher precision in detection of the strain point.

## 4.2 Introduction

Supramolecular polymeric materials offer a broad range of mechanical properties based on their structure, molecular weight and the recognition motif.[3] The improvement in the mechanical properties of these materials can be achieved through different methods such as introduction of inorganic/organic fillers[2,4] or incorporation of a UV curable motif in order to add a secondary reinforcing covalent network.[5] However, much effort has been focused on producing a material with enhanced uniform properties without weak points which promptly fracture or fail mechanically upon applicant of force/stress. Therefore, considerable effort has been expended on the improvement of the dispersion of the filler within the matrix by a wide variety of different methods *e.g.* surface functionalisation in order to promote uniformity and avoid aggregation.[6]

Recently a new inspired-by-nature design has found its way into materials chemistry in which the composition changes gradually along the sample. The most famous instance of a gradient material in nature are squid beaks[7] and byssus threads.[8] These threads' role is to attach the mussel to rocks in order to prevent its movement by the water flow. Therefore, in order to minimise the energy imposed to the animal's body these threads are stiffer at the ends and more flexible (lower Young's modulus) where it is connected to the mussels soft body tissue.[9] Mechanical gradient polymers describe as a new approach to produce shapes and parts with differing mechanical properties within its structure which can be produced by controlled changes in the concentration of the reinforcing component. Adopting this approach enables making parts that offer specific failure points,[10] mode of force distribution[10] or cell adhesion[11] based on the design. These materials can offer a broad range of application from artificial skin sensor, security tags[10] *etc.* based on bearing a desired site of function. For instance, a security tag with a brittle section can be produced which would only open/break from the designated point and cannot be resealed.

The gradient within the structure is usually built by varying the degree of crosslinking and therefore, altering the modulus of the material. In brief, introduction of covalent crosslinking results in increasing the stiffness of the materials.[12] Tuning the concentration of crosslinking can be imposed by printing a UV cross-linkable material and optimisation of the UV irradiation (time, power, etc.).[10,13] However, the method requires presence of UV curable motifs which impose difficulties in storing and handling of the material in terms of its oxygen and humidity sensitivity. This issue becomes more challenging when it comes to printing the materials since the printing process involves formulation, loading and deposition of the material prior to curing and the material needs to be protected in all of the production stages. There are 3D printers available which are able to operate under inert atmosphere, the procedure would be more expensive and limiting *e.g.* the size of the confinement.[14] In addition, formulation of the ink is also more practically challenging in this approach *e.g.* use of any organic solvent is limited to anhydrous solvents and the material must be maintained at inert atmosphere for any mixing or mechanical process.

In terms of a design example, for instance, in order to produce an artificial skin or glove for a hand a mechanical gradient material should be 3D printed where the softest material lies in the middle of the fingers or thumb where it could mimic a flexional joint. There has been extensive research into designing appropriate sensor for artificial skins of the humanoid robots, however, these substrates has been left under-studied.[15,16] In fact, the proposed substrates are although functional with suitable mechanical properties, they do not contain much of design in terms of suitability for the real application and the focus has been on developing progressed sensors combining with available polymeric substrate.[17,18] By applying the proposed MGP design to make an artificial skin sensor, the full hand can be covered with the polymeric substrate such that the most elastic and flexible formulation is located at the joints with stiffer materials connecting to these points. Consequently, by placing the sensors within the artificial skin, precise monitoring of hand movements and accurate tracking of the contribution of each joint in production of any single movement would be possible (Figure 4.2.1). A device of this nature would be extremely valuable in applications ranging from haptic rehabilitation devices to space suits.[19,20]

***Figure 4.2.1:*** *An illustration of an artificial skin sensor featuring flexible joints. Image is adapted and modified figure from PowerPoint 3D models library.*

In this chapter, the physical method of reinforcement of a supramolecular polyurethane was investigated in order to produce a gradient design by varying the content of an organic filler in the bulk polymer phase in a controlled manner.[1] As described in Chapter 3 introduction of the corresponding LMWA in a supramolecular polyurethane increases the stiffness and UTS of the material such that too high a concentration of LMWA results in a brittle material from which a continuous malleable film cannot be generated. However, if this high-content reinforced SPU can be mixed with the pristine corresponding SPU in varying ratios to generate materials with adjustable contents of LMWA then 3D printed objects with variable flexibility or stiffness could be produced. Efficient mixing of these materials will be needed to enable production of materials with a range of mechanical properties as a result of the varying concentration of the LMWA. In this project, a customised REX 3D printer based in the Centre for Additive Manufacturing (CfAM) research laboratory at the University of Nottingham was employed to test the ability to mix two materials in well-defined volumetric ratio. The REX 3D printer set-up is shown in Figure 4.2.2.

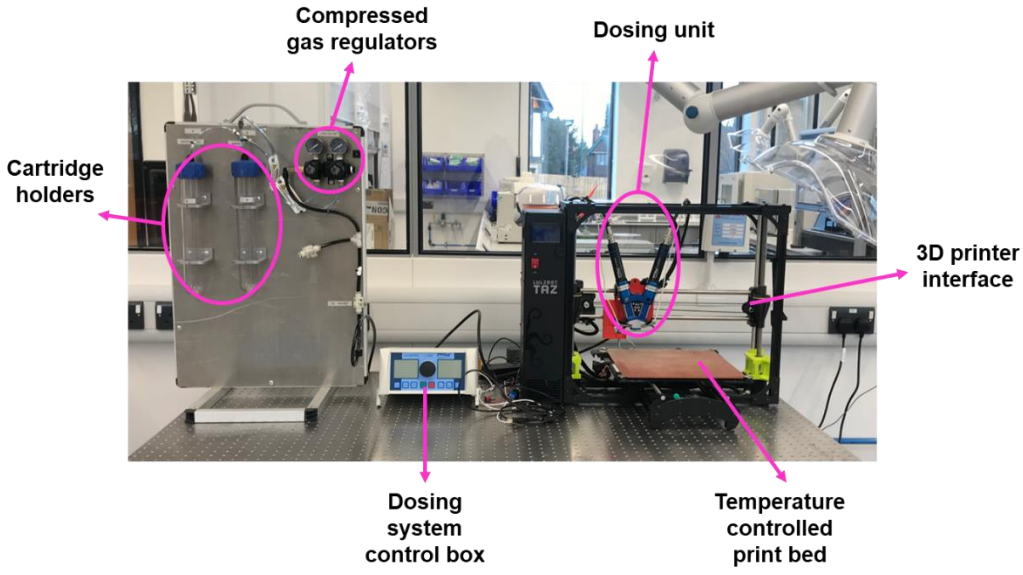


***Figure 4.2.2:*** *Picture of the customised REX 3D printer with specified components.*

As shown in Figure 4.2.2, the prepared inks are secured inside the cartridge holders and connected to a compressed gas line (depending on the ink properties this could either be compressed air or nitrogen) and the regulated pressure from this source pushes the inks to the dosing system. The dosing system shown in the middle of Figure 4.2.2 can be programmed as such that it controls the amount of each ink to be deposited. The dosing unit contains a self-sealing rotor system in each arm and holds a static mixer as the print head. The dosing is not only controlled by compressed gas, but a secondary unit (rotor arm) also controls the dosing amount in a mechanical fashion. The rotor system in each arm which is controlled by the dosing unit determines the amount of ink that passes and enters the mixer (Figure 4.2.3). Additionally, a suckback function was also in place which helps with precision of dosing by preventing any leakage from the nozzle. The inks were mixed in a static Groβ mixer head and subsequently deposited on the print bed. Therefore, by adjusting the ratio of ink A from printhead A to ink B from printhead B during the printing on the dosing unit, a gradient material can be generated in a continuous manner.

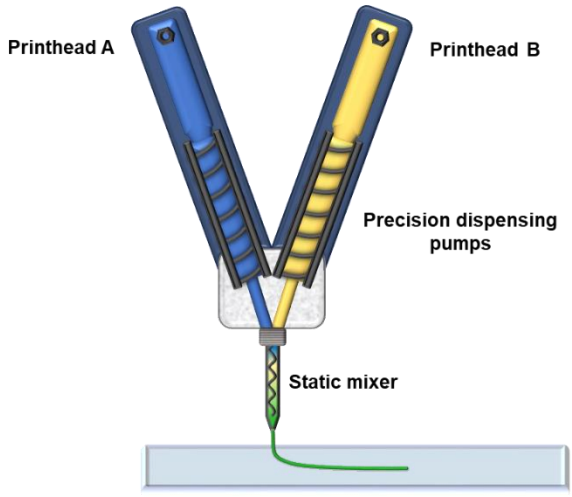


***Figure 4.2.3**: Schematic figure of the mixer of the dosing unit showing the self-sealing rotor system in each arm and the final static Groβ mixer. The rotor system in each arm enables a precise dosing of the material.*

## 4.3 Results and Discussion

### 4.3.1 Synthesis and formulation of polyurethane inks

In order to prepare a material suitable for generating a MGP, **SPU 3.1 (AmMorph)** and its reinforced analogous with known properties was selected. The reinforced analogue material containing 15 wt% of corresponding LMWA (**RSPU (AmMorph)-15%**) was synthesised as the stiffest material which is still capable of forming a film yet is not too brittle to be

manipulated. **SPU 3.1 (AmMorph)** was synthesised as the elastomeric component. The synthesis of the materials used in this Chapter are described in Chapter 3, Section 3.3.1. Scheme 4.3.1 A and B shows the structure of the materials synthesised.

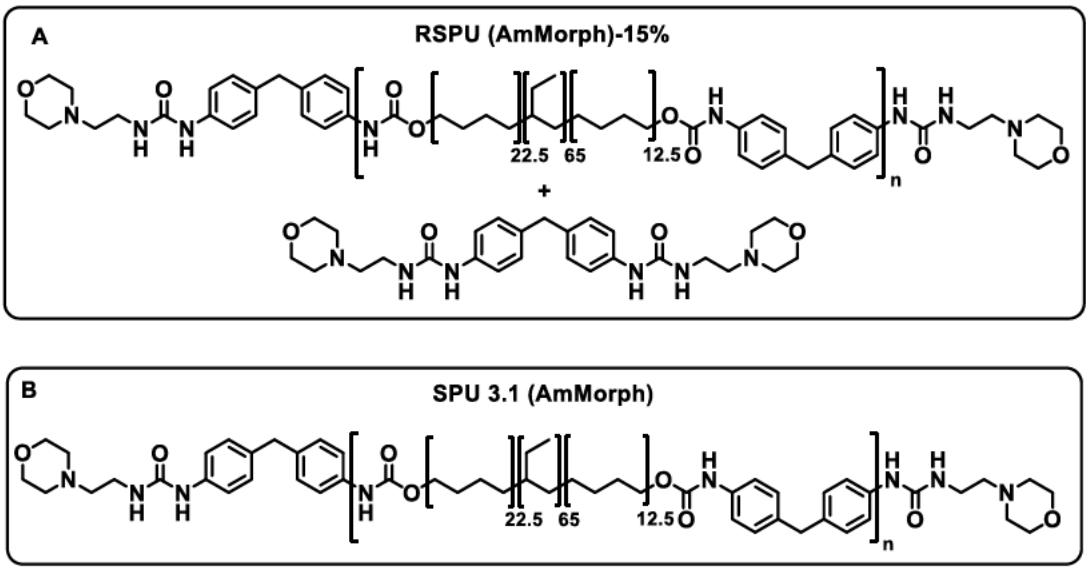


***Scheme 4.3.1**: The chemical structures of the materials used to produce MGP.*

The hypothesis under examination in this study was the use of the REX printer equipped with a dosing unit and a mixer to mix **SPU 3.1 (AmMorph)** and **RSPU (AmMorph)-15%** to generate varied wt% of LMWA in a precise fashion in the formulation and consequently vary the mechanical properties of the 3D object produced by a gradient along one axis. The dosing unit cannot be heated, therefore the material had to be heated in order to be softened otherwise extrusion was not possible. In order to tackle this practical problem, a small volume of ethyl acetate (EtOAc) was used to plasticise the polymers and generate a processable formulation for the printer's setting. In brief, each gram of **SPU 3.1 (AmMorph)** and **RSPU (AmMorph)-15%** was plasticised using 0.4 and 0.5 mL of ethyl acetate, respectively. The solvent was added to the materials and the mixtures left overnight to soften and were then homogenised in a DAC mixer. Figure 4.3.1 shows the change in the physical properties of the material and the consistency of the produced formulated inks.

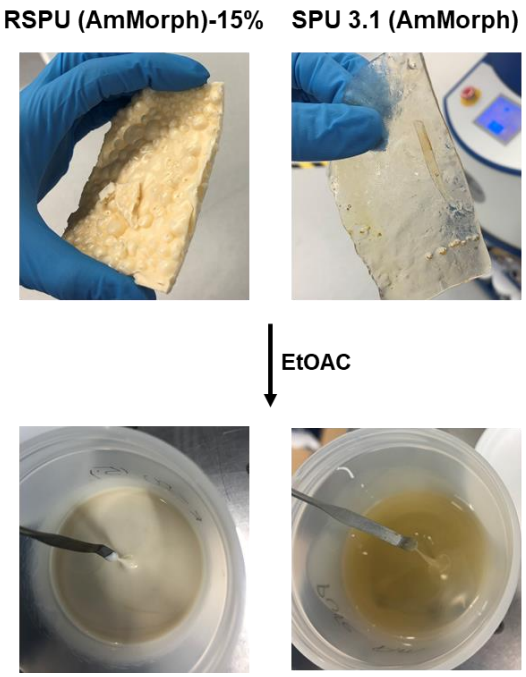


***Figure 4.3.1****: Top images: dried synthesised materials and bottom images: the plasticised inks used to generate MGP.*

It must be noted that, upon formulation of the inks, the container must be kept airtight in order to prevent evaporation of the EtOAc.

### 4.3.2 Physical characterisation of the ink formulations

In order to examine the suitability of the formulated inks for 3D printing, the rheological properties of the inks upon the application of shear during printing process were determined. To that aim, the linear viscoelastic region (LEVR) for each formulation determined and a suitable shear strain (pink point specified in Figure 4.3.2 Top) was selected to perform the next analysis at that constant strain. The oscillatory rheology experiment was carried out on the inks to measure the change in moduli upon application of varying shear stress at constant strain. Figure 4.3.2 bottom shows the result of this experiment. The rheological data revealed that although there is a drop in modulus at high shear stress, the storage and loss modulus did not cross over and therefore the material does not present a yield stress,[21] and thus proved suitable for deposition using a REX printer. Yield stress can be defined as the point at which upon exceeding the shear stress, the structure of the material breaks. Therefore, within the scope of the experiments, the chemical integrity of the ink formulations remains unchanged.

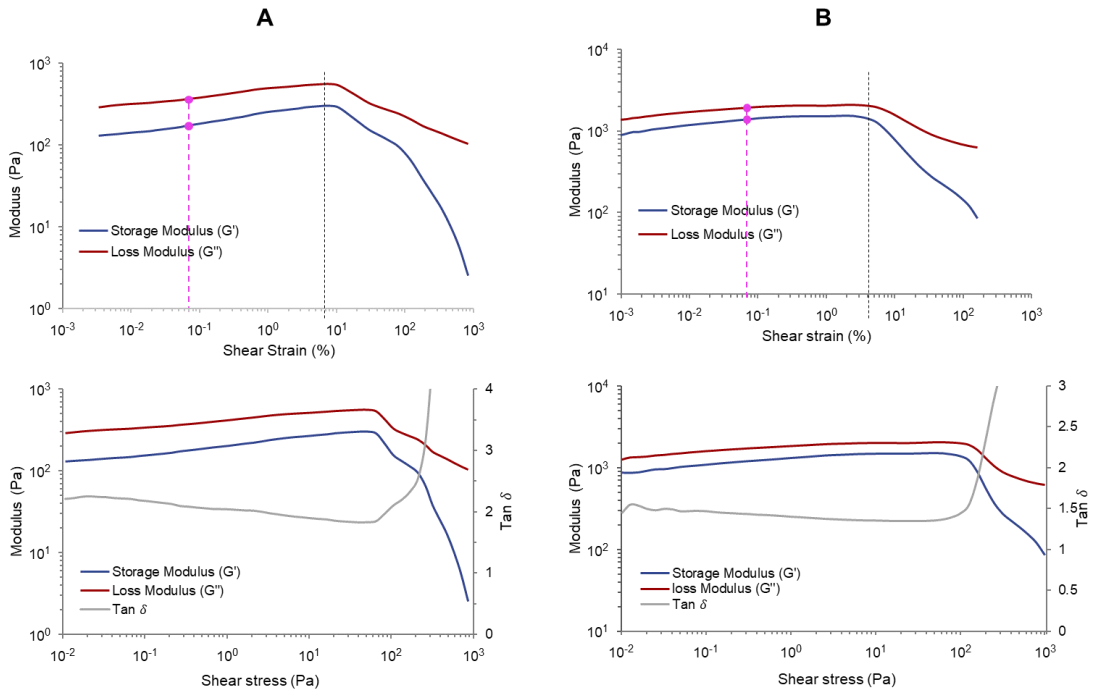


***Figure 4.3.2**: Top: LVER determination and Bottom: changes of modulus by shear stress applied for A) **SPU 3.1 (AmMorph)** B) **RSPU (AmMorph)-15%.***

After performing a short test deposition of the material utilising REX, it was found out that the plasticised SPU inks exhibit some degree of wetting upon deposition on the print bed. One solution to minimise the wetting effect and maintaining the printed structure intact is to heat the print bed moderately in order to increase the solvent evaporation rate. However, if the temperature of the print bed was set too high the material would also soften and deform. To investigate the viscosity profile of the inks upon temperature elevation, another rheological investigation proved beneficial (Figure 4.3.3). The test performed at constant shear rate and it can be seen from the viscosity profile of the inks, by increasing the temperature, the viscosity of the inks decreases. Surprisingly, the decrease is at higher rate at lower temperatures, and it becomes slower, gradually. At lower temperatures, as a result of the presence of solvent the small shear applied by the instrument was able to dissociate the intermolecular interaction which results in steep decrease of the viscosity. The overall decrease of viscosity can be explained by the fact that the dissociation of the supramolecular interactions outweighs the solvent evaporation effect on viscosity of the ink. In addition, the significant effect of dissociation of supramolecular interactions can be observed by comparing the viscosity profiles of **RSPU (AmMorph)-15%** and **SPU 3.1 (AmMorph)**. The drop in viscosity of **RSPU (AmMorph)-15%** is more evident at higher rate since the concentration of supramolecular assembly motif is higher when compared to the pure **SPU 3.1 (AmMorph)**. Consequently, based on these finding, heating the print bed did not prove to be an efficient and practical approach for the prevention of the wetting effect since the material viscosity

decreases at elevated temperatures and deforms. Therefore, attention turned to optimising other print settings to avoid the detrimental deformation.

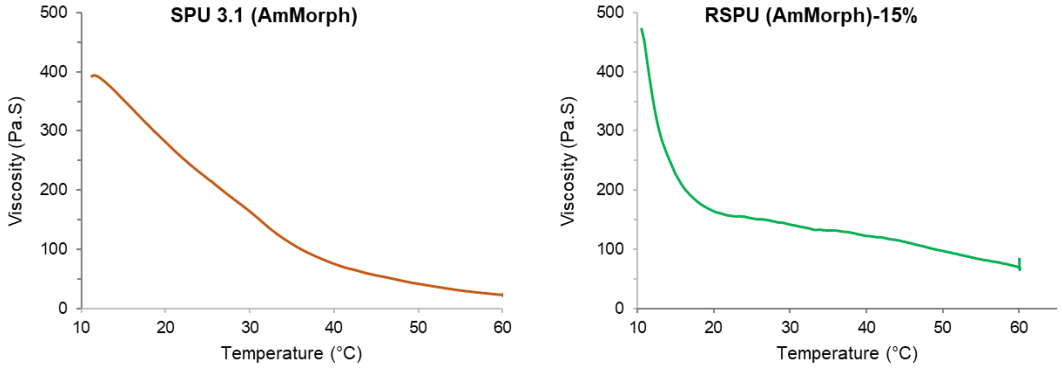


***Figure 4.3.3:*** *The viscosity profile of the plasticised inks vs. temperature.*

### 4.3.3 3D printing of the mechanical gradient part

In order to print a MGP part, a bar shape was selected to be printed with a longitudinal gradient composition. To that aim, the file of the 3D structure of the design in. stl format which is readable by the printer imported into the software v3.6.20 called CURA-Lulzbot. The optimised setting for printing was identified experimentally then based on the given setting (Table 4.3.1), the bar design was sliced in CURA and a layer-by-layer pattern including the printing path was generated.

***Table 4.3.1****: Printing parameters input in CURA for slicing and printing the bar design.*

| Parameters | Infill | Layer thickness | Bed temperature | Nozzle D | Speed |
|---|---|---|---|---|---|
| amount | Zigzag (20%) | 1 mm | RT | 1 mm | 15 mm/s |

A continuous infill pattern was needed to generate a smoother gradient within the part, which means the nozzle has to continuously print rather than printing a line-by-line pattern. Therefore, a zigzag pattern was selected with 20% concentration (a factor of the pattern density) was selected. A value of 20% was found experimentally to be the optimum concentration with minimum line overlap considering the wetting effect outlined above in Section 4.3.2.

The REX printer was controlled via two different system separately, the movement and the dosing unit. The movement of the nozzle is controlled by the CURA software independently from the dosing unit. In fact, the movement of the printhead is controlled by the CURA software and it can be programmed by GCode. However, the amount of material deposition

and its composition is controlled manually by the dosing unit independent from the CURA software. Therefore, it is not possible to include the mixing ratio needed to generate the gradient in the GCode and the printing had to be conducted semi-automatically. To enable alteration of the ratio of the materials while being printed, the movement of the nozzle had to be stopped in place, and after adjusting the molar ratio at the dosing system, printing was then resumed. To that aim, the x and y coordinates of the locations where the feed ratio was changed were thus identified so that the GCode could be modified accordingly *i.e.* the stop points. The primary GCode was generated by slicing the 3D bar design in CURA and it was then modified in Notepad. GCodes is a script which can be modified by simple text editing by addition or removal of commands. However, knowledge of the GCode commands was required. To that purpose, the M0 command was utilised to stop the movement of the printer at the desired coordinates. This command stops the movement of the printhead and waits for the user input to resume the printing. Upon successfully stopping the movement of the print head, the ratio of the feed materials was adjusted on the dosing unit. To clarify, after loading the inks into the mixing heads, the dosing unit was calibrated volumetrically (with respect to each ink formulation) to ensure the production of correct ratio of the materials. This system is capable of producing from 9.00:1.00 to 1.00:1.00 mixing ratios of feed materials A:B.

With the mentioned parameters and features in mind, the 3D bar design was sliced in CURA and the suitable GCode thus generated. Figure 4.3.4 shows an illustration of the generated GCode in CURA (the grey lined shape) as well as the orange lines which determine the coordinates where the M0 command was applied. This figure also indicates the ratios and the corresponding percentages of the **SPU 3.1 (AmMorph)** to **RSPU (AmMorph)-15%** employed in the dosing unit.

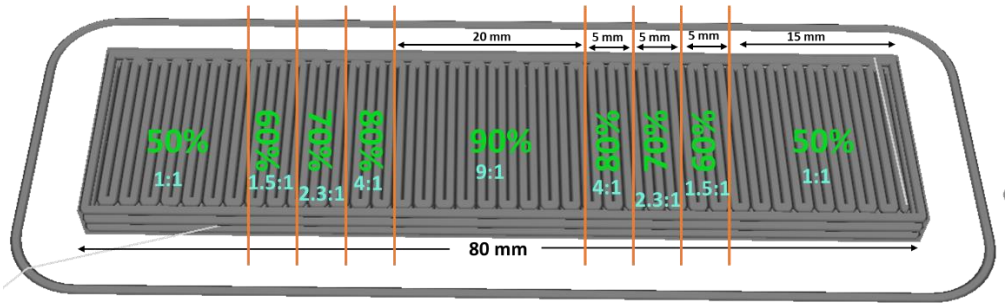


***Figure 4.3.4****: The sliced 3D bar design with CURA illustrating the ratio and percentage of* ***SPU 3.1 (AmMorph)*** *to* ***RSPU (AmMorph)-15%*** *required to generate the desired MGP.*

In addition to optimisation of the printer's setting, the dosing unit parameters had to be optimised. Prior to printing, achieving a steady filament-like withdrawal of the material from the nozzle was necessary. To that aim the dosing unit was also optimised experimentally, and the optimised flow rate speed was found to be 0.8 $mL.min^{-1}$. Additionally, a 0.2 mL of

suckback volume at 3.00 mL.min$^{-1}$ was employed in order to obtain a clean stop at the end of each composition deposition. The modified GCode was then sent to the printer and the skirt and walls were printed at 1.00:1.00 ratio. When the printhead stopped moving by reaching the M0 command, the dosing was paused by the user, a new ratio is set and the nozzle was carefully flushed for two minutes to ensure that the new composition was printed. The movement and dosing were then simultaneously resumed by the user. This process was continued until the printing of the desired object was complete which only takes few minutes. Four bars (80 × 7 × 3 mm) of the MGP were printed following the same procedure in order to provide enough repeats for subsequent mechanical properties analysis. Figure 4.3.5 represents a MGP bar printed with this method. As is evident from the image in Figure 4.3.5, the middle of the bar is composed of softer material (90%) and it gradually becomes less translucent nearer the edges, where the composition is 1:1. The modification of the GCode by M0 command proved to be the most practically effective method, as the layers of each composition has been printed directly on top of each other and as it can be seen in the image, similar compositions have been printed directly on top of each other between layers which illustrates the successful utilisation of M0 command as well as the efficient flushing of the dosing unit.

***Figure 4.3.5:*** *Picture of a printed MGP bar semi-automatically.*

These printed MGP bars were then left at room temperature for 2 days to dry slowly, and it was then put into a vacuum oven at 40 °C overnight to ensure the samples are totally dry for subsequent mechanical analysis. In order to study the difference in mechanical properties of each composition separately, which can be then correlated to mechanical properties of the sections within the MGP bar, 4 bars (40 × 10 × 2 mm) of each composition were printed separately for tensile testing (Figure 4.3.6). The printed bars were dried following the same procedure for the printed MGP bars.

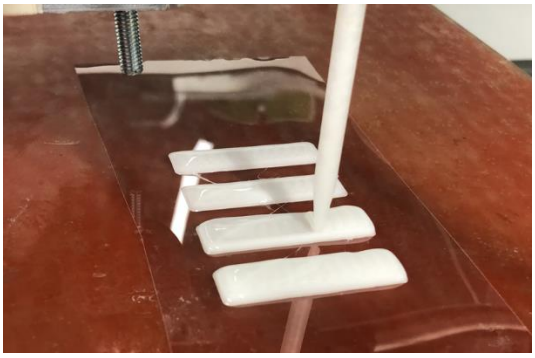

***Figure 4.3.6:*** *4 bars of 80% composition being printed. Same procedure utilised to print every composition used in generation of the MGP.*

### 4.3.4 Mechanical analysis of the printed samples

In order to facilitate handling, drying and storing the printed bars, acetate sheets were placed on the print bed and the bars deposited on it. After drying the printed bars of each composition suitable for tensile testing, they had to be peeled from the acetate sheet. The parts were placed in freezer for a few minutes and they were then peeled from the sheet. However, since EtOAc has a relatively low boiling point (77 °C) and high vapour pressure of (9.70 kPa at 20 °C), it exhibits high specific surface evaporation (9.3 $m.s^{-1}$).[22] As a result of quick evaporation of the organic solvent in ambient condition, bubbles were unfortunately generated within the printed bars, regardless of the effort made to slow down the evaporation.

After peeling the samples, they were subjected to tensile testing. The bars were secured between grips of the tensile testing machine and pulled at the rate of 10 $mm.min^{-1}$. The experiment was repeated three times for each composition while stress *vs.* strain was recorded for each sample. The tensile properties of these bars were calculated based on the data collected and the results are shown in Figure 4.3.7. Regarding the ultimate tensile strength, by increasing the content of **SPU 3.1 (AmMorph)** (which means the ratio of LMWA decreases) a downward trend was observed. Likewise, upon decreasing the content of LMWA, the Young's modulus also decreases which is indicative of an increase in the elastomeric nature of the material. However, interestingly the modulus of toughness remained almost unchanged within the range of error. This can be explained by the decrease in UTS while the elasticity increased upon increasing of the composition percentage. It must be noted that, the relatively big error bars are originated from the fact that the tested specimens did contain a number of small bubbles which led to inconsistency within the tensile properties of these samples.

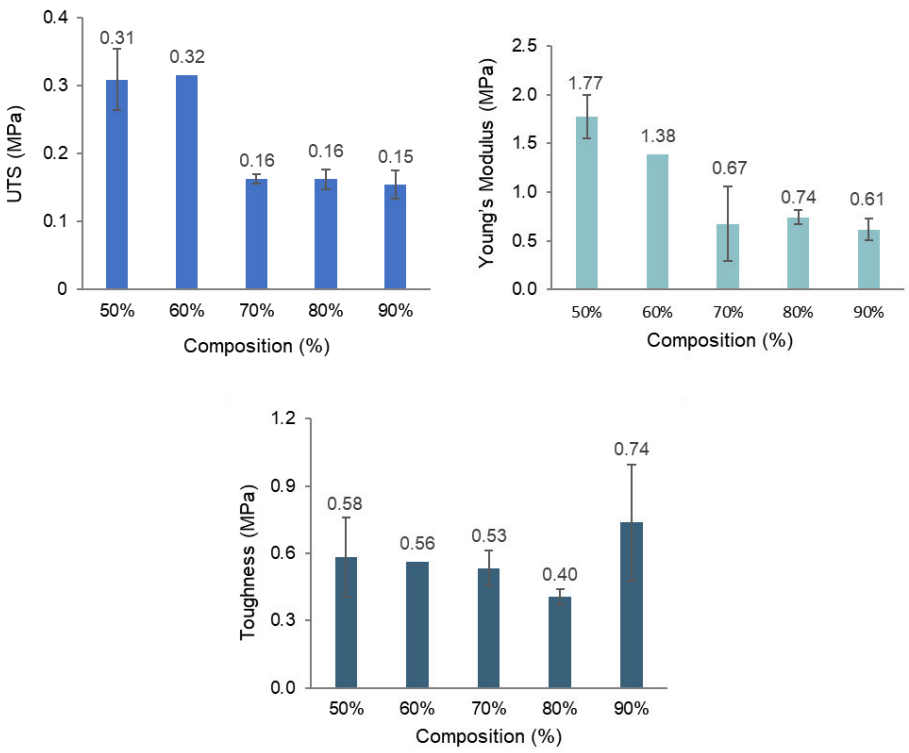


***Figure 4.3.7:*** *Calculated tensile properties of different compositions of SPU* ***3.1 (AmMorph)*** *to* ***RSPU (AmMorph)-15%****. Error bars are standard deviation of three repeat experiments.*

### 4.3.5 Digital image correlation of the printed MGP

After establishing the presence of mechanical properties difference among different composition of the mixed materials, exploring their behaviour within a single sample is interesting. One of the attractive analyses that can be done in this regard is digital image correlation (DIC). This analysis method involves producing speckles on the sample which can be read by a recognition algorithm to follow the displacements and subsequently local strains. Figure 4.3.8 shows a speckled sample of a printed MGP. The speckles produced by airbrushing the sample with paint using mesh against the sample. However, while the speckle size was a highly uniform 3.9 pixel on smooth sections of the specimen, some sections lost correlation early within this test as a consequence of rough surfaces derived from some bubbles in the sample.

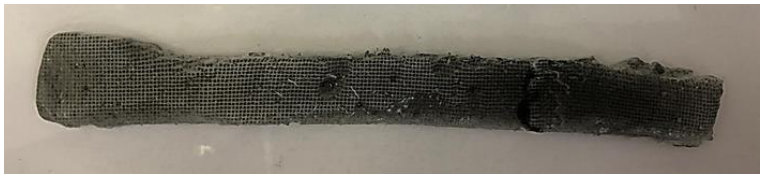

***Figure 4.3.8:*** *Picture of a speckled sample by airbrushing.*

The DIC method can be defined as the measurement of the distribution of the microstrains on the surface of a sample based on the displacement of points in a deformation experiment. These speckles are the points that are to be followed by the algorithm. One advantage of this technique is that it is capable of examining a large surface when compared to other strain measurement methods.[23] Additionally, since the method involves taking photos/videos of the specimen and correlating the movement of the points to strain, a visual understanding of the strain map can also be obtained. To perform the experiment, a speckled specimen was placed between the grips of a tensile test machine equipped with a 1 kN load cell. A Pointgrey camera and two polarised light sources were then directed at the sample. In order to mitigate the effect of reflections, polarised light was used. The light source was polarised at 0°, and a linear polarising filter at 90° was placed over the lens. This eliminated most spectral reflections, reducing glare and improving the quality of the images. Figure 4.3.9 shows the experimental set up (these tests were carried out in the research laboratories of Professor Clive Siviour in the Department of Engineering Science at Oxford University).

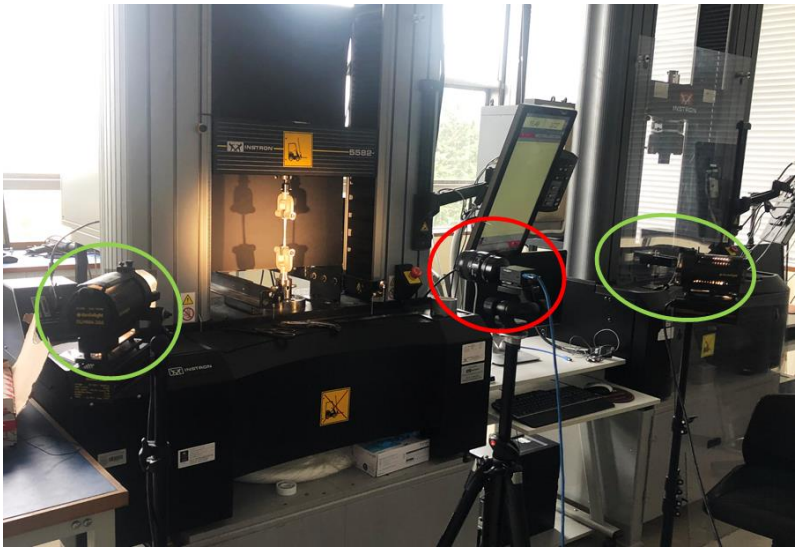

***Figure 4.3.9:*** *Image of the DIC experiment setting. The camera in the middle defined by red circle and two spotlights determined by green circles.*

The camera recording and the tensile tester start simultaneously and the sample was elongated at 20 $mm.min^{-1}$. The pixel to mm ratio was calibrated at the beginning of the experiment and then using the algorithm, the pixels movement was correlated to the strain recorded by the tensile tester. As a result of the large final strains and displacements, the DIC formulation updated the reference with each frame. This resulted in a more robust DIC formulation, but at the cost of slightly higher error. Indeed, DIC normally calculates the displacements for each image relative to the first (reference) image, but the formulation used here calculates the displacement of each image relative to the previous image, and then adds them all up to find the displacement relative to the first image. In practice, this leads to slightly higher noise in

the results, but much more robust processing. Interestingly, it was possible to observe the presence of subsurface bubbles in the light of the effect that they had on the strain field, long before necking or yielding occurred. Figure 4.3.10 illustrates the visual result from the DIC analysis. Each image is taken from the video which was recorded during the tensile test after application of the correlation algorithm. Colours are indicative of the strain tolerated by each section of the printed MGP upon application of stress.

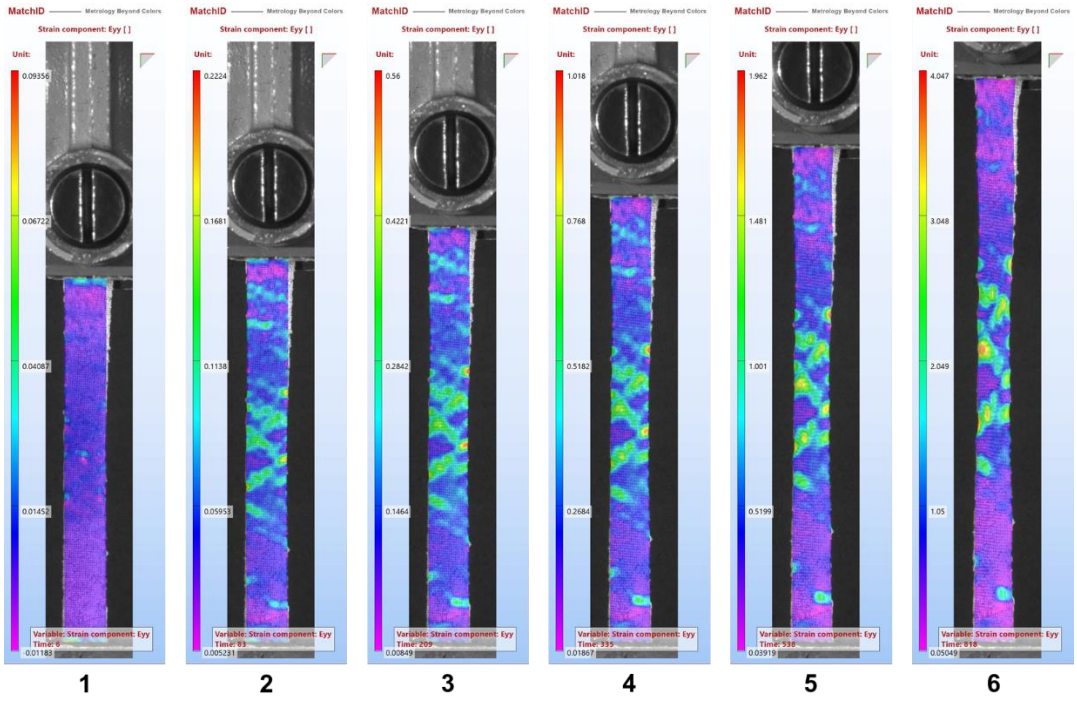


***Figure 4.3.10**: Images of the specimen during a tensile test at time interval after application of the recognition algorithm. Warmer colours indicative of higher strain component (Eyy).*

It can be realised from Figure 4.3.10 that upon application of stress by pulling the sample using the tensile tester, the strain is mainly tolerated by the middle of the sample where there is lower concentration of LMWA and hence the material is more elastomeric. By moving toward top/bottom of the sample, where the composition is 50% of **SPU 3.1 (AmMorph)** and **RSPU (AmMorph)-15%,** the material is relatively stiffer and therefore far less elongated. However, it should be noted that, as mentioned previously, since the specimen contains bubbles, some areas of higher strain can be seen in the stiff regions of the sample.

In order to quantify the findings and examine if the similar composition located in either ends present similar mechanical properties, different points along the sample were selected (located in the middle of each composition section) and their strain screened during the time frame of the tensile experiment. Figure 4.3.11 reveals the changes in strain by time as well as the point selection method.

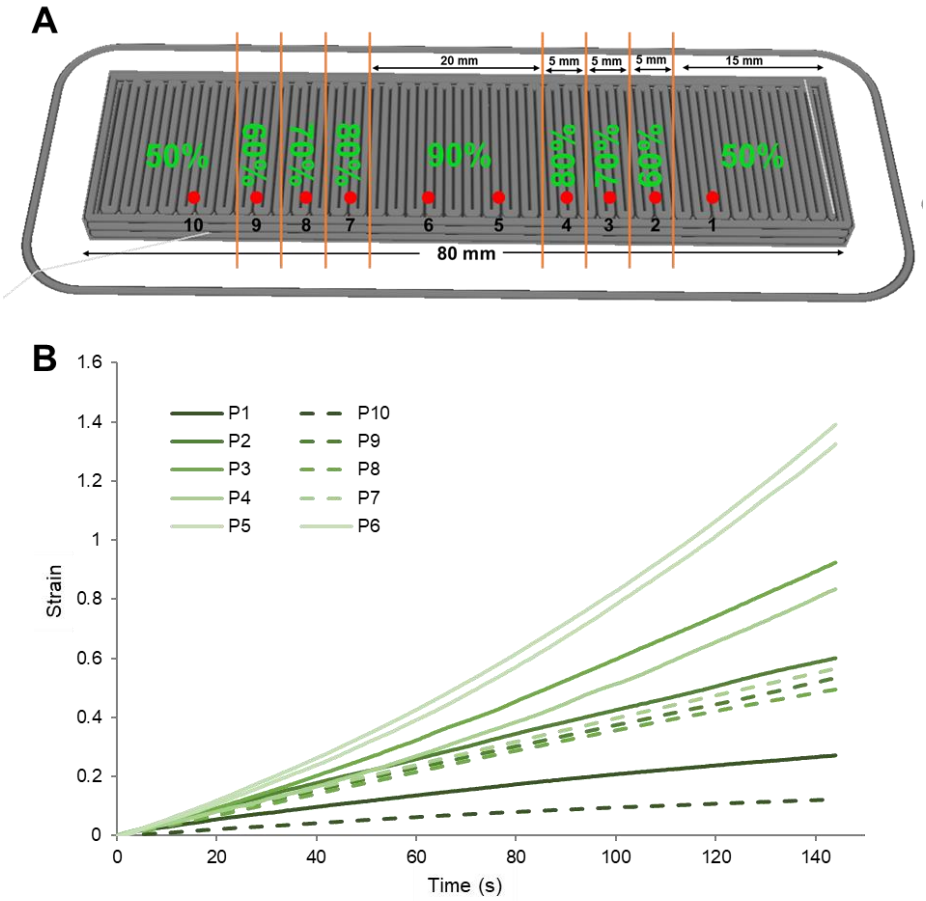


***Figure 4.3.11:*** *A) A schematic representation of the MGP sample representing the location of points selected along the sample to screen the strain changes by time. Each twin points (solid and hashed lines) corresponds to similar compositions. B) the strain vs time graph showing the increase in strain over time.*

Figure 4.3.11 A represents the points at which the strain has been screened. It must be noted that points 1 and 10 were selected because that they are closer to the next composition region taking into account the gripping of the sample into the tensile machine. Twin points which represent the same compositions on either side of the sample were selected to ensure the reproducibility of the composition printing. The strain changes of these points are presented in Figure 4.3.11 B graph with the same colour in solid or hashed lines. The graph represents the first 144 seconds of the experiment since the tensile test features large deformation and the DIC cannot capture such large deformation values. It can be seen that similar compositions exhibit fairly similar strain changes. However, points 3,8 and 4,7 repeats possess big differences which could be explained by the location of one of these points near to a bubble. Overall, the graph follows an expected trends in terms of increase in strain by increasing the ratio of the purified material to the reinforced SPU. For instance, points number 5 and 6 (the middle section of the sample) which represents the highest ratio of **SPU 3.1 (AmMorph)** has the highest rate of change in strain upon elongation of the sample.

## 4.4 Conclusion and future work

Using a combination of REX 3D printer equipped with a dosing system with a static mixer proved to be an efficient approach for the production of a MGP part using reinforced SPUs without the need to UV light. The process of producing an MGP structure can be optimised by considering different factors including the solvent plasticiser, differing the percentages of the LMWA in each composition or other printing parameters. The strain map of the printed MGP bars proved the effectiveness of the overall method by showing the difference in the strain which is sensed by each composition section. Nevertheless, the experiment proved that customised materials with specific local mechanical properties can be 3D printed utilising a precise physical mixing method. Potentially this method can be extended and refined to enable the printing of a customised artificial skin and a subsequent deposition of a conductive sensor ink to generate a specific skin sensor which respond selectively to movement of joints and provide the user with valuable sensory awareness. However, since the dosing unit was only capable of changing the ratio of printhead A to printhead B production of a broader range of compositions was limited . However, this problem can be addressed by swapping the feedstock, nevertheless it would involve wasting too much material as it would require flushing the whole system every time. Longer flush time consequently meant that more material would be wasted which was not feasible within the constraints of this preliminary investigation.

## 4.5 Experimental

All the materials, solvents and characterisation instrumentation used in this Chapter is reported in Chapter 2, Section 2.5, unless otherwise specified below. The material synthesis procedure is also described in detail in Chapter 3, Section 3.5.2 and 3.5.4.

The reactive extrusion printer used in this study was described in detail in Section 5.6.7. The dosing system used was Preeflow™ eco CONTROL EC200 DUO with eco DUE 450 dispenser equipped with a Groβ static mixer set. This dosing system is capable of dosing 1.00:1.00 to 9.00:1.00 mixing ratios. A speed mixer Dual Asymmetric Centrifuge DAC 400.1 mixer FVZ was used to homogenise the plasticiser solvent and the SPUs.

The rheological analysis for determination of LVER and yield stress was carried out using a Kinexus Pro equipped with a 40 mm geometry parallel plate at constant temperature (25 °C) and frequency (5 Hz) and data collected between strain of 0.01% to 1000%. The shear viscosity rheological measurement was performed using an Anton-Paar Physica MCR302

Rheometer, in oscillatory shear equipped with a 25 mm parallel plate geometry and samples were heated at 2 °C.min$^{-1}$.

### 4.5.1 Formulation of the SPU inks

The materials were plasticised using EtOAc, 0.4 mL and 0.5 mL of the solvent was used per gram of material for **SPU3.1 (AmMorph)** and **RSPU (AmMorph)-15%**, respectively. The solvent was added to the polymer in a mixer container and was left overnight. It was then mixed in a DAC mixer for 8 minutes at 2500 rpm which resulted in a paste like ink. Following the loading of the inks into the printer cartridges and the mixer, the dosing unit was calibrated by volume of each material.

### 4.5.2 Printing method

The bar shape 3D design input into CURA-Lulzbot v3.6.20 software and the GCode produced using parameters outlined in Table 4.3.1. The generated GCode was then modified in Notepad by manually adding M0 commands where appropriate. In brief, the sample was printed between X177.5 to X102.5 between Y143.5 to Y136.5. Therefore, the M0 command was applied before coordinates: X164 Y143.5, X159.5 Y136.5, X155 Y143.5, X150.5 Y136.5, X129.5 Y136.5, X125 Y143.5, X120.5 Y136.5, X116 Y143.5 and the same coordinates for subsequent layers. The new GCode was transferred into the printer's SD card to print the MGPs.

### 4.5.3 Digital Image correlation analysis

Specimens were speckled using a black water-based paint and airbrush, with the white background provided by the natural colour of the specimen. The speckle method was employed by pressing a mesh of known pore size up against the specimen before spraying both the mesh and the specimen, and then remove the mesh once the paint has dried. In order to mitigate the effect of reflections, polarised light was used. The light source was polarised at 0°, and a linear polarising filter at 90° was placed over the lens.

A pointGrey camera was used equipped with a 60 mm Nikon lens with a f/4 aperture and field of view 16.9 × 119.4 mm. The speckle feature size was 3.9 pixel per 0.165 mm. Images acquired in 7 Hz rate with 400 × 2824 px resolution in TIF, 16-bit greyscale format (greyscale noise: 0.639%). The acquired images were analysed using MatchID 2D DIC version 2021.1.2 and the analysis parameters are shown in Table 4.5.1. The Green-Lagrange strain was calculated which is better suited for large strains to state how much a displacement differed from the rigid body displacement.

***Table 4.5.1:*** *Detailed DIC analysis parameters.*

| | |
|---|---|
| **Image filtering** | Gaussian filter, 5x5 pixel kernel |
| **Subset size** | 31 pixels/1.31mm |
| **Step size** | 4 pixels/0.169mm |
| **Subset shape function** | Irregular quadrangle |
| **Matching criterion** | Zero-normalised sum of square differences (ZNSSD) |
| **Interpolant** | bi-cubic spline |
| **Strain window** | 11 datapoints |
| **Strain interpolant** | Q8 |
| **Visual strain gauge size** | 71 pixels/3.003mm |
| **Strain formulation** | Green-Lagrange |

## 4.6 References


1 M. Shen and M. B. Bever, *J. Mater. Sci*., 1972, **7**, 741–746.

2 S. Salimi, L. R. Hart, A. Feula, D. Hermida-Merino, A. B. R. Touré, E. A. Kabova, L. Ruiz-Cantu, D. J. Irvine, R. Wildman, K. Shankland and W. Hayes, *Eur. Polym. J*., 2019, **118**, 88–96.

3 P. Woodward, D. H. Merino, B. W. Greenland, I. W. Hamley, Z. Light, A. T. Slark and W. Hayes, *Macromolecules*, 2010, **43**, 2512–2517.

4 D. Pedrazzoli and I. Manas-Zloczower, *Polymer (Guildf)*., 2016, **90**, 256–263.

5 M. Masuda, P. Jonkheijm, R. P. Sijbesma and E. W. Meijer, *J. Am. Chem. Soc*., 2003, **125**, 15935–15940.

6 H. Kim, J. Ko, D. Sohn, J. Ryu, J. Lee and J. Shin, *Colloids Surfaces A Physicochem. Eng. Asp.*, 2016, **511**, 55–63.

7 A. Miserez, T. Schneberk, C. Sun, F. W. Zok and J. H. Waite, *Science*, 2008, **319**, 1816–1819.

8 K. U. Claussen, T. Scheibel, H. W. Schmidt and R. Giesa, Macromol. *Mater. Eng*., 2012, **297**, 938–957.

9 J. E. Smeathers and J. F. V. Vincent, *J. moll. Stud*., 1979, **45**, 219–230.

10 D. Kokkinis, F. Bouville and A. R. Studart, *Adv. Mater*., 2018, **30**, 1–9.

11 R. Sunyer, A. J. Jin, R. Nossal and D. L. Sackett, *PLoS One*, 2012, **7**, e46107.

12 J. Godleman, T. S. Babra, A. Afsar, A. Kyriacou, M. Thompson, J. L. Harries, H. M. Colquhoun and W. Hayes, *Prog. Org. Coatings*, 2021, **151**, 106105.

13 X. F. Yao, D. L. Liu and H. Y. Yeh, *J. Appl. Polym. Sci*., 2007, **106**, 3253–3258.

14 C. Mendes-Felipe, J. Oliveira, I. Etxebarria, J. L. Vilas-Vilela and S. Lanceros-Mendez, *Adv. Mater. Technol*., 2019, **4**, 1–16.

15 G. Cannata, M. Maggiali, G. Metta and G. Sandini, in *IEEE International Conference on Multisensor Fusion and Integration for Intelligent Systems*, 2008, pp. 434–438.

16 T. Someya, T. Sekitani, S. Iba, Y. Kato, H. Kawaguchi and T. Sakurai, in *Proceedings of the National Academy of Sciences of the United States of America*, 2004, vol. 101, pp. 9966–9970.

17 C. Mu, Y. Song, W. Huang, A. Ran, R. Sun, W. Xie and H. Zhang, *Adv. Funct. Mater*., 2018, **28**, 1707503.

18 Y. L. Park, B. R. Chen and R. J. Wood, *IEEE Sens. J.*, 2012, **12**, 2711–2718.

19 W. Sarwar, W. Harwin, B. Janko and G. Bell, *Multi-compliance printing techniques for the fabrication of customisable hand exoskeletons*, IEEE, 2019.

20 R. H. C. Bonser, W. S. Harwin, W. Hayes, G. Jeronimidis, G. R. Mitchell and C. Santulli, *EAP-Based artificial muscles as an alternative to space mechanisms*, 2004.

21 M. Dinkgreve, J. Paredes, M. M. Denn and D. Bonn, *J. Nonnewton. Fluid Mech*., 2016, **238**, 233–241.

22 S. Akterian, *Food Sci. Appl. Biotechnol*., 2020, **3**, 77–84.

23 S. Hensley, M. Christensen, S. Small, D. Archer, E. Lakes and R. Rogge, *Acta Bioeng. Biomech*., 2017, **19**, 187–195.

# Chapter 5

## An Investigation into the Effect of the Incorporation of Silica Nanoparticles on the Mechanical Properties of Supramolecular Materials: – A Comparison of Methods

*Note regarding contributions to this Chapter: Section 5.3.8 discusses the application of the functionalised SiNP in reactive extrusion printing as a reactive rheology modifier filler and is part of a submitted manuscript. This study was completed by Yuyang Wu, Sara Salimi, Zuoxin Zhou, Lewis Hart, Christopher Tuck, Wayne Hayes, Derek Irvine and Ricky Wildman. Yuyang Wu and Zuoxin Zhou performed the printing and mechanical properties analysis of the printed parts under the supervision of Christopher Tuck, Derek Irvine and Ricky Wildman at the University of Nottingham. Sara Salimi carried out the design, synthesis and characterisation of the functionalised SiNP materials under the supervision of Lewis Hart and Wayne Hayes at the University of Reading.*

## 5.1 Abstract

In order to improve the mechanical performance of supramolecular polyurethanes, silica nanoparticle (SiNP) was synthesised and characterised. The synthesised NPs were then blended with a established supramolecular polyurethane (SPU) via two different methods to generate new composites. The synthesised SiNPs were first blended into a solution of the polyurethane of interest using a magnetic stirrer, and in the alternative approach, incorporation of SiNPs into the polymer matrix was achieved by *in situ* mixing with the PU prepolymer during the SPU synthesis. These two approaches were used in order to investigate the effect of the energy involved in the preparation method on the dispersion of SiNP and consequently, the mechanical performance of the material. Additionally, amine functionalised SiNPs (**$H_2N$-SiNP**) were also synthesised using a co-condensation method to introduce a reactive functionality on the surface of the SiNPs in order to covalently incorporate the SiNP within the PU network. However, this proved to be ineffective in a low-shear mixing method (e.g. magnetic stirring) as a result of the high tendency of the particles to aggregate. As a consequence, an alkyl functionality was also introduced on the surface of **$H_2N$-SiNP** to act as a spacer between the amino residues at the particles surfaces and to reduce the possibility of particle agglomeration. Additionally, a different preparation method that involved a higher energy of mixing was utilised to prepare the desired supramolecular silica nanocomposite, *i.e.* a combination of DAC mixing and reactive extrusion 3D printing. The nanocomposite prepared using this method in conjunction with the 'hybrid' **$NH_2$/$CH_3$-SiNP** filler exhibited improved mechanical properties in comparison to the nanocomposite prepared using a SiNP with unreactive surface functionality by providing a hybrid reinforcing effect through formation of intermolecular and intramolecular interaction between the filler and the polymer network. Indeed, the mechanical properties of this new nanocomposite were comparable to a nanocomposite generated using a commercially available silica NP with a PDMS functionality. However, interestingly the mechanical properties of the 3D printing precursor inks of the SiNP with PDMS functionality was superior to those of **$NH_2$/$CH_3$-SiNP**. Furthermore, the dynamic thermoreversible nature of the SPU functionality opens the route in additive manufacturing (AM) field to generate a dual-network nanocomposite by introducing a reactive filler within the polymer network. By introduction of reactive functionality on the surface of the filler, the filler is capable of reacting with the prepolymer during the synthesis and form a second network. In fact, it is the thermoreversible nature of the SPU that makes them suitable for 3D printing as their viscosity drops upon elevating the temperature by dissociation of the intermolecular interactions.

## 5.2 Introduction

Improving the mechanical properties of supramolecular polymers through the introduction of a filler into the bulk phase is of growing interest nowadays[1-3]. Nanocomposites are a type of material that are comprised of an organic polymer which contains a nano (*ca*. nm) scale inorganic filler. A potential advantage of these dual-material systems is the synergistic combination of the attractive characteristics of each component. For example, combining the rigidity and thermal stability of the inorganic fillers with the flexibility and processability of the polymer matrix to achieve elastomeric materials with improved storage moduli is an attractive proposition.[4] Additionally, the incorporation of nanosize filler helps with the dissipation of the energy within the network by increasing the surface area when the material is subject to stress.[5] The distribution and absorption of the induced energy by the nanoparticles results in enhancement of the ultimate tensile strength (UTS) and Young's modulus which are, respectively, representative of the material's strength and flexibility. In these nanocomposite systems, the applied force distributed within the network and subsequently absorbed by the fillers, therefore the deformation of the polymer network would be minimal until the failure of the filler.[5] Therefore, the key parameter is the particles and polymer interphase, at which the energy is transferred into the filler, and is a factor of the particles surface area. However, as a result of the poor interface compatibility between the filler particles and the polymer network, the resulted nanocomposites are usually brittle and less ductile than their parent polymer component. Improvements of mechanical properties of the nanocomposites in relation to the bulk polymer phase characteristics are directly related to the even dispersion of NPs within the polymer. Therefore, avoiding aggregation of filler particles is a key processing parameter in the production of nanocomposites with enhanced physical properties.

Silica nanoparticles (SiNP) are one of the most extensively used nanofiller to generate nanocomposites since they are relatively cheap and, easy to access or synthesize in a variety of morphologies and sizes plus they can be functionalised. In addition, silica nanoparticles have been proven safe to be used in many biomedical applications as they are harmless inside the human body and undergo biodegradation in contact with water and enzymes and produce safe by-products or are eventually excreted.[6,7] In the light of these attributes, there is considerable effort to develop efficient methods to produce silica-based nanocomposites with desirable properties.

Complementary to silica nanoparticles, thermoplastic polyurethanes are among the most widely used polymers, ranging from adhesive and coating to clothes and biomedical industries.[8-12] Therefore, developing and optimising a method to incorporate SiNP within a

polyurethane matrix may be beneficial in order to access a new class of nanocomposite. The most common method of nanocomposites preparation is the post-synthesis blending of the NPs directly with the polymer.[13,14] In this method, the polymeric phase is often dissolved[15] or melted[16] and the NPs are blended with the polymeric phase mechanically, then upon drying or solidification the nanocomposite is formed. However, as a result of high affinity among the NPs and the low energy produce during the preparation by mechanical magnetic stirring, the nanocomposites generate by solution mixing usually presents low level of NP dispersion and high aggregation of the particles is frequently produced within the network. The inorganic fillers also tend to aggregate around the hard polar segments of the polyurethane network and this also serves to disturb efficient dispersion of the NPs. One approach to tackle this aggregation problem is tuning the properties of the surface of the particles with the polymer network. This will reduce the natural tendency of the particles to agglomerate at the hard domain of the polymer and consequently improve the dispersion of NPs within the network. For example, tuning can be achieved through functionalising the surface of SiNP with the polymer chains in which the hydrophobicity/hydrophilicity of the particles are adjusted to that of the polymer network.[17] Additionally, the introduced functionality could be reactive toward the polymer molecules and the particles dispersion within the matrix occurs by forming chemical bonds with the network.[18] The introduction of suitable functional group can be performed through two different methods: i) grafting-to method and ii) co-condensation method. The grafting to method involves initial synthesis of unfunctionalised silica particles prior to introduction of the functionality of interest as a post synthesis process.[19] Alternatively, during the co-condensation method, specific silane coupling agents and tetraethyl orthosilicate (TEOS) are used as precursors and react simultaneously to form the desired functionalised particles.[20]

In this Chapter, a range of SiNPs were synthesised and these were then incorporated into polyurethane network utilising different preparation methods, i.e. solution blending, reactive *in-situ* mixing and reactive extrusion (REX) 3D printing. Solution blending is the most common form of nanocomposite preparation, however, it offers low efficiency. However, upon introduction of reactive functionality on the surface of NPs other preparation methods can also be investigated. In order to introduce the reactive filler NP within the network, they are first magnetically mixed with a solution of the polymer following a conventional synthesis method. Secondly, a REX printer with an automatic and more efficient mixer compared to magnetic stirrer bar is used to incorporate the NPs during the synthesis procedure of the polymer. Each of these afforded nanocomposites are then evaluated in terms of their mechanical and physical properties with respect to the effect of preparation methods on dispersion of the particles within the matrix. In essence, different functionalised particles

were prepared based on suitability for each nanocomposite preparation techniques. In fact, a short chain primary amine was introduced on the surface of the SiNPs as a reactive functional group in order to improve the dispersion by formation of covalent bonds between the NPs and the polyurethane matrix, therefore, improving the mechanical properties of the material through a hybrid reinforcing effect combining physical and covalent crosslink network. Figure 5.2.1 schematically illustrates the difference in the nanocomposites' structures formed from functionalised/unfunctionalised SiNPs.

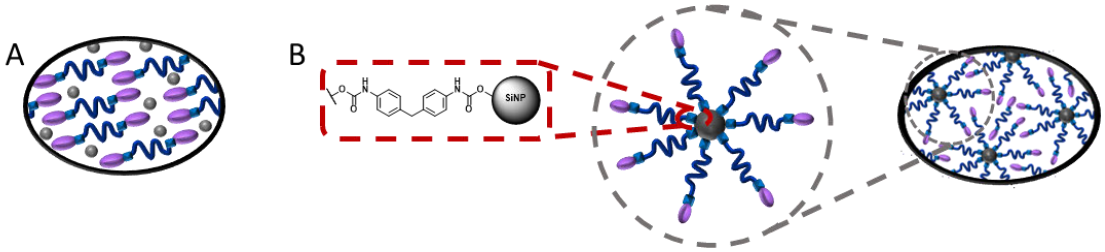


***Figure 5.2.1:*** *The schematic representing the A) nanocomposite prepared by unfunctionalised SiNP using solution blending method and B) prepared nanocomposite by functionalised SiNP exploiting reactive in-situ method.*

## 5.3 Results and discussion

One proposed way to improve the mechanical properties of supramolecular polymers whilst retaining many attractive aspects of these relatively low molecular weight materials (especially their low processing temperatures) is the introduction of inorganic fillers such as SiNP or carbon nanotubes. In this study, in order to study the effect of incorporation of SiNPs on the mechanical properties of SPUs, nanocomposites with varying content of SiNPs were produced. To further optimise the method of preparation of SPU/SiNP nanocomposites, an amine functionalised SiNPs (**$H_2N$-SiNP**) was also synthesised, and the composites were prepared by the *in situ* incorporation of **$H_2N$-SiNP** into the SPU network. Additionally, the **$H_2N$-SiNP were** modified by introduction of alkyl spacer and these SiNP derivatives were utilised in a reactive extrusion (REX) 3D printer to produce a dual-network polyurethane nanocomposite.

### 5.3.1 Synthesis and Characterisations of SiNP

The synthesis of the SiNPs was carried out following a well-established Stöber method.[21] Monodispersed silica particles ranging from 10 nm to 2 μm can be made with this method by adjusting pH of the solution.[14] The Stöber process involves hydrolysis of the orthosilicate of interest followed by its condensation. The condensation could be through production of water or the corresponding alcohol to form the siloxane bridging bonds which are the particles building blocks. Upon reaching the critical concentration, these dimers start to grow and

aggregate to form the particles by generating a 3D network of siloxane bonds (Scheme 5.3.1).[22]

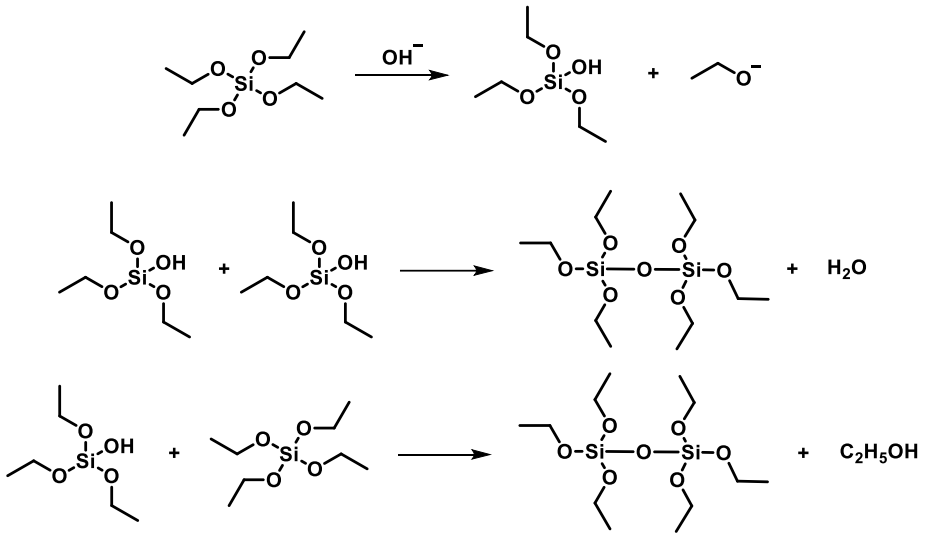


***Scheme 5.3.1:*** *Hydrolysis and condensation steps in the synthesis of SiNP.*

Initially tetraethyl orthosilicate (TEOS) was used to make SiNP in a basic alcoholic solution. Upon formation of the particles, the solvent was removed *in vacuo* and the particles washed with ethanol and centrifuged to remove any unreacted reagents. After drying the particles in a vacuum oven, attention turned to study the morphology of the synthesised nanoparticles (NPs). Initially, the sample was examined under transmission electron microscope (TEM) to analyse the shape and the average size of the synthesised NP (see Figure 5.3.1). TEM images of the synthesised SiNP revealed that the particles have spherical geometry with a relatively uniform size; the graph (Figure 5.3.1 B) represents the size distribution of the synthesised particles indicating their uniformity and standard dispersion in size (mean = 50.28 nm ± 7.40 nm)

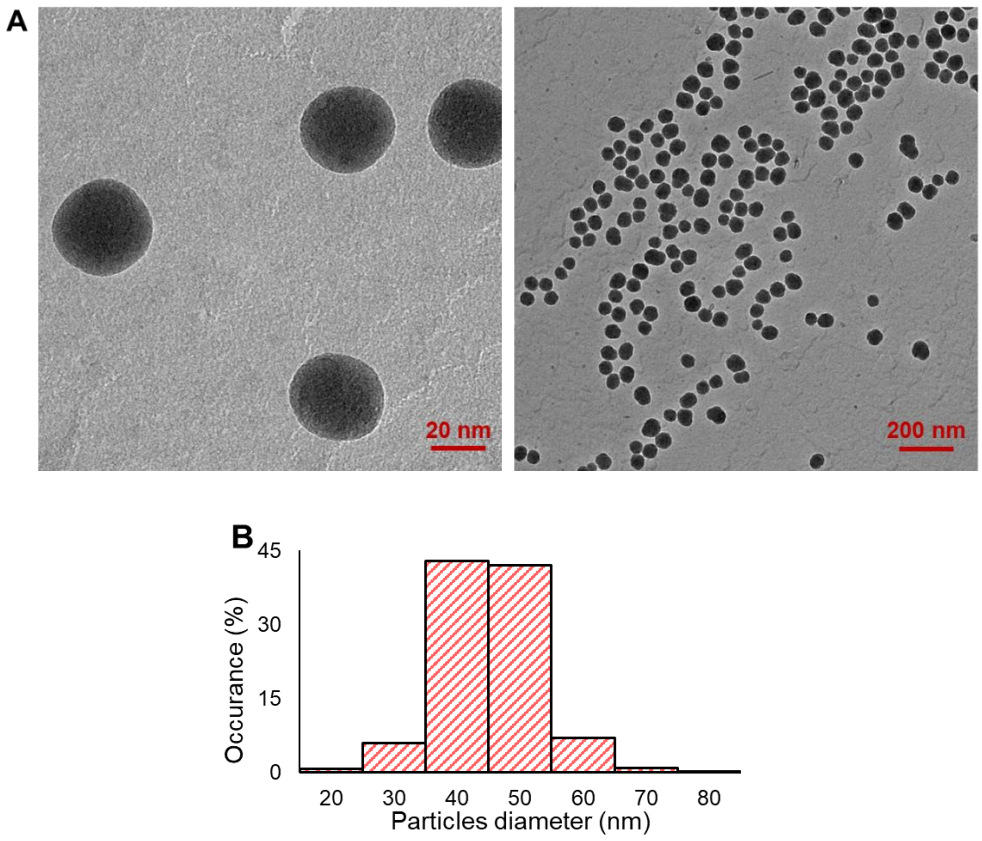


***Figure 5.3.1:*** *A) TEM images of synthesised SiNP with different magnification size and B) The size distribution graph of the particles.*

IR spectroscopic analysis of the SiNP particles was also obtained to examine their composition (see Figure 5.3.2). The small transmittance peak at 2978 $cm^{-1}$ was attributed to the C-H vibration and essentially, indicating the successful hydrolysis of TEOS and removal of the alkoxy groups (Figure 5.3.2 A). Additionally, a broad transmittance peak corresponding to the stretching vibration of -OH on the surface can be seen at *ca.* 3370 $cm^{-1}$. The IR spectrum shown in Figure 5.3.2 B of SiNP focusing on the absorbance bands arising from vibrations of $SiO_2$ which is the building block of the particles. In brief, the absorbance band at 1043 $cm^{-1}$ resulted from the asymmetric vibration of Si-O-Si, meanwhile its bending vibration gives rise to the band at 796 $cm^{-1}$.[23] In addition, the absorbance band observed at 950 $cm^{-1}$ was assigned to silanol (Si-OH) functional groups proving the presence of hydroxyl functional group on the surface of the synthesised NP.[24]

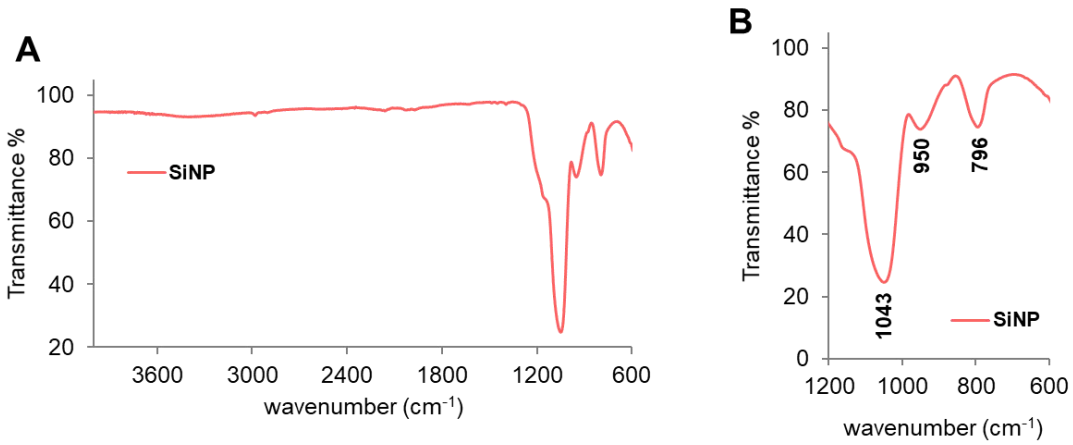


***Figure 5.3.2:*** *A) Full IR spectrum of the synthesised* ***SiNP*** *and B) the transmittance bands arising from $SiO_2$ vibrations.*

After the successful synthesis and characterisation of SiNPs, attention turned to exploiting the particles for nanocomposite preparation and to examine the modification of the mechanical properties of the polymeric material. To that aim, a polyurethane of interest was selected and synthesised in order to be blended with the SiNPs reported in this section.

### 5.3.2 Synthesis of the polyurethane (PU1)

In order to fully understand the variation in the mechanical properties of a parent polyurethane and its analogous silica nanocomposite, a well-studied polyurethane was required. To that end, SPU **3.1 (AmMorph)** that features urea-morpholine end groups that was reported in Chapter 3 was selected.[25] This selection was made since a thorough investigation of the properties, characteristics and morphology of this supramolecular polymer was reported in Chapter 3. Thus, the focus of this Chapter is the study of the effect of using SiNP as an inorganic filler on the mechanical properties of this known supramolecular polyurethane.

The synthesis of SPU **3.1 (AmMorph)** (renamed in this Chapter to **PU1** for the ease of understanding) is reported in Chapter 3, Section 3.3.1 (see Scheme 5.3.2).

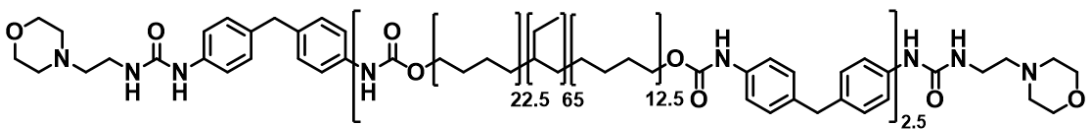


**PU1 ≡ SPU1 ≡ 3.1 (AmMorph)**

***Scheme 5.3.2****: The structure of the supramolecular polyurethane* ***PU1****.*

The synthesised polyurethane was then drop cast from its THF solution into PTFE moulds and dried in a vacuum oven overnight at elevated temperature (40 °C) and reduced pressure (600 mBar). The **PU1** films thus obtained had a thickness of *ca.* 0.5 mm.

### 5.3.3 Preparation of PU1+SiNP nanocomposite

The first nanocomposite samples were prepared as follows: **PU1** was first dissolved in THF. The desired amount of **SiNP** (5 wt%) was dispersed in THF and sonicated for 2 hours to ensure complete dispersal. The resultant **SiNP** suspension was added to the solution of **PU1**, and this mixture was then brought to and held under reflux for 16 hours prior to casting.

Additionally, in order to examine the efficacy and effect of the preparation method on the mechanical properties of the resultant PU nanocomposites, an alternative route to nanocomposite production was investigated. In fact, by taking advantage of the step-wise polymerisation method described in Section 3.3.1 and increased nucleophilicity of the primary amine of the amino-morpholine to end cap the prepolymer *vs.* the silanol groups, **SiNP** was introduced to the system at the end-capping stage. To this aim, the desired amount of **SiNP** was added to the prepolymer solution and refluxed for 1 hour (**PU1+SiNP 5wt%**) prior to the addition of the 4-(2-Aminoethyl)morpholine end-capping group. The resultant polymer nanocomposite was precipitated in methanol and drop cast to form a film suitable for performing mechanical analyses. The nanocomposites prepared by both the solution-mixing and *in situ* mixing methods contained theoretical 5 wt% of the **SiNP**s.

In order to be able to compare the mechanical properties of the two nanocomposites, assessment of the molecular weight characteristics of the polymer component of these blends was necessary. Gel Permeation Chromatography (GPC) was thus used to compare the **PU1** used to prepare the nanocomposites and the molecular weight of the nanocomposite prepared by reaction method (Figure 5.3.3). The analytes are pure synthesised **PU1** in the case of ″PU1 for blend″ and the 5 wt% SiNP composite synthesised *in-situ* in the case of **PU1+SiNP 5wt%**. This is an important parameter since the mechanical properties of polymers are related to their molecular weights. Although the relationship is not fully quantitative, increasing the molecular weight to a certain maximum results in improvement of the mechanical properties of this class of polymer *i.e.* the polymer exhibited a higher tensile strength.[26] In fact, this maximum molecular weight can be defined as the point above which the mechanical properties do not show a meaningful improvement.

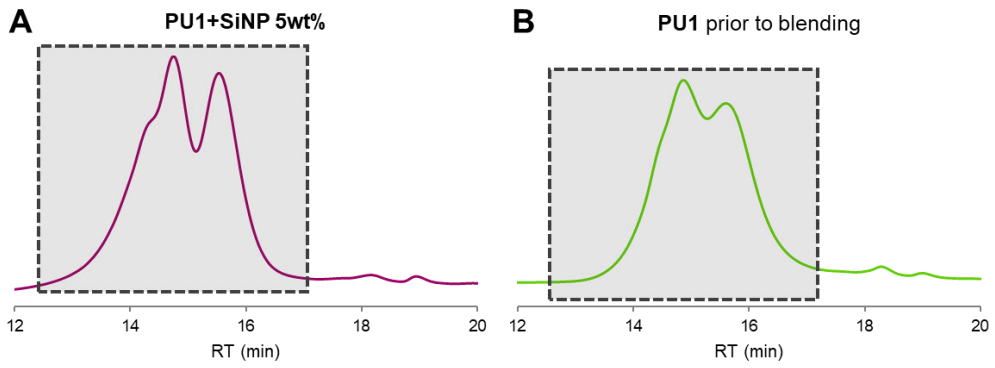


C

| | Mn | Mw | Đ |
|---|---|---|---|
| **PU1+SiNP 5wt%** | 6800 | 11000 | 1.65 |
| **PU1 prior to blending** | 5000 | 8000 | 1.55 |

***Figure 5.3.3:*** *GPC eluograms of the **PU1** prior to composite preparation and the **SiNP** nanocomposite prepared by reaction method. The table represents the molecular weight results from the corresponding analysis.*

The GPC eluograms showed in Figure 5.3.3 were obtained by injection of a solution of each analyte in THF (2 mg.mL$^{-1}$) to the GPC instrument. As evident from Figure 5.3.3, both samples feature bimodal distributions. It was revealed that the molecular weight of the synthesised **PU1** is in good agreement with literature and showed a chain extension of two degrees.[25,27] In the case of **PU1+SiNP 5wt%**, there is a shoulder evident at *ca.* 14 minutes (i.e., a higher molecular weight species) which can be explained by the presence of **SiNPs** within the end-capping reaction mixture. The silanol groups presence on the surface of the NPs can react with the isocyanate end groups of the prepolymer **2.4** and act as a chain extender/branching unit thus increasing the molecular weight of the polymer justifying the molecular weight data presented in Figure 5.3.3 C.

After determining the molecular weight characteristics of **PU1** synthesised for composite preparation, tensile tests were performed on the prepared composite films as well as the parent **PU1** supramolecular polymer. The standard tensile test procedure described in this thesis (see Section 3.5.1) was used for these samples. Samples of dimension 5 mm × 40 mm were cut from the cast films and elongated to break at the rate of 10 mm.min$^{-1}$ using a uniaxial tensile test machine. The recorded stress-stain graphs are shown in Figure 5.3.4.

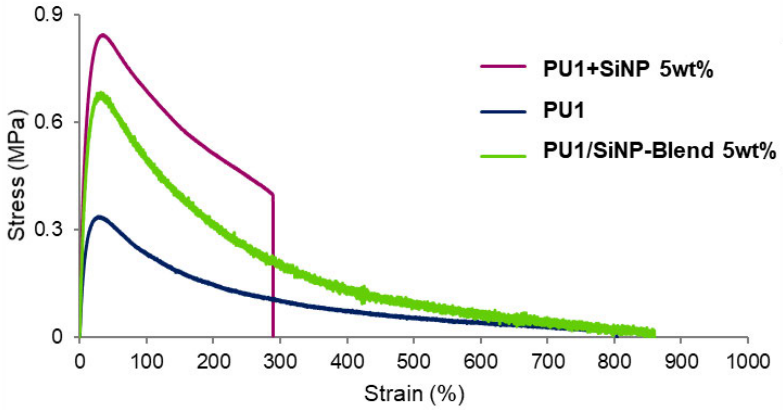


***Figure 5.3.4:*** *Stress-Strain graphs of the parent **PU1** supramolecular polymer and the corresponding composites. Each colour represents a graph from 3 repeat experiments.*

As evident from Figure 5.3.4, the ultimate tensile strength (UTS) for (**PU1**+**SiNP 5wt%**) is substantially improved (an increase of *ca.* 164%) in comparison to the parent **PU1** when SiNPs are introduced during the synthesis of **PU1**. However, the elongation at break was reduced for (**PU1**+**SiNP 5wt%**) when compared to the parent **PU1** and the mechanically blended SiNP composite sample. The tensile test analysis results are summarised in Table 5.3.1. Although the elongation of the **PU1+SiNP 5wt%** was reduced by a factor of 2.5 in comparison to **PU1**, the toughness of the composite increased (by *ca.* 219%) and therefore, the composite is able to absorb more energy before fracturing. Regarding the elasticity of the materials, the Young's Modulus increased in the following order: **PU1** → **PU1/SiNP-Blend 5wt%** → **PU1+SiNP 5wt%** indicating that reinforcement of **PU1** with the SiNPs led to stiffer materials, especially when the SiNPs were incorporated into the end-capping stage of the polyurethane synthesis.

Interestingly, the composite prepared by the two different methods exhibited considerably different tensile properties. In brief, when the **SiNP** is mixed *in-situ* during the synthesis, the mechanical properties of the material are remarkably improved when compared to **PU1**. In conclusion, although post-synthesis blending of SiNP into **PU1** exhibited improvements in mechanical properties, this improvement is more noticeable when SiNP is introduced during the end-capping reaction in tensile properties did not observe when **SiNP** is mixed after synthesis.

***Table 5.3.1:*** *The tensile test properties of the SiNP composites made with different methods.*

| | UTS | Toughness | Young's modulus |
|---|---|---|---|
| **PU1** | 0.33 ± 0.05 | 0.84 ± 0.21 | 3.74 ± 0.30 |
| **PU1/SiNP-Blend 5wt%** | 0.69 ± 0.08 | 1.62 ± 0.07 | 5.59 ± 1.04 |
| **PU1+SiNP 5wt%** | 0.87 ± 0.05 | 1.84 ± 0.65 | 6.21 ± 0.74 |

In order to explain this observation, attention turned to study the dispersion of the **SiNP**s within the nanocomposite matrix. Introduction of **SiNP**s during the end-capping stage of the polyurethane synthesis could enhance dispersion of the NPs as the silanol functional groups could react with the isocyanate end groups from the prepolymer (in effect chain-extending the polymer) and hence secure the **SiNP** position within the polymer network minimising aggregation in any post-synthesis processing. However, the formation of silyl carbamate bond could not be tracked spectroscopically apart from the shoulder that was observed in the GPC eluograms representing the formation of high molecular weight species. In order to study the dispersion of the **SiNP** within the nanocomposite networks, scanning electron microscope (SEM) images of the cross section of the composites obtained (see Figure 5.3.5**:** SEM images of a cross-sectional cut of the composites prepared with two different methods, i.e., **PU1+SiNP 5wt%** (in situ mixing) and **PU1/SiNP-Blend 5wt%** (post-synthesis blend).).

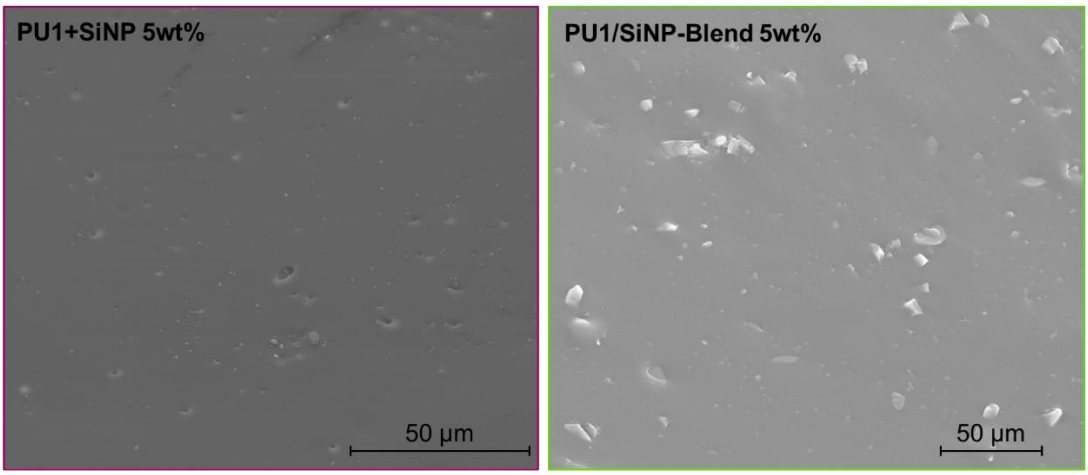


***Figure 5.3.5:*** *SEM images of a cross-sectional cut of the composites prepared with two different methods, i.e.,* ***PU1+SiNP 5wt%*** *(in situ mixing) and* ***PU1/SiNP-Blend 5wt%*** *(post-synthesis blend).*

In order to obtain the desired SEM images, after drying the composites in a vacuum oven, they were transferred to a freezer (-4 °C). Freezing the samples reduced the cutting effect on the imaging surface. The cross-section of the cut samples were then analysed by SEM and the images are shown in Figure 5.3.5. As anticipated, the post-synthesis blended sample (**PU1/SiNP-Blend 5wt%**) featured a poor distribution of the **SiNP**s in the polymer matrix and

the particles aggregated. In contrast, although aggregates of the **SiNP**s were evident in the **PU1+SiNP 5wt%** sample, they were generally smaller and more evenly dispersed within the polymer matrix.

In conclusion, addition of the **SiNP** *in situ* during the synthesis of the supramolecular polyurethane proved to be more effective in improving the mechanical properties of the polyurethane composites. In the light of this finding, functionalisation of **SiNP**s was targeted in order to increase its reactivity toward the isocyanate moieties of the prepolymer. In particular, by introducing of primary alkyl amine groups onto the surface of the **SiNP**s, the particles are more likely to react with the isocyanate of the prepolymer when added *in-situ*. This would secure the location of the particles more evenly within the network and minimise aggregation. Additionally, the formation of the secondary covalent particle-matrix network could improve the mechanical properties of the material.[28] It must also be noted that, over crosslinking of the material could result in formation of a processable material. Also, by introduction of the alkyl amine, the hydrophobicity of the alkyl chain makes them less susceptible to aggregation.

### 5.3.4 Synthesis and Characterisations of $H_2N$-SiNP

In order to study the effect of surface functionality of the silica NPs on the mechanical properties of the composites, silica NPs with surface amine functionality were also synthesised. The mechanical properties of a polymer composite containing inorganic fillers are highly dependent on the dispersion of the particles within the polymer network as well as the particles morphology and its aspect ratio.[20] One approach to improve the dispersion of the silica NPs is to introduce reactive functionality on their surface to induce organic-inorganic crosslinking without compromising the size of the NPs. In order to produce **$H_2N$-SiNP**, a co-condensation method was employed (Scheme 5.3.3). This selection was made since the grafting to method imposed synthetic difficulties during the functionalisation especially upon activating the surface of the already synthesised **SiNP**. Since the grafting to method could destroy the morphology and shape uniformity of the particles, the activation procedure required careful acid/base wash which could partially dissolve and destroy the siloxane bridges of the SiNP core.

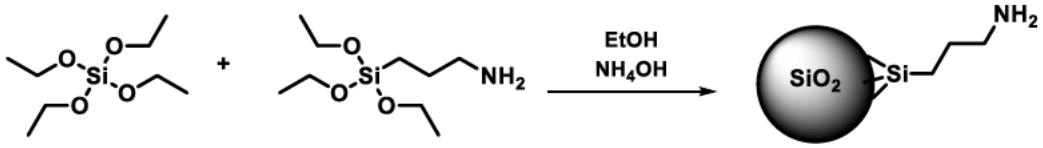


***Scheme 5.3.3:*** *Schematic representing the general co-condensation reaction of TEOS and APTES to generate* ***$H_2N$-SiNP****.*

The co-condensation approach involved utilising TEOS and (3-aminopropyl)triethoxysilane (APTES) in a basic alcoholic solution. In order to characterise the synthesised amine functionalised SiNPs, IR spectroscopic analysis of the particles was used to ensure the introduction of $NH_2$ on the surface of the particles. The IR spectra of **SiNP** and **$H_2$N-SiNP** is compared in Figure 5.3.6 revealing the characteristic stretching absorbance band attributed to the primary amine functional groups. The stretching appeared at *ca.* 1600 and 2900 $cm^{-1}$, respectively, were attributed to NH bending and the C-H stretching of the alkyl chain.

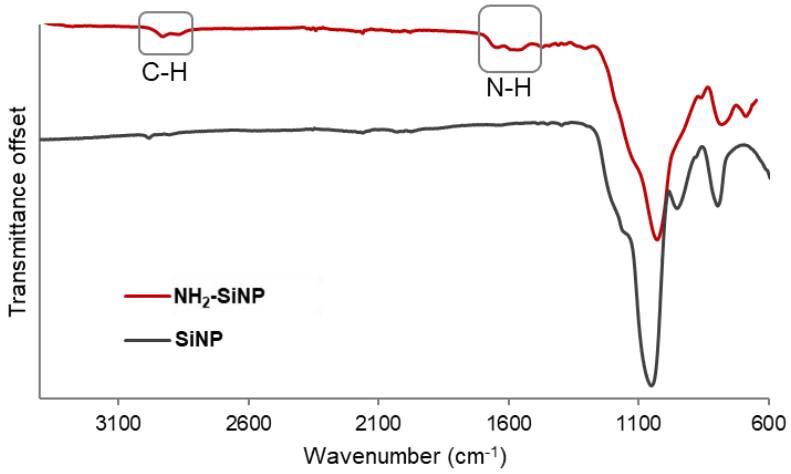


***Figure 5.3.6:*** *IR spectra of the amine- functionalised silica NP (red) in comparison with the unfunctionalised SiNP (grey).*

In order to further prove the successful functionalisation of the synthesised SiNP, $^{29}$Si NMR in solid state was performed using the magic-angle spinning (MAS) technique and the spectrum obtained was compared with that of the SiNP sample. Figure 5.3.7 A illustrates the chemical structures of various types of silica present in the synthesised particles and Figure 5.3.7 B shows the spectra obtained that indicates the presence of propylamine on the surface of the **$H_2$N-SiNP** sample. In the case of the SiNP sample, the dominant type of silica is form $Q^4$ (Figure 5.3.7 A) which is attributed to the core structure of the particles. However, on the surface of the particles the forms $Q^3$ and $Q^2$ are observed which represents the single silanol and geminal silanol groups, respectively.[30] In the case of the $^{29}$Si NMR spectrum of **$H_2$N-SiNP**, the $Q^4$ and $Q^3$ silica species evident, however, the appearance of the $T^3$ and $T^2$ species confirms the presence of the propylamine on the surface of these functionalised particles. Indeed, the presence of the $T^3$ species demonstrates that APTES was fully hydrolysed and also contributes to formation of the SiNP core during the co-condensation method. In addition, the presence of a small percentage of the $T^2$ species reveals that the hydrolysation of APTES could also result in formation of silanol group as well as the propylamine on the surface of the particles.

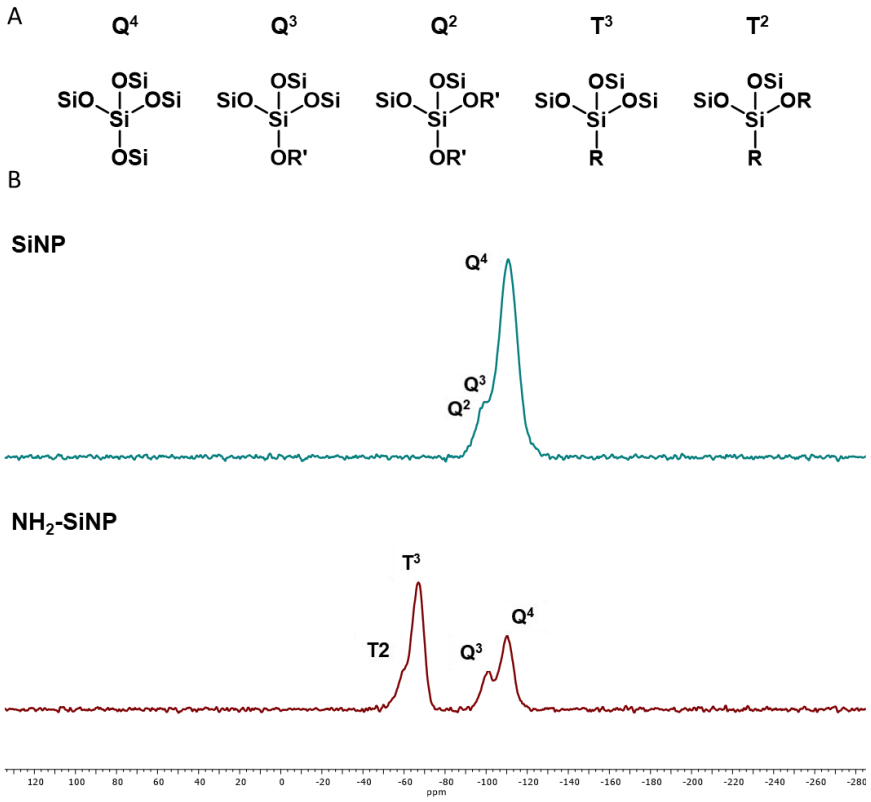


***Figure 5.3.7:*** *A) Chemical structures of types of silica present in the analysed systems (R = $(CH_2)_3NH_2$, R' = H OR Ethyl) and B) Solid state $^{29}Si$ NMR spectra of the synthesised* ***SiNP*** *and* ***$H_2N$-SiNP*** *showing the successful functionalisation of SiNP and validating the method.*

Additionally, the implementation of 1D polarisation method with long recycle delay (30 minutes) in acquiring the spectra enabled integration of the resonances and consequently, calculation of the relative concentration of each silicon species.[31]

***Table 5.3.2****: Relative composition of silicon atoms involves in the formation of the different types of synthesised SiNPs.*

| Sample | $Q^4$ (%) | $Q^3$ (%) | $Q^2$ (%) | $T^3$ (%) | $T^2$ (%) |
|---|---|---|---|---|---|
| **SiNP** | 85.5 | 7.7 | 6.8 | N.D.[a] | N.D.[a] |
| **$H_2N$-SiNP** | 29.6 | 13.0 | N.D.[a] | 48.8 | 8.6 |

[a]N.D. not detected

From the relative composition of different silicon groups shown in Table 5.3.2, it can be noted that the siloxane bridges ($Q^4$) was reduced by more than 2 times upon formation of functionalised NP during the co-condensation of TEOS and APTES (in comparison to condensation of TEOS) but the contribution of surface type silicon groups had increased.

After establishing the successful amination of SiNPs the synthesis procedure was optimised carefully by changing the molar ratios of TEOS to APTES. During the optimisation, the volume of ethanol and ammonium hydroxide was kept constant. The synthesised particles were then characterised to find the optimum reaction condition. Characterisation involved thermogravimetric analysis (TGA) as well as TEM imaging of the samples to study their morphology. Table 5.3.3 summarised the variation in molar ratios of the precursors to synthesise various **$H_2N$-SiNP** for comparison.

***Table 5.3.3:*** *Table showing the molar ratios of the precursors used in co-condensation synthesis of* ***$H_2N$-SiNP*** *as well as unfunctionalised* ***SiNP*** *(Sample 0). The highlighted sample 3 was proved to be the optimum ratios which will be discussed.*

| | Sample number | 0 | 1 | 2 | 3 | 4 | 5 |
|---|---|---|---|---|---|---|---|
| Precursors | TEOS 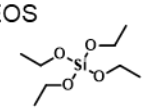 | 1 | 1 | 1 | 1 | 1 | 1 |
| | APTES 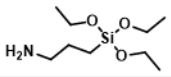 | 0 | 0.5 | 1 | 1.5 | 2 | 2.5 |

To study the morphology of the particles TEM images of the samples were obtained. Figure 5.3.8 shows the images obtained from the particles.

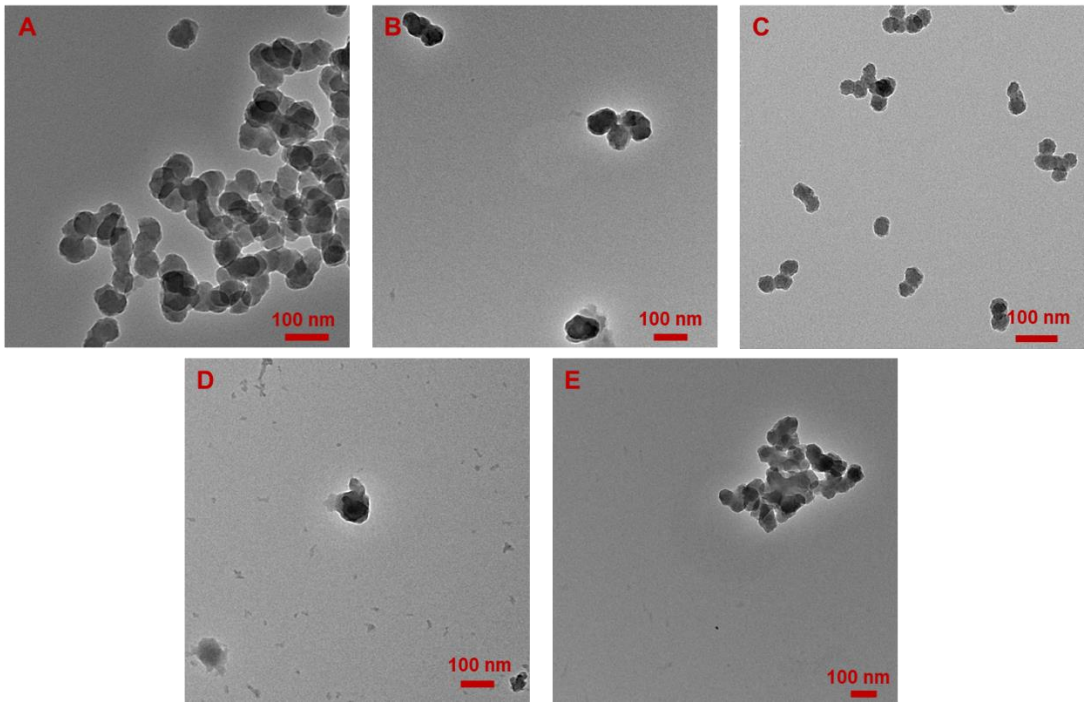


***Figure 5.3.8:*** *TEM images of* ***$H_2N$-SiNP*** *synthesised by varying the stoichiometric ratio of the reagents A to E show* ***$H_2N$-SiNP-01*** *to* ***$H_2N$-SiNP-05*** *in order.*

Upon increasing the content of APTES, the formation of silica gel predominates, this phenomenon was observed in the batches number 4 and 5 in which the formation of discrete spherical particles was not observed. Although the effect of gel formation is visible in TEM images by the irregular shapes of the particles, it is less detectable as a result of grinding the gel network (which produces irregular sized and shaped particles). It is known that upon introduction of amine functionality using silane coupling agents with more than one alkoxy groups, the coupling agent is capable of bridging between two silica particles.[29] The phenomenon was observed especially when the APTES to silica core ratio exceeds a limit (1:200 APTES to silica by weight) and thus an irreversible aggregation occurs.[29]

After introduction of amine functionality on the surface of the SiNPs using different molar ratios, quantifying the functionality was of importance. To this aim, thermogravimetric analysis (TGA) of the synthesised particles were carried out (Figure 5.3.9). The results further approved the introduction of the alkylamine functionality on the surface of the Si nanoparticles by appearance of a degradation at *ca.* 400 °C which is attributed to organic materials. Using this degradation temperature, the amine functionality was quantified in order to find the optimum ratio of the reagents to produce **$H_2$N-SiNP**. The obtained TGA thermograms exhibited a weight loss at around 100 °C with different intensity which is related to the evaporation of the absorbed water on the surface of the particles.

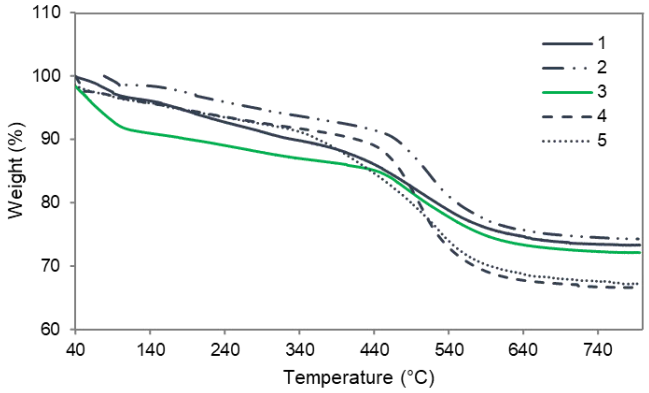


TGA Decomposition

| Sample No. | Organic Decomposition (wt%) |
|---|---|
| 1 | 15.5 |
| 2 | 16.8 |
| 3 | 13.1 |
| 4 | 23.1 |
| 5 | 22.9 |

***Figure 5.3.9:*** *TGA thermograms of the synthesised* ***$H_2$N-SiNP*** *and decomposition weight percentage from the analysis showing the difference in the organic content i.e. the alkylamine functionality.*

Based on the results from the characterisation of the synthesised NPs using varying percentage of reagents, **$H_2$N-SiNP-03** in which the theoretical molar ratio of TEOS:APTES was 1:1.5, was selected as the optimum synthesis condition in this study. The IR spectra of all functionalised samples were similar and proved the introduction of amine functionality when compared to the unfunctionalised SiNPs. The next important factor to consider was the morphology of the particles and the composition of the functionality on the surface of the particles which contribute to the mechanical performance of the composite. As a result of the

high content of APTES in samples number 04 and 05 (where the APTES:TEOS feed was 2:1 and 2.5:1, respectively), a continuous network of silica gel was formed, discrete spherical particles were not isolated. This is evident in the TEM images Figure 5.3.8 D and E, respectively, where the irregular shape of the particles reveals the destruction of continuous silica gel network as a result of the sample preparation method. Therefore, although sample number 4 and 5 showed the highest content of organic component (Figure 5.3.9), their morphology was not suitable for preparation of silica NP/PU composites. In the case of samples number 1, 2 and 3, the difference in organic content obtained from TGA analysis was negligible. However, the morphology of sample number 3 (Figure 5.3.8) was superior to the other two. The particles are for this sample were smaller, less aggregated and possessed smoother spherical shapes. Given these attributes, **$H_2N$-SiNP-03** was selected for the preparation of the SiNP/PU composites (discussed later in this Chapter). After selection of **$H_2N$-SiNP-03** as the optimum synthesis condition and utilising thermal analysis to determine the organic content of the particles, quantification of the amine loading was important for the subsequent composite preparation. Hence, elemental analysis of the synthesised particles was employed to quantify the concentration of the amine (Table 5.3.4). In brief, the elemental analysis determines the wt% of the elements of interest which are carbon, hydrogen and nitrogen in this experiment.

***Table 5.3.4****: Elemental analysis result of* ***$H_2N$-SiNP-03*** *showing the content of each element in 1199.6 µg of the analysed sample.*

| Element | C | H | N |
|---|---|---|---|
| % Found | 13.17 | 3.53 | 4.42 |

The wt% of the nitrogen obtained from each experiment was converted into the number of nitrogen moles present in the unit weight of the analysed sample. Therefore, the concentration of the amine functionality was calculated to be 3.16 $mmol.g^{-1}$ of the **$H_2N$-SiNP-03**. However, the stochiometric calculation to convert the obtained nitrogen moles to the number of hydrogen moles showed a small error which can be contributed to the unhydrolysed ethoxy silane groups remained from the precursors. This claim is further validated by the presence of the similar amount of carbon in the elemental analysis experiment.

Eventually, in order to visualise the presence of the amine functionality on the surface of the **$NH_2$-SiNP-03**, the ninhydrin test was performed.[19] Generation of Ruhemann's blue/purple colour indicates the presence of amine (Scheme 5.3.4).

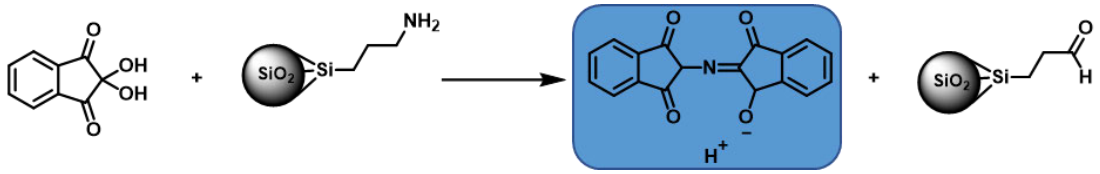

***Scheme 5.3.4:*** *Ninhydrin reaction with amine functionalised NP to produce Ruhemann's blue colour.*

An ethanolic solution of Ninhydrin (0.01 $g.mL^{-1}$) was added to 100 mg of the particles and the mixture sonicated for 5 minutes. The suspension was then centrifuged, and the solvent decanted. Then particles washed 3 times with ethanol, vortexed, centrifuged and decanted. The particles colour changed to Ruhemann's blue as shown in Figure 5.3.10 when the ethanol remained colourless indicating the presence of primary amine on the surface of the particles.

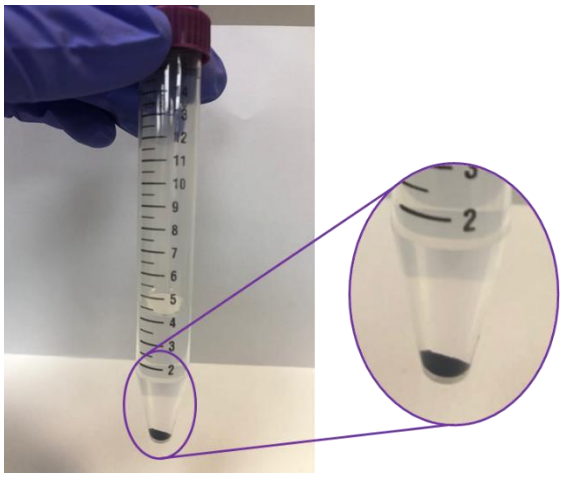

***Figure 5.3.10:*** *An image of the* ***$H_2N$-SiNP-03*** *sample subjected to ninhydrin solution.*

### 5.3.5 Preparation and characterisation of PU1+$NH_2$-SiNP nanocomposite

The next step after developing the amine functionalised silica particles was to utilise them to prepare polyurethane composites in order to study their mechanical properties and the behaviour of the **$H_2N$-SiNP-03** within the polymer network. The *in situ* approach (see Section 5.3.3) was first used to prepare a nanocomposite using **$H_2N$-SiNP-03** involving appropriate amount of the filler (5 wt%).

One of the main characteristics of the nanocomposite which can affect the mechanical properties is the molecular weight of the parent polymer. In order to determine the molecular weight of the synthesised nanocomposite and to compare it with the previously synthesised materials (see Section 5.3.3), GPC analysis was performed. Figure 5.3.11 shows the eluograms of the **PU1+$H_2N$-SiNP 5 wt%** and the area that the molecular weight calculation was applied to.

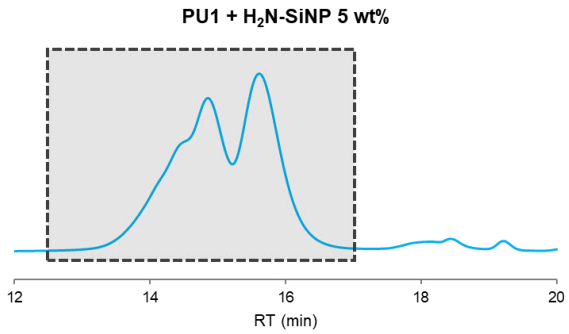


| Sample | Mn | Mw | Đ |
|---|---|---|---|
| PU1 + $H_2$N-SiNP 5 wt% | 7300 | 10400 | 1.43 |

***Figure 5.3.11:*** *GPC eluograms of* ***PU1+H₂N-SiNP 5 wt%*** *and the table showing the corresponding calculated molecular weights.*

Indeed, a comparison between these results and the GPC analysis results of the previously synthesised nanocomposites shown in Figure 5.3.3 demonstrates that the nanocomposites possess comparable molecular weights and the synthetic method is reliable; comparison of the mechanical properties of these nanocomposites and the parent **PU1** can be considered valid.

In order to study the mechanical properties of the **PU1+$H_2$N-SiNP 5wt%** samples and to also compare it with the unfunctionalised **PU1+SiNP 5wt%** nanocomposite, tensile tests were performed. Strips were cut from the cast nanocomposite film and subjected to a tensile test at the speed of 10 mm.min$^{-1}$ and the obtained stress-strain graph recorded. This experiment was repeated three times and the tensile properties reported in Table 5.3.5 and shown in Figure 5.3.12 are an average of this data Surprisingly, using **$H_2$N-SiNP-03** as the filler does not appear to improve the mechanical properties when compared to the incorporation of unfunctionalised SiNP *in situ*.

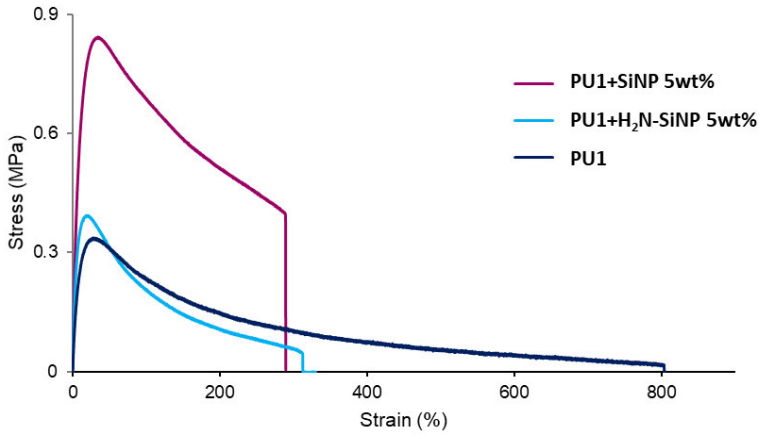


***Figure 5.3.12:*** *Representative stress-strain graphs from the tensile tests of the nanocomposites and the parent* ***PU1****.*

In fact, the UTS value of **PU1+SiNP 5wt%** was more than twice than that of **PU1+$H_2$N-SiNP 5wt%**. Although the elongation at break of these nanocomposites were

similar, **PU1+SiNP 5wt% e**xhibits 243% higher toughness as a result of its higher UTS value. In terms of flexibility, the materials follow the same trend and the **PU1+SiNP 5wt%** showed the highest Young's modulus and therefore is the stiffest material of three composites.

***Table 5.3.5:*** *Summary of the mechanical properties of the reported materials.*

| | UTS | Toughness | Young's modulus |
|---|---|---|---|
| **PU1** | 0.33 ± 0.05 | 0.84 ± 0.21 | 3.74 ± 0.30 |
| **PU1+SiNP 5wt%** | 0.87 ± 0.05 | 1.84 ± 0.65 | 6.21 ± 0.74 |
| **PU1+$H_2N$-SiNP 5wt%** | 0.38 ± 0.04 | 0.52 ± 0.20 | 4.25 ± 0.48 |

Nevertheless, these finding revealed that amine functionalisation of the **SiNP** and its incorporation in the **PU1**, did not improve the mechanical properties of the parent polyurethane and it even presents inferior mechanical properties compare to the **PU1+SiNP 5wt%**. The dispersion of the NPs within the polymer network could explain the inferior mechanical properties. In order to study the dispersion of the particles within the matrix, cross-sectional SEM images of the composites were obtained, see Figure 5.3.13. These SEM images clearly reveal the differences in the dispersion of the particles within the **PU1** network with highly aggregated particles evident in the **PU1+$H_2N$-SiNP 5 wt%** nanocomposite. Such aggregation interrupts the polymer network and serves as a failure point during a mechanical analysis which resulted in the inferior mechanical properties e.g., the elongation at break decreased by more than 160%. This could be explained by the difference in the hydrophilicity of the particles and the polymer network hence the particles tend to aggregate. Even if the particles aggregate at the polar hard section of the polymer, it would interrupt the supramolecular interactions form between the hard segments of different polymer molecules, as a result of their big dimensions.

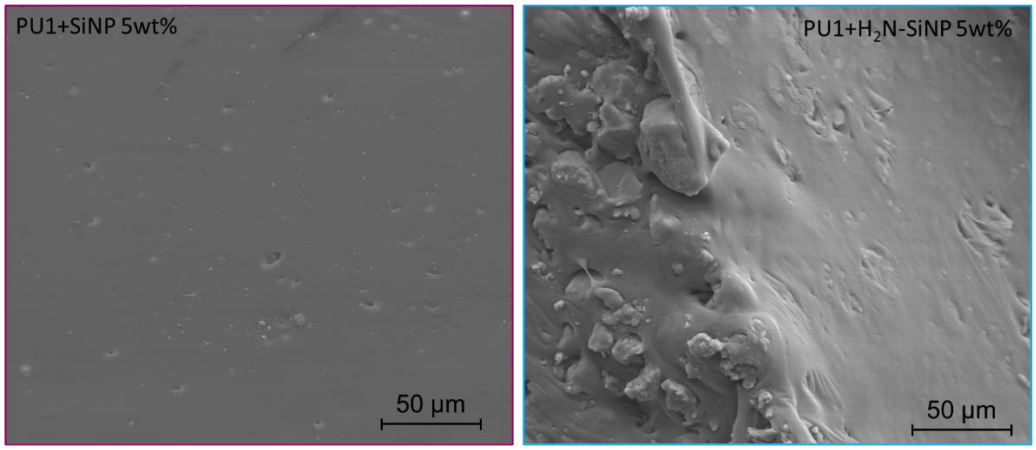


***Figure 5.3.13:*** *Cross-sectional SEM images of the nanocomposites prepared by in situ incorporation of* ***SiNP*** *and* ***H₂N-SiNP****.*

Additionally, the level of agglomeration observed in **PU1+$H_2$N-SiNP 5 wt%** could result from the **'**low energy' preparation method, i.e., dispersion and separation of the particles was dependent only on the magnetic stirring of the reaction mixture. Consequently, one possible approach could be to exploit a higher energy preparation method in order to maximise dispersion of the NPs to take advantage of the reactive functional group on the surface of the SiNP.

An alternative method of incorporation of silica nanoparticles with reactive functional surfaces into a polymer network is to utilise the Reactive Extrusion Printing (REX) method. This method involves feeding multiple reactive 'inks' into the printer and to mix them using a static mixer prior to be deposition.

### 5.3.6 Functionalised silica nanoparticles as reactive fillers using Reactive Extrusion (REX)

A Reactive Extrusion (REX) 3D printer is capable of mixing a couple of feed input material in a mixer with a defined ratio and to print the mixture onto a substrate. Since the feed materials (referred to as 'inks') are processed through a static mixer in the solution phase during the synthesis, the mixing is considered highly efficient. Therefore, the method was selected to be exploited to investigate the nanocomposite production. The effect of the surface functionality of the SiNPs on the rheology and viscosity profile of a polyurethane precursor ink were studied. In order to be able to print the precursors successfully, the reagents had to be viscous liquids. Therefore, a different formulation suitable for printing was developed that used different polymer components in comparison to those described in previous Sections. This process involves the *in situ* synthesis of the polyurethane during printing using a REX printer (Figure 5.3.14). In brief, a polyol mixture of poly (ethylene glycol)-block-poly

(propylene glycol)-block-poly (ethylene glycol) (PEG-PPG-PEG, Average Mn = 1900) and 1,4 butanediol containing dibutyltin dilaurate (DBTDL) as the catalyst was mixed with the functionalised SiNPs in a mixer prior to loading into one of the printer's cartridges. The other cartridge was filled with the desired isocyanate-prepolymer namely Poly [(phenyl isocyanate)-co-formaldehyde] (PMDI, Average Mn=340). Using pressure applied from a $N_2$ cylinder, these inks were then 'forcefed' into the dispensing unit which was controlled by the dosing system. Upon application of pressure, the inks entered a printhead with static mixer accessory which allows formation of the desired polyurethane composite prior to deposition.

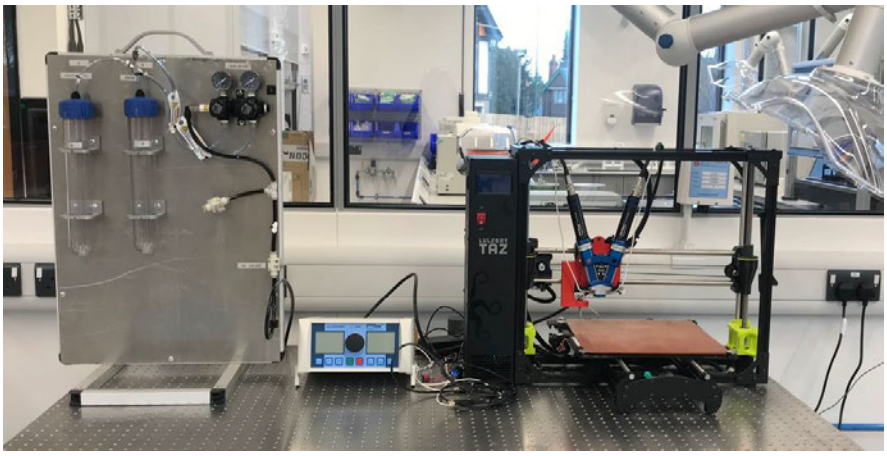

***Figure 5.3.14:*** *A picture of the REX printer setting used. Left: the board holding the ink cartridges middle: Dosing system control unit. Right: LulzBot TAZ6 the 3D printer interface.*

The feedstock formulations made up of the polyol ink system (a polymer with alcohol functionalities) and the polyisocyanate ink each of which reinforced with appropriate functionalised SiNP. The polyol ink comprised PEG-PPG-PEG ($M_n$ = 1900), a chain extender 1,4-butanediol and dibutyltin dilaurate as the catalyst. The polyisocyanate component contained poly[(phenyl isocyanate)-*co*-formaldehyde] ($M_n$ = 340). Each of these formulations was pneumatically transferred from the feed cylinders into the dosing unit (Figure 5.3.15 A) from which each formulation is withdrawn into the mixing dispenser (Figure 5.3.15 B) using the screw pump inside each arm of the dosing unit.

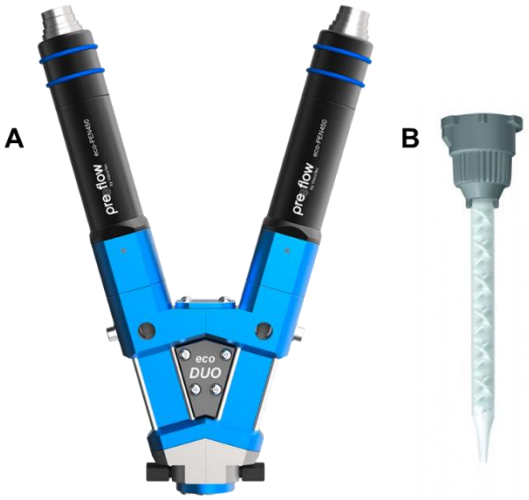


***Figure 5.3.15:*** *A) Picture of the mixing dispenser of the high-precision dosing unit and B) the static mixer used in the reactive extrusion printing. Images are not to the correct scale.*

In order to study the effect of the functionalised SiNPs on the mechanical properties of each feedstock, different functionalised SiNPs were either purchased or designed and synthesised. A small library of NPs including PDMS coated SiNPs as a hydrophobic filler, amine and amine/alkyl functionalised SiNPs as a hydrophilic and reactive filler were studied. The synthesis and characterisation of **$H_2N$-SiNP-03 is** described in Section 5.3.4 and the **PDMS-SiNP** was provided from a commercial source (Cabosil TS720 from Cabot Corporation).

### 5.3.7 Synthesis and characterisation of $NH_2/CH_3$-SiNP

Observing the high level of aggregation in the **PU1+$H_2N$-SiNP 5 wt%** composites led to different strategies being sought in order to reduce the agglomeration whilst also maintaining the reactivity of the particles. Consequently, an alkyl functionality was also introduced to the surface of the SiNPs in order to tune the hydrophobicity of the particles. It was anticipated that the increase in the level of the alkyl surface functionality would reduce the possibility of aggregation, however, the degree of reactivity of the filler would also reduce as a consequence of the lower number of surface amine groups. It was, therefore, necessary to tune the amine and alkyl group loading on the SiNP surfaces. **$NH_2/CH_3$-SiNP** particles were synthesised following the same general procedure used for synthesis of **$H_2N$-SiNP** (See Scheme 5.3.5).

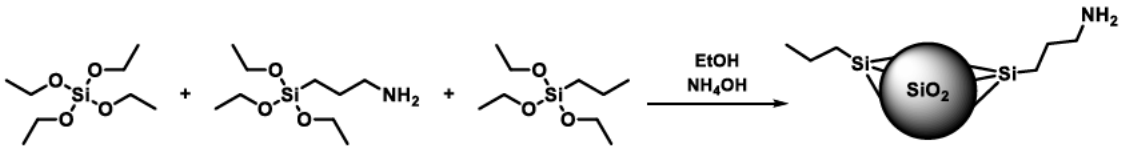


***Scheme 5.3.5:*** *Schematic representation of the synthesis procedure of the* ***NH₂/CH₃-SiNP****.*

In brief, TEOS in basic alcoholic solution was mixed with APTES and PTES and the mixture was then stirred for 16 hours. The nanoparticles thus formed were washed with ethanol to remove the excess reagents. In order to optimise the functionalities on the surface of the particles, the molar ratio of precursors was varied. This enabled the investigation of the effect of the functionalities' ratio on the properties of the particles and eventually the composites formed from them. Table 5.3.6 shows the molar ratio of the reagents used to synthesise each class of **$NH_2/CH_3$-SiNP**s. In fact, based on the theoretical stoichiometric ratio of the precursors, the concentration of amine must follow **$NH_2/CH_3$-SiNP-02 > $NH_2/CH_3$-SiNP-01 > $NH_2/CH_3$-SiNP-03**.

***Table 5.3.6:*** *Shows the amount of silica coupling agents used to synthesise the dual-functionalised SiNPs.*

| | **$NH_2/CH_3$-SiNP-01** | | **$NH_2/CH_3$-SiNP-02** | | **$NH_2/CH_3$-SiNP-03** | |
|---|---|---|---|---|---|---|
| | Eq. | amount | Eq. | amount | Eq. | amount |
| **TEOS** | 1 | 3.00 mL | 1 | 6.00 mL | 1 | 6.00 mL |
| **APTES** | 0.75 | 2.36 mL | 1 | 6.28 mL | 0.5 | 3.14 mL |
| **PTES** | 0.75 | 2.33 mL | 0.5 | 3.01 mL | 1 | 6.22 mL |

The successful functionalisation of the SiNPs was confirmed by FT-IR spectroscopy plus TGA analysis (Figure 5.3.16) as well as via elemental analysis.

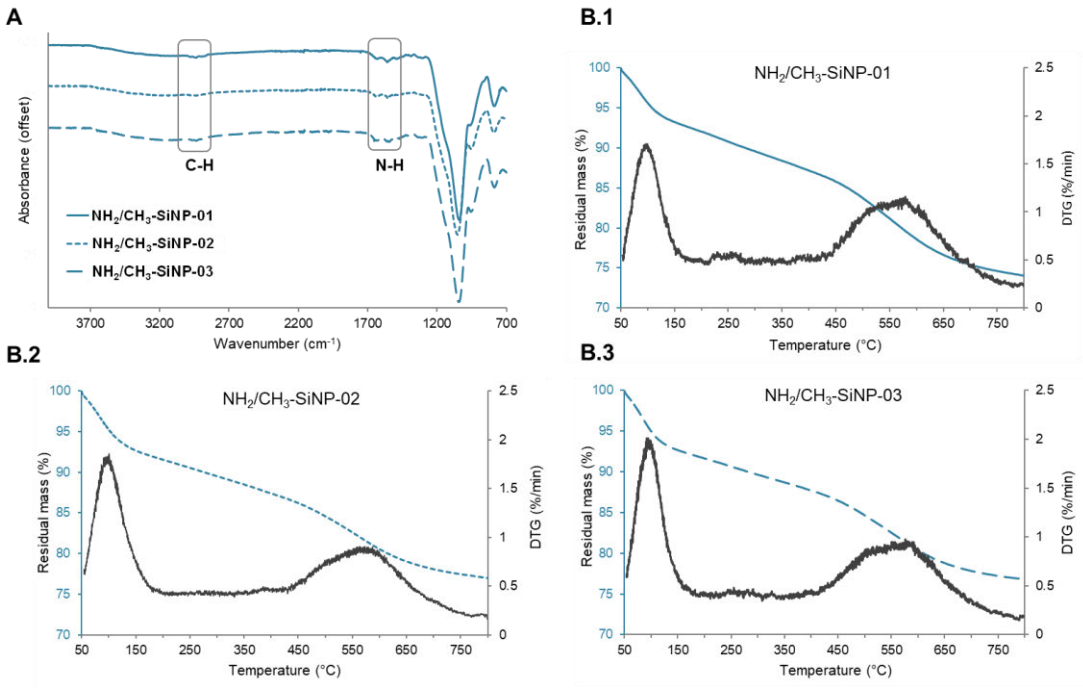


***Figure 5.3.16:*** *A) IR spectra and B) TGA thermogram of 3 classes of the synthesised* ***$NH_2/CH_3$-SiNP*** *showing the characteristic vibrations as well as their organic content.*

In particular, the characteristic vibrations found in FT-IR spectra which confirm the successful functionalisation of the SiNP are the C-H stretching at 2970 $cm^{-1}$ and N-H bending at *ca.* 1600 $cm^{-1}$.[32] Additionally the characteristic asymmetrical vibration of Si-O-Si was evident at *ca.* 1100 $cm^{-1}$ which confirms the formation of the $SiO_2$ core (Figure 5.3.16 A). Additionally, the TGA analysis of the particles reveal two key decomposition steps. The weight loss below 200 °C was attributed to the evaporation of absorbed water or solvent on the surface. Also, the weight loss above 400 °C is related to the organic alkyl chain which are covalently attached to silica core and therefore confirms the successful functionalisation of the organic compounds on the surface of SiNP. (See Figure 5.3.16 B.1 – B.3)

Additionally, the elemental analysis was exploited to quantify the functionalisation of the different classes of the **$NH_2/CH_3$-SiNP** in order to investigate the effect of the concentration of the precursors on the final concentration of the functionalities. The calculations were similar to those reported in Section 5.3.4. The percentage nitrogen content of the particles was attributed to the concentration of the amine functionality. Subsequently, the percentage of carbon contribution towards the propylamine was calculated and deducted from the total carbon percentage. The remainder was assigned to the propyl functionality and thus the ratio of the propylamine to propyl units was also calculated (Table 5.3.7).

***Table 5.3.7:*** *Calculated concentration of the functionalities based on the elemental analysis results.*

| | $NH_2/CH_3$-SiNP-01 | $NH_2/CH_3$-SiNP-02 | $NH_2/CH_3$-SiNP-03 |
|---|---|---|---|
| **Propylamine** (mmol.g$^{-1}$) | 2.89 | 2.27 | 2.52 |
| **Propyl** (mmol.g$^{-1}$) | 0.36 | 0.18 | 0.36 |
| **Amine:Propyl** | 8.03 | 12.6 | 7.00 |
| **Theoretical Amine:Propyl** | 1 | 2 | 0.5 |

Although the concentration found by elemental analysis are not directly proportional to the theoretical ratio of the precursors, they follow the same trend. Thus, **$NH_2/CH_3$-SiNP-02** was generated using the greatest number of equivalents of APTES of all three and the highest propylamine:propyl ratio was confirmed by elemental analysis.

TEM analysis was used to study the morphology of the synthesised dual-functionalised SiNPs (see Figure 5.3.17).

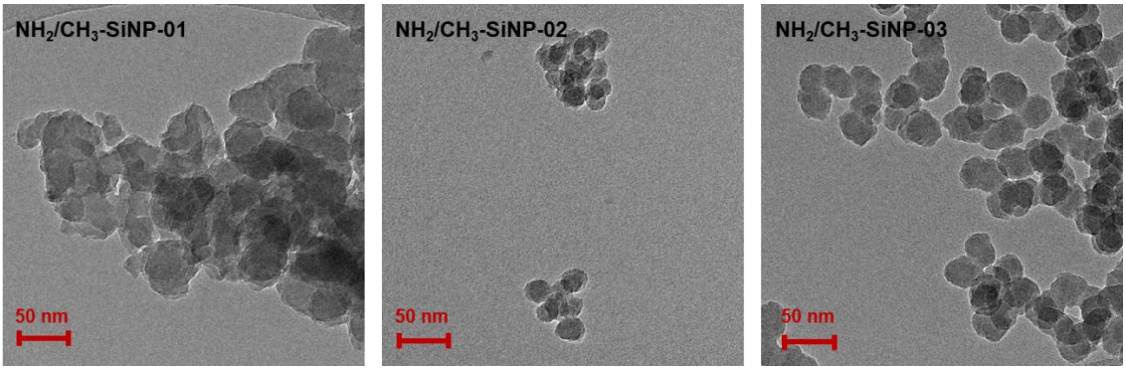


***Figure 5.3.17:*** *TEM images of the different classes of the dual-functionalised SiNPs illustrating the difference in their morphology.*

As it can be seen in Figure 5.3.17, the concentration of the reagents and therefore the ratio of the final functionalities have a pronounced effect on the morphology of the formed particles. Briefly, **$NH_2/CH_3$-SiNP-01** has a non-uniform structure in which the particles have grown unexpectedly and formed non-uniform large aggregates. However, samples 02 and 03 of the dual-functionalised particles were characterised by smaller particles *ca.* 50 nm in diameter. The sample **$NH_2/CH_3$-SiNP-03** NPs were less agglomerated and discrete spherical particles are evident in the image.

To conclude, in terms of particle size and morphology, samples **$NH_2/CH_3$-SiNP-02**, and **$NH_2/CH_3$-SiNP-03** were ideal. Despite the higher propylamine content in **$NH_2/CH_3$-SiNP-02**, **$NH_2/CH_3$-SiNP-03** was selected as the best dual-functionalised particles to be incorporated into the polyurethane composite formulation and compared with other SiNPs. This selection

was made in order to maximise the difference between **$H_2N$-SiNP** and the **$NH_2/CH_3$-SiNP-03** and facilitate the investigation of the effect of propyl spacers on the property of the corresponding nanocomposites.

### 5.3.8 Preparation and characterisation of nanocomposite ink formulations for REX printing

In order to synthesise a reinforced polyurethane using REX printing technology, two formulations were developed (See Table 5.3.8); a polyol and an isocyanate formulation (as described in Section 5.3.6). These formulations (as polyurethane precursors) were mixed during the printing process and the resultant printed material was the polyurethane composite of interest. In order to improve the printability and rheologic properties of the ink formulations both formulations were reinforced by incorporation of appropriate functionalised SiNP.[33,34] In brief, the NCO ink consists of poly[(phenyl isocyanate)-*co*-formaldehyde] (PMDI) which was improved by incorporation of 53 wt% **PDMS-SiNP** and the composition of this was constant within the experiments. In the case of the other ink, the polyol was reinforced by incorporation of 5 wt% of the 3 different functionalised SiNPs; namely, **PDMS-SiNP**, **$H_2N$-SiNP** and **$CH_3/NH_2$-SiNP**.

***Table 5.3.8:*** *A Summary of the composition of the formulations of each ink.*

| | Chemicals | Functionality | **PDMS-SiNP** (wt%) | **$H_2N$-SiNP** (wt%) | **$NH_2/CH_3$-SiNP** (wt%) |
|---|---|---|---|---|---|
| Isocyanate (NCO) Ink | PMDI | -NCO | 53 | 53 | 53 |
| | Fumed Silica (PDMS-SiNP) | Rheology modifier | 1 | 1 | 1 |
| Polyol (OH) Ink | PEG-PPG-PEG | -OH | 30 | 30 | 30 |
| | 1,4 Butadiene | -OH | 16 | 16 | 16 |
| | Fumed Silica (PDMS-SiNP) | Rheology modifier | 5 | 0 | 0 |
| | $H_2N$-SiNP | Rheology modifier | 0 | 5 | 0 |
| | $NH_2/CH_3$-SiNP | Rheology modifier | 0 | 0 | 5 |
| | DBTDL | catalyst | 1 | 1 | 1 |

In order to prepare the inks prior to be fed into the printer, each formulation component was mixed using a Dual Axial Centrifugal (DAC) mixing unit to achieve a homogenous mixture of the NPs within the polymer network. Subsequently the nanocomposite mixture was sonicated for 10 minutes to further improve the dispersion of the particles and minimise the

aggregate formation. The TEM images of the different types of the SiNPs were compared to optical microscopic images of the prepared polyol nanocomposite inks. TEM images of the particles (Figure 5.3.18) revealed more aggregation in the case of **$H_2$N-SiNP.** These results show that the **$H_2$N-SiNP** have higher tendency to aggregate and form clusters even in the absence of any polymeric network. Firstly, this could be originated from the inherent possible aggregation of the particles during synthesis procedure since the APTES is capable of forming a bridge between formed silica core when the APTES to silica ratio exceeds a specific limit.[29] In addition, owing to the hydrophilic nature of the (-$NH_2$ and -OH on the surface of the particle), **$H_2$N-SiNP** was inherently more susceptible to aggregation when mixing with non-polar polyol matrix, in contrast to the other two investigated silica nanoparticles with more hydrophobic nature. Next, the dispersion of the particles within the matrix was also compared in Figure 5.3.19 using optical microscopy. Likewise, the composite ink containing **$H_2$N_SiNP-03** exhibited poor dispersion of the particles which resulted in a higher optical contrast between the polymer matrix and the aggregated particles. In the case of the other two SiNP used with PDMS and alkyl surface units, respectively, they exhibited better dispersion in the polyol matrix and therefore, the particles are consequently less distinguishable with lower visual contrast between the particles and the polymer network under the optical microscope.

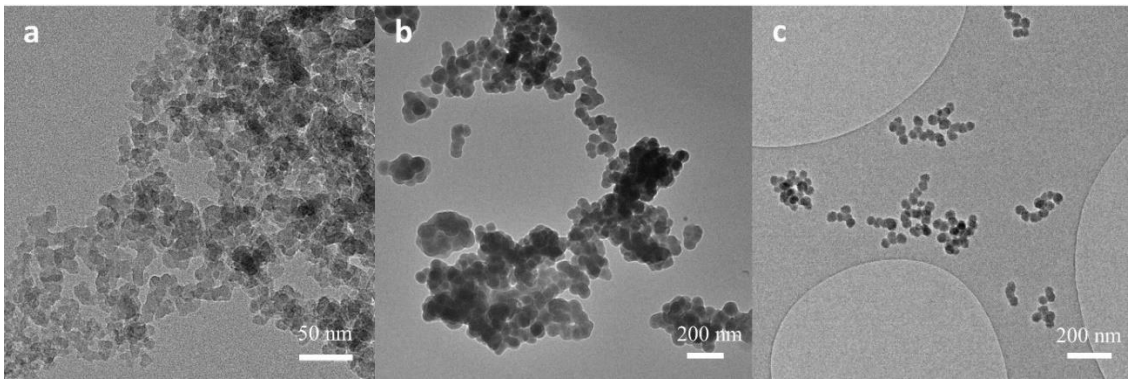


***Figure 5.3.18:*** *TEM images of functionalised SiNPs used to prepare the polyol inks. a)* ***PDMS-SiNP****, b)* ***$H_2$N-SiNP-03*** *c)* ***$NH_2$/$CH_3$-SiNP****.*

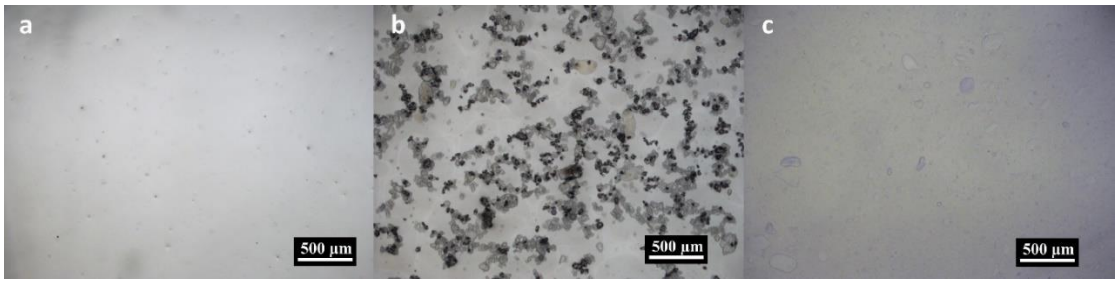


***Figure 5.3.19****: Optical microscopic images of the polyol inks with the formulation presented in Table 5.3.8 a)* ***PDMS-SiNP****, b)* ***$H_2$N-SiNP*** *and c)* ***$NH_2$/$CH_3$-SiNP-03****.*

After visual investigation of the functionalised SiNP and their corresponding polyol nanocomposite inks, the effect of the observed dispersion on the mechanical properties of the polyol inks was examined. To that aim, the prepared polyol inks were subjected to oscillatory rheology analysis using a 40 mm parallel plate geometry. Changes in viscosity of the polyol ink as a function of shear rate were recorded. Figure 5.3.20 shows the changes in shear viscosity of the polyol inks containing the three different classes of amine/alkyl functionalised SiNPs as a function of shear rate. The graphs illustrate that the viscosity of the polyol inks follows the order of: **NH2/CH3-SiNP-02** < **NH2/CH3-SiNP-01** < **NH2/CH3-SiNP-03**. This order is in agreement with the concentration of the amine functionality i.e by decreasing the concentration of the amine the viscosity increases. Indeed, by decreasing the concentration of the amine the tendency of the particles to aggregate decreases thus the improvement in the viscosity of the polyol formulation.

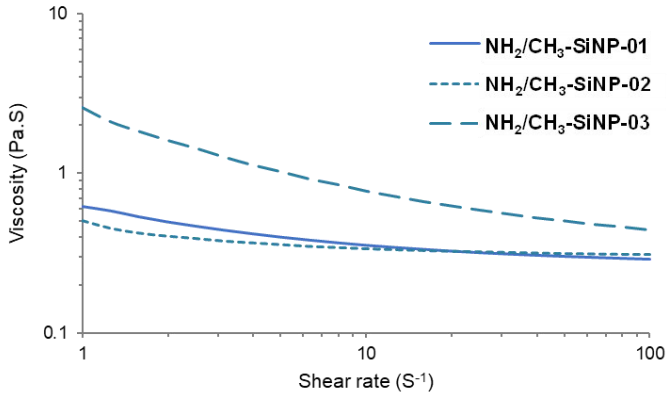


***Figure 5.3.20:*** *Viscosity profiles of the polyol nanocomposite inks formulated with the dual-functionalised SiNPs as a function of shear rate.*

This dataset also revealed that the polyol ink contains **PDMS-SiNP** undergo the most substantial decrease in viscosity (by an order of magnitude) upon increasing the shear rate from 1 to 100 $S^{-1}$ (Figure 5.3.21). In contrast, only a negligible change of viscosity was recorded for the parent polyol formulation without any type of SiNP present. In conclusion, shear-thinning properties was recorded for all of the nanocomposite polyol formulations, however, the viscosity of the bare polyol formulation without any silica filler was independent of shear rate. Interestingly, **OH+5% $NH_2$/$CH_3$-SiNP**, which contains SiNPs with both the alkyl and amine surface functionalities, exhibited a higher viscosity when compared to **OH+5% $H_2$N-SiNP**. This enhanced viscosity could be explained by improved dispersion of **$NH_2$/$CH_3$-SiNP** within the polyol network in comparison to **$H_2$N-SiNP-03** as observed in Figure 5.3.19 b and c.

Additionally, the viscoelastic profile of the prepared inks was also obtained by plotting the storage and loss moduli *vs.* frequency from the rheology experiments. The results illustrated in Figure 5.3.21 B showing that the introduction of functionalised SiNPs generally increases the moduli of the neat polyol ink. For example, the polyol ink as well as the **OH+5% $H_2N$-SiNP** formulation exhibit viscous-like properties because of the domination of the loss modulus within the selected frequency range (0.1 to 10 Hz). In contrast, the polyol inks containing **PDMS-SiNP** and **$NH_2/CH_3$-SiNP-03** exhibit a solid-like behaviour, although a cross-over point between G' and G" can be observed at 7 Hz in **OH+5% $NH_2/CH_3$-SiNP-03** and therefore the ink exhibited viscous behaviour at higher frequencies.

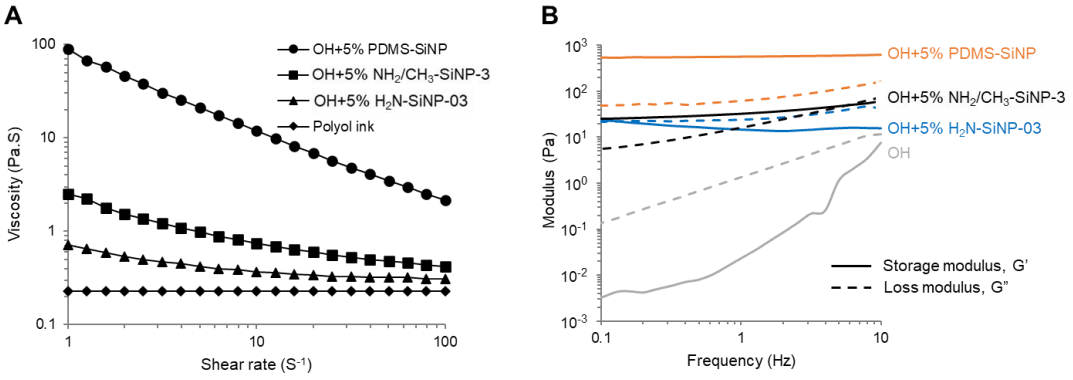


***Figure 5.3.21:*** *Rheological properties of the polyol inks with three different types of SiNPs (**PDMS-SiNP**, **$H_2N$-SiNP-03** and **$NH_2/CH_3$-SiNP-03**). a) Viscosity as a function of shear rate, b) Storage modulus and loss modulus as a function of frequency.*

Another crucial property of the ink materials is their yield stress. Yield stress is defined as the smallest stress at which a plastic deformation occurs. In fact, considering ink materials, yield stress is the highest stress that can be applied to the material before it flows. Therefore, yield stress is of high importance in determining a suitable ink for extrusion printing. Herein, an oscillatory rheological experiment was used to determine the yield stress of the prepared nanocomposite polyol inks. Although, various method of determining the yield stress in an oscillatory experiment have been reported,[35] the "characteristic modulus" method has been employed here. In particular, the characteristic modulus is where G' = G" when the moduli are plotted *vs*. the shear stress (Figure 5.3.22). Indeed, when G" is higher than the G', the material is a viscous liquid. Nanocomposites **OH+5% $NH_2/CH_3$-SiNP-01** and **OH+5% $NH_2/CH_3$-SiNP-02** are a viscous liquid regardless of the shear stress applied. However, **OH+5% $NH_2/CH_3$-SiNP-03** exhibited an elastic-like behaviour at low shear stresses and viscous liquid behaviour above a stress value of 0.13 Pa (Figure 5.3.22 A). Therefore, **OH+5% $NH_2/CH_3$-SiNP-03** was considered to be the optimum formulation among the three classes of the dual-functionalised SiNP nanocomposite, since it flows during

printing when stress is applied, and it holds its structure at stable condition after being deposited.

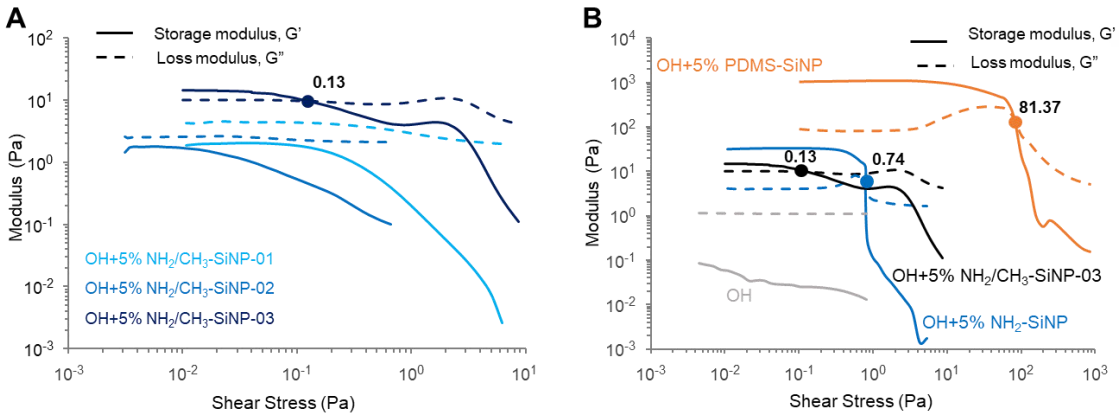


***Figure 5.3.22:*** *Oscillatory rheology data of polyol inks. A) polyol inks with three classes of* ***$NH_2/CH_3$-SiNP****, B) polyol inks with three different silica particles (****PDMS-SiNP****,* ***$H_2N$-SiNP-03*** *and* ***$NH_2/CH_3$-SiNP-03****). Yield stress of the inks obtained from oscillatory rheology test using the 'characteristic modulus' method.*

The yield stress of the nanocomposite inks was examined and compared among **PDMS-SiNP**, **$H_2N$-SiNP** and **$NH_2/CH_3$-SiNP-03** in (Figure 5.3.22 B). All of the nanocomposite polyol inks exhibited higher moduli than the neat polyol formulation over an increasing shear rate. It was also observed that yield stresses exhibited by the polyol inks with 5% **PDMS-SiNP** were over 100 times and 600 times higher than that of polyol inks with 5% **$H_2N$-SiNP** and 5% **$NH_2/CH_3$-SiNP-03**, respectively. The calculated yield stresses from these experiments are shown in Table 5.3.9. It must be noted that polyol nanocomposites prepared with dual functionalised SiNP **OH+5% $NH_2/CH_3$-SiNP-01** and **OH+5% $NH_2/CH_3$-SiNP-02** did not show any characteristic modulus and therefore no yield stress over the range of the shear stress of the performed experiment.

***Table 5.3.9:*** *Yield stresses calculated from the characteristic modulus of the prepared nanocomposite polyol inks.*

| Ink | Yield Stress (Pa) |
|---|---|
| OH+5% PDMS-SiNP | 81.37 |
| OH+5% $H_2N$-SiNP | 0.74 |
| OH+5% $NH_2/CH_3$-SiNP-03 | 0.13 |

In conclusion, the introduction of silica nanoparticles into the polyol inks successfully adjusted the rheology of the ink, affording both shear-thinning and gel-like properties, which are critical for extrusion-based 3D printing process. However, the next interesting question

was how different functionalised SiNPs affect the printing performance and the final PU composite properties. From the rheology characterisation, inks with **PDMS-SiNP** characterised with superior viscoelastic properties and yield stress in comparison to the inks with **$H_2N$-SiNP-03** and **$NH_2/CH_3$-SiNP-03**, are less susceptible to distortion during extrusion printing process.[33] Hence, the printed filament maintains its shape more easily upon deposition onto the substrate. The single filament printing profile was characterised under microscope, showed that the width of the printing single filament for formulations with **$H_2N$-SiNP-03** was 97% and 25% larger than the width of filament from formation with **PDMS-SiNP** and **$NH_2/CH_3$-SiNP-03**, respectively (Figure 5.3.23). The results indicates that unsatisfactory rheological properties of the inks could result in printing deviation, and potentially disrupt the entire structure during the layer stacking process as a result of the low apparent yield stress.

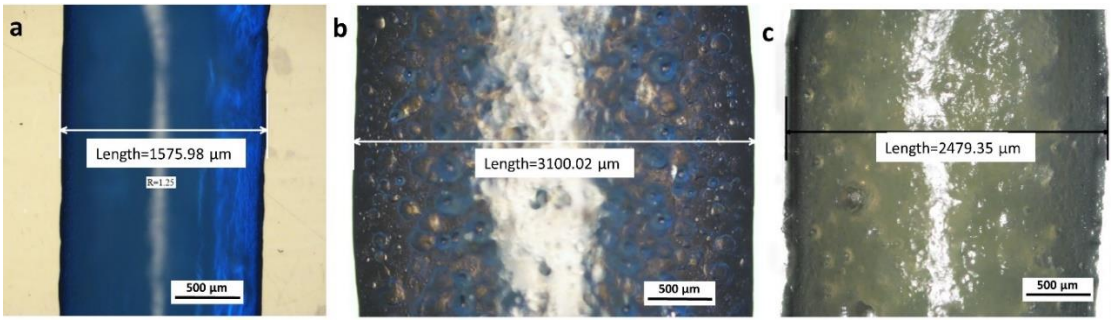


***Figure 5.3.23:*** *Extruded single filament under microscope. a)* ***PDMS-SiNP****, b)* ***$NH_2$-SiNP*** *and c)* ***$NH_2/CH_3$-SiNP-03****.*

Attention then turned to understanding the reaction kinetic of the polyurethane formation. The reaction is between the isocyanate ink and the polyol ink containing the reactive filler, the kinetics of which determine the suitability of the REX printing to produce a printed polyurethane part or image. Accordingly, the kinetics of the reactions corresponding to the printing of the isocyanate ink and different polyol inks were monitored and compared using FT-IR analysis. Figure 5.3.24 a shows the FT-IR spectra of the printed part at 1 min and 10 min after printing.

The absorption peak at *ca.* 2250 $cm^{-1}$ attributed to isocyanate reduces over time as the reaction progress Figure 5.3.24 B.[36] The degree of reduction of the isocyanate stretching absorbance was used to determine the rate of each reaction. For example, the PU part printed using **OH+5% PDMS-SiNP** showed the highest reduction level of the isocyanate stretching during 9 minutes, demonstrating the highest reaction rate of all. Additionally, the relative intensity of the C-H stretching in the 2865 – 2968 $cm^{-1}$ region remained unchanged during the time frame of the experiment and consequently was used as the reference for this quantitative analysis.[37]

The absorption peaks at 1725 $cm^{-1}$ and 1701 $cm^{-1}$ were attributed to free and hydrogen bonded carbonyl bands of the urethane groups, respectively 38,39 (Figure 5.3.24 A). This region was widely used for investigating the structure property relationship in the synthesised PU, to reveal the hydrogen bonding state in the structure.[39-41] A more intense hydrogen bonded carbonyl band in contrast to free carbonyl peak was displayed in all of the samples printed from **PDMS-SiNP**, **$H_2$N-SiNP-03** and **$NH_2$/$CH_3$-SiNP-03**. However, the ratio between the hydrogen bonded carbonyl peak and free carbonyl band was more pronounced in samples printed from **PDMS-SiNP**. In fact, the more intense hydrogen bonded C=O carbonyl band was expected to improve the stiffness of the PU, as the result of higher degree of agglomeration of hydrogen bonded hard segments and the induced micro-phase separation within the network. Furthermore, within the spectra region of N-H stretching band, between 3400 $cm^{-1}$ and 3200 $cm^{-1}$, a more pronounced hydrogen bonded N-H peak were shown for samples printed from **$NH_2$/$CH_3$-SiNP-03** formulation, when compared to the other two formulations. In addition, an amide III band (C-N stretching and N-H bending) was evident in the IR spectra of all of the composite samples at 1223 $cm^{-1}$.[42] These bands indicated N-H in the hydrogen bonded state and the formation of urethane-urea network.[41,42]

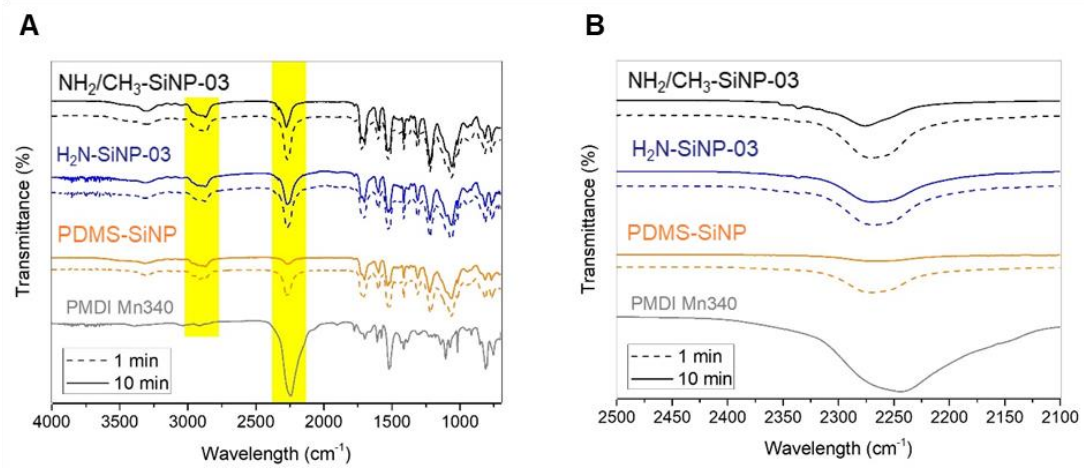


***Figure 5.3.24**: FT-IR spectra of samples after printing at 1 min (dash line) and 10 min (solid line). a) FT-IR spectra of PMDI and printed PU samples using three different silica particles (**PDMS-SiNP**, **$H_2$N-SiNP** and **$NH_2$/$CH_3$-SiNP-03**). Amplified spectra of **b)** Isocyanate peak (-NCO).*

In order to calculate the kinetics of the reactions, the reaction conversion was calculated based on the changes in the intensity of the -NCO band (Equation 5.A).

$$\text{Reaction conversion } = 1 - \frac{A_{NCO(t)}/A_{CH(t)}}{A_{NCO(t_0)}/A_{CH(t_0)}} \qquad (5.A)$$

In this equation, $A_{CH(t_0)}$ and $A_{CH(t)}$ are the reference alkyl stretching at time 0 and time t, respectively. Similarly, $A_{NCO(t_0)}$ and $A_{NCO(t)}$ correspond to the peak area of the isocyanate after printing at time 0 and t, respectively. These peak areas were obtained using the Perkin

Elmer Spectrum software and the corresponding amounts were calculated for individual formulations at t = 0 and 10 minutes after printing. Table 5.3.10 compares the results of these calculations indicating that the progress of the reactions is similar at t = 0 irrespective of the functionality of the SiNP used in its polyol formulation. nevertheless, the difference becomes more substantial over 10 minutes.

***Table 5.3.10:*** *Calculated reaction conversion for REX printing of each polyol ink with the isocyanate ink using Equation 5.A.*

| | Time (min) | PDMS-SiNP | $NH_2$-SiNP | $NH_2/CH_3$-SiNP-03 |
|---|---|---|---|---|
| **Reaction** | 1 | 85% | 82% | 83% |
| **Conversion** | 10 | 95% | 85% | 89% |

Thermal properties of the REX printed PUs were also studied in order to compare their stability and physical properties. Figure 5.3.25 shows the derivatives extracted from the TGA graphs identifying two distinct decomposition temperature in every PU nanocomposite. Indeed, the PU nanocomposite containing **$H_2N$-SiNP-03** exhibited the quickest weight loss at *ca.* 100 °C corresponds to the loss of the water/solvent which are physically absorbed on the surface. Additionally, there are two pronounced peaks visible in the thermograms of all PU nanocomposites each of which represents the decomposition of the urethane and ether bonds. In fact, the decomposition peak between 300 °C and 400 °C attributed to the decomposition of urethane bonds and the later corresponds to ether groups of the soft segment.[88,234] Table 5.3.11 summarises the temperatures at which each decomposition occurs in different printed PU nanocomposite.

Additionally, Figure 5.3.25 B illustrates the DSC thermograms of these printed PU nanocomposites. Although, a melting endotherm was not observed as a result of the amorphous nature of the materials, they all exhibited a glass transition. The printed PU nanocomposite containing **$NH_2$-SiNP** exhibited the lowest Tg at 53.7 °C. In contrast, the Tg values of the printed samples containing **$NH_2/CH_3$-SiNP-03** and **PDMS-SiNP** were detected at 74.8 °C and 80.5 °C, respectively.

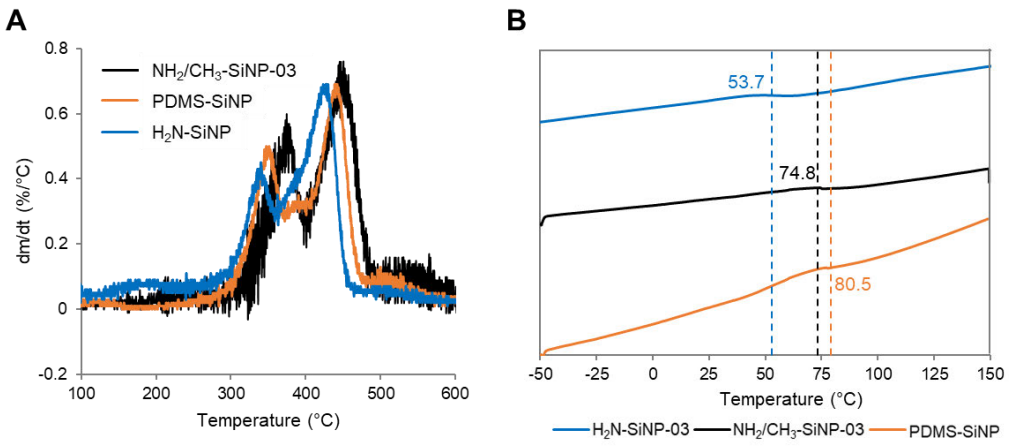


***Figure 5.3.25:*** *A) DTG curves and B) DSC curves of the REX printed PU nanocomposites.*

***Table 5.3.11:*** *DTG $(I)_{max}$ and DTG $(II)_{max}$: lower and higher peak temperatures in the DTG curves, respectively showing the decomposition temperatures.*

| Samples | DTG $(I)_{max}$ (°C) | DTG $(II)_{max}$ (°C) |
|---|---|---|
| **PDMS-SiNP** | 351.5 | 442.5 |
| **$NH_2/CH_3$-SiNP-03** | 374.4 | 450.3 |
| **$H_2N$-SiNP** | 340.8 | 430.2 |

The introduction of amine group onto the surface of the particles were expected to enhance the PU material properties through generation of the secondary network within the polymeric network by formation of the urea bonds. However, considering the reaction kinetics and thermo-mechanical properties, the formulation containing **$H_2N$-SiNP-03** under-performed in comparison to the formulations contains commercial **PDMS-SiNP** and **$NH_2/CH_3$-SiNP-03**. The slowest kinetics among the three formulation was caused by the agglomeration of **$H_2N$-SiNP-03**. Since the agglomeration was present in great extent, it hindered the reaction by blocking the reaction path between NCO of the polymer and the OH and $NH_2$ residues present on the surface of the silica nanoparticles. Consequently, as a result of this hindrance, formulation with **$H_2N$-SiNP-03** exhibited a weaker cross-linking network in the final structure. Hence, the printed PU with **$H_2N$-SiNP-03** exhibited lower thermal stability, glass transition temperature and storage modulus.

Eventually, mechanical properties of the printed PU nanocomposites were examined. Dynamic mechanical analysis (DMA) was obtained from the samples in a range of temperature from 25 °C to 150 °C. Figure 5.3.26 illustrates the resulted storage modulus by the change in temperature. In fact, the PU contains **$H_2N$-SiNP-03** demonstrates the lowest modulus, in contrast to the **PDMS-SiNP** containing sample which is proved to be the stiffest

within the experiment temperature range. Likewise, the storage modulus of samples containing **PDMS-SiNP** and **$NH_2/CH_3$-SiNP-03** remained comparable within the temperature region. The results illustrate that the high temperature does not totally destroy the material's network.

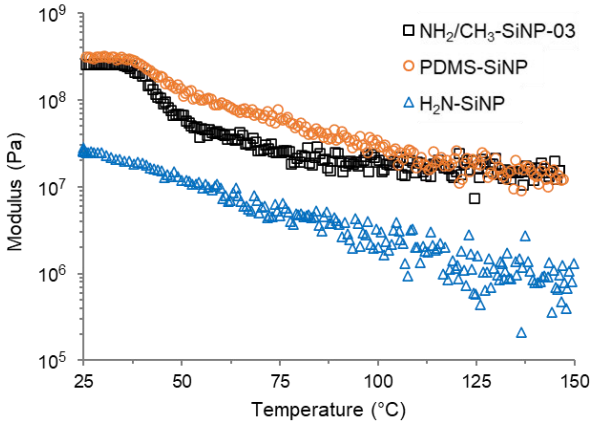


***Figure 5.3.26:*** *DMA temperature scan of PU samples containing three different silica NPs (**PDMS-SiNP**, **$H_2N$-SiNP-03** and **$NH_2/CH_3$-SiNP-03**).*

In conclusion, it should be noted that the polyol ink prepared with **$NH_2/CH_3$-SiNP-03** showed inferior physical and mechanical properties i.e., relatively lower viscosity, storage modulus, yield stress and poorer particle dispersion when compared to the polyol ink containing the commercial **PDMS-SiNP**. Therefore, it was expected that the extruded PU part exhibits similar poor properties compare to the PU containing **PDMS-SiNP**. However, interestingly comparable material properties (i.e., thermal stability and mechanical properties) were observed in printed PU samples using **$NH_2/CH_3$-SiNP-03** and **PDMS-SiNP**. Indeed, sample contains **$NH_2/CH_3$-SiNP-03** revealed to have more hydrogen bonded hard segments (Figure 5.3.27) after printing which suggests stronger cross-linking network formed as a result of the aggregated hydrogen bonded hard segments. This additional cross-linking network could be achieved through the urea bonding between the reactive **$NH_2/CH_3$-SiNP-03** filler and the polymeric-NCO ink during the extrusion process.

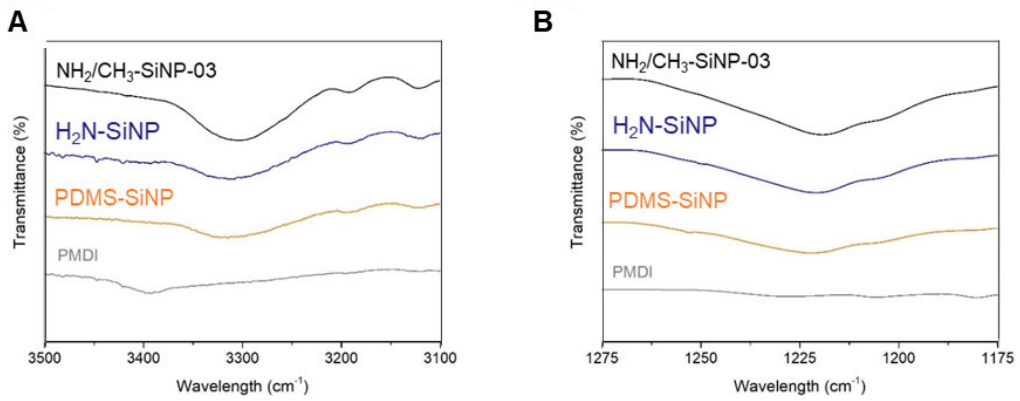


***Figure 5.3.27:*** *FT-IR spectrum of PMDI (NCO ink) and PU samples printed from formulations with (**PDMS-SiNP**, **H₂N-SiNP-03** and **NH₂/CH₃-SiNP-03**. A) hydrogen bonded N-H stretching vibration. B) Amide III peak (C-N stretching and N-H bending).*

The prepared polyol nanocomposite with different functionalised SiNPs were 3D printed using a REX printer and the properties of the resultant material from the dual-functionalised SiNP was comparable to that produced using commercially available SiNP (**PDMS-SiNP**). The findings have profound impact for future AM users, in tailoring the filler with different functionalities on the surface and the use of functionalised SiNP as reactive fillers to reinforce the overall printing results without interfering with the printing process.

## 5.4 Future Perspectives

In this Chapter, a variety of functionalised SiNP have been prepared in addition to the use of different methods to incorporate these novel fillers into supramolecular polymer matrices in order to improve their processability and mechanical properties. For example, it was shown that by incorporation of dual-functionalised SiNP into the precursors ink can produced a polyurethane material with superior mechanical properties, despite the mechanical properties of the precursors. Meanwhile, the reinforcement of Low Molecular Weight Additives (LMWAs) through introduction of suitable SiNP can also be proposed.[27,44] The proposed LMWA improves the mechanical properties of supramolecular polymers by introduction of added supramolecular interactions which can assemble or form micro phase-separation with the polymer. This feature can be combined with inorganic filler to enhance the mechanical properties of supramolecular polymers and gel which would also potentially result in a more even dispersion of the inorganic filler within the polymeric network.

A class of organic gelators that has gained interest recently is sorbitol-based gelators. These gelators are of special interest since they are produced from a sustainable source with potential applications ranging from personal care industries to energy technology.[44] Additionally, unlike conventional polymer-based organogelators, the sorbitol-based gelators

are a class of low molecular weight gelators with higher responsiveness to stimuli such as pH or temperature. Another possible application of SiNPs could be reinforcement of these supramolecular gel structures. In order to investigate the effect of SiNPs on the mechanical properties of supramolecular gels, one of these sorbitol-based organogels, namely, 1,3:2,4-di(4-isopropylbenzylidene)-D-sorbitol (**DBS-iPr**) was selected to be grafted to the surface of the SiNP (Figure 5.4.1).

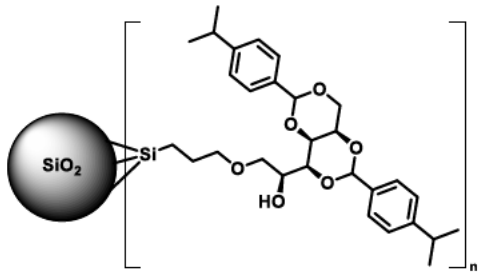


***Figure 5.4.1**: Proposed chemical structure of the **DBS-iPr** functionalised SiNP.*

As an initial attempt to functionalise the particles with **DBS-iPr** both grafting to and co-condensation method was employed and studied. However, a modified grafting to method proved to be the most promising approach to realisation of this novel filler material.

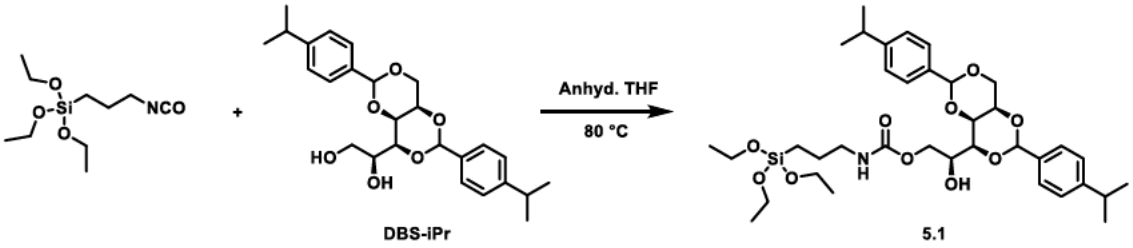


***Scheme 5.4.1:** Synthesis of DBS-iPr@silane coupling agent to be grafted to SiNP.*

A propyl isocyanate silane coupling agent used to link to the **DBS-iPr** via a urethane bond was subsequently reacted with SiNP in order to produce the functionalised particles (Scheme 5.4.1). Preliminary characterisation using MS, TGA (Figure 5.4.2) confirmed the successful grafting of the LMWG to the SiNP. In addition, elemental analysis revealed successful grafting of 0.35 mmol **DBS-iPr** per gram of the SiNP sample.

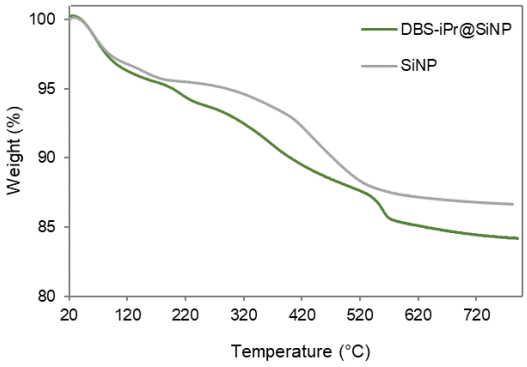


***Figure 5.4.2**: TGA thermograms of SiNP and **DBS-iPr** functionalised SiNP exhibiting more organic content in the latter case.*

The synthesised functionalised **DBS-iPr+SiNP** shall be used for improving the mechanical properties of these organogels. After mixing the LMWG with the functionalised SiNP, the gelation ability of the system should be studied. Pure **DBS-iPr** forms a gel in a mixture of ethanol water and in a number of organic solvents, however, further examination will be needed in the case of the nanocomposite gel to optimise its composition as well as investigating and comparing the thermomechanical properties.

## 5.5 Conclusion

It has been shown that improvements of the mechanical properties of SPUs can be made through careful functionalisation of silica particles and their dispersal within the polymeric matrix. The surface functionality can prevent aggregation of the SiNPs by tuning the electrophilicity/electrophobicity of the SiNPs with respect to the polymer network. Additionally, the surface functionality of the SiNPs can be altered so that the particles act as reactive fillers that can form a secondary network within the system. This type of reactive filler can be incorporated into polyurethane precursors to tune and optimise the mechanical properties of the starting material and facilitate the production process. Overall, by changing the surface chemistry of the SiNP in conjunction with use of the most appropriate dispersal method (in the case of this study this was 5% loading of $H_2N$-SINP combined with the reactive extrusion preparation method), it is possible to generate nanocomposites with superior mechanical properties in comparison to that of the parent polymer or even tune these characteristics.

## 5.6 Experimental

The materials and analytical instrumentation used in this Chapter is reported in Chapter 2, Section 2.5 and Chapter 3, Section 3.5, unless otherwise specified. Polydimethylsiloxane

(PDMS)-coated hydrophobic fumed silica particles (PDMS-SiNP) (Cabosil TS720) was purchased from Cabot Corporation, United States.

$^{29}$Si NMR spectroscopy (500 MHz) were recorded with Bruker AVIII 500, using 70.59 mg of the **$H_2$N-SiNP** in a one pulse experiment with 60° tip angle and 1800 second relaxation delay. Data was processed using MestReNova version 11.0.3-18688. Chemical shifts (δ) are reported in ppm with respect to TMS (δ 0.00 ppm) in $D_2O$.

TEM images of the functionalised and unfunctionalised SiNPs were obtained using a JEOL 2100Plus operated at 200 kV in bright field mode equipped with a $LaB_6$ filament as the electron source. Each TEM samples was prepared using either continuous or holey carbon films with copper grid. The analyte particles were ground in an agate mortar and pestle prior to making the corresponding ethanol suspension. The suspension was then mixed thoroughly, and one drop was pipetted on an appropriate TEM grid. After drying the grid was loaded into the TEM microscope to be imaged.

TGA analysis was performed using a TA-TGA Q50 instrument which was calibrated with a platinum pan. Approximately 3 – 8 mg of sample was loaded in a ceramic crucible and placed in the standard platinum TGA pan for the analysis. The sample was then heated to 790 °C from room temperature at a ramp rate of 20 °C.min$^{-1}$ and the weight of the sample was recorded as a function of temperature.

Elemental analysis was carried out at MEDAC LTD.

The dynamic rheological properties of the NCO and OH inks (Table 5.3.8) were measured by the Kinexus Pro+ rheometer (Malvern Instruments) equipped with a 40 mm parallel plate geometry. The apparent viscosity and shear stress were recorded at 25 °C as a function of shear rate ranging from 1 $s^{-1}$ to 100 $s^{-1}$. Amplitude sweeps were performed to determine the linear viscoelastic region and this was automatically calculated by Malvern rSpace software. Subsequently, frequency sweep analysis was carried out to determine the viscoelastic profile of the different samples with varying compositions at frequencies from 10 to 0.1 Hz with a constant 1% shear strain within the pre-determined linear viscoelastic region at 25 °C. The gap between the parallel plates were set at 1 mm. Oscillatory stress ramp tests were performed to reveal the yield stress of the NCO and OH inks. In this test, inks were subject to increasing shear stress from 0.01 Pa to 1000 Pa. The yield stress was determined at the cross-over point between G′ and G″ data under stress-controlled oscillatory measurements.

### 5.6.1 Synthesis of the SiNPs

Silica NPs were prepared utilising the method reported by Stöber and Fink[21] as following: tetraethyl orthosilicate (6.61 mL, 31.50 mmol) was added to a mixture of ammonium hydroxide (9 mL, 35%) and ethanol (225 mL) and stirred overnight at 1000 rpm at ambient temperature. The solvent was then removed *in vacuo* to provide a fine white powder. The powder was then washed with ethanol (3 × 25 mL) and the mixture was centrifuged in order to isolate the solid. The particles were vortexed with ethanol before centrifuging for each wash. The powder was then dried in a vacuum oven at 100 °C for 2 hours at 400 mbar to yield a fine white powder. m = 2.11 g, 77.3% Yield. IR (ATR) ν ($cm^{-1}$): 3387, 2982, 1137, 1050, 951, 794, 572.

### 5.6.2 Preparation of PU1-5%-Blend nanocomposite

**PU1** (see Section 3.5.2, Chapter 3 for the synthesis protocol used to generate **PU1**) (7.00 g) was dissolved in THF (50 mL). A desired amount of **SiNP** (0.35 g) was dispersed in THF (20 mL) and sonicated for 2 hours. The SiNP suspension thus produced was then added to the polymer solution and stirred, this mixture was then brought to and maintained under reflux for 16 hours. The mixture was then concentrated *in vacuo* and drop cast into a PTFE mould (5 × 5 × 1 cm). Finally, the nanocomposite film was dried at ambient condition prior to drying in a vacuum oven at 70 °C and a pressure of 600 mbar for 16 hours.

### 5.6.3 Preparation of PU1+SiNP 5wt%

Krasol-HLBH P2000 (2.00 g, 0.95 mmol) was dried in oven at 100 °C under 600 mbar for 1 hour prior to use. 4,4′-MDI (0.55 g, 2.20 mmol) was added and stirred at 80 °C under $N_2$ for 3 hours. Meanwhile, 0.14 g SiNP was dried at 120 °C under vacuum for 3 hours. The prepolymer mixture was dissolved in anhydrous THF (20 mL) and cooled to room temperature and transferred to the round-bottom flask containing the dried SiNPs. The mixture was stirred for 3 hours at 80 °C prior to addition of AmMorph (0.28 mL, 2.20 mmol). Then the mixture stirred at 80 °C overnight. Finally, the reaction mixture was concentrated *in vacuo* and the crude product was then dissolved in the minimum volume of chloroform (*ca.* 10 mL) and precipitated into methanol. The obtained nanocomposite was dissolved in THF and drop cast into a PTFE mould. The film was dried at room temperature for 1 day prior to drying inside a vacuum oven at 40 °C and 600 mbar for 24 hours. m = 2.5 g. IR (ATR) ν ($cm^{-1}$): 3329, 2957, 2920, 2862, 2853, 1730, 1702, 1653, 1598, 1542, 1511, 1458, 1445, 1411, 1379, 1266, 1221, 1205, 1180, 1145, 1114, 1068, 1018, , 856, 814, 768, 720; GPC (THF): $M_n$ = 6800 Da, $M_w$ = 11000 Da, $Đ$ = 1.65; DSC: $T_g$ = -48.16 °C.

### 5.6.4 Synthesis of the amine functionalised SiNPs ($H_2N$-SiNP)

Using a modification of the method reported by Stober and Fink,[21] tetraethyl orthosilicate (5.8 mL, 25.97 mmol) was added to a mixture of ammonium hydroxide (8 mL, 35%) and ethanol (200 mL) and stirred at 1000 rpm at ambient temperature for 3 hours. APTES (see Table 5.6.1 below for the quantities employed) was then added slowly to the mixture and this was stirred for another 3 hours. The volume of solvent was reduced *in vacuo*. The obtained white powder was washed and dried following the same procedure employed for the SiNPs (see section 5.6.1). m = 7.22 g. IR (ATR) ν ($cm^{-1}$): 3268, 2924, 2861, 1591, 1025, 779, 691.

***Table 5.6.1:*** *The amount of APTES reagent used in synthesis of the* ***$NH_2$-SiNP****.*

| Sample number | 1 | 2 | 3 | 4 | 5 |
|---|---|---|---|---|---|
| mmol | 12.98 | 25.97 | 38.95 | 51.94 | 64.95 |
| Amount (mL) | 3.03 | 6.07 | 9.12 | 12.15 | 15.19 |

### 5.6.5 Preparation of PU1+$H_2N$-SiNP nanocomposite

Krasol-HLBH P2000 (2.00 g, 0.95 mmol) was dried in oven at 100 °C under 600 mbar. 4,4′-MDI (0.55 g, 2.20 mmol) was added and stirred at 80 °C under $N_2$ for 3 hours. Meanwhile, 0.14 g **$H_2N$-SiNP** was dried at 120 °C under vacuum for 3 hours. The prepolymer mixture was dissolved in anhydrous THF (20 mL) and transferred to the round-bottom flask containing the **$H_2N$-SiNP**. The mixture stirred for 3 hours at 80 °C prior to addition of AmMorph (0.28 mL, 2.20 mmol), the mixture was then stirred at 80 °C overnight. Finally, the reaction mixture was concentrated *in vacuo*, then dissolved into the minimum volume of chloroform (*ca*. 10 mL) and precipitated into methanol. The obtained nanocomposite was dissolved in THF and drop cast into a PTFE mould. The film was dried at room temperature for 1 day prior to drying inside a vacuum oven at 40 °C at 600 mbar for 24 hours. m = 2.13 g, 64% yield. IR (ATR) ν ($cm^{-1}$): 3315, 2941, 2916, 2851, 1731, 1704, 1655, 1595, 1537, 1511, 1460, 1440 1411, 1378, 1306, 1269, 1219, 1203, 1179, 1142, 1113, 1066, 1033, 1017, 941, 913, 851, 808, 766, 717, 632, 609; GPC (THF): $M_n$ = 7300 Da, $M_w$ = 10400 Da, $Đ$ = 1.43; DSC: $T_g$ = -46.26 °C.

### 5.6.6 Synthesis of $NH_2$/$CH_3$-SiNP

Absolute ethanol (110 mL) and 4.4 mL of ammonium solution (35%) were mixed in a flask prior to the addition of tetraethyl orthosilicate (TEOS). The solution was stirred at room temperature for 2.5 hours. (APTES) and *n*-propyltriethoxysilane (PTES) were then added slowly simultaneously to the solution and the mixtures was left stirring overnight (See Table

5.3.6 for the reactant amounts). The solution was then centrifuged at 4000 rpm for 10 minutes and the solvent was decanted. The particles were washed 3 more times with fresh ethanol following the same procedure as employed for the SiNPs (Section 5.6.1). The samples were then dried in an oven at 30 °C under vacuum. IR (ATR) ν ($cm^{-1}$): 2940, 2865, 1638, 1567, 1131, 1037, 951, 785; TGA: $T_{decomp}$ = 140 °C, 481 °C.

### 5.6.7 Reactive extrusion (REX) process and instrumentation

The reactive extrusion system employed in this study was modified from a LulzBot TAZ6 printer (FAME 3D, Fargo, North Dakota, USA) integrated with a high precision volumetric dosing unit (Preeflow eco-DUO450 two-component mixing dispenser, ViscoTec). Both the isocyanate and polyol feeds were transferred into 360 ml Optimum® syringe barrels (Nordson EFD). Subsequently, a home-built feed supplying system pneumatically transported the reagent mixtures from the Optimum® syringe barrels to the dosing unit by pressurised nitrogen (3 bar). Feeds from both syringe barrels were then driven by a screw pump inside the dosing unit to efficiently mix the components. The mixing ratio and the flow rate were regulated using a control box (Preeflow eco-Control EC200-DUO). The isocyanate and polyol feeds (Table 5.3.8) were mixed at 1/1 (v/v) and 1.1/1 (mol/mol) in the static mixer (IDMMKH03-16S, Intertronics) (outlet internal diameter (ID) = 1 mm, inlet ID = 3.2 mm, length (L) / diameter (D) = 23, the number of mixing elements = 16), and extruded onto the print bed. Initial trial studies established that the ideal flowrate was 2 $ml.min^{-1}$, at this flow rate, the filament was deposited consistently without any material clogging in the mixer. Bar samples (2 layers, 80 mm × 4 mm) were printed using inks from three functionalised SiNPs. The printed bar samples were later used for thermo-mechanical characterisations.

### 5.6.8 Synthesis of 5.1

**DBS-iPr** (0.2 g, 0.45 mmol, 1.5 equiv.) was dissolved in anhydrous THF (20 mL). 3-(Triethoxysilyl)propyl isocyanate (78.19 µL, 1 equiv.) was then added to the solution and stirred at 80 °C under inert condition for 3 hours. The resultant compound was used in the next step without further purification. MS (m/z) calc. for $[C_{36}H_{55}O_{10}NNaSi]^+$ = 712.3493 Da, found = 712.3481 Da

### 5.6.9 Synthesis of DBS-iPr@SiNP

SiNP (0.6 g) was dried at 120 °C under reduced pressure for 2 hours and then dispersed in ethanol (20 mL) and sonicated for 20 minutes. The solution of **5.1** and ammonium hydroxide (0.5 mL, 35%) were then added to the suspension and the mixture was stirred for 30 minutes

at 75 °C. The suspension was cooled to room temperature and then stirred for 12 hours. The synthesised particles were washed with THF (3×) and once with ethanol in combination with a centrifuge to separate the solids and solvent following the general procedure described for the washing of SiNP (see Section 5.6.1). The modified particles were then dried in oven at 80 °C overnight. (0.59 g). IR (ATR) ν ($cm^{-1}$): 3292, 1652, 1549, 1046, 941, 792.

## 5.7 References


1 X. Zhai, Y. Ma, C. Hou, F. Gao, Y. Zhang, C. Ruan, H. Pan, W. W. Lu and W. Liu, *ACS Biomater. Sci. Eng*., 2017, **3**, 1109–1118.

2 F. Lin, R. Wang, L. Liu, B. Li, L. W. Ouyang and W. J. Liu, *Express Polym. Lett*., 2017, **11**, 690–703.

3 L. Jin, H. Wang and Y. Yang, *Compos. Sci. Technol*., 2013, **79**, 58–63.

4 L. Wei, N. Hu and Y. Zhang, *Materials (Basel).*, 2010, **3**, 4066–4079.

5 A. J. Clancy, D. B. Anthony and F. De Luca, *ACS Appl. Mater. Interfaces*, 2020, **12**, 15955–15975.

6 A. Liberman, N. Mendez, W. C. Trogler and A. C. Kummel, *Surf. Sci. rep*, 2014, **69**, 132–158.

7 J. G. Croissant and C. J. Brinker, *Biodegradable Silica-Based Nanoparticles: Dissolution Kinetics and Selective Bond Cleavage*, Elsevier Inc., 1st edn., 2018, vol. 43.

8 N. Guermazi, K. Elleuch, H. F. Ayedi and P. Kapsa, *J. Mater. Process. Technol*., 2008, **203**, 404–410.

9 S. Salimi, T. S. Babra, G. S. Dines, S. W. Baskerville, W. Hayes and B. W. Greenland, *Eur. Polym. J*., 2019, **121**, 109264.

10 S. Mondal and J. L. Hu, *Indian J. Fibre Text. Res*., 2006, **31**, 66–71.

11 M. Gorji, A. A. A. Jeddi and A. A. Gharehaghaji, *J. Appl. Polym. Sci*., 2010, **125**, 4135–4141.

12 J. Joseph, R. M. Patel, A. Wenham and J. R. Smith, *Trans. Inst. Met. Finish*., 2018, **96**, 121–129.

13 E. A. Wilder, M. B. Braunfeld, H. Jinnai, C. K. Hall, D. A. Agard and R. J. Spontak, *J. Phys. Chem. B*, 2003, **107**, 11633–11642.

14 H. Zou, S. Wu and J. Shen, *chem. Rev*., 2008, **108**, 3893–3957.

15 D. Pedrazzoli and I. Manas-Zloczower, *Polymer (Guildf).*, 2016, **90**, 256–263.

16 M. Z. Rong, M. Q. Zhang, S. L. Pan, B. Lehmann and K. Friedrich, *Polym. Int*., 2004, **53**, 176–183.

17 B. Lin and S. Zhou, *Prog. Org. Coatings*, 2017, **106**, 145–154.

18 H. Kim, J. Ko, D. Sohn, J. Ryu, J. Lee and J. Shin, *Colloids Surfaces A Physicochem. Eng. Asp*., 2016, **511**, 55–63.

19 E. Soto-Cantu, R. Cueto, J. Koch and P. S. Russo, *Langmuir*, 2012, **28**, 5562–5569.

20 A. Idris, Z. Man, A. S. Maulud, M. A. Bustam, H. A. Mannan and I. Ahmed, *Appl. Surf. Sci*., 2020, **506**, 144978.

21 W. Stöber and A. Fink, *J. Colloid Interface Sci.*, 1968, **26**, 62–69.

22 L. P. Singh, S. K. Bhattacharyya, R. Kumar, G. Mishra, U. Sharma, G. Singh and S. Ahalawat, *Adv. Colloid Interface Sci*., 2014, **214**, 17–37.

23 Q. Guo, P. Zhu, G. Li, J. Wen, T. Wang, D. (Daniel) Lu, R. Sun and C. Wong, *Compos. Part B Eng*., 2017, **116**, 388–397.

24 J. R. Martínez, F. Ruiz, Y. V. Vorobiev, F. Pérez-Robles and J. González-Hernández, *J. Chem. Phys*., 1998, **109**, 7511–7514.

25 A. Feula, X. Tang, I. Giannakopoulos, A. M. Chippindale, I. W. Hamley, F. Greco, C. Paul Buckley, C. R. Siviour and W. Hayes, *Chem. Sci*., 2016, **7**, 4291–4300.

26 R. W. Nunes, J. R. Martin and J. F. Johnson, *Polym. Eng. Sci*., 1982, **22**, 205–228.

27 S. Salimi, L. R. Hart, A. Feula, D. Hermida-Merino, A. B. R. Touré, E. A. Kabova, L. Ruiz-Cantu, D. J. Irvine, R. Wildman, K. Shankland and W. Hayes, *Eur. Polym. J*., 2019, **118**, 88–96.

28 H. Behniafar and M. K. Nazemi, *Polym. Bull*., 2017, **74**, 3739–3749.

29 K. N. Pham, D. Fullston and K. Sagoe-Crentsil, *Aust. J. Chem*., 2007, **60**, 662–666.

30 M. Luhmer, J. B. D'Espinose, H. Hommel and A. P. Legrand, Magn. Reson. *Imaging*, 1996, **14**, 911–913.

31 T. Kobayashi, D. Singappuli-Arachchige, Z. Wang, I. I. Slowing and M. Pruski, *Phys. Chem. Chem. Phys*., 2017, **19**, 1781–1789.

32 S. Liu, R. Eijkelenkamp, J. Duvigneau and G. J. Vancso, *ACS Appl. Mater. Interfaces*, 2017, **9**, 37929–37940.

33 Q. Chen, P. F. Cao and R. C. Advincula, *Adv. Funct. Mater*., 2018, **28**, 1–9.

34 N. S. Hmeidat, J. W. Kemp and B. G. Compton, *Compos. Sci. Technol*., 2018, **160**, 9–20.

35 M. Dinkgreve, J. Paredes, M. M. Denn and D. Bonn, *J. Nonnewton. Fluid Mech*., 2016, **238**, 233–241.

36 J. Xu, L. Cheng, Z. Zhang, L. Zhang, C. Xiong, W. Huang, Y. Xie and L. Yang, *RSC Adv*., 2019, **9**, 8184–8196.

37 P. Krober, J. T. Delaney and U. S. Schubert, *J. Mater. Chem*., 2009, **19**, 5234–5238.

38 A. Pattanayak and S. C. Jana, *Polymer (Guildf)*., 2005, **46**, 5183–5193.

39 P. K. Behera, K. M. Usha, P. K. Guchhait, D. Jehnichen, A. Das, B. Voit and N. K. Singha, *RSC Adv*., 2016, **6**, 99404–99413.

40 H. S. Lee, Y. K. Wang, W. J. MacKnight and S. L. Hsu, *Macromolecules*, 1988, **21**, 270–273.

41 S. Zhang, Z. Ren, S. He, Y. Zhu and C. Zhu, Spectrochim. *Acta - Part A Mol. Biomol. Spectrosc*., 2007, **66**, 188–193.

42 C. Zhang, Z. Ren, Z. Yin, H. Qian and D. Ma, *Polym. Bull*., 2008, **60**, 97–101.

43 G. Trovati, E. A. Sanches, S. C. Neto, Y. P. Mascarenhas and G. O. Chierice, *J. Appl. Polym. Sci*., 2010, **115**, 263–268.

44 G. C. Dizon, G. Atkinson, S. Argent, L. T. Santu and D. B. Amabilino, *Soft Matter*, 2020, **16**, 4640-4654

# Chapter 6

## A Thermoresponsive Composite Adhesive that can be heated by an Oscillating Magnetic Field to facilitate debonding

*This chapter has been published as a peered review research article: S. Salimi, T. S. Babra, G. S. Dines, S. W. Baskerville, W. Hayes and B. W. Greenland, Composite polyurethane adhesives that debond-on-demand by hysteresis heating in an oscillating magnetic field, Eur. Polym. J., 2019, 121, 109264.*

*Note regarding contributions to this study: S. Salimi performed the synthesis, characterisation and analysis of the material with the guidance and help of T. S. Babra under the supervision of W. Hayes and B. W. Greenland. G. S. Dines and S. W. Baskerville work for Stanelco RF Technologies Ltd. who manufacture industrial heating equipment utilising RF technology and set up and supervised the OMF experiment.*

*Note: The initial investigation, design and characterisation of the composite material in this Chapter were reported in the author's MSc thesis and partially reported in her dissertation. S. Salimi, MSc Dissertation, University of Reading, 2017.*

### 6.1 Abstract

A thermoresponsive composite adhesive has been synthesized that can be heated to facilitate debonding by application of an oscillating magnetic field (OMF). The adhesive is composed of a polyurethane (**SPU 3.1 (AmMorph)**) continuous phase with iron oxide particles ($Fe_3O_4$) as the filler (between 1 and 20 wt%). Under standard thermal activation, the adhesives behave as a thermoplastic and can undergo three bond/fracture/heal cycles. The values of the Young's modulus (*E*) and the ultimate tensile strength (UTS) were essentially constant over the series of composites examined. In contrast, the modulus of toughness for the composite containing 1% $Fe_3O_4$ was significantly greater (67%) than that of the pure **SPU 3.1 (AmMorph)**. For each adhesive composition, both the UTS and modulus of toughness tended to increase over the healing cycles (healing efficiencies over 100%) showing that these parameters were dependent on the thermal history of the adhesive. At $Fe_3O_4$ loading levels of 8 wt% and above, the adhesive heats rapidly when placed in an OMF, resulting in debonding of a 50 g static load under the force of gravity in less than 2 minutes.

## 6.2 Introduction

In recent years there have been significant efforts to produce adhesives with added functionality beyond the ability to securely bond materials.[1,2] For example, adhesives have been produced that can detect specific chemicals,[3] damage,[4] strain,[5] changes in temperature[6] or be activated under specific conditions.[7] Furthermore, responsive adhesives have been produced that exhibit the ability either to heal and rebond two surfaces after fracture or debond-on-demand in response to a specific stimulus.[8-10] A broad range of applications may be envisaged for healable and debondable adhesives, for example, in removable prosthetics,[11] dentures[12-14] or to facilitate recycling of complex multicomponent products including vehicles and mobile phones.

The dynamic nature of specific covalent bonds[15-16] has been successfully used to introduce reversibility into adhesive materials.[9] For example, Michal *et al.* have taken advantage of disulfide bonds to make a reversible shape-memory adhesive[17] whereas Aubert and co-workers have employed Diels-Alder chemistries to generate an adhesive in which the debonding reaction occurs above 90 °C.[18] In addition, Tang *et al.* have produced a dynamic vitrimer based on triazolium salts which proved to be an extremely high strength re-healable adhesive.[19]

A conceptually distinct route to obtain the functionality required to produce healable adhesives is to exploit the inherent reversibility of supramolecular bonds.[20,21] Supramolecular materials typically contain relatively low molecular weight species that self-assemble into higher pseudo-crosslinked networks in the solid state.[22] The strength of the supramolecular interactions can be tuned by varying the structure of the supramolecular motifs at the molecular level which can lead to predictable changes response of polymer in the solid state.[23-25] Furthermore, application of an appropriate stimuli results in real time, reversible changes in strength of the supramolecular bonds in the materials which has a dramatic effect on the physical properties (tensile strength/viscosity) of the bulk polymer. For example, hydrogen bonding,23,26 π-π stacking[27,28] and metal-ligand bonds[8,29,30] have found widespread application as healable and self-healing materials.[27,28,31-33] In these systems, loss of strength caused by damage can be reversed by application of a specific stimulus, for example pressure, temperature or UV radiation. Recently, a rebondable adhesive was reported which harnessed the thermo-reversibility of a hydrogen bonded polyurethane but had the added functionality brought by the inclusion of a chemo-responsive monomer in the backbone of the polymer.[34] This adhesive underwent multiple bonding/debonding cycles in response to heat and/or force yet could also undergo irreversible reduction of adhesion after depolymerisation on contact with fluoride ions.

A key factor in designing healable and debondable adhesives is the selection of the debonding stimulus because it will constrain the utility of the final adhesive.[35] A hot melt adhesive material is reversible if the adhesive can be heated to a suitable temperature. However, frequently reprocessed in this manner is not practical because the bonded region may not be accessible, or the bonded substrates not sufficiently thermally conductive or stable to achieve and maintain the temperatures required to melt the adhesive. In addition, although materials that respond to other stimuli such as UV radiation have been realized,[17] this stimulus can only be used in an adhesive setting if the bonded substrates are transparent at the appropriate wavelengths. For example, Kihara *et al.* took advantage of azobenzene photoisomerization and produced a rebondable adhesive which leaves substrate intact upon debonding as a result of no heat requirement.[36,37] However, the application of this adhesive is limited to assemblies that featured at least one UV/light-transparent substrate. This constraint precludes debonding of many common materials by UV/vis radiation (such as wood, metals, optically opaque polymers).

An alternative method of transferring energy to a material is by induction heating (IH).[4,38,39] During IH, energy is transferred to conductive materials from an oscillating magnetic field (OMF), which is converted to heat through eddy current loss and then transferred to the surrounding matrix.[4,40] In case of magnetic particles under IH condition, particles are aligned with induced magnetic field. Upon reversing the field, the induced magnetic field has to overcome the residual magnetism in the particles as well. This work done by an induced magnetic field is called hysteresis loss and generates heat which provide the thermal energy required to activate the SPU adhesive in this study. OMFs can be routinely generated by passing an alternating current through a conductive coil. IH is used widely on an industrial scale for welding and melting metals. Also, induction sealing has been extensively used for *ca*. six decades for hermetic sealing of different thermoplastic packages with no effect on the contents.[41] Adzima *et al.* have investigated the use of induction heating to provide the energy for healing in a Diels-Alder crosslinked networks.[39] More recently, Ahmed *et al.* produced a multifunctional healable material through induction heating of a polyvinyl acetate nanocomposite.[4]

## 6.3 Results and Discussion

It would be possible to harness the energy transfer of an OMF to iron oxide particles within a SPU[42] thermoplastic adhesive to produce a healable and debondable composite system (Figure 6.3.1).[43] IH as a means of addressing a healable adhesive would offer significant advantages over conventional thermal heating because the OMF does not have an effect on non-conductive or non-ferromagnetic materials. Thus, many commonly bonded materials

such as wood, plastic and glass do not experience direct heating from an OMF. This overcomes problems associated with melting or degrading the bonded substrates that may be encountered when heating a thermo-responsive adhesive to its melting temperature. A further advantage of the ability of OMF to penetrate non-conductive materials is that it potentially allows for the debonding of surfaces that could not be accessed by direct heating or UV radiation as a consequence of being contained within larger components.

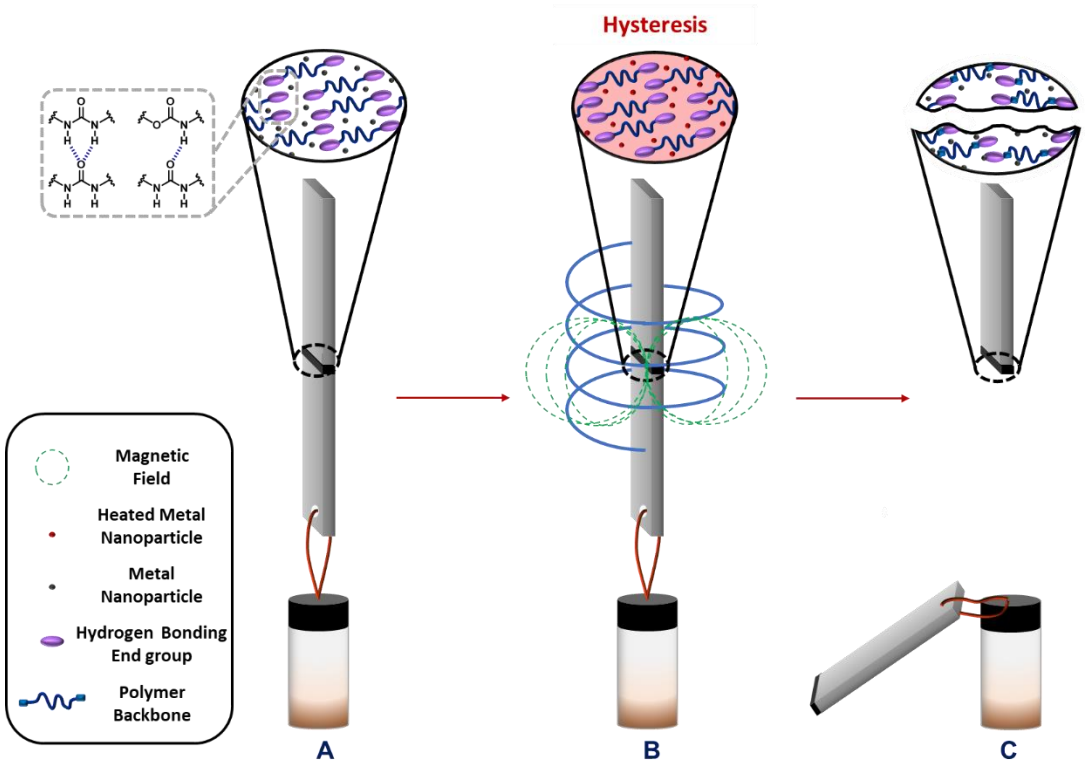


***Figure 6.3.1:*** *Concept schematic of a healable and OMF debondable $Fe_3O_4$ composite adhesive: A) the PU-composite bonding two substrates; B) application of OMF from a coil which heats the adhesive via energy dissipated from hysteresis loss in $Fe_3O_4$ particles and C) the supramolecular bonds in the PU network weakened by the heat, allowing facile debonding of the substrates.*

In this chapter is described the synthesis of the first healable composite adhesive that can be heated and therefore readily debonded on the application of an OMF. This is achieved by the addition of iron oxide particles to the PU, which are known to be heated efficiently under OMF conditions.[44] The composite adhesive can bond a range of substrates including glass, aluminium and Polyvinyl chloride (PVC), and can be rapidly heated to facilitate successful debonding when placed in an OMF.

### 6.3.1 Design and synthesis of the continuous polyurethane phase of the adhesive

The SPU adhesive **3.1 (AmMorph)** which was also reported in Chapter 3, was synthesized from three components; a hydrogenated hydroxyl-terminated polyolefin diol **2.2** (Krasol

HLBH-P2000), methylenebis(phenyl isocyanate) (MDI) **2.3** to afford the pre-polymer in the absence of solvent[45] (**2.4**) which was end-capped by the addition of 4-(2-aminoethyl)morpholine (**3.3**) (Scheme 6.3.1). The chemical composition of the polymer was selected because closely related materials have been shown to be non-toxic and to be adhesive to biological surfaces.[33] The polymer was isolated in a yield of 80% after precipitation into methanol (10.3 kg.mol$^{-1}$, Đ = 1.63).

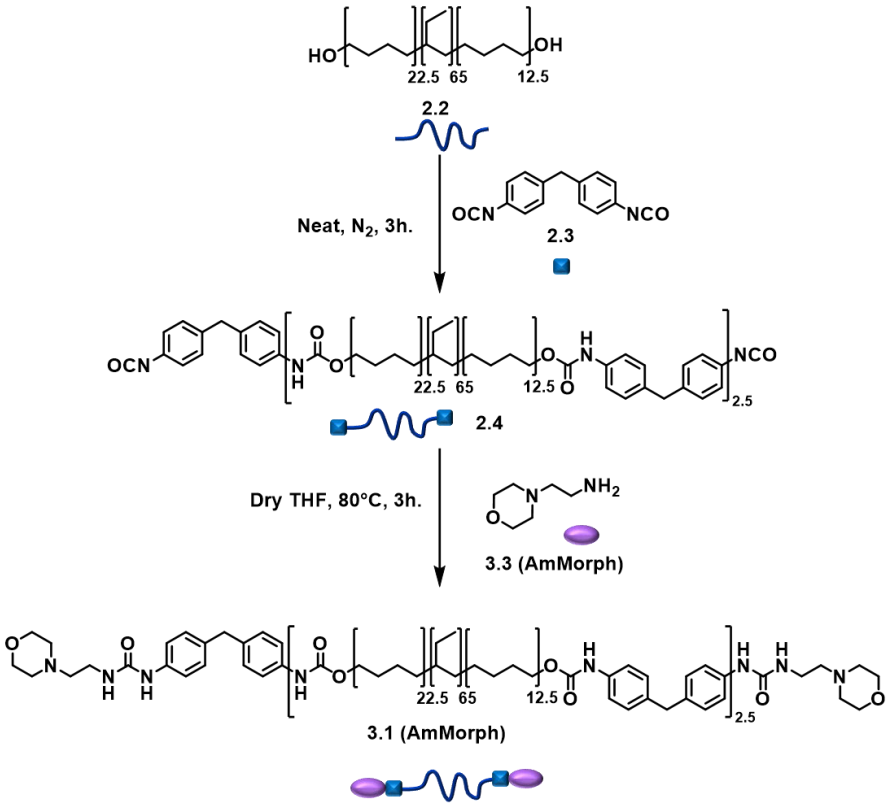


***Scheme 6.3.1****: The synthesis of PU adhesive* ***3.1 (AmMorph)****. Each chemical structure is also denoted schematically (ratio of OH:NCO = 1:1).*

Thin films suitable for tensile testing were cast from THF in PTFE moulds (15 × 15 cm) and dried slowly under vacuum for 18 hours. Variable temperature analysis of the polymer by $^{1}$H NMR spectroscopy in solution and IR spectroscopy in the solid state revealed the presence of the expected hydrogen bonding interactions between the urea and urethane components. In the $^{1}$H NMR spectrum recorded at ambient temperature, resonances were evident at *ca.* 5.2 ppm and *ca.* 6.5 ppm which were attributed to the urea and urethane's protons – these resonances exhibited downfield shifts as the temperature of the sample solution was decreased indicating the increase in the concentration of hydrogen bonded species. (Figure 6.3.2).

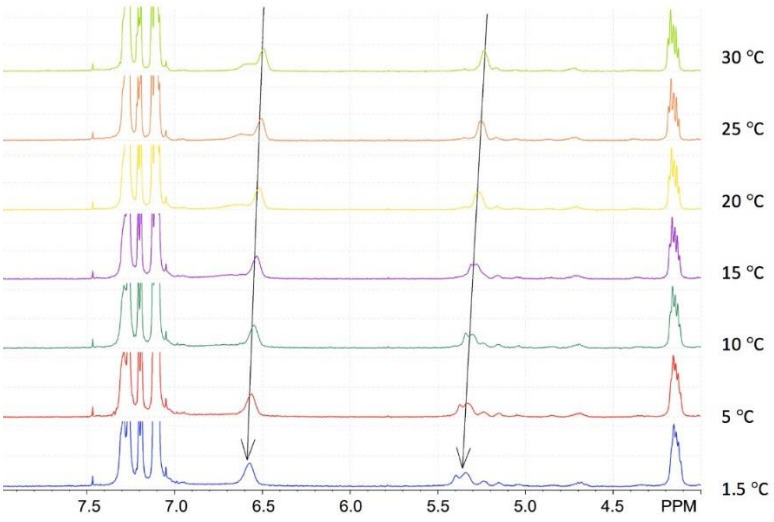


***Figure 6.3.2:*** *Partial VT-NMR (500 MHz) spectra of* ***SPU 3.1 (AmMorph)*** *showing changes in chemical shifts of NH group of urea and urethane. Also differences in the splitting of the resonances of exchangeable hydrogens by changing temperature is negligible.*

VT-IR experiment was also performed on the thin film. The sample was placed between two discs of the metal sample holder. The temperature shown are the temperature of the sample holder. The integration of the N-H absorption was carried out between 3200 to 3400 $cm^{-1}$ for each temperature. As the temperature of the sample increased, the intensity of the signal indicative of a hydrogen bonded NH (3320 $cm^{-1}$) decreased (≈ 14%), confirming a reduction in the strength of the hydrogen bonds as also shown by a decrease in the breadth of the N-H absorbance band,[46] proving the thermo-responsive nature of the synthesised polymer occurs as a result of its supramolecular nature (Figure 6.3.3).

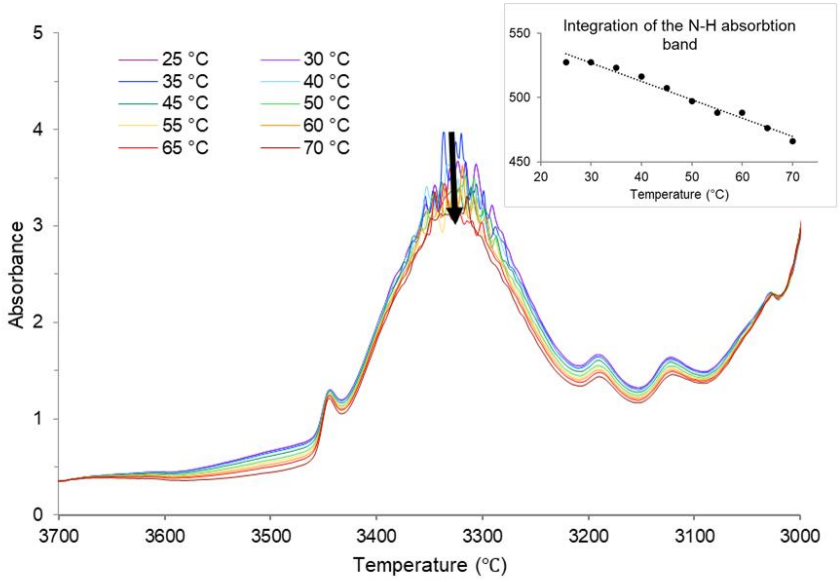


***Figure 6.3.3:*** *VT-IR spectra of the* ***SPU 3.1 (AmMorph)*** *adhesive film. Insert showing a decrease in the absorption of the N-H band.*

The synthesis and characterisation of the SPU **3.1 (AmMorph)** was carried out as described in Chapter 3, see Section 3.3.1.

### 6.3.2 Composite preparation and analysis

A series of nanocomposites were produced from SPU **3.1 (AmMorph)** which differed in the quantity of iron oxide particles incorporated in the mixture (up to 20 wt%). Each nanocomposite was formulated by melt processing. The required wt% of iron oxide NP was hand mixed with a known quantity of the SPU above the melting temperature of the polymer (100 °C) to produce six nanocomposite samples which varied by the filler loading level (1, 5, 8, 12, 16 and 20 wt%).

Initial adhesion studies were carried out by taking a circular sample of the 8 wt % composite (*ca*. 2 mg, 2 mm diameter, 0.6 mm thickness) to bond a range of different substrates: wood, aluminium, PVC and glass. The cut samples were sandwiched between two substrates and they were then placed on a preheated hot plate at 80 °C for 3 minutes on each side. After cooling to room temperature, all the samples had bonded securely, and they could be handled without breaking. Regardless of the substrate, the composite showed the ability to hold a static load of 100 g (Figure 6.3.4). The weight was hung for *ca.* 5 min for photography purpose and it was then removed from the substrates.

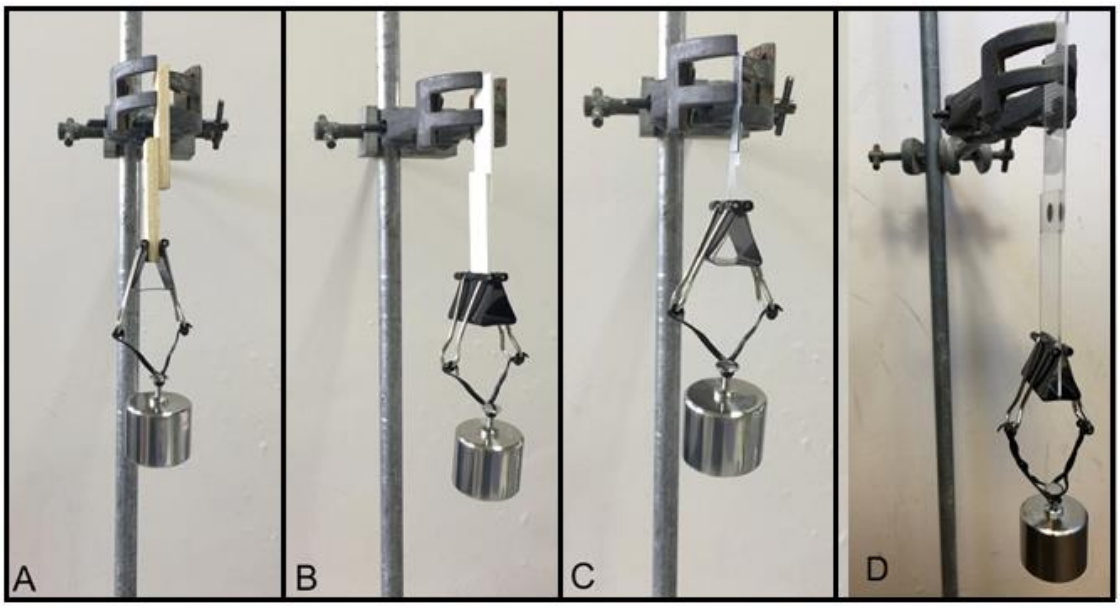


***Figure 6.3.4:*** *Substrates (A) wood, (B) PVC, (C) aluminium and (D) glass bonded by 2 mg of the 8% composite supporting a static 100 g load. The surfaces were not treated prior to use.*

Visual inspection of the adhered glass slides showed that the iron oxide particles were not homogeneously dispersed throughout the **SPU 3.1 (AmMorph)** in the bonded samples.[31]

Figure 6.3.5 shows the images taken of each wt% composite as viewed through the adhered glass slide. During the bonding process the polymer has flowed outward resulting in a final diameter of approximately 7 mm (starting diameter = 2 mm), accounting for the spoke-like distribution of the particles. It can be seen that the samples all contain dense, black, highly aggregated regions (approximately 20 - 80 microns particle clusters) and cloudy-looking regions where the particles are more evenly dispersed.

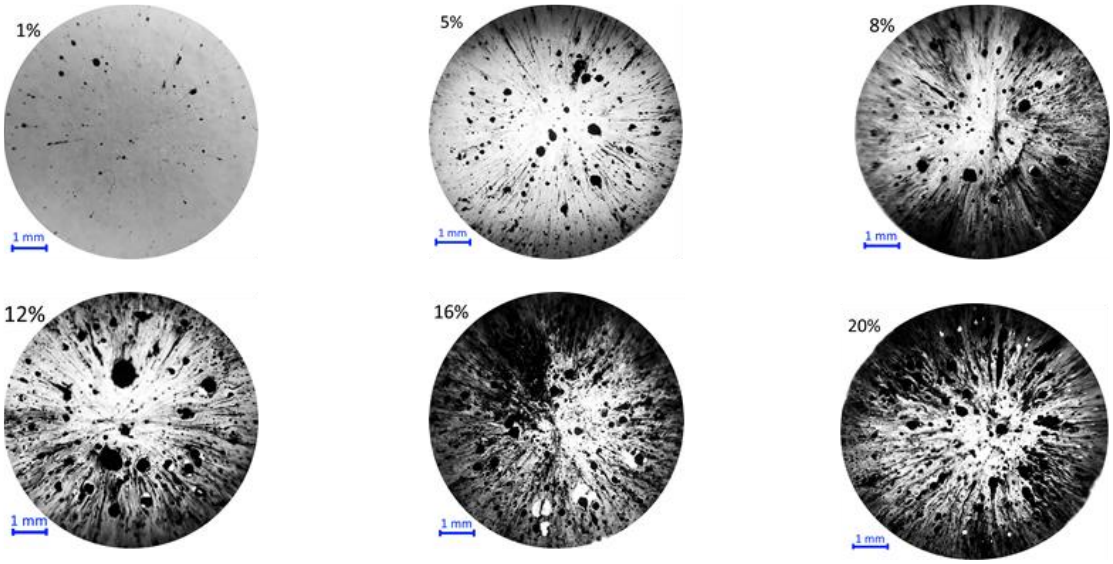


***Figure 6.3.5:*** *Black and white pictures of the composites taken with macro lens to investigate Fe3O4 particle aggregation at each wt% loading level.*

The area covered by the particles, whether aggregated or finely dispersed was determined by comparison of the dark and light regions by image analysis using the software package ImageJ. In which the dark areas are representative of $Fe_3O_4$ particles. After preparing the samples, a clip macro lens was attached to a phone camera. A torch was used behind the samples to provide backlight. Black and white images were then obtained from each sample. Images were then assessed using the ImageJ software and the black and white threshold was adjusted. These finalised images were analysed in ImageJ and the black areas were measured. The calculated black area determined by ImageJ were compared to the actual particle loadings. The results are shown in Table 6.3.1. Although even dispersion of filler particles in polymer/particle composites is desirable for improvement of the mechanical properties in comparison to the parent polymer, in this case aggregation of the particles was beneficial for more efficient localised heating.[47]

***Table 6.3.1****: The formulated iron oxide particle loading level and the coverage of particles (from Figure 6.3.5) for each composite as determined from the images of the adhesives as determined using ImageJ.*

| **Formulated loading level (wt%)** | 1.0 | 5.0 | 8.0 | 12.0 | 16.0 | 20.0 |
|---|---|---|---|---|---|---|
| **Area coverage of particles (%)** | 1.2 | 6.3 | 13.1 | 12.6 | 21.0 | 24.0 |

The deviation between the area covered by the iron oxide particles and the known loading may be accounted for by the low energy involved in the generation of the composite by hand mixing which did not efficiently separate the highly magnetic nanoparticles.[74,271,272] Thus, the dense areas contain particles in three dimensions, but they are only observed in two dimensions in the processed image of the adhesives. Indeed, the fabrication of adhesives with higher filler loading levels was not attempted as a consequence of the difficultly in dispersing the particles using this low energy formulation technique even at 20 wt% $Fe_3O_4$. However, the inhomogeneity of the composite clearly did not prevent adhesion (Figure 6.3.5) and therefore attention turned towards quantifying the effect of the level of filler on the thermally reversible properties of the adhesive.

### 6.3.3 Thermal healing and adhesive testing

Each composite (1-20 wt% filler) and the pristine **SPU 3.1 (AmMorph)** that did not contain iron oxide particles were used to bond two glass slides together, as described during the bonding experiments (see Section 6.3.2). In brief, a specified amount of each composite cut and sandwiched between two glass slides. The slides were secured using paperclips and then was placed on a pre-heated oven on each side in order. The samples were then cooled down and ready for subsequent analysis. (Figure 6.3.6)

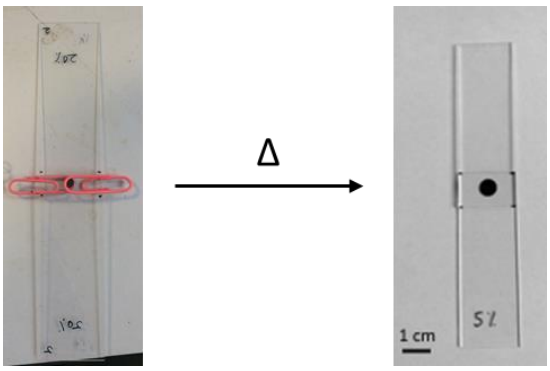


***Figure 6.3.6:*** *Preparation of the lap shear glass slide samples.*

Additionally, Tecbond™ 484-9900 which is delivered by a hot glue gun was selected as a typical commercial example with which to compare these novel materials to in terms of adhesion strength and samples were prepared using the same method. The selected commercial adhesive is recommended for attaching substrates such as wood, plastic, light gauge metals or paper and packaging applications and therefore suitable for most regular applications. The samples were subject to lap shear testing until failure by placing the prepared sample in a uniaxial tensile testing machine (see Appendix Figure A4 for stress-strain graphs). This process was repeated three times for each sample and the average tensile properties calculated (Figure 6.3.7). Significant differences were not observed in the ultimate tensile strength (UTS) between **SPU 3.1 (AmMorph)** and each of the different wt% composites (Figure 6.3.7 A) which indicate that the presence of filler does not inhibit the adhesion ability of the polyurethane matrix.

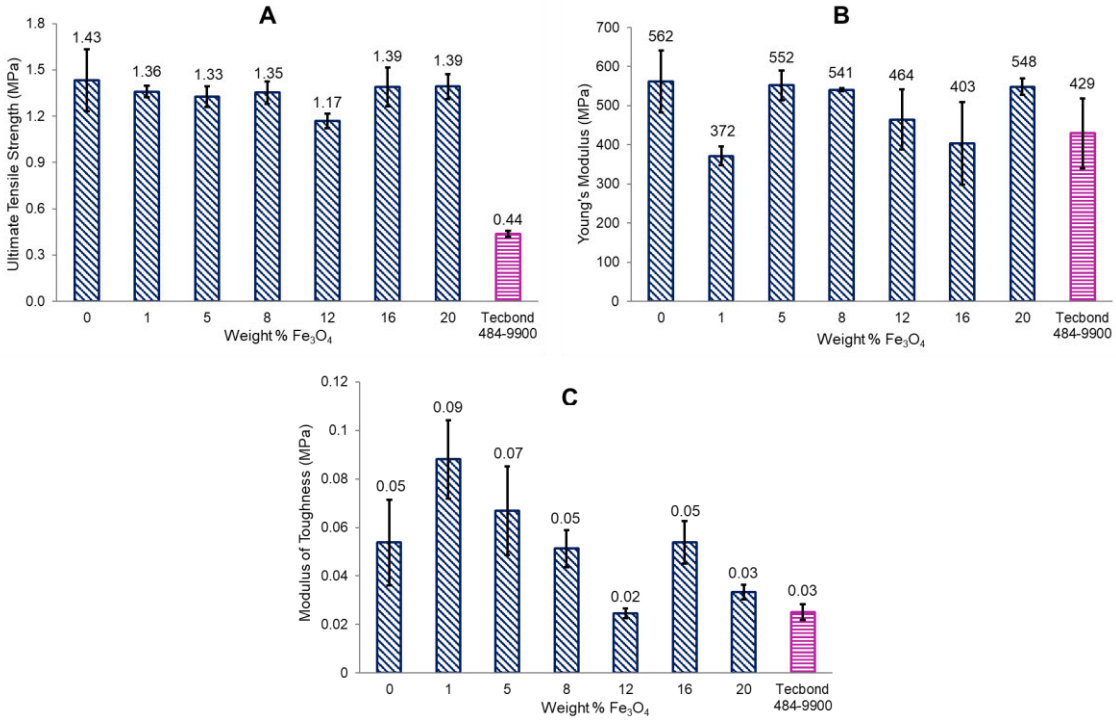


***Figure 6.3.7:*** *Lap shear tensile data for composites containing varying quantities of iron oxide nanoparticles compared with a commercially available hot melt adhesive. Errors are from 3 repetitions.*

In this study, since efforts were not concentrated upon improvement of the dispersion of the particles, the presence of the $Fe_3O_4$ particles in these composite samples did not reinforce the polymer matrix as demonstrated by conventional inorganic fillers[48,51] exploited in polymer composite preparation. Iron oxide particles are highly magnetic, and they tend to aggregate easily if preventative measures are not taken during the preparation of the composite. The bonding strength data from the lap shear tests revealed the magnitude of the Young's modulus

for SPU **3.1 (AmMorph)** and the composite adhesives was also largely independent of the iron oxide particle loading level (Figure 6.3.7 B).

In these comparative strength tests Tecbond™ (*ca*. 2 mg) was also used to adhere two glass slides which were then tested under the same lap-shear conditions as used previously for the composite materials (Figure 6.3.7). Table 6.3.3 shows a direct comparison of the UTS and modulus of toughness of the 8% composite with the Tecbond™ (See Appendix Figure A5 for raw data). It can be seen that the novel composite adhesive performed favourably with respect to the commercial sample and exhibited an improvement in UTS and modulus of toughness of 210% and 67%, respectively.

***Table 6.3.2:*** *A comparison of UTS and Toughness of a commercial hot-melt glue gun adhesive (Tecbond 484-9900) and the 8% composite adhesive. Errors are standard deviations of 3 repeat Experiments.*

| Tensile properties (MPa) | Ultimate Tensile Strength | Modulus of Toughness |
|---|---|---|
| Tecbond 484-9900 | 0.44 ± 0.02 | 0.025 ± 0.003 |
| 8% Composite Adhesive | 1.35 ± 0.07 | 0.051 ± 0.008 |

Afterward, to examine the thermo-reversible nature of the adhesive the lap shear glass slide samples which had been tested in the tensile testing machine, were put into contact again, secured with paper clips and put into oven at 80 °C for 10 minutes. After cooling down to room temperature, samples were pulled at the tensile tester and the process repeated two more times in total. The tensile test revealed that all nanocomposites became stiffer after each cycle (Figure 6.3.8). This phenomenon has been reported for related supramolecular materials[52] and occurs as a consequence of the repeated heating required to rebond the substrates. During each heating cycle the material can equilibrate to a lower energy supramolecular network. Thus, the rebonded materials are stronger and more resistant to permanent deformation. However, no meaningful difference was observed between different wt% of composites in terms of UTS (Figure 6.3.8 B). However, it was revealed that the modulus of toughness is dependent on the wt% of iron oxide NP (Figure 6.3.8C). At low wt% (NP $\leq$ 5%) the composites were tougher than the pure polymer. This could be attributed to interfacial interaction between filler and the polymer molecules which results in more efficient dissipation of the applied energy within the network. However, at higher wt% values, the material is phase separated and aggregation of the $Fe_3O_4$ particles occurs which results in reduction in the surface area and consequently a decrease in toughness.[31]

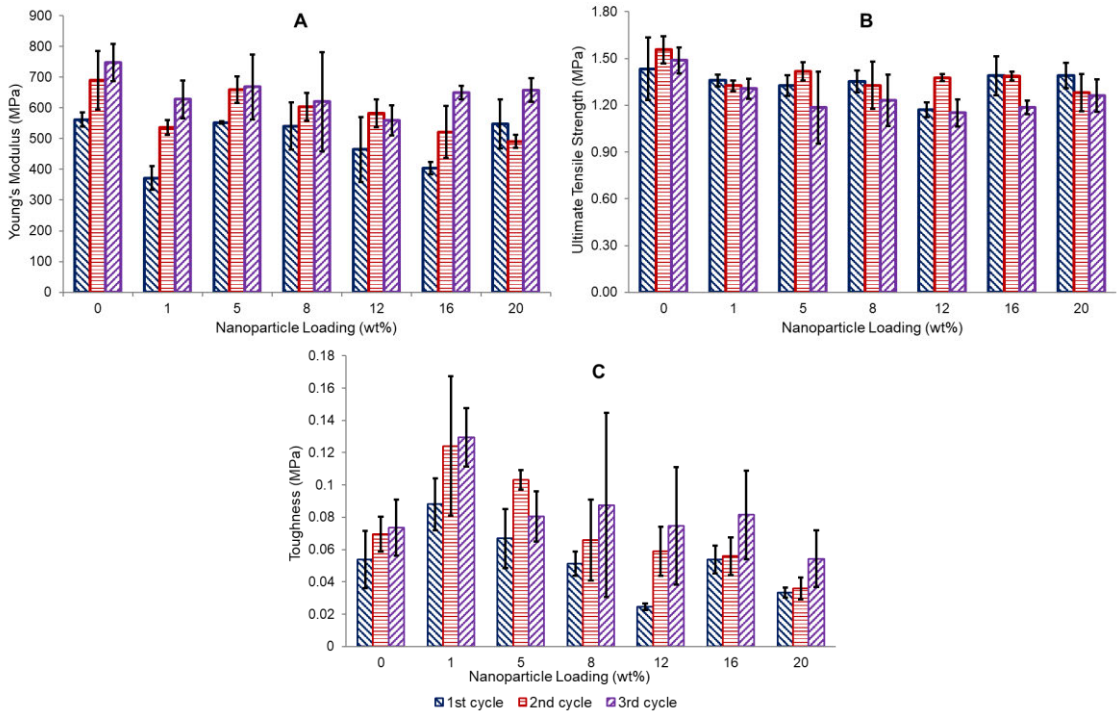


***Figure 6.3.8:*** *Calculated **l**ap shear tensile properties of composites containing varying quantities of iron oxide nanoparticles over two break/heal cycles (blue hatched bars: pristine material; red hatched bars: 1st healing cycle; purple hatched bars: 2nd healing cycle, errors are the standard deviations from the mean of 3 repetitions): (A) Young's modulus; (B) Ultimate Tensile Strength (UTS); and (C) modulus of toughness.*

### 6.3.4 Induction heat production experiment

After establishing the reversible adhesive nature of the composite, the material's response to OMF conditions was investigated. Firstly, a circular sample (*ca.* 2 mg) of each composite was placed on a petri dish with a pristine polyurethane in the middle with no content of magnetic filler. The petri dish was placed on top of the OMF generator coil, and the heating of the samples was monitored using FLIR™ IR thermal camera. Figure 6.3.9 illustrates the experiment setting and shows the temperature change over one minute of applying OMF observed by the thermal camera.

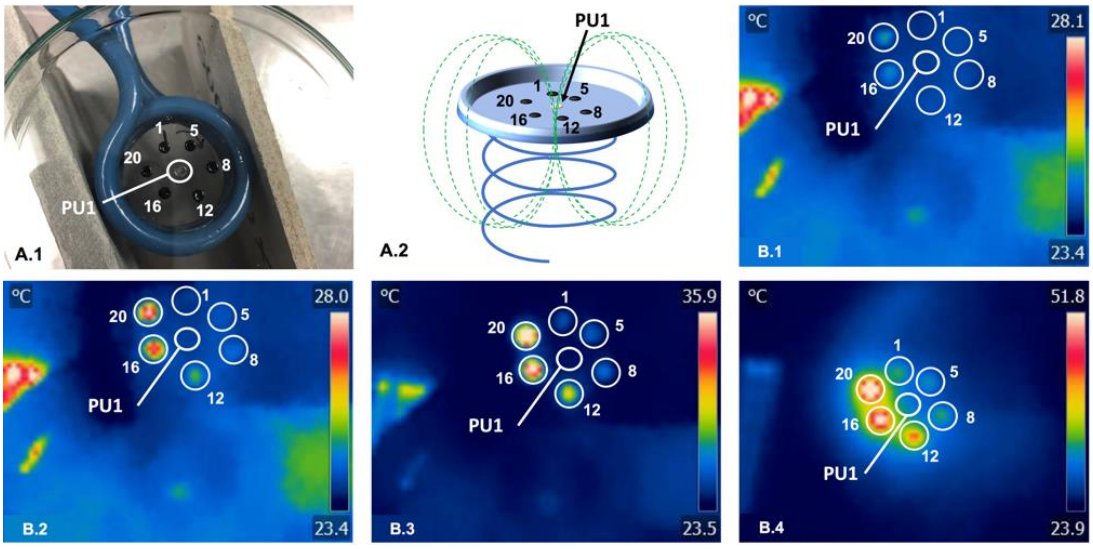


***Figure 6.3.9:*** *A.1) Image of the experiment setting and A.2) schematic side view it with the pristine SPU sample placed in the middle B.1-B.4) Thermal images of the samples showing the temperature change within almost 1 minute of OMF heating.*

Analysis of the thermal images show that the SPU **3.1 (AmMorph)** that does not contain $Fe_3O_4$ is not heated by OMF at all which proves the role of magnetic particles in heating. In this experiment set-up, where the samples are positioned above the inductor, the 20 wt% sample was heated to approximately 50 °C in one minute, whereas the temperature of the composite samples containing less than 8 wt% $Fe_3O_4$ were heated to approximately 27 °C, which was only just above ambient (23 °C) over the same time period revealing that the concentration of the magnetic particle has pronounced effect on the heat production.

### 6.3.5 Hysteresis heating debonding experiments

In order to study the debond-on-demand properties of the composite adhesives, an industry standard dog bone-shaped tensile test piece was halved, the cut surfaces sanded and then re-bonded in butt joint form using 2 mg of the adhesive by heating at 60 °C for 30 minutes in an oven (Figure 6.3.10 A). The butt joint form was used in order to effectively eliminate any vertical sheer 'friction' load from the test results. After cooling, the dog bone samples were suspended by their top end with the butt bonded central region positioned in the centre of a three-turn solenoidal inductor and a 25 g weight was hung from the bottom end (Figure 6.3.10 B).

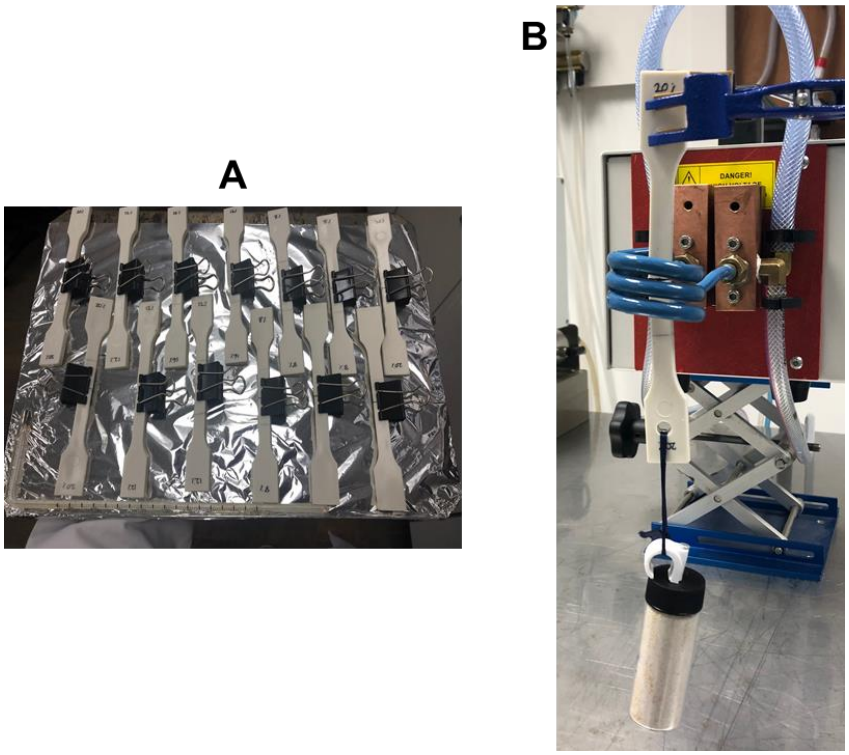


***Figure 6.3.10:*** *Images of the A) adhered half-dog bone sample preparation and B) experiment setting for the OMF initiated debonding experiments with the dog bone sample hung in the middle.*

Figure 6.3.11 shows the time required for bonding failure for composite adhesive samples containing increasing wt% of particles. It can be seen that among adhesives containing between 1 and 20 wt% iron oxide particles, OMF induced debonding occurred at decreasing times (307.5 and 22.5 seconds for 1 and 20 wt%, respectively). This can be accounted for by the greater loading of the $Fe_3O_4$ particles converting an increasing amount of OMF to heat, consequently, it takes a shorter time for the adhesives with higher loading levels of particles to reach the debonding temperature (≈ 60 °C).

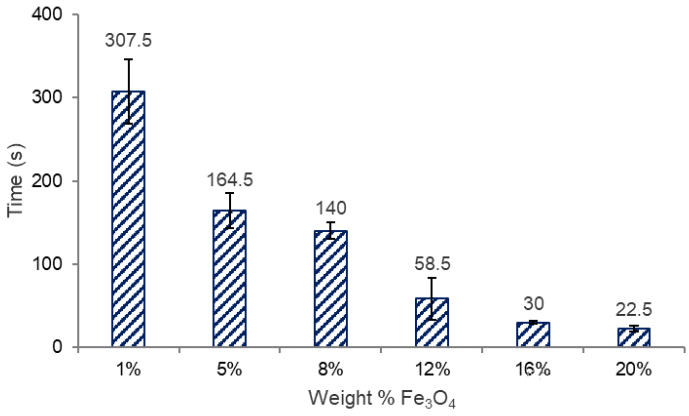


***Figure 6.3.11****: Debonding time for the composite adhesives under hysteresis heating condition. Mean values are reported above each bar. Errors are the standard deviations from the mean of 2 repetitions.*

The broken samples were then put in contact again inside the coil and OMF applied to each sample for a particular amount of time (Figure 6.3.12). The experiment proves that, after cooling down the sample for 30 seconds substrates were attached again and able to hold a 25 g weight.

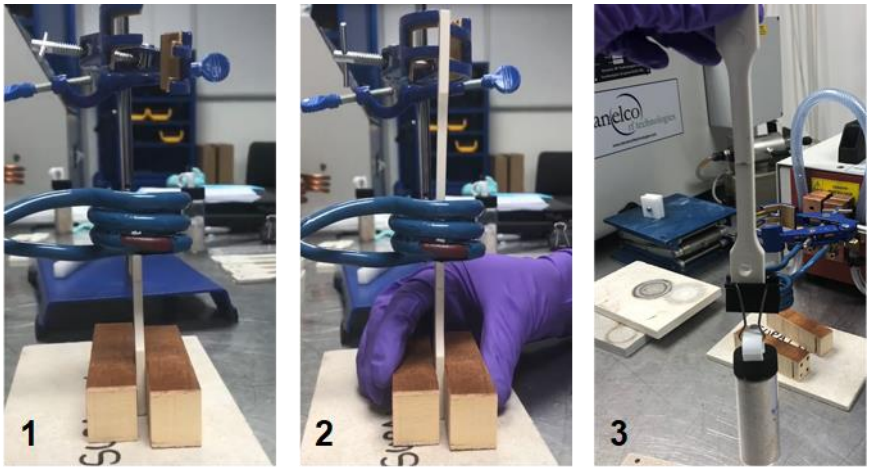


| Sample composition | 1% | 5% | 8% | 12% | 16% | 20% |
|---|---|---|---|---|---|---|
| Exposure time (s) | 160 | 140 | 120 | 100 | 80 | 60 |

***Figure 6.3.12:*** *Re-bonding process of the broken bond between plastic pieces using OMF and the related exposure time of each sample.*

Since a short-length coil is selected for the experiments, an outer magnetic field is still generated[53] and its ability to activate the magnetic particles was investigated. Two circular samples of composite adhesive were cut from the standard film cast material (d = 2 mm, approx. 2 mg). The circles of adhesive were put on a glass slide which was placed on a pre-heated hot plate (80 °C) and the polypropylene lid of a glass vial was placed on top. A 500 g weight was placed on top of the vial lid to compress the bond. After 3 minutes at 80 °C under pressure, the sample was left to cool to ambient temperature then a vial containing sand was screwed into the lid (weight of lid, vial and sand = 50 g). The debonding experiment set-up is shown schematically in Figure 6.3.13 A. The glass slide was placed between turns 2 and 3 of the coil, the distance between the centre of the coil and centre of the lid of the vial was 60 mm. A FLIR™ IR camera utilised to monitor the local changes in temperature (Figure 6.3.13 B).

The advantage of using the outer field is that the adhesive heating can be achieved by placing the sample near coil rather than in the centre of the coil. Experimentally, this allows for easier viewing of the sample and means the size of the bonded substrates is not restricted by the

dimension of the coil. However, the outer magnetic field comprises of defined magnetic field lines it is substantially less intense and evidently, less efficient in magnetizing the particles to generate heat.

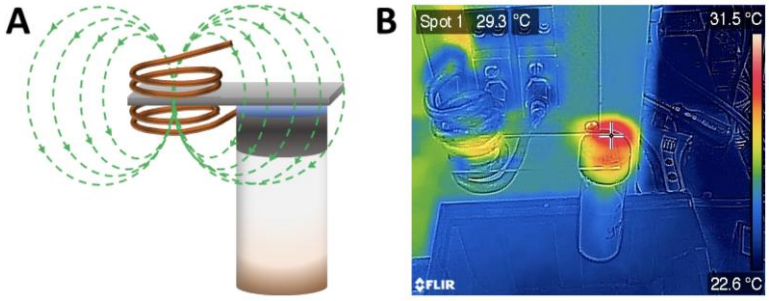


***Figure 6.3.13**: (A) Schematic view of the hysteresis debonding experimental setup; (B) thermal camera image of a vial adhered to a glass slide by the 8 wt% $Fe_3O_4$ composite adhesive and exposed to an OMF for 10 seconds. Blue/Green colours indicate ambient temperatures.*

Figure 6.3.13 B shows a thermal image of the experimental set up 10 seconds after the OMF has been switched on. The temperature of the coil has slightly increased as a result of coil resistance to the applied current.[39] It can be seen that the region where the glass slide is bound by the composite adhesive to the weight has increased in temperature by approximately 8 °C and it continued to increase until around 60 °C when the weight debonded from the glass slide under the force of gravity. The experiment was done on the composite adhesives with different wt% loading of the $Fe_3O_4$ particles. Figure 6.3.14 shows the time required for bonding failure for composite adhesive containing increasing wt% of magnetic particles. Within the timescale of the experiment (300 seconds) the composites containing 1 and 5 wt% of $Fe_3O_4$ particles did not heat sufficiently to result in debonding. However, among adhesives containing between 8 and 20 wt% iron oxide particles, OMF induced debonding occurred at decreasing times (115 and 76 seconds for 8 and 20 wt%, respectively). The phenomenon was similar to what was observed when the samples were located in the middle of the solenoid and further confirms the ability of the magnetic NPs to generate heat in OMF condition. Therefore, higher concentration of magnetic NPs results in quicker heating of the sample to debonding temperature (*ca.* 60 °C).

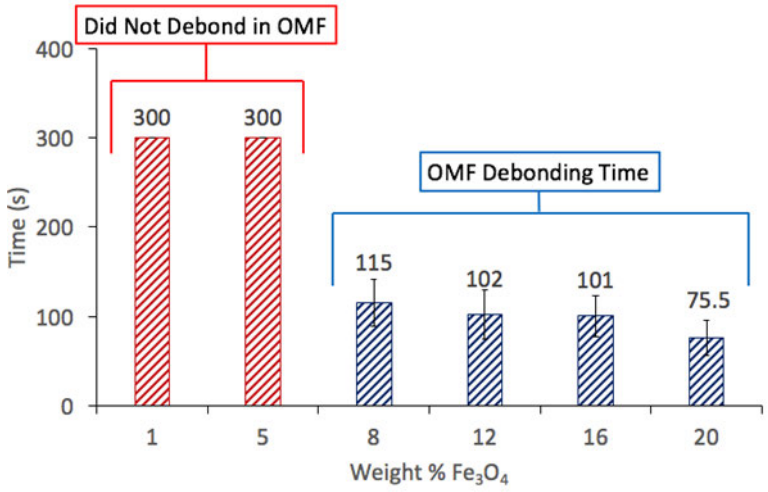


***Figure 6.3.14**: Bar chart showing the debonding time under outer OMF condition. Mean values are reported above each bar. Errors are the standard deviations from the mean of 2 repetitions.*

**Conclusions**

In conclusion, a SPU-based adhesive was synthesized that could adhere to different substrates including wood, aluminium, glass and PVC under thermal conditions. Dispersion of unmodified $Fe_3O_4$ particles up to 20 wt% was achieved by a simple melt processing protocol. Although inhomogeneously dispersed, the composite adhesives exhibited bond strengths comparable to a commercial hot melt adhesive. At 1 wt % incorporation of iron oxide particles the adhesive exhibited a significant increase in its modulus of toughness (66%) when compared to SPU **3.1 (AmMorph)**, but further addition of filler resulted in a reduction in the modulus of toughness. The composites could be heated by interaction with an OMF generated by a three-turn solenoidal inductor. The rate of heating derived from a constant source field was dependent on the loading level of iron particles. Debond-on-demand tests were carried out by placing the butt-joint bonded section of a dog bone sample in the center of the inductor and applying a 25 g weight. The time taken to debond the system under the force of gravity was inversely related to the loading level of the filler, reducing from over 5 minutes to less than 30 seconds as the filler loading increased from 1 to 20 wt%. It was also shown that the outer OMF is also capable of heating the sample to high enough temperature that the SPU soften to debond the substrates.

Adhered plastic samples were placed in an OMF and the heat dissipated by the nanoparticles weaken the adhesive and resulted in debonding the substrates in almost 5 mins at loading levels greater than 1 wt% iron oxide particles. In comparative tests, this unique OMF responsive composite exhibits considerably higher strength (210%) and toughness (67%) than commercial hot melt adhesive.

## 6.4 Future perspectives

This work shows that OMFs may be used to heat an iron oxide composite adhesive to facilitate debonding. However, this method of heating would not be as suitable for joints containing ferromagnetic or conductive materials. These materials may heat preferentially to the adhesive in an OMF, although this may also lead to softening and debonding, but by conduction from the bonded substrate to the adhesive rather than selective heating of the particles in the adhesive. The investigation of how to improve dispersion of the particles would be beneficial in effort to improve the strength of the adhesive without compromising the rapid heating and debonding behaviour of the system through non-invasive interaction with an OMF.

## 6.5 Experimental

**Materials and general methods:**

All the materials and characterisation instrumentation used in this Chapter is reported in Chapter 2, Section 2.5, unless otherwise specified. For the synthesis of SPU **3.1 (AmMorph)**, see Chapter 3, Section 3.5.2. In order to obtain IR images, a FLIR C2 camera equipped with a FOL 2 mm lens with IR resolution of 80 × 60 was used.

**OMF generator specification:** The OMF generator used (Model RFP-7500-0.4) had a maximum rating of 7.5 kW and was operating at 308 kHz with a maximum of 800 A AC current passing through a short-length solenoidal induction coil (L= 2.9 cm, d = 3.5 cm, number of turns = 3). In this experiment setting a magnetic field strength of 5000-10000 $A.m^{-1}$ was calculated to have been generated in the centre of the solenoidal inductor. Outer OMF generator specification: The OMF 7.5 kW generator was operating at 323-340 kHz with 62 A AC current passed through a short-length coil (L= 6 cm, d = 2 cm, number of turns = 5).

**Casting of PU films:** The polymer was dissolved in THF at room temperature and poured into a 15 cm × 15 cm PTFE mould and left at room temperature for 5 hours during which time a tacky film formed. The mould was then placed into a vacuum oven at 40 ºC and 800 mbar overnight for complete removal of the residual solvent. After cooling down to room temperature the homogeneous, bubble-free polymer film was easily removed in one piece from the mould.

**Composite formation:** Six composite samples which varied by the filler loading level (1, 5, 8, 12, 16 and 20 wt%) were produced using 1.0 g of the SPU **3.1 (AmMorph)** film. The film was placed on a PTFE plate and heated to 100 ºC on a preheated hot plate. When the polymer viscosity decreased sufficiently to allow mixing of the iron oxide the appropriate amount of

iron oxide was added and stirred until further mixing did not visually change the appearance of the composite.

**Lap shear sample preparation:** Using a 2 mm circle cutter, ~ 2 mg of each composite film was cut and sandwiched between two glass slides to adhere them (total weight of 10 samples = 21 mg). The glass slides were secured using paperclips to minimize movement during adhesion. The samples to be bonded were placed on a preheated hot plate at 80 °C for 3 minutes on each side. After cooling down to room temperature, the paperclips were removed, and the samples were ready for testing (Figure 6.3.6).

**Lap Shear:** The bonded glass slides were placed between the grips of the tensiometer and separated at a speed of 1 $mm.min^{-1}$ while the change in stress *vs.* changes in strain was recorded using THSSD 2020 software and the collected data plotted in Excel 365.

**Dog-bone sample preparation:** The dog-bone shaped plastic pieces were cut in half and sanded to produce a smooth to the touch cut surface. Using a 2 mm circle cutter, ~ 2 mg of each composite was sandwiched between two pieces to re-attach the sides. The pieces were then secured using paper clips. Samples were then put inside an oven at 60 °C for 30 minutes. After cooling down to room temperature, the paperclips were removed, and the samples were ready for testing (Figure 6.3.10 A).

**Imaging and image processing the composites:** After preparing the samples, a clip macro lens was attached to an iPhone 8 camera. The samples were backlit to increase the image contrast and black and white images were obtained for each sample. Images were then processed using *ImageJ* software to assess the ratio of black (iron oxide particles) to white (SPU).

**Tecbond 484-9900 testing:** A glue gun was used to continuously extrude Tecbond 484-9900 on a PTFE plate with the same thickness as our composite films (approximately 0.8 mm). A circle with 2 mm diameter was cut using a die and placed between two glass slides which were fixed with 2 paper clips to minimise movement during adhesion (weight of 10 adhesive samples = 26 mg). Samples were place on a pre-heated hot plate (80 °C) for 3 minutes before turning and heating for a further 3 minutes. After cooling to room temperature paper clips were removed prior to stress/strain testing as described above.

**OMF debonding experiment:** A prepared dog-bone shaped sample was suspended vertically through the axis of the solenoidal inductor (Figure 6.3.10 B) and a 25 g weight attached to it. An OMF (as specified above) was applied and the time required for the adhesive to fail was recorded.

## 6.6 References


1 A. H. Hofman, I. A. van Hees, J. Yang and M. Kamperman, *Adv. Mater*., 2018, **30**, 1704640.

2 C. Heinzmann, C. Weder and L. M. De Espinosa, *Chem. Soc. Rev*., 2016, **45**, 342–358.

3 W. Tan, L. Zhang and W. Shen, *ACS Appl. Mater. Interfaces*, 2017, **9**, 42366–42371.

4 A. S. Ahmed and R. V. Ramanujan, *Sci. Rep*., 2015, **5**, 13773.

5 M. Liao, P. Wan, J. Wen, M. Gong, X. Wu, Y. Wang, R. Shi and L. Zhang, *Adv. Funct. Mater*., 2017, **27**, 1703852.

6 S. B. Khan, M. T. S. Chani, K. S. Karimov, A. M. Asiri, M. Bashir and R. Tariq, *Talanta*, 2014, **120**, 443–449.

7 S. Fujii, S. Sawada, S. Nakayama, M. Kappl, K. Ueno, K. Shitajima, H.-J. Butt and Y. Nakamura, *Mater. Horiz*., 2016, **3**, 47–52.

8 C. Heinzmann, S. Coulibaly, A. Roulin, G. L. Fiore and C. Weder, *ACS Appl. Mater. Interfaces*, 2014, **6**, 4713–4719.

9 A. M. Asadirad, S. Boutault, Z. Erno and N. R. Branda, *J. Am. Chem. Soc*., 2014, **136**, 3024–3027.

10 J. Liu, Y. Tan, C, S and O. A. Scherman, *Angew. Chem*, 2018, **130**, 8992-8996.

11 M. L. B. Palacio, B. Bhushan and S. R. Schricker, *Mater. Lett*., 2013, **92**, 409–412.

12 A. O. Matos, J. O. Costa, T. Beline, E. S. Ogawa, W. G. Assunção, M. F. Mesquita, R. X. Consani and V. A. Barão, *J. Prosthodont*., 2018, **27**, 169–176.

13 S. K. Gill, N. Roohpour, Y. An, J. E. Gautrot, P. D. Topham and B. J. Tighe, *J. Biomed. Mater. Res. - Part A*, 2018, **106**, 1355–1362.

14 S. K. Gill, N. Roohpour, P. D. Topham and B. J. Tighe, *Acta Biomater*., 2017, **63**, 326–335.

15 S. J. Rowan, S. J. Cantrill, G. R. L. Cousins, J. K. M. Sanders and J. F. Stoddart, *Angew. Chemie Int. Ed*., 2002, **41**, 898–952.

16 J. Dahlke, S. Zechel, M. D. Hager and U. S. Schubert, *Adv. Mater. Interfaces*, 2018, **5**, 1800051.

17 B. T. Michal, E. J. Spencer and S. J. Rowan, *ACS Appl. Mater. Interfaces*, 2016, **8**, 11041–11049.

18 J. H. Aubert, *J. Adhes*., 2003, **79**, 609–616.

19 J. Tang, L. Wan, Y. Zhou, H. Pan and F. Huang, *J. Mater. Chem. A*, 2017, **5**, 21169–21177.

20 L. R. Hart, J. L. Harries, B. W. Greenland, H. M. Colquhoun and W. Hayes, *Polym. Chem*., 2013, **4**, 4860–4870.

21 T. Aida, E. W. Meijer and S. I. Stupp, *Science*, 2012, **335**, 813–817.

22 Y. Yang and M. W. Urban, *Adv. Mater. Interfaces*, 2018, **5**, 1800384.

23 A. W. Bosman, R. P. Sijbesma and E. W. Meijer, *Mater. Today*, 2004, **7**, 34–39.

24 P. Woodward, D. H. Merino, B. W. Greenland, I. W. Hamley, Z. Light, A. T. Slark and W. Hayes, *Macromolecules*, 2010, **43**, 2512–2517.

25 D. H. Merino, A. Feula, K. Melia, A. T. Slark, I. Giannakopoulos, C. R. Siviour, C. P. Buckley, B. W. Greenland, D. Liu, Y. Gan, P. J. F. Harris, A. M. Chippindale, I. W. Hamley and W. Hayes, *Polymer (Guildf).*, 2016, **107**, 368–378.

26 P. Cordier, F. Tournilhac, C. Soulié-Ziakovic and L. Leibler, *Nature*, 2008, **451**, 977–980.

27 S. Burattini, B. W. Greenland, D. H. Merino, W. Weng, J. Seppala, H. M. Colquhoun, W. Hayes, M. E. Mackay, I. W. Hamley and S. J. Rowan, *J. Am. Chem. Soc.*, 2010, **132**, 12051–12058.

28 S. Burattini, H. M. Colquhoun, J. Fox, D. Friedmann, B. W. Greenland, P. J. F. Harris, W. Hayes, M. E. Mackay and S. J. Rowan, *Chem. Commun.*, 2009, **44**, 6717–6719.

29 J. B. Beck, J. M. Ineman and S. J. Rowan, *Macromolecules*, 2005, **38**, 5060–5068.

30 M. Burnworth, L. Tang, J. R. Kumpfer, A. J. Duncan, F. L. Beyer, G. L. Fiore, S. J. Rowan and C. Weder, *Nature*, 2011, **472**, 334–337.

31 R. Vaiyapuri, B. W. Greenland, H. M. Colquhoun, J. M. Elliott and W. Hayes, *Polym. Int.*, 2014, **63**, 933–942.

32 S. Burattini, B. W. Greenland, D. Chappell, H. M. Colquhoun and W. Hayes, *Chem. Soc. Rev.*, 2010, **39**, 1973-1985.

33 A. Feula, X. Tang, I. Giannakopoulos, A. M. Chippindale, I. W. Hamley, F. Greco, C. Paul Buckley, C. R. Siviour and W. Hayes, *Chem. Sci.*, 2016, **7**, 4291–4300.

34 T. S. Babra, A. Trivedi, C. N. Warriner, N. Bazin, D. Castiglione, C. R. Siviour, W. Hayes and B. W. Greenland, *Polym. Chem.*, 2017, **8**, 7207–7216.

35 B. K. Storm, M. Gwisdalski, D. Lindvang and M. Rann, *Macromol. Symp.*, 2005, **225**, 205–219.

36 S. Ito, H. Akiyama, M. Mori, M. Yoshida and H. Kihara, *Macromol. Chem. Phys.*, 2019, 1900105, 1–6.

37 S. Ito, H. Akiyama, R. Sekizawa, M. Mori, M. Yoshida and H. Kihara, *ACS Appl. Mater. Interfaces*, 2018, **10**, 32649–32658.

38 C. C. Corten and M. W. Urban, *Adv. Mater.*, 2009, **21**, 5011–5015.

39 B. J. Adzima, C. J. Kloxin and C. N. Bowman, *Adv. Mater.*, 2010, **22**, 2784–2787.

40 Z. Li, M. Kawashita, N. Araki, M. Mistumori and M. Hiraoka, *Bioceram. Dev. Appl.*, 2011, 1 DOI:10.4303/bda/D110128.

41 S. L. Semiatin and S. Zinn, in Elements of Induction Heating: Design, Control, and Applications, ed. C. publication Service, Electric power research institute, 6th edn., 2002, p. 291.

42 R. Belouadah, D. Guyomar, B. Guiffard and J. W. Zhang, *Phys. B Condens. Matter*, 2011, **406**, 2821–2826.

43 N. Hohlbein, A. Shaaban and A. M. Schmidt, *Polymer (Guildf).*, 2015, **69**, 301–309.

44 T. Bayerl, M. Duhovic, P. Mitschang and D. Bhattacharyya, *Compos. Part A Appl. Sci. Manuf.*, 2014, **57**, 27–40.

45 K. A. Houton, G. M. Burslem and A. J. Wilson, *Chem. Sci*., 2015, **6**, 2382–2388.

46 M. M. Coleman, K. H. Lee, D. J. Skrovanek and P. C. Painter, *Macromolecules*, 1986, **19**, 2149–2157.

47 A. S. Eggeman, S. A. Majetich, D. Farrell and Q. A. Pankhurst, *IEEE Trans. Magn.*, 2007, **43**, 2451–2453.

48 J. Fox, J. J. Wie, B. W. Greenland, S. Burattini, W. Hayes, H. M. Colquhoun, M. E. Mackay and S. J. Rowan, *J. Am. Chem. Soc*., 2012, **134**, 5362–5368.

49 M. Shahrousvand, M. S. Hoseinian, M. Ghollasi, A. Karbalaeimahdi, A. Salimi and F. A. Tabar, *Mater. Sci. Eng. C*, 2017, **74**, 556–567.

50 P. Jayakrishnan and M. T. Ramesan, *Mater. Chem. Phys*., 2017, **186**, 513–522.

51 S. J. Eichhorn, A.Dufresne, M. Aranguren, N. E. Marcovich, J. R. Capadona, S. . Rowan, C. Seder, W. Thielemans, M. Rowan, S. Renneckar, W. Gindl, S. Veigel, J. Keckes, H. Yano, K. Abe, M. Nogi, A. N. Nakagaito, A. Mangalam, J. Simonsen, A. S. Benight, A. Bismarck, L. A. Berglund and T. Peijs, *J. Mater. Sci*., 2010, **45**, 1–33.

52 S. Burattini, H. M. Colquhoun, B. W. Greenland and W. Hayes, *Faraday Discuss*., 2009, **143**, 251–264.

53 A. Boghi, F. Russo and F. Gori, *J. Magn. Magn. Mater*., 2017, **437**, 86–97.

# Chapter 7

## Conclusions and Future Studies

### 7.1 Conclusions

3D printing is a new method of production giving rise to generation of customisable and complex structures. Structures with high level of architectural complexity can potentially be produced with precision exploiting various methods of 3D printing. However, it has been proven that the limiting factor for the uptake of 3D printing in mainstream manufacturing processes is the choice and availability of suitable materials. Indeed, construction of any 3D design is possible by considering use of the most appropriate 3D printers and associated hardware, however, at the present time the library of materials that is available is insufficient in terms of mechanical properties and functionality in order to fulfil this objective. Therefore, establishing a library of diverse materials that possess different mechanical, thermal and rheological properties would advance the field of 3D printing towards industrial use considerably. This project has attempted to address this need by developing and accessing supramolecular polymers as the inks for 3D printing. Although the mechanical properties of supramolecular polymers are often inferior to those of conventional covalently-linked polymers, their responsiveness to appropriate stimuli (in the case of this study, heat) was shown to be beneficial in hot melt extrusion 3D printing. The other focus of this project was the investigation of different methods of modification and optimisation of supramolecular polymers suitable for 3D printing techniques as well as some initial study of the application of these materials within different manufacturing sectors.

In order to fulfil these aims, a supramolecular polyurethane was first selected to be used as excipient for 3D printing of a drug release implant. 3D printing can give rise to customisable implant containing different active drugs for individual patient, however, hot melt extrusion printing of conventional materials has proved problematic. The advantage of supramolecular materials is that their supramolecular interactions dissociate at relatively lower temperature which results in a material with low viscosity that is processable and printable. Such a low processing temperature is desired since the contained active drugs targeted for use in the implants are typically low molecular weight species possessing functionalities which are prone to degradation at high temperatures. In this study, the supramolecular polyurethane

(SPU) was formulated with PEG and paracetamol as the model drug and then extruded at elevated temperature to form an implant. It was also shown that incorporation of PEG results in an increase of the rheological cross over temperature at which the formulation switches from an elastic material to a viscous mixture. Although the processing temperature was still within the temperature window of the experiment. It was illustrated that by formulating the selected supramolecular polyurethane with PEG the release rate can increase and the model drug can be released over a timeframe of ~8.5 months which is a suitable timescale for implant applications. Interestingly, after analysis of the dissolution characteristics of the 3D printed prototype implant, the bulk material was found to undergo a significant deformation in shape at body temperature, this was attributed to the rheological cross-over temperature (42.1 °C and 46.0 °C) of the formulation that is close to body temperature (37 °C) at which the experiment was carried out.

In order to address this problem, reinforcement of the material could be beneficial. By increasing the content of the hard segment within the phase separated SPU, the processing temperature of the material would also increase potentially leading to the shape of the 3D printed implant material being maintained at elevated temperatures. However, the increase in the processing temperature should be as such that the material remains processable at the 3D printing temperature frame. To that aim, the *in situ* production of complementary low molecular weight additive (LMWA) was studied. During the synthesis of the polyurethane the bis urea LMWA **3.2 (R)** was made as a by-product by controlling the stochiometric ratios of the starting materials. By taking this approach reinforced polyurethane with different content of LMWA were synthesised and their mechanical and thermal properties studied. It was found that by increasing the content of LMWA the material reinforced and the tensile strength increased, however, the material became more brittle in nature. Consequently, based on the binding constant and the concentration of the LMWA **3.2 (R)**, a material with desired properties can be synthesised. This investigation also revealed that the *in situ* method results in more efficient mixing of LMWA with the polyurethane network compared to post synthesis mixing of the two components. Therefore, the *in situ* method was taken and a small library of reinforced supramolecular polyurethane was synthesised containing 4 wt% LMWA. These synthesised materials were studied under hot-melt extrusion 3D printing condition and it was shown that the polyurethane with self-assembly motifs namely, *N*-(4-methoxybenzyl)-1-(4-nitrophenyl)methanamine, 2-morpholinoethan-1-amine and 3-aminopropane-1,2-diol were suitable to be printed under extrusion condition. In stark contrast, the SPUs with 2-ureido-4[1H]-pyrimidinone (UPy) and benzylamine (BenzAm) could not be extruded under the desired experimental conditions since even the highest temperature that could generate by

the printer was insufficient to dissociate the supramolecular interactions within the polymer networks to generate a viscous-like material.

The same procedure of reinforcing supramolecular polymers by introduction of bis-urea moieties was taken to produce a mechanical gradient material using a reactive extrusion (REX) printer. A reinforced SPU was synthesised containing 15 wt% LMWA as well as the pure SPU, each of which demonstrate different mechanical properties. They were then introduced into the REX printer and the feed ratio adjusted by a controlling unit. Upon making careful variations in the ratio of the feed stock a printed part with varied percentage of LMWA along its length was created. It was shown that each section of the printed part exhibited distinct mechanical properties. Therefore, it is suggested that this design can be applied to produce parts with either desired point of failure or elasticity.

Additionally, the reinforcement of SPU utilising inorganic silica nanoparticles (SiNP) and the application of these composites in 3D printing was studied. Unfunctionalised silica nanoparticles were synthesised and the corresponding nanocomposite generated utilising different methods. Firstly, a solution of the SPU was blended under reflux with the SiNP and in an alternative approach, the SiNPs were added to the reaction mixture after formation of the prepolymer. It was shown that the second method was more efficient in reinforcing the material by an increase of 26% in the ultimate tensile strength when compared to the blended material. Furthermore, amine functionalisation introduced on the surface of the SiNP and the same *in situ* approach was taken to produce nanocomposites. Interestingly, the amine functionalised SiNPs nanocomposites featuring the amine functionalised SiNPs exhibited inferior mechanical properties when compared to the nanocomposites containing unfunctionalised SiNP as a result of the high tendency of the nanoparticles to aggregate in the SPU bulk phase. To address this problem a new method of preparation involved with higher shear was utilised *i.e.* a reactive extrusion 3D printer equipped with a static mixer. Implementation of the REX printer enables nanocomposite production taking advantage of its high shear as well as the established *in situ* incorporation method. Additionally, in order to reduce the tendency of the amine functionalised SiNPs to aggregate in the SPU bulk phase, alkyl functionality (propyl) was also introduced on the surface to control the hydrophilicity as well as acting as a steric spacer. The molar ratio of propyl to propylamine functionality was varied to identify the optimised percentage to achieve reactive nanoparticles with acceptable morphology characteristics. Two inks, namely the isocyanate ink and the polyol ink containing the SiNP of interest, were prepared and fed into the printer. The inks were then mixed and react during the deposition to form a polyurethane nanocomposite. By analysing the printed nanocomposites, it was revealed that the utilisation of SiNPs at which the

theoretical molar ratio of propyl to propylamine is doubled, afforded a polyurethane nanocomposite with superior mechanical properties when compared to the parent SPU.

In order to further validate this method and make a comparison with a commercially available SiNP, the same approach was taken to produce a polyurethane containing commercial SiNPs (the commercial SiNP have polydimethylsiloxane (PDMS) functionality on its surface). As it was expected the precursor ink contain the commercial SiNP exhibited superior mechanical properties when compared to the synthesised dual-functionalised SiNP with regard to its considerably higher viscosity and modulus (*ca.* 2 orders of magnitude). Interestingly, when it comes to comparing the printed polyurethane composites of the two inks, they demonstrate similar mechanical properties regardless of their precursors. This phenomenon is highly desirable as the processability of an ink with lower viscosity and modulus in a 3D printer is more straightforward and requires less energy.

A different inorganic filler was also introduced into a supramolecular polyurethane system in order to make a responsive polyurethane. The selected supramolecular polyurethane was an hot melt adhesive and was able to adhere to different substrates upon solidification. Since $Fe_3O_4$ nanoparticles are able to produce heat upon exposure to oscillatory magnetic field (OMF), they were incorporated into the SPU system. The prepared magnetic nanocomposite was then used to adhere two substrates together and these assemblies were transferred into an OMF inside a solenoid and it was shown that the heat produced by the magnetic nanoparticles was sufficient to dissociate the supramolecular interaction and therefore a loss in viscosity of the adhesive which results in successful debonding.

## 7.2 Future Studies

A variety of different avenues of research can be suggested to pursue the field of 3D printing of supramolecular polymers by development of different classes of supramolecular polymers and their composites. Currently several research groups are investigating this route for various applications.[1-4] However there is still a demand to not only develop specific materials for targeted niche applications but to also investigate generic methods of material preparation or reinforcement that can be applied to a wide range of supramolecular polymers so they can be used readily in an industrially-relevant applications. An example of such use could be the 3D printing of a drug release implant or the reinforcement method discussed in Chapter 2 and 3 of this thesis. In addition, combination of these methods and the production technique used to generate the mechanical gradient polymer image reported in Chapter 5 can give rise to a customised multiple drug implant (See Figure 7.2.1). Since the introduction of low molecular weight additives into the supramolecular system increases the concentration of the

supramolecular interactions and reinforces the material, the decomposition process and its rate would change. Therefore, materials with different concentration of the reinforcement organic additives would present different decomposition time. By taking advantage of this feature of 3D printing, a multi-drug implant could also be printed in which the excipient releases each drug at different rates and tailored to an individual patients need. In order to realise this idea, the biocompatibility of the LMWA and the percentage of cell viability is of high importance.

In order to ensure the biocompatibility of the filler, one method could be to utilise a nature-base biocompatible filler to produce a gradient system. For example, instead of synthesising a bis-urea moity as the LMWA, a sorbitol-based gelator could be used to reinforce the mechanical properties of a SPU through formation of a secondary supramolecular network.[5,6]

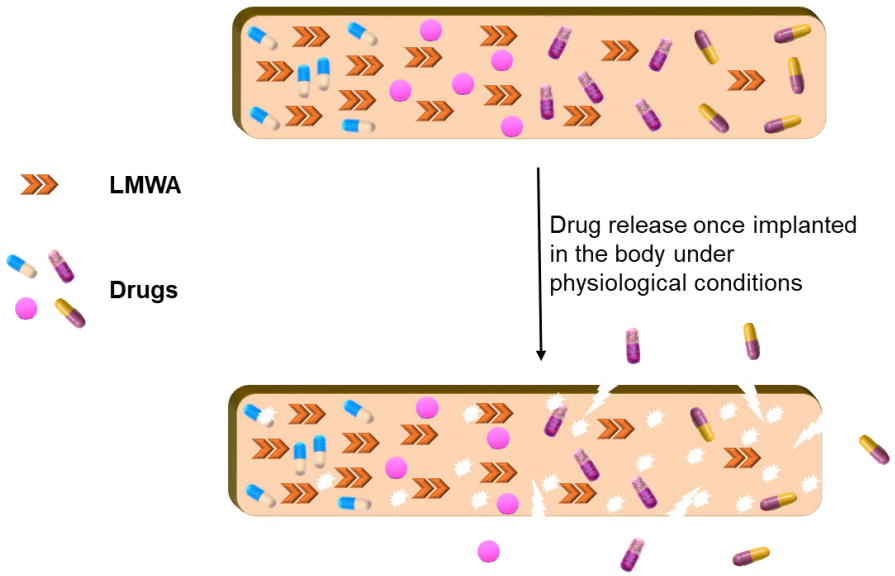


***Figure 7.2.1****: An illustration of the proposed multi-drug implant representing different concentration of the released drugs.*

In addition to the sorbitol-based gelator and natural materials, a variety of other low molecular weight gelators have been reported that could be used to form a secondary network and increase the concentration of the supramolecular interaction. LMWGs with reactive functionality on their chain-end can either be used as chain extender during the polymerisation or to be blended into a supramolecular polymer (see Figure 7.2.2 for example structures). The blended and covalently attached LMWG in supramolecular polymers are anticipated to offer very distinct properties. A comparison of the mechanical properties and structure to property relationship of the two types of organo-reinforced materials could be interesting. However, it is worth to note that considering the properties that each of these preparation methods could offer, the blending method has proven to be the more efficient and

practical of the two within the scope of the 3D printing. For example, in order to establish a library of materials including their properties and potential applications for a "plug and play" 3D printing, the blending method would be more feasible and easier to implement. The blending method would also be more practical within the industrial scope, since it does not involve any synthesis method development or modification.

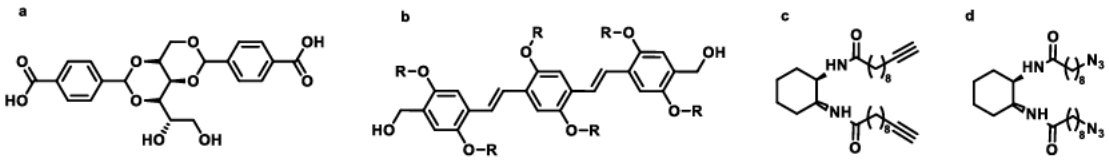


***Figure 7.2.2:*** *Structures of some difunctional LMWGs that have potential application in reinforcement of supramolecular polymers.*[7-9]

The main advantage of exploiting LMWGs in reinforcing the supramolecular polymers in 3D printing is their dynamic nature. Indeed, the reinforcing filler would not result in the blockage of the printer's nozzle, rather it would contribute towards the loss in viscosity of the material upon melt or dissolution by dissociation of the supramolecular interactions. In fact, it can be said that by incorporation of LMWG within a supramolecular polymer network, a dual supramolecular network would form which could potentially enhance the mechanical properties in a synergistic fashion.

## 7.3 References


1 X. Zhai, Y. Ma, C. Hou, F. Gao, Y. Zhang, C. Ruan, H. Pan, W. W. Lu and W. Liu, *ACS Biomater. Sci. Eng*., 2017, **3**, 1109–1118.

2 A. M. Pekkanen, R. J. Mondschein, C. B. Williams and T. E. Long, *Biomacromolecules*, 2017, **18**, 2669–2687.

3 L. R. Hart, S. Li, C. Sturgess, R. Wildman, J. R. Jones and W. Hayes, *ACS Appl. Mater. Interfaces*, 2016, **8**, 3115–3122.

4 H. Rupp, D. Döhler, P. Hilgeroth, N. Mahmood, M. Beiner and W. H. Binder, *Macromol. Rapid Commun*., 2019, **40**, 1–6.

5 X. Chen, C. E. Zawaski, G. A. Spiering, B. Liu, C. M. Orsino, R. B. Moore, C. B. Williams and T. E. Long, *ACS Appl. Mater. Interfaces*, 2020, **12**, 32006–32016.

6 L. Jin, H. Wang and Y. Yang, *Compos. Sci. Technol*., 2013, **79**, 58–63.

7 D. J. Cornwell and D. K. Smith, *Mater. Horizons*, 2015, **2**, 279–293.

8 D. Dasgupta, S. Srinivasan, C. Rochas, A. Ajayaghosh and J. M. Guenet, *Langmuir*, 2009, **25**, 8593–8598.

9 D. D. Díaz, K. Rajagopal, E. Strable, J. Schneider and M. G. Finn, *J. Am. Chem. Soc*., 2006, **128**, 6056–6057.

# Appendix

## A.1 Rheology profiles of the 3.1 and the reinforced analogues

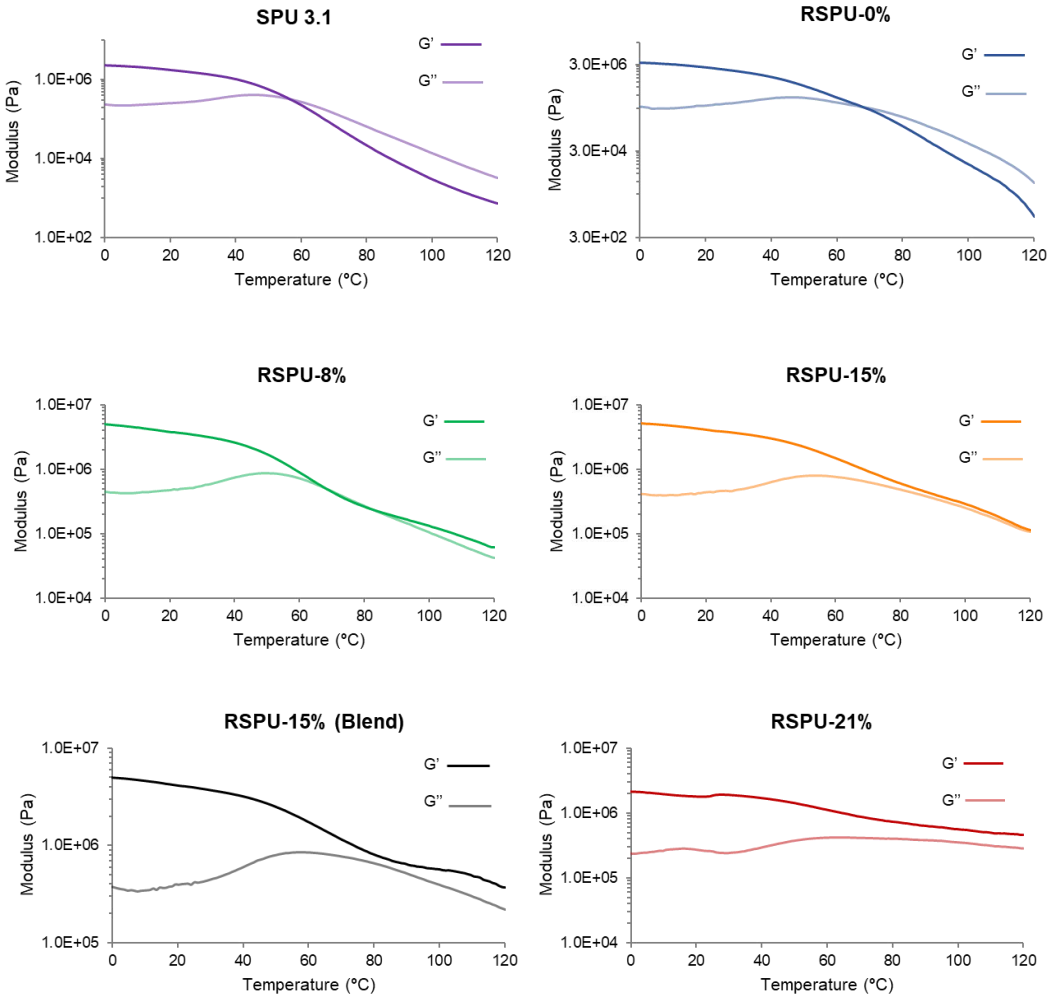


***Figure A 1**:* Rheology graph of moduli vs temperature for **SPU 3.1** and **RSPU**s.

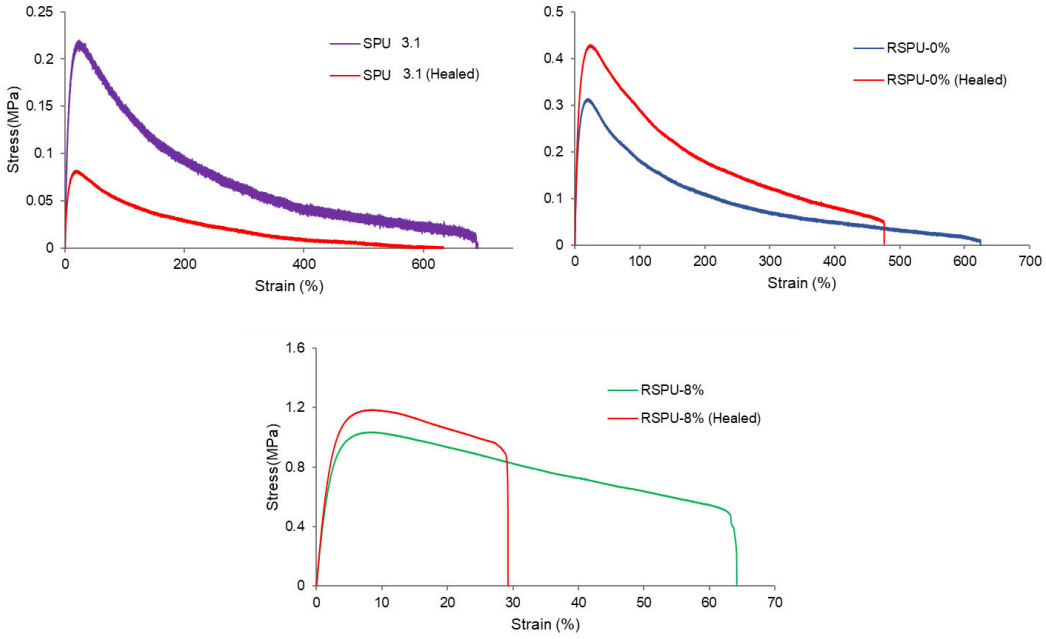


***Figure A 2**: Healing tensile graph of **SPU 3.1**, **RSPU-0%** and **RSPU-8%**.*

## SPU 3.1 (PropDiol)

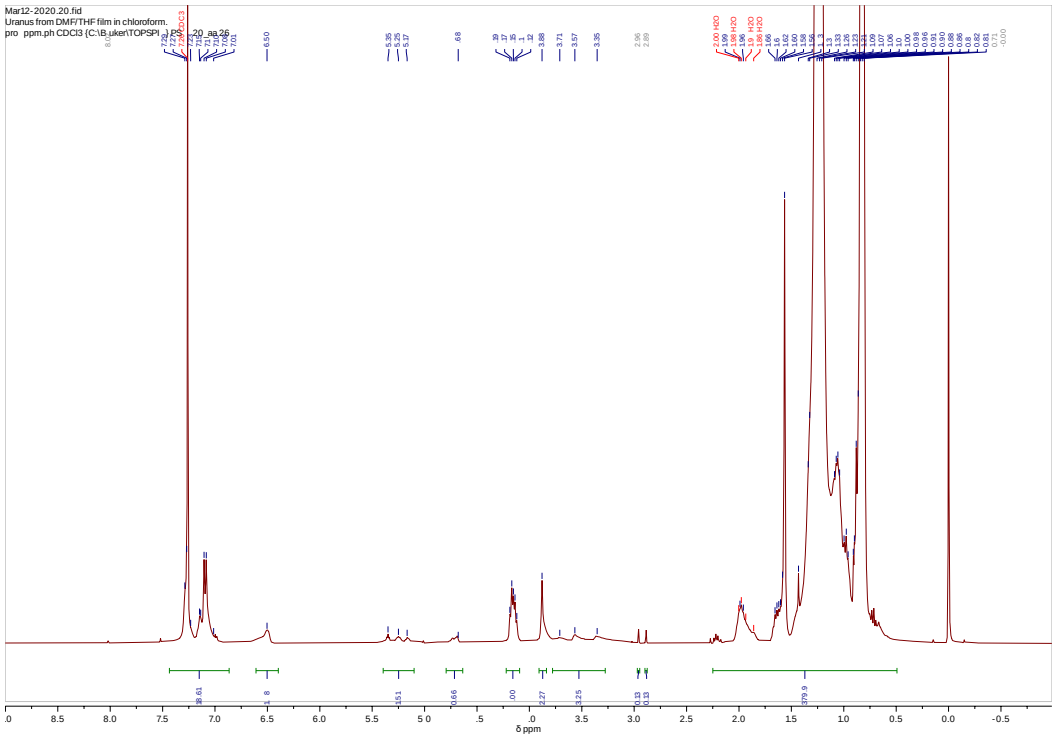


***Figure A 3**: [1]HNMR of the **SPU 3.1 (PropDiol).***

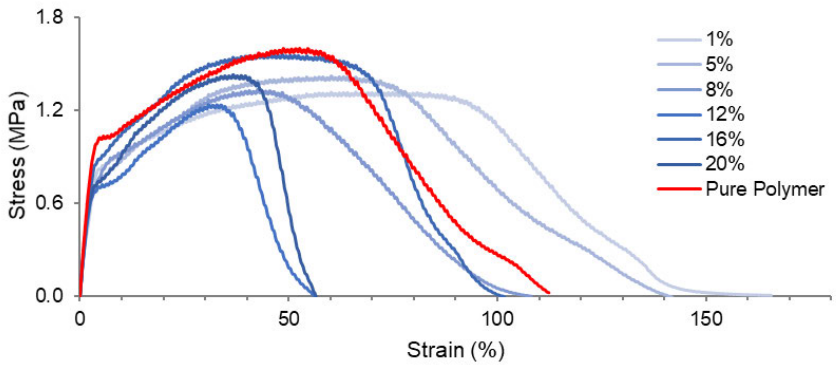


***Figure A 4**: Representative stress-strain graph of the magnetic nanocomposites and the **SPU 3.1 (AmMorph)**.*

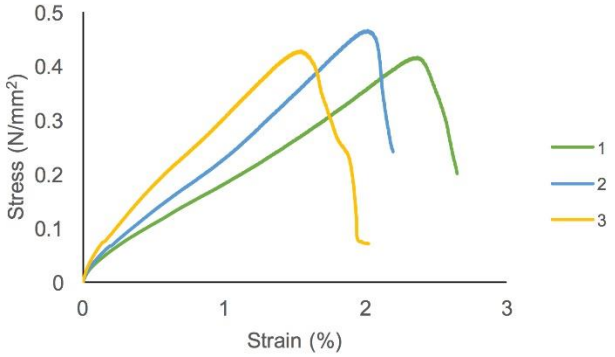


***Figure A 5:** Lap shear test result of three repeats of the glass slides samples adhered by the Tecbond™ hot glue.*